An X-Ray Absorption Fine Structure Study

of

Semiconductor Nanoclusters

A Thesis
Presented to
The Academic Faculty

By

Raed Saed Shorrosh

In Partial Fulfillment
of the Requirements for the Degree
Doctor of Philosophy in Chemistry

Georgia Institute of Technology
November 1993

An X-Ray Absorption Fine Structure Study

of

Semiconductor Nanoclusters

Approved by :

Ronald H. Felton, Advisor

Lawrence A. Bottomley

Sidney L. Gordon

Date Approved by Chairman November 23, 1993

DEDICATION

This dissertation is dedicated to my parents, Saed and Samera Shorrosh, and to my beloved Suhad.

ACKNOWLEDGMENTS

The author would like to express his appreciation to Professor R. H. Felton, for suggesting this thesis, and for his guidance and help.

Thanks also to Dr. L. A. Bottomley for his helpful suggestions. Thanks also to Joe Coury and Tiger Pitts for the excellent AFM and STM work.

The author greatly acknowledges the help of Dr. L. R. Furenlid at the NSLS and the support of technicians and staff at the X-11 beam line. X-11 is supported by DOE grant DE-AC02-76CH00016. Also the author greatly acknowledges the department of Chemistry & Biochemistry for financial support and travel funds.

The author extends his deepest thanks for his parents and brothers for their love and support. Special thanks to my brother Bishara, his wife Rebecca, and their children Matthew and Deanna. Also, the author extends his gratitude to the members of the Bible study group that meet at the house of Byron and Florence Attridge for their prayers and spiritual support. The author is very thankful for the prayers, love, and friendship of Ann Carter and Florence Attridge.

Finally, the author offers his deepest thanks to the One who gave him breath to breath, life to live, and hope to seek. To the One who is eternal and glorious, to the merciful and most gracious LORD, to Him be all honor, glory, and praise, in Christ Jesus, for ever and ever.

TABLE OF CONTENTS

LIST OF TABLES

LIST OF ILLUSTRATIONS

Page

LIST OF ABBREVIATIONS

AFM	Atomic Force Microscopy
FT	Fourier Transform
MPA	3-Mercaptopropanoic Acid
PhSH	Thiophenol
QCE	Quantum Confinement Effects
RSeH	Benzeneselnol
STM	Scanning Tunneling Microscopy
ZnSPH45	MPA Capped ZnS Cluster with $[S^{2-}]/[MPA] = 45$, and pH Adjusted.
ZnS20 or SZn20	Zn-Edge or S-Edge XAFS for ZnS Cluster with R = 20
XAFS	X-Ray Absorption Fine Structure
XRD	X-Ray Diffraction
$\chi(k)$	Normalized XAFS Function
$\mu(k)$	X-Ray Cross Section

SUMMARY

Zinc sulfide nanoclusters ranging in size from 1 to 6 nm in diameter were prepared using various methods. The structure of the clusters was studied using XAFS, XRD, structure simulations, and chemical analysis. The XAFS of ZnS clusters showed a relatively strong second shell that was much reduced from what was expected due to surface bond truncations. The reduction of the second shell was explained with a model that assumed the presence of a disordered layer of the cluster. The XAFS second shell coordination number was used to calculate the thickness of the disordered layer, which was found to be the largest for small clusters and on the order of a second shell distance. The capping groups were found to be mostly in a bridging rather than in a terminating position. The surface of the smallest cluster was almost completely passivated by the capping group; in larger clusters ~20% of the surface sites were capped. We have shown that a smooth range of cluster size can be prepared for ZnS ranging from 15 Å to 40 Å by using different ratios of capping group to sulfide in the reaction mixture or by changing the pH of the solutions. Clusters capped with terminal thiamine and thiocarboxylates were prepared and used for imaging using AFM and STM methods. The nature of the interactions between the clusters and the surfaces was dominated by electrostatic interactions. Cadmium sulfide clusters also were prepared, but in most cases the clusters were a mixture of cubic and hexagonal phases. XAFS and XRD data were obtained on CdS clusters both in Nafion and as capped particles.

CHAPTER I

INTRODUCTION

Semiconductor Nanoclusters

Semiconductor clusters of diameters from 1 to about 20 nm in diameter, often called nanoclusters, quantum dots, or Q-particles, have been the object of intensive study in the last few years[1,2]. The reason for this interest is that small clusters have optical and/or electronic properties that are dramatically different from those of the bulk, even though the short-range structure is essentially the same as in bulk. In addition to the optical and electronic properties of these clusters, they are also of interest as a new class of magnetic materials[3], catalytic materials[4], and precursors to bulk synthesis[5], and in the preparations of highly crystalline thin films[6,7].

Historically these materials drew attention in the early 1980s when A. I. Ekimove and his colleagues at the Vavilov Optical Institute in St. Petersburg, noticed unexpected peaks in the absorption spectra from glass samples containing cadmium sulfide or cadmium selenides[8]. These samples were subjected to intense heating to change the color of the glass. Shortly after, Efros *et. al*[9] explained that the unusual peaks in the optical spectra were due to quantum-confinement effects (QCE) of cadmium sulfide/selenide nanoclusters that precipitated in the glass during the heat treatment process used to change

the color of the glass. Similar results were achieved independently by Louis E. Brus and co-workers[10,11,12] at AT&T Bell Laboratories using colloidal suspensions of semiconductor nanocrystals in solution. The growth and size of the nanocrystal were controlled by arrested precipitations after a certain time. Brus and co-workers found that the absorption edge (threshold) shifted dramatically from that of the bulk to higher energies. This shift in the absorption energy was correlated with the size of the cluster and was shown to be caused by quantum confinement[13,14].

Essential to the understanding and controlling of the optical, electronic, physical, and chemical properties of these samples is the structure of the nanocrystals, especially at the surface. In this work, the structure of the nanoclusters of CdS and ZnS is studied using X-ray Absorption Fine Structure (XAFS), X-ray diffraction (XRD) and chemical analysis. Of interest to this work was investigating the bonding geometry of the surface capping group, its concentration, and effect on the crystallinity of the clusters as seen by XAFS and XRD. Also of prime interest was the preparation of nanoclusters that were capped with special capping groups that enabled the clusters to adsorb on surfaces. The assembling of these nanoclusters on different surfaces was investigated by Scanning Tunneling Microscopy (STM) and Atomic Force Microscopy (AFM). The importance of these experiments is that they offer new methods in which concentrated nanocluster arrays can be fabricated for potential applications as nonlinear material optical material.

In this chapter the quantum confinement effect is explained and the optical properties of the nanoclusters and their possible applications are presented. Finally, the methods of synthesis and characterization of nanoclusters, especially of those for CdS and ZnS nanoclusters, are reviewed.

Quantum Confinement Effects (QCE)

The properties of semiconductor nanoclusters depend on their size[1]. One of the most studied examples is the quantum confinement effect which is manifested by the shift of the absorption edge of the semiconductor to the blue as the size of the cluster increases. In bulk semiconductors, the electron and the hole interact together with a screened Columbic interaction to form the so-called Mott-Wannier exciton. The radius of the interaction is called the Bohr radius of the exciton a_B and is given by

$$a_B = \frac{\hbar^2 \varepsilon}{e^2}\left[\frac{1}{m_e} + \frac{1}{m_h}\right] \qquad \textbf{(1.1)}$$

where ε is the dielectric constant and m_e and m_h are the electron and hole effective mass, respectively. For CdS (m_e=0.18, m_h=0.51)[15], the Bohr radius of the exciton is ~28 Å, and for ZnS (m_e=0.25, m_h=0.59)[16] is ~17 Å. Quantum confinement effects occurs when the radius of the semiconductor cluster is comparable to or less than the exciton radius[1,2]. At such sizes the effect of the confinement of the electron and the hole resembles the confinement of an electron in a box. The size dependent shift in the exciton energy relative to the bulk band gap was derived[9,13,17] as

$$\Delta E = \frac{\hbar^2\pi^2}{2R^2}\left[\frac{1}{m_e}+\frac{1}{m_h}\right] - \frac{1.786e^2}{\varepsilon R} - 0.248e^4E^*_{RY} \qquad (1.2)$$

where R is the radius and E^*_{Ry} is the effective Rydberg energy, $e^4/(2\varepsilon^2\hbar^2[m_e^{-1} + m_h^{-1}])$. The first term, which has a $1/R^2$ dependence is the particle-in-a-box quantum localization energy; the second term is the columbic energy with 1/R dependence; the last term is due to correlation effects. This model predicts that the excitonic energy will shift to higher energy with respect to the absorption edge as the size decreases. This model is therefore physically correct but fails to give accurate quantative results as compared with experimental values, especially for small clusters where this approximation (also known as the effective mass approximation) is no longer valid. For a more accurate description of the exciton energy, a higher level calculation was performed[18].

Quantum confinement effects on ionization potentials, electron affinities, and redox potentials are discussed in the literature [11,13,14].

Nonlinear optical properties

Another manifestation of the size effect are the nonlinear properties of the semiconductor nanoclusters[19]. The importance of the nonlinear properties of the nanoclusters stems from the possible applications of these materials in an all-optical or opto-electronical computer technology[20,21]. The concept of such technology has attracted much attention because of its potential for extreme speeds and parallel processing capabilities. These technologies depend on the development of bistable devices which

acts as light amplifier and switches. The requirement of such materials is the capability of rapid switching speed (picosecond) and extreme photostability. One fulfillment of such conditions is the use of third-order nonlinear optical properties, $\chi^{(3)}$. Such materials, when illuminated with high intensity laser, will affect the refractive index of the material leading to a switch from an opaque to transmitting state. The semiconductors can perform such switching near their band-edge wavelength, but the speed of the refractive index effect is slow, usually, due to a long free-carrier life time. Therefore increasing the speed of switching involves providing more sites for efficient removal of these free-carriers. This can be accomplished by increasing the defect sites. The surface sites can be viewed as such defect sites. Thus to increase the defect sites, smaller semiconductors particles are needed[22]. This was the major reason for the development of these new class of materials.

Third-order nonlinear effects can be classified as those that affect the index of refraction, n_2 (n_2-effect), and those that affect the ability of the material to absorb energy (resonant or photochromic effects)[21]. Nanoclusters of CdS were found to have attractive nonresonant $\chi^{(3)}$ properties. The first study of the nonresonant third-order optical nonlinearity of quantum-confined CdS clusters was reported by Cheng *et. al.*[23] using third order harmonic generation from 1.91 to 0.64 μ. They observed that the nonlinearity increases with the increase in the cluster size. The intrinsic, nonresonant $\chi^{(3)}$ for approximately 30 Å, approximately 15 Å thiophenolate-capped CdS clusters, and $(Cd_{10}S_4(SPh)_{16})^{-4}$ molecular clusters were 3.3×10^{-10}, 2.5×10^{-11}, and 4.7×10^{-12} esu, respectively. To utilize this large nonresonant nonlinearity, the authors suggested that it

is necessary to incorporate these clusters into a sample in high concentrations. Recently, Wang and Herron [24] reported the third-order nonlinear susceptibilities $\chi^{(3)}$ of CdS clusters from 7 to 120 Å, measured by a third-harmonic generation technique at a fundamental wavelength of 1.91 μ. In the size regime studied, the value of $\chi^{(3)}$ first increases with cluster size and then levels off for a cluster diameter larger than 60 Å. The volume normalized $\chi^{(3)}$ of CdS cluster was found to be about a factor of two higher than that of the bulk. These data can be explained by the enhancement in electric field inside the clusters due to the dielectric confinement effect [25,26]. When CdS clusters, imbedded in a dielectric medium, are illuminated with light, the field intensity near, at, and inside the cluster surface can be enhanced considerably compared to the incident intensity due to the boundary established by the different refractive indicies of the clusters and the surroundings.

Resonant nonlinear effects in semiconductor nanocrystal were also observed and were found to be correlated with size. For CdS nanoclusters, the resonant nonlinear effects were found to be the largest for the smaller ($R<a_B$)clusters due to an increase in the oscillator strength per unit volume of the exciton for the smaller clusters [13,17,28]. Wang *et. al.*[29] reported the optical nonlinearity, expressed as α_2/α_o ,of 50 Å CdS clusters in Nafion (perfluoroethylenesulfonic acid ion exchange polymer) film to be -6.1 x 10^{-7} cm^2/W at 480 nm. The nonlinearity originates from the bleaching of the excitonic absorption owing to the presence of trapped carriers on the cluster surfaces. By passivating the surfaces with ammonia, the authors have shown that the nonlinearity can be controlled by surface chemistry. This number for the nonlinear parameter of CdS is

to be compared with the commercial Corning 3-69 glass nonlinearity of α_2/α_o =-1 x 10^{-7} [30].

Preparation Methods and Literature Review of Nanoclusters

Various methods of preparations of nanoclusters were developed. The goal in synthesis of nanoclusters is to prepare samples in large quantities that have narrow size distributions. Synthesis methods that have been developed include the use of polymers, inverse micelles, organic capping reagents, zeolites, porous glass, biosynthesis, Langmuir-Blodgett films, layered phosphonates, and lipid bilayer membranes. Each of these methods uses a macromolecular stabilizer or surface reactions that terminate the particle growth by "capping" the surface of the cluster. In this section, some of the most important method of preparation will be discussed and their advantages and disadvantages are emphasized.

Polymer Grown Clusters

Nanocluster preparation in a polymer[31-37] is a quite promising method of preparation, since the clusters prepared are already packaged in an useful medium for commercial application. One method of preparation of metal sulfide or selenide nanoclusters in the polymer is to absorb the metal ion in the polymer cavities and then to treat the polymer with H_2S or H_2Se gas for certain time followed by removal of the excess gas. Wang *et. al.*[29] prepared CdS nanoclusters in Nafion (perfluoroethylenesulfonic acid polymer) by the above method. Cluster sizes of 55 Å (measured by X-ray diffraction) with particle size distribution of +/- 20% were reported, and nonlinear optical

properties where measured. Bard *et. al.* [4] reported the preparation of CdS in hydrated Nafion prepared as mentioned above or with an aqueous solution of sodium sulfide. The authors reported that the CdS clusters formed (1-2 μ) could be used for photocatalyzed reduction of methylviologen. Smotkin *et. al.* [38] prepared small CdS and CdSe clusters in dehydrated Nafion films. The size control was achieved by loading the film with a certain ratio of Cd^{2+}/Ca^{2+} in the polymer and then reacting with H_2S or H_2Se in acetonitrile. By decreasing this ratio, the authors reported the preparation of smaller clusters as measured by the shift in the absorption edge. Recently, Wang *et. al.* suggested new method of loading CdS clusters in polymer films [39]. The authors have grown CdS clusters in N-polyvinylcarbazole (PVK) polymer with the molecular cluster, $Cd_{32}S_{14}SPh_{36}DMF$, [5] by dissolving the cluster along with PVK in pyridine and then spin-coating the film onto an aluminum disk. The dried thin film was exposed to H_2S gas to form larger clusters of CdS. The sample was shown to be photoconductive, where the cluster acts as the charge generator and polymer as the carrier-transporting medium. The authors found that this new approach of preparing films of semiconductor, rather than the conventional route of starting with Cd^{2+} ions, produces better photoconductive films with less deep traps. The authors also suggest that this approach of preparing photoconductive films can be extended to include many narrow gap semiconductors, which are not good photoconductors in the bulk, but may be useful as polymer doped nanoclusters, since the band gap would be larger, consequently the dark current decay becomes smaller.

Inverse Micelle Preparation Method

The use of the inverse micelle in the preparation of nanoclusters was first reported by Steigerwald *et. al.* [40] for CdSe clusters and applied for other clusters such as CdS and ZnS [41]. The method of preparation consists of using of bis(silyl)chalcogenide reagents in the arrested precipitation reaction. The metal ion is mixed with a microemulsion made of surfactant, water and heptane. To this mixture, the bis(silyl) chalcogenide in heptane is added resulting in a surfactant-stabilized colloid. This colloid can be dried to give the redissolvable solid surfactant in which the metal chalcogenide clusters are embedded. Instead of drying the colloid, the authors also precipitated the clusters by adding a capping reagent such as PhSeTMS or PhSH (Ph=C_6H_5, TMS=trimethylsilyl) following filtration. The cluster size control is achieved by controlling the molar ratio of water to the surfactant. By using larger molar ratio, the size is increased. The clusters are completely soluble in pyridine.

The advantage of this method is the ability to prepare samples that are highly soluble and capped with variety of surface capping agents thus controlling the surfaces. The main disadvantage of this preparation is the relatively low yield (about 55% by mass) and the low crystalinity of the sample. Consequently, the samples have to be annealed to get crystalline samples.

CdS clusters capped with thiophenol, prepared using the above method, were studied using ^{1}H NMR in acetonitrile solution [42]. The authors studied the NMR line width and suggested that the line broadening is due to hindered rotation of the capping groups. The authors suggested a model that assumes that the thiophenol is bonded only

to one cadmium on the surface (terminal ligand) rather than being bonded to two surface cadmium (bridging ligand). In another study, the techniques X-ray diffraction and diffraction simulation [43] were employed to study the crystal structure of CdSe clusters prepared in the above method. They found that the samples consisted of two phases: hexagonal and cubic phases. Goldestein *et. al.* [6,7] have prepared CdS clusters using this method and measured the melting of the cluster by monitoring the (220) diffraction peak. The authors found that the clusters melted at 575 K. This melting temperature is in contrast to the 1750 K melting temperature of the bulk. Recently Marcus *et. al.*[44] performed an XAFS study on CdS, CdSe, and CdTe clusters prepared using this method. The Cd-XAFS results showed that the clusters had bulk like bond distances for CdS clusters. The reduction of the first shell was attributed to surface truncations. The second coordination numbers were very small even for the largest clusters.

Surface Capped Cluster Preparation Method

This method of preparation was suggested by Herron *et. al.* for the preparation of large quantity of CdS nanoclusters[45]. The method of preparation consists of adding methanol solution of cadmium acetate to sodium sulfide/thiophenol solution prepared by certain ratio of S^{2-}/SPh^- in methanol/water. Precipitated powder can be filtered and purified. The authors prepared cubic (zinc-blende) clusters ranging in size from ~15 Å to ~40 Å by varying the ratio of S^{2-}/SPh^- with the largest clusters arose from the largest ratio values. Chemical analysis on these clusters showed that they only consist of Cd, S, C, and H. X-ray diffraction showed the samples to be crystalline in the zinc-blende crystal

structure. The advantage of this method is that large quantities of clusters can be easily synthesized. The main disadvantage of this method is that large clusters have very low solubility.

Recently, this method was used to prepare small nanoclusters of ZnS capped with thiophenol [46]. The authors prepared three sizes of ZnS clusters with diameters of 7, 15, and 23 Å, and indicated that only particular-sized stable particles could be synthesized. X-ray photoelectron spectroscopy was utilized for examining stoichiometry and purity of the clusters.

A similar method of capping the cluster was recently presented by Colvin *et. al.*[47] The authors prepared CdS clusters capped with mercaptoacetic acid by the addition of sodium sulfide aqueous solution to a mixture of $CdCl_2$ and sodium mercaptoacetate at pH of 3.5. The preparation also was done by substituting the sodium mercaptoacetate with mercaptoacetic acid at pH greater than 8.5. The authors were able to deposit these cluster on a freshly cleaved aluminum slide with coverage of half monolayer and to characterize the sample with x-ray photoemission spectroscopy and other techniques. The authors were able for the first time to study the valence band dependence on the cluster size.

Clusters Grown in Zeolites

This method of preparation of semiconductor nanoclusters has advantage over the other method of synthesis since clusters produced in zeolites are very uniform in size. This synthesis for semiconductor nanoclusters was first demonstrated for CdS by Herron and coworkers[48]. Their method of synthesis was to introduce Cd^{2+} ions in the cavities of

the zeolite Y (zeolite 5A, 13X, or LZY-52) by ion exchange at pH of 5. After filtration, washing and drying, the ion-exchanged zeolites were exposed to H_2S gas at 100 °C. The optical absorption showed a considerable blue shift from the bulk CdS. The size was controlled by adjusting the loading percentage of cadmium ion in the zeolite; at low loading, CdS molecular units formed. X-ray single-crystal analysis and XAFS analysis on these cluster consisted of eight-atom cube of $(CdX)_4$ (X=S or O) located inside the sodalite cages of the zeolite. At higher loading the clusters interconnect electronically through a Cd-Cd distance of 6.2 Å, and as result the absorption edge shifted to the red. Other clusters were synthesized in zeolites including CdSe [49,50], ZnS[51], PbS [50], and GaP[52].

Clusters Grown in Porous Glasses

This method of preparation is probably the most active method of preparation in the literature[3,8,53-58]. Unlike zeolites, the pore structures of the glass is not part of the crystal structure of the matrix, but have a distribution of sizes and connectivities. However, the advantage of growing nanoclusters in glass over other methods is that metal ions can be introduced to the original fluid/sol stage of the synthesis and remain available from the reaction to form the semiconductor clusters after the formation of the rigid glass matrix. This provides excellent uniformity of the cluster dispersion in the matrix. Other advantages of this method are (1) contamination from atmosphere is minimized, and (2) the mechanical properties of the glass allows cutting and polishing as for normal glass. The first preparation of clusters of semiconductor was by Ekimov[8] which lead to the discovery of the quantum size effect and thus started this field. Several methods of

preparation are available. In one method[53], the gel is prepared by the hydrolysis of the solution of $Si(OC_2H_5)_4$ with cadmium acetate at 500 °C followed by reaction with H_2S gas to form a hexagonal CdS cluster that showed quantum confinement. Usually, the length of the reaction time and the reaction temperature affect the sizes of the clusters and their distributions. Lui and Risbud[58] have analyzed the size distribution and precipitation stages in semiconductor doped glasses and have constructed a time-temperature master plot that is useful for precipitating nanoclusters of a given sizes. In a recent study[3], size-quantized dilute magnetic semiconductor Mn doped ZnS clusters were prepared in glass matrix. The authors characterized the optical and the magnetic properties of this material. The structure was studied by XAFS and XRD. The XAFS work supported the idea that Zn^{2+} is randomly substituted in the clusters and that the Mn^{2+} are located inside the cluster.

Other Methods of Preparations

Other methods of preparations of nanoclusters are biosynthesis[60,61], Langmuir-Blodgett films[63], layered phosphonates[63], and lipid bilayer membranes[64].

Endnotes

1) M. L. Steigerwald, and L. E. Brus, *Ann. Rev. Mater. Sci.*, **19,** 471(1986).

2) M. G. Bawendi, M. L. Steigerwald, and L. E. Brus, *Ann. Rev. Phys. Chem.*, **41,** 477(1990).

3) Y. Wang, N. Herron, K. Moller, and T. Bein. *Solid State Com.*, **77**, 33(1991).

4) M. Krishnan, J. White, M. A. Fox, A. J. , Bard, *J. Am. Chem. Soc.* **105,** 17002(1983).

5) N. Herron, J. C. Calabrese, W. E. Farneth, Y. Wang, *Science*, **259**, 1426(1993).

6) A. N. Goldestein, C. M. Echer, and A. P. Alivisatos, *Science*, **256**, 5062(1992).

7) A. N. Goldestein, A. P. Colvin, and A. P. Alivisatos, *Mat. Res. Soc. Symp. Proc.*, **206**, 271(1991).

8) A. I. Ekimove, A. A. Onushchenko, *Sov. Phys. Semicon.*, **16**, 775(1982).

9) Ai. L. Efros, A. L. Efros, *Sov. Phys.-Semiconductor. (Engl. Transl.)*, **16**, 772 (1982).

10) R. Rossetti, J. L. Ellison, J. M. Gibson, and L. E. Brus, *J. Chem. Phys.*, **80**, 4464(1984).

11) R. Rosetti and L. E. Brus, *J. Phys. Chem.* **86**, 4470(1982).

12) R. Rossetti, S. Nakahara, and L. E. Brus, *J. Chem. Phys.*, **79**, 1086(1983).

13) L. E. Brus, *J. Chem. Phys.*, **80**, 4403(1984).

14) L. E. Brus, *J. Chem. Phys.* **79**, 5566 (1983).

15) A. P. Alivisatos, T. D. Harris, P. J. Carrol, M. L. Steigerwald, and L. E. Brus, *J. Chem. Phys.*, **90**, 3463(1989).

16) E. O. Kane, *Phys. Rev.*, **18**, 6849(1987).

17) Y. Kayanoma, *Phys. Rev. B*, **38**, 9797(1988).

18) M. V. Rama and R. A. Friesner, *J. Chem. Phys.*, **95**,8309(1991).

19) Y. Wang and N. Herron, *J. Phys. Chem.*, **95**, 525 (1991).

20) D. F. Eaton, *Science*, **253**, 281(1991).

21) D. F. Eaton, *CHEMTECH*, **V22,** 308(1992).

22) N. Herron, in Materials for Nonlinear Optics: Chemical Prospective. S. R. Marder, J. D. Stuckey, and G. D. Stucky, editors. American Chemical Society, Washington, DC 1991.

23) L.-T Cheng, N. Herron, and Y. Wang, *Journal of Applied Physics*, **66**, 3417 (1989).

24) Y. Wang, and N. Herron, *Int. J. Non. Opt. Phys.*, **1**, 683(1992).

25) D. V. Merphy, S. R. Brueck, *J. Opt. Lett.*, **8**, 496(1983).

26) S. Hayashi, R. Koh, Y. Ichiyama, K. Yamamoto, *Phys. Rev. Lett.*, **60** 1085(1983).

27) Y. Wang, *J. Phys. Chem.*, **95**, 1119(1991).

28) Y. Wang, A. Suna, J.McHugh, E. Hilinski, P. Lucas, R. D. Johnson, *J. Phys. Chem*, **92**,6927(1990).

29) Y. Wang, N. Herron, W. Mahler, and A. Suna, *J. Opt. Soc. Amer. B*, **6**, 808(1989)

30) O. R. Olbright, N. Peyghambarian, S. W. Koch, and L. Banyai, *Opt. Lett.*, **12**,

413(1987)

31) Y. Wang, W. Mahler, *Opt. Commun.*, **61**, 233(1987).

32) E. Hilinski, P. Lucas, Y. Wang, *J. Chem. Phys.*, **89**, 3435(1988).

33) Y. Wang, A. Suna, J. MucHugh, E. Hilinski, P. Lucas, and R. Johnson, *J. Chem. Phys.* **92**, 6927(1990).

34) W. Mahler, *Inorg. Chem.*, **27**, 435(1988).

35) A. Fotjik, H. Weller, U. Koch, and A. Henslein, *Ber. Bunsengen. Phys. Chem.*, **88**, 969(84).

36) A. Henslien, *Ber. Bunsengen. Phys. Chem.*, **88**, 949(84).

37) M. Meyer, C. Walberg, C. Kurihara, and J. Fender, *J. Chem. Soc. Chem. Commun.*, **90** (1984)

38) E. S. Smotkin, R. M. Brown, L. K. Rabenberg, K. Salomon, A. J. Bard, A. Campion, M. A. Fox, T.E Mallouk, S. E. Webber, and J. M. White, *J. Am. Chem. Soc.*, **94**, 7543(1990).

39) Y. Wang, N. Herron, *Chem. Phys. Lett.*,**200**, 71(1992).

40) M. L Steigerwald, A. P. Alivisatos, J.M Gibson, T.D. Harris, R.Kortan, A.J Muller, A.M. Thayer, T.M Duncan, D.C. Douglas, and L.E. Brus, *J. Amer. Chem. Soc.*, **110**, 3046(1988).

41) M. Marcus, W. Flood, M. Steigerwald, L. Brus, and M. G. Bawendi, *J. Phys. Chem.*, **95**, 1572(1991).

42) J. R. Sacheben, E.W. Wooten, L. Emsley, A. Pines, V.L. Colvin, and A.P.Alivisatos, *Chem. Phys. Lett.*, **198**, 431(1992).

43) M.G. Bawendi, A.R Kortan, M.L Steigerwald, and L.E. Brus, *J. Chem. Phys.*, **91**, 7282(1989).

44) M. A. Marcus. L. E. Brus, C. Murray, M. G. Bawendi, A. Prasad, and A. P. Alivisatos, *Nanostructured Materials*, **1**, 323(1992).

45) N. Herron, Y. Wang, and H. Eckert, *J. Am. Chem. Soc.* , **112**, 1322(1990).

46) S. Mahamuni, A. A. Khosravi, M. Kundu, A. Kshirsagar, A. Bedekar, D. B. Avasare, P. Singh, and S. K. Kulkarni, *J App Phys*, **73**, 5237(1993).

47) V. L. Colvin, A. N. Goldstein, and A.P Alivisatos, *J. Am. Chem. Soc.* , **114**, 5221(1992).

48) N. Herron, Y. Wang, M.E. Eddy, G.D. Stucky, D.E. Cox, K. Moller, and T. Bein, *J. Am. Chem. Soc.*, **111**, 530(1989)

49) K. Moller, M.M. Eddy, G.D. Stucky, N. Herron, and T. Bein, *J. Am. Chem. Soc.*, **111**, 2564(1989)

50) S. Miyazaki, H. Yoneyama, *Denki Kagaku*, **58**, 37(1990).

51) G.D Stucky, and J.E Mac Dougall, *Science*, **247**, 669(1990).

52) J. E. Mac Dougal et. al., *J. Am. Chem. Soc.*, **111**, 8006(1989)

53) M. Nogami, K. Nagaska, E. Kato, *J. Am. Ceram. Soc.*, **73,** 2097(1990).

54) B. G. Potter, H. J. Simmons, *Phys. Rev. B*, **37**, 10838(1988)

55) N. F. Borelli, D. W. Hall, H. J. Holland, and D. W. Smith, *J. App. Phys.*, **61,** 5399(1987).

56) A. I. Ekimov, Ai. I. Efros, *20th Int. Conf. Phys. Semi. Micr.*, **3**, 2387(1990).

57) L. Liu, M. J. Kim, S. H. Risbud, and R. W. Carpenter, *Philos. Mag. B*, **63**,

796(1991).

58) L. Liu, and S. H. Risbud, *J. App. Phys.*, **68**, 28(1990).

59) H. Rosmann, A. Schulzgen, F. Henneberger, and M. Muller, *Phys. Stat. Sol. B*, **159**, 287(1990).

60) C. Dameron, R. Rees, R. Mehra, A. Kortan, P. Carol, M. L. Steigerwald, L. E. Brus, and D. R. Winge, *Nature*, **338**, 596(1989).

61) C. Dameron, and D. R. Winge, *Inorg. Chem.*, **29**, 1343(1990).

62) E. S. Smotkin, C. Lee, A. J. Bard, A. Campion, M. A. Fox, T. E. Mallouk, S. Webber, and J. White, *Chem. Phys. Lit.*, **52**, 265(1988).

63) G. Gao, L. K. Rabenberg, C. M. Nunn, and T. E. Mallouk, *Chem. Mater.*, **3**, 149(1991).

64) X. Zhao, S. Baral, R. Rolandi, and J. H Fendler, *J. Am. Chem. Soc.*, **110**, 1012(1991).

CHAPTER II

XAFS AND OTHER CHARACTERIZATION METHODS

This chapter will describe XAFS theory, experiment, and data analysis methods which pertain to work described in this thesis. Then other characterization methods used in this work, X-ray diffraction, and theoretical simulations will be discussed.

The conventional methods of characterizing the structure (e.g. NMR and single crystal x-ray diffraction) can not be used for nanoclusters becuase the prepared samples are usually composed of a distribution of sizes, and crystallizations are not possible. Also, these samples lack long range order, a requirement for a single crystal X-ray diffraction. The poor solubility of nanoclusters in common solvents along with the poly-dispersed nature of the sample preclude the use of characterization techniques such as NMR. Therefore, XAFS and XRD were the main physical methods that were used in characterization of nanoclusters samples. Other methods including chemical analysis, UV-VIS and IR absorption spectroscopies, were employed and are described in later chapters. Finally Scanning Tunneling Microscopy and Atomic Force Microscopy were also used, and the key results are described in Chapter V.

Physical Basis of XAFS

Introduction

X-ray Absorption Fine Structure (XAFS) refers to the oscillatory variation of the X-ray absorption as a function of the photon energy beyond the absorption edge. This fine structure is understood to rise from final state interference of the outgoing photoelectron with components scattered off the neighboring atoms[1]. It is the interference among the possible scattering path of the photoelectron that is responsible for the oscillatory feature above the absorption edge. The absorption is normally expressed in term of the absorption coefficient μ and can be determined by measuring the attenuation of the X-ray intensity upon passing through a sample or by indirect methods such as fluorescence or electron yield experiments. Therefore, one can tune the X-ray photon energy E to correspond to the binding energy of a some core electron of an atom in the material and measure the XAFS due to the excitation of that specific atom. The experimental spectrum can be analyzed by using known experimental standards or theoretical standards to give local structural information with great precision to material in the solid (crystalline or amorphous), liquid, solution, or gaseous state.

The XAFS has been traditionally divided into two regions: near edge region, and extended region. The near edge region of XAFS extends from the edge energy up to 50 eV, and it arises due to multiple scattering of the photoelectron with the surrounding atoms. The extended XAFS region extends from >50 eV above the edge up to several hundred electron volts. For very high energy above the edge the XAFS oscillation

becomes very weak and thus the signal to noise gets poorer. Thus, normally the XAFS is measured up to ~1000 eV above the absorption edge energy. In the following sections, the scattering theory of XAFS is first introduced and the XAFS equation is derived for a specific model. Then the XAFS parameters will be discussed.

Derivation of The XAFS Equation

The derivation of the XAFS equation in this section is based on the derivation presented by Boland, Crane, and Baldschwieler [2]. The equation to be derived below is based on the small atom approximation (also known as the plane wave approximation). The equation is given by

$$\chi(k) \equiv \frac{\mu(k) - \mu_o(k)}{\mu_o(k)} = -\sum_j 3N(\hat{e}.\hat{r})^2 \, |f(\pi,\vec{k})| \, \frac{\sin(2kr_j+\delta'_1 k + \theta(\pi,k))}{kr_j^2} \qquad (2\text{-}1)$$

where $k = [2m (\hbar\omega - E_o)]^{1/2}/\hbar$ is the photoelectron wave number, E_o is the nominal energy of the edge, $f(\pi,k) = |f(\pi,k)|\exp(i\theta(k))$ is the back scattered amplitude of the photoelectron, $\delta_1'(k)$ is the $\ell = 1$ partial wave phase shift due to the central atom potential, $\mu(k)$ is the observed linear absorption coefficient, $\mu_o(k)$ is the hypothetical absorption coefficient without scattering, $\hat{e}$ is the polarization vector of the incident radiation, r_j is the distance of atom j from the central atom, and N_j is the number of atoms of the jth type. Other modifications are included for a real system to account for the thermal effects and loses due to inelastic scattering and are described at the end of this section.

The X-ray absorption cross section in the one-electron and dipole approximation is written as

$$\sigma = 4\pi^2 \alpha \hbar\omega \, |\langle f|\hat{e}.\vec{r}|i\rangle|^2 \, N(\omega), \tag{2-2}$$

where α is the hyperfine structure, ω is the photon frequency, $N(\omega)$ is the density of the final states of the photoelectron, and i and f are the initial and final states of the systems and are eigenfunctions of the approximate unperturbed Hamiltonian H,

$$H = \frac{-\hbar^2}{2m} \nabla_r^2 - \frac{Ze^2}{r} + V, \tag{2-3}$$

where V is the total potential seen by the final state photoelectron. The assumption made is that V is non-overlapping, spherically symmetric, and finite-range centered around each atomic site. This potential between the sites is also assigned to be constant. Now at energies that correspond to a bound K shell electron, the potential of the neighboring atoms can be ignored, and for the purpose of illustration one can write the 1s wave function of the initial state as

$$\langle r|i\rangle = \pi^{-1/2}\left(\frac{Z}{a_o}\right)^{\frac{3}{2}} \exp\left(\frac{-Zr}{a_o}\right) \tag{2-4}$$

The final state of the photoelectron is influenced by both the potential of the neighboring atoms as well as the potential of the central atom. However at kinetic energies of the ejected photoelectron (≥3 times the plasma frequency) the central potential becomes negligible and the Schrödinger equation reduces to

$$(E-H^o)|f\pm\rangle = V\ |f\pm\rangle \tag{2-5}$$

where H^o is the free particle hamiltonian. This equation can be inverted to give the Lippman-Schwinger equation

$$|f\pm\rangle = |k\rangle + G_o^{\pm}V|f\pm\rangle = |k\rangle + G_o^{\pm}T|\ k\ \rangle \tag{2-6}$$

where $\langle r|k\rangle$ is the r-space representation of the wave function of H^o, $G_{\pm}^{-}$ is the Green operator, and T is the usual T matrix operator. The G^-_o and T^- will be used so $\langle r|k\rangle$ represents the outgoing asymptote of the scattering process described by $\langle r|f\rangle$.

The T operator can be expanded in term of the t_j operators associated with each scattering center at $\mathbf{r}_j$ as

$$T = \sum_j t_j + \sum_{i=j} t_j G_o t_i + \sum_{i=j,j=k} t_j G_o t_i G_o t_k + \ldots \tag{2-7}$$

using only the first two terms, T is substitiuted into (2-6) and with the use of the unitarity of G

$$\langle f-| = \langle k| + \langle k|T^+G_o^+ = \langle k| + \sum_j \langle k|t_j^+G_o^+ + \sum_{i=j}\langle k|t_j^+G_o^+t_i^+G_o^+t_k^+ \tag{2-8}$$

and the matrix element appearing in (2-2) has the explecit form,

$$\langle f-|\hat{e}.r|i\rangle = \langle k|\hat{e}.r|i\rangle + \sum_j \langle k|t_j^+G_o^+\hat{e}.r|i> + \sum_{i=j}\langle k|t_j^+G_o^+t_i^+G_o^+\hat{e}.r|i\rangle \tag{2-9}$$

Note that quantities in (2-7) such as t_j, t_i, and t_iG_ot all multiply G_o, which is the free propagator of the electron. This can be represented for a three atomic centers as shown in Fig. 2.1. In Fig. 2.1 diagrams 1 and 2 represent the single scattering of a photoelectron

by a neighboring atom at either j or i. Diagrams 3 and 4 represent the events where the second scattering center is the central atom. Diagrams 5, 6 and 7 represent multiple scattering, and diagram 8 is the case were no scattering has occurred.

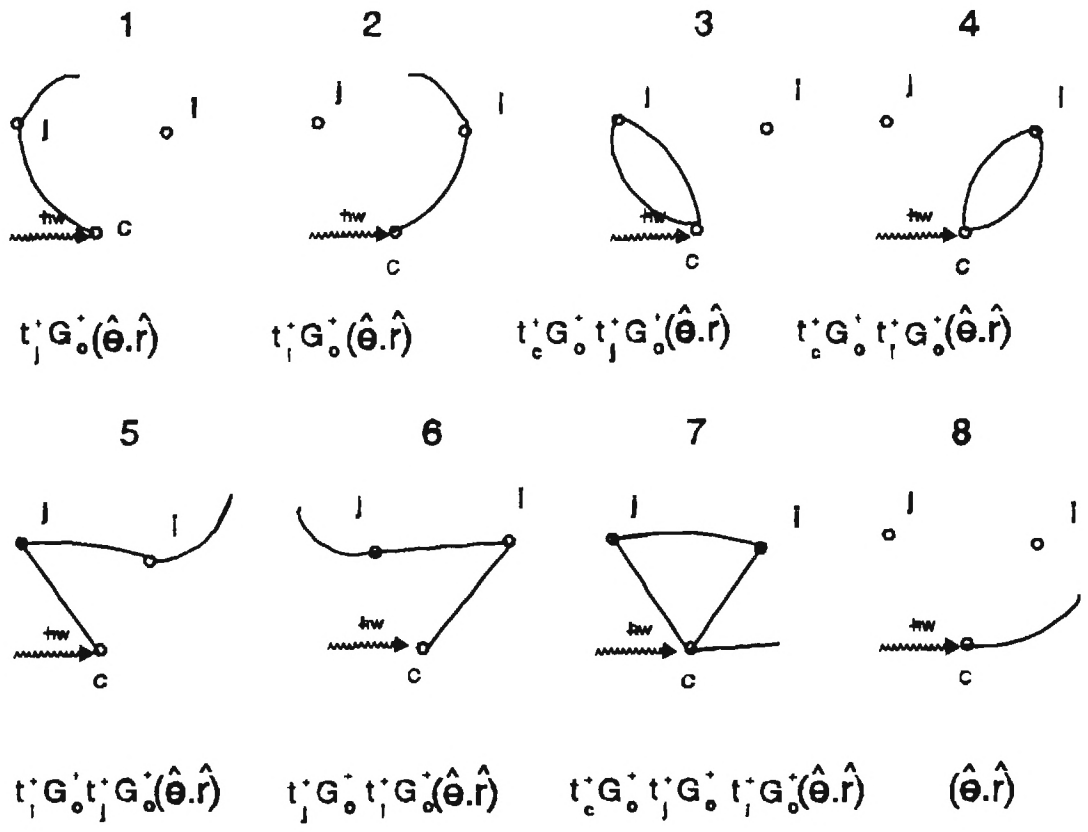

Figure 2.1: diagrams 1-7 represent the first three terms in the expansion of the full T operator. Diagram 8 represents the unscattered event.

Figure 2.2 (right): The vectors pertaining to the evaluation of green function.

What left then is to evaluate the equation 2-9. The first term contribution, $\langle k|\hat{e}.\mathbf{r}|i\rangle$ is due to core atom absorption. The contribution of this first term is M(k,Z)(k.ê) where

$$M(k,Z) = -\frac{\sqrt{2}i}{\pi} \frac{8k\left(\frac{z}{a_o}\right)^{\frac{5}{2}}}{\left(\frac{z^2}{a^2}+k^2\right)^3} \tag{2-10}$$

The second (II) and third (III) contributions can be expanded as follows:

$$II = \sum_j \int \langle k|t_o^+|r_1\rangle\langle r_1|G_o^+|r\rangle\langle r|\hat{e}.r|i\rangle dr dr_1 \tag{2-11}$$

$$III = \sum_j \int \langle k|t_c^+|r_3\rangle\langle r_3|G_o^+|r_2\rangle\langle r_2|t_i^+|r_1\rangle\langle r_1|G_o^+|r\rangle\hat{e}.r\langle r|i\rangle dr dr_1 dr_2 dr_3 \tag{2-12}$$

now chose a coordinate by placing the central atom at the as shown in Fig. 2.2. thus for small atoms where $\mathbf{r}' \approx \mathbf{r}_j$, one can expand $|\mathbf{r}'-\mathbf{r}| \approx r_j + r_j.(\mathbf{r}'-\mathbf{r}_j-\mathbf{r})$, so that

$$\langle r'|G_o^+|r\rangle \approx \frac{-m}{2\pi\hbar^2}\frac{e^{ik_f(r'-r)}}{|r'-r|} \tag{2-13}$$

can be approximated as

$$\langle r'|G_o^+|r\rangle \approx \frac{-m}{2\pi\hbar^2}\frac{1}{r_j} e^{ik_f(r'-r)} \tag{2-14}$$

where $\mathbf{k}_j = kr_j$ is the direction of the photoelectron. Next, substitute $\langle r'|G^+|r\rangle$ into II and III, to give :

$$II = -\sum_j \frac{m(2\pi)^2}{\hbar^2}\frac{1}{r_j} M(k,Z)(\hat{e}.\hat{r}_j)\langle k|t_j^+|k_j\rangle \tag{2-15}$$

$$III = \sum_j \frac{m^2 (2\pi)^4}{\hbar^4} \frac{1}{r_j^2} M(k,Z)(\hat{e}.\hat{r}_j)\langle k|t_c^+|k_j'\rangle\langle k_j'|t_j^+|k_j\rangle \qquad \textbf{(2-16)}$$

where $\mathbf{k'}_j = -kr_j$ is the direction of the back-scattered photoelectron. It is now helpful to relate the matrix element of t^+_j to those of t°_j which is centered at the central atom so to write it in term of the scattering amplitude $\langle k|t^+_j|k_j\rangle = e^{i(r'-r).rj}\langle k|t^\circ_j|k_j\rangle$ hence using the well known relation $\langle k|t^\circ_j|k_j\rangle = -\hbar^2/(m(2\pi)^2)\, f_i(\theta_j)$, where $f_i(\theta_j)$ is the scattering amplitude of the photoelectron due to atom at j, and $\cos(\theta_j)=\hat{k}.\hat{k}_j=\hat{k}.\hat{r}_j$. Using these relations, II and III can be rewritten as

$$II = \sum_j M(k,Z) \frac{1}{r_j} (\hat{e}.\hat{r}) f_i(\theta_j)\, e^{ikrj(1-\cos(\theta j)}, \qquad \textbf{(2-17)}$$

$$III = \sum_j M(k,Z) \frac{1}{r_j^2} (\hat{e}.\hat{r})\, f_j(\pi)\, f_c(\pi-\theta_j)\, e^{2ikr_j} \qquad \textbf{(2-18)}$$

Therefore the complete matrix element of equation 2.9 is a sum of three components corresponding to a contribution of the photoelectron that did not scatter (first term), a contribution from the electron that experience a simple scattering with an atom at $\mathbf{r}_j$ (term II), and finally a contribution from the photoelectron that experience scattering with atom at $\mathbf{r}_j$ and then a secondary scattering by the absorber (i.e central atom). In an XAFS experiment a very large number of these scattering occurs, and the ejected photoelectron scatters into many directions of k. Therefore, one has to average the absorption cross section of such macroscopic system over all such directions as follows:

$$\sigma \propto \int |\langle f|\hat{e}.r|i\rangle|^2 \frac{d\Omega_k}{(4\pi)} = \int |I + II + III|^2 \frac{d\Omega_k}{(4\pi)} \qquad \textbf{(2-19)}$$

The first diagonal term can be evaluated into :

$$\mu_o = \int |M(k,Z)|^2 (\hat{k}.\hat{\epsilon})^2 \frac{d\Omega_k}{4\pi} = \frac{1}{3} \mid M(k,Z)|^2 \qquad (2\text{-}20)$$

The second diagonal term can be evaluated into :

$$\int |II|^2 \frac{d\Omega_k}{4\pi} = |M(k,Z)|^2 \sum_j \frac{(\hat{e}.\hat{r})^2}{r_j^2} \int |f_j(\theta_j)|^2 \frac{d\Omega_k}{4\pi} \qquad (2\text{-}21)$$

The third diagonal term is $O(1/r^4)$ and can be ignored.

Next are the cross terms :

$$\int IxIII \frac{d\Omega_4}{4\pi} = -|M(k,Z)|^2 \sum_j \frac{(\hat{e}.\hat{r})^2}{kr_j^2} Im\left[(e^{2i\delta_1}-1)\ e^{2ikr_j} f_j(\pi)\right] \qquad (2\text{-}22)$$

$$\int IxII \frac{d\Omega_k}{4\pi} = -|M(k,Z)|^2 \sum_j \frac{(\hat{e}.\hat{r})^2}{kr_j^2} Im\left[e^{2ikr_j} f_j(\pi) + f_j(0)\right] \qquad (2\text{-}23)$$

Summing all these terms together shows that the forward-scattering terms of IxII cancels with the second diagonal term by using the optical theorem $\mathrm{Im}|f(0)| = k/4\pi \int |f(\theta)|^2 d\Omega_k$. So the macroscopic absorption coefficient $\mu = n\sigma_o$ (n is the number density) is proportional to

$$\mu = n\sigma_a \propto \frac{1}{3} \mid M(k,Z)|^2 - \sum_j |M(k,Z)|^2 \frac{(\hat{e}.\hat{r})^2}{kr_j^2} Im\left[e^{2i(kr_j+\delta_1')} f_j(\pi,k)\right] \qquad (2\text{-}24)$$

In XAFS we normally normalize the oscillatory part of the absorption coefficient to $\mu_o = 1/3|M(k,Z)|^2$:

$$X(k) \equiv \frac{(\mu-\mu_o)}{\mu_o} = -\sum_j \frac{3N}{kr_j^2} (\hat{e}.\hat{r})^2 \mid f_j(\pi,k) \mid \sin(2kr_j + \delta_1'(k) + \theta(\pi,k)) \qquad (2\text{-}25)$$

wher N_j is the number of atoms of the jth type. For polycrystalline samples, the average over all the polarization direction must be computed, that is $\int(\hat{e}.r)^2\, d\Omega_k/4\pi = 1/3$.

In order to apply this equation into a real system, further modifications are needed so as to account for inelastic contributions and static and thermal effects. These effects are to be described briefly in the next section.

Modification of The XAFS Formula

Inelastic Scattering Effects: There are two processes that contribute to the inelastic scattering of the photoelectron as it leaves the absorbing atom. The first effect is caused by a multiple excitations at the central atom which is collectively known as shake up/off processes. These are due to the excess energy of the photoelectron which can excite (shake up) or ionize (shake off) the low-binding (outer or valence) electrons within the central atom. The effect of these processes tend to reduce the XAFS amplitude. This reduction can be approximated by the square of the overlap matrix of the (Z-1)-electrons wave function Φ_{Z-1} before photoexcitations with the wave function after excitation Φ'_{Z-1} i.e

$$S_c^2(k) = |\langle \Phi'_{Z-1} | \Phi_{Z-1} \rangle|^2 \qquad \textbf{(2-26)}$$

Calculations have showed that this factor is roughly independent of k for $k \geq 7$ Å^{-1} and ranges from unity at low k to a value between 0.6-0.8 at high k.

The second process by which the amplitude is reduced in XAFS is associated with excitations of the neighboring atoms environment. This is approximated by a damping

exponential factor $e^{-2r/\lambda(k)}$ where $\lambda(k)$ is the electron inelastic mean free path. The Universal Curve[3,4] for the electron mean free path λ as a function of the photoelectron can be used as a first approximation in theoretical calculation.

Static and Thermal Effects: The last modification to be discussed here is the effect of thermal and static disorders on the XAFS. These effects are accounted for σ, the Debye-Waller factor for small disorder. σ has two components, σ_{vib} due to thermal vibrations, and σ_{stat}, which is due to structural disorder. For small disorder, the Debye-Waller factor can be written as $\sigma^2 = \sigma_{stat}^2 + \sigma_{vib}^2$. An exponential damping factor of $\exp(-2\sigma^2k^2)$ is usually appended to the XAFS equation. This factor is good for a Gaussian distributions; for other type of distributions, the distribution function has to be convoluted with the XAFS equation.Therefore the usual XAFS equation is written as :

$$X(k) = -\sum_j \frac{N_j S_c^2(k)}{kr_j^2} e^{-2r_j/\lambda(k)} e^{-2\sigma_j^2 k^2} \, | f_j(\pi,k) | \sin(2kr_j + \delta_1(k) + \theta(\pi,k)) \qquad (2\text{-}27)$$

XAFS Experimental Methods

Transmission

Two methods of XAFS measurements were used in this work: transmission and fluorescence. The two measurment methods are illustrated in Fig. 2.3. The transmission mode of measurement is experimentaly the simplest and consists of measuring the attenuation of the transmitted beam radiation as a function of the photon energy from

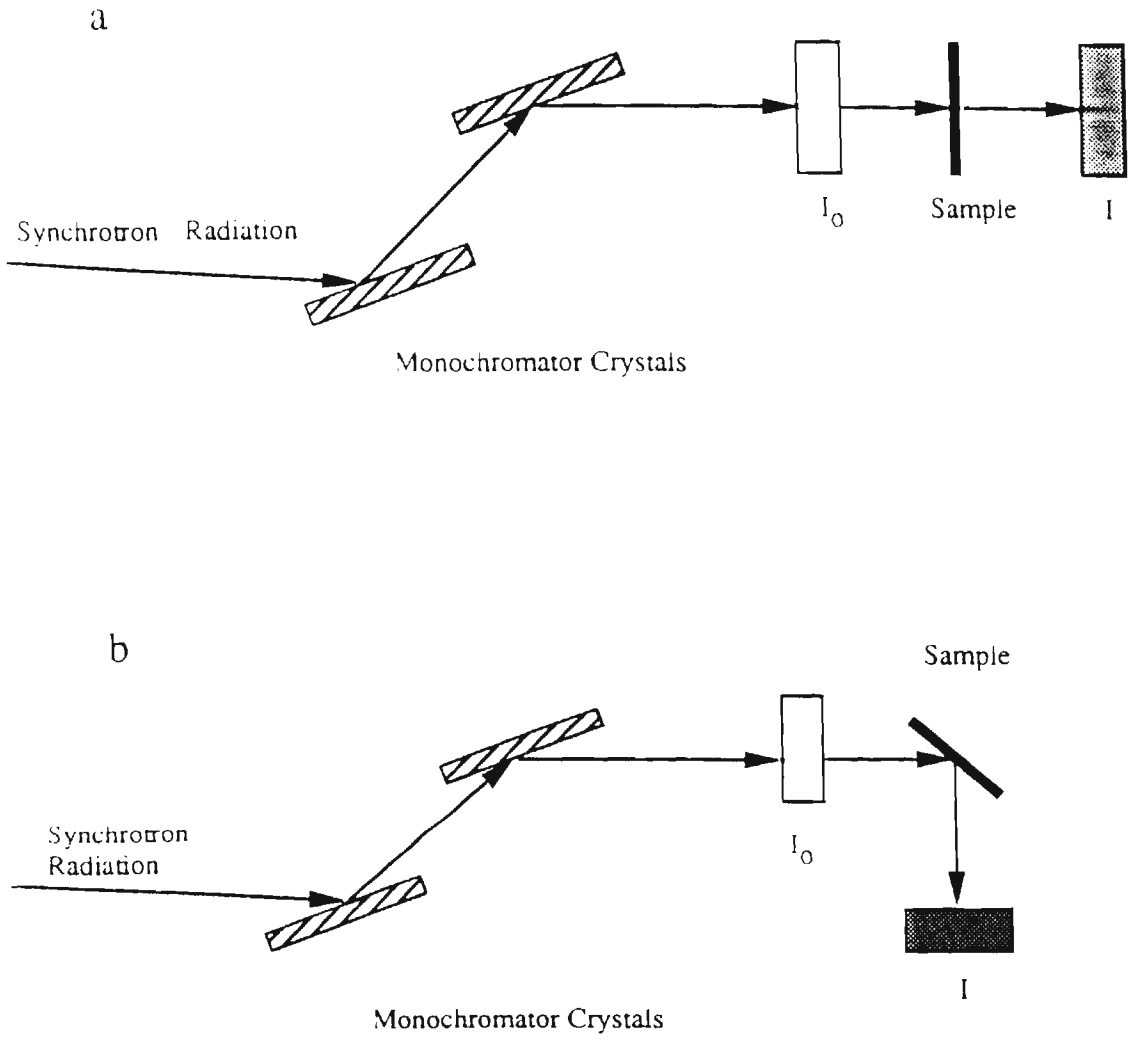

Figure 2.3. Block Diagrams Showing The XAFS Transmission Experiment (a) and Fluorescence XAFS Experiment (b).

synchrotron intensity (Fig 2.3a). The white beam from the synchrotron is monochromatized and focused on a sample. The detection is usually done using gas ionization chambers. It is recommended for optimum signal to noise measurement that the absorption step, $\log(I_o/I)$, be ~1. The sample uniformity also has to be insured in order to minimize thickness effects. The thickness effect occurs when some of incoming beam is not attenuated by the sample due to pinholes. This "leakage" becomes a larger fraction of the measured signal for a thicker sample, causing the absorption signal to appear to depend on the thickness of the sample. Another type of leakage arises from the x-ray fluorescence of the sample itself, which if detected, will cause the absorption to be reduced. Again in thicker samples, this effect will be more significant. To minimize this effect, a smaller detector solid angle should be used. However, it was found empirically that samples with absorption step height of <1.5 will have negligible distortion. Another experimental difficulty, due to the monochromator crystal, are reproducible sharp features at specific energies above the edge known as glitches. These glitches are due to variation in the intensity from the monochromator crystal. They occur when, at a particular angle, harmonics satisfying the Bragg conditions contribute to the intensity of the primary beam. These glitches can be reduced by detuning the crystal such as to lower the intensity by 20% of the maximum diffraction intensity.

For low temperature measurements, the sample is usually mounted on metal surface such that the lower end of the metal mount is submerged in liquid nitrogen or cold nitrogen gas. Most samples in this work were measured in the transmission mode by spreading a finely ground powder of the sample on Scotch tape, which was folded into

several layers. For low temperature measurement, the sample was covered with 2-mil Kapton tape. Sample uniformity was checked by moving the radiation across the sample and observing the intensity of the transmitted radiation.

Fluorescence Detection in XAFS

The fluorescence detection in XAFS is a very important method of detection because it extends the application of XAFS to the study of samples that are not feasible to study in the transmission mode of detection [5]. Such samples are usually very dilute samples in which the absorption edge of the element of interest is of a few percent of the total absorption of the sample. Example of such samples are the biological samples in which the concentration of the element of interest is usually very low. Another important application of the fluorescence detection is for samples that can not be prepared thin or uniform enough for the transmission experiment. However, application of the fluorescence detection in XAFS is not as straight forward as the transmission experiment since usually corrections have to be made for the measured fluorescence signal, especially if comparison with transmission data is desired[6].

The fluorescence radiation is due to the filling of a core hole which was created by the absorption of x-ray photon. For the 1s electron (K-shell) this process is dominated by the emission of K_α radiation, the energy of which is characteristic of the absorbing atom and is of lower energy than the original exciting radiation. The background consists of elastically and Compton scattered radiation and is of higher energy than the fluorescence radiation. Thus, to discriminate the background from the fluorescence signal, a suitable

energy dispersive detector is needed. For that purpose, solid state detectors were first used, but they suffered from low counting rate (about 40 KHz)[5]. Another method of discriminating the background from the fluorescence signal is the use of monochromators[7] between the sample and the detector (usually a gas chamber). The draw back of this method is the significant decrease in the signal intensity due to the low diffraction efficiency of the crystals (10-50%) and also due to the low solid angle of ~15% of 4π subtended by the current designs[2]. A more common method of discriminating the background is the use of x-ray filters and ion chambers [8]. These filters use x-ray absorption edges to attenuate the background radiation. The filters are selected to have an absorption edge energy higher than the fluorescence radiation but lower than the background radiation, thus absorbing the background and transmitting the fluorescence signal. The main problem in using the x-ray filters is that the radiation that is absorbed by them is reemitted as unattenuated fluorescent radiation. When this is a problem, a suitable set of Soller-type slits is placed between the filter and the detector and can block most of the filter re-fluorescence radiation. Most filters used are a thin (5-10 μ) metal film of the Z-1 element. The effect of the background on the S/N for the fluorescence becomes important as the dilution of the absorbing atom increases. In such cases the background intensity can exceed the fluorescence signal and the S/N deteriorates[9].

The fluorescence detection method is best applied for dilute or thin samples. Under these conditions, the fluorescence signal (I_f/I_o) is to a good approximation proportional to the absorption coefficient of the absorbing element. Therefore, the

analysis of the signal can be used to obtain structural parameters as is done in the transmission experiment. However, for concentrated or thick samples (with respect to the penetration depth of the incident radiation), the fluorescence signal will be distorted compared to the true absorption edge. This distortion is known as the self-absorption effect. Self-absorption results in the lowering of the XAFS amplitude such as the coordination number and Debye-Waller factor obtained will be lower than the absolute values. Thus corrections must be applied if absolute values of the structural parameters are sought[10].

Qalitatively, the self-absorption effect can be understood by noting that the structure in XAFS is due to the different probabilities of absorption at different energies, which for very concentrated samples approaches unity and causes the fine structure to be washed out. To understand the effect more quantitatively, it is useful to discuss the fluorescence signal using analytical expressions. The fluorescence intensity I_f, for x-ray incident at an angle ϕ, and a fluorescence exit angle θ with respect to the sample normal is[6]

$$I_f = I_o \frac{\Omega}{4\pi} \epsilon \frac{\mu_{AH}(E)/\cos(\phi)}{\frac{\mu_T(E)}{\cos(\phi)} + \frac{\mu_T(E_f)}{\cos(\theta)}} \left(1 - \exp\left[-\left(\frac{\mu_T(E)}{\cos(\phi)} + \frac{\mu_t(E_f)}{\cos(\theta)}\right)d\right]\right) \qquad (2\text{-}28)$$

where I_o is the incident beam intensity, d is the sample thickness, ϵ is the fluorescence yield, μ_T is the total absorption coefficient which includes the central atom absorption μ_A, E and E_f are the incident photon energy and fluorescence photon energy, respectively. Here μ_{AH} is the central atom absorption coefficient of the core-hole and is approximated

as $\mu_{AH}(E) = \mu_A(E) - \mu_{A1}$ where μ_{A1} is the absorption coefficient bellow the absorption edge.

As can be seen from the expression above that for thin samples or for very dilute samples, the exponential factor can be expanded which leads to $I_f/I_o \propto \mu_A(E)$. However, for thick samples or concentrated ones, the exponential factor can be ignored, and the fluorescence signal has to be corrected. As mentioned above, the effect of the self-absorption is to lower the amplitude of the XAFS. A method for correction of the amplitude has been presented in the literature using tabulated absorption coefficient.

Tan et al.[6] have derived simple equations to correct for σ^2 and N of thick concentrated samples relative to the transmission samples:

$$A_o = \frac{N_f}{N_t} = \frac{2+2(\mu_{A1}/\mu_{A2}-1)C}{2+(\mu_{A1}/\mu_{A2}-1)C} \qquad \textbf{(2-29)}$$

$$\Delta\sigma^2 = \sigma^2_f - \sigma^2_t = \frac{-11.46}{E_o}\frac{C}{2+(\mu_{A1}/\mu_{A2}-1)C} \qquad \textbf{(2-30)}$$

where $C = \mu_{A2}/(\mu_{Total})$, N_f and N_t are the coordination numbers of from fluorescence and from transmition (absolute), repectively. The absorption coefficients μ_{A1} and μ_{A2} refer to these quantities for the central atom before and after the edge, respectively. The authors concluded from simulations, using these equations, and from experiments that for samples thin enough such that $\mu_A x \leq 0.1$ or dilute enough such that $\mu_A/\mu_{Tot} \leq 0.1$, the reduction in N is less than 5% and $\Delta\sigma^2 \leq 0.0001$ Å^2.

In this work, fluorescence measurements were used to measure the sulfur-edge in ZnS and CdS clusters, samples which were strongly self-absorbing (~20%). The samples were prepared by spreading a very fine powder of the samples on a Kapton tape. The sample was mounted on the sample holder that was aligned at 45 degrees respect with respect to the beam and the detector. The ZnS and CdS standards were measured similarly. The self-absorption effect was minimized in the analysis because the standards and the cluster samples have a similar absorption fraction of sulfur in the sample, which results in the amplitude reduction being similar. Chemical analysis of the samples enabled the calculation of the sulfur absorption fraction in these samples according to the above equations. The results of these calculations showed that the correction is very small and is within experimental error.

XAFS Data Analysis and Interpretation

The first step in the data analysis is to convert the collected data into the linear absorption coefficient μ(E). This is done for according to the following equations:

$$\mu(E)d = \ln\left(\frac{I_o}{I}\right) \tag{2-31}$$

$$\mu(E)d = \frac{I_f}{I_o} \tag{2-32}$$

for transmission and fluorescence data, respectively. I_o, and I are the incident and the transmitted intensities, d is the sample density, and I_f is the fluorescence intensity.

The next step is to isolate the oscillatory part of the absorption coefficient from the smooth $\mu_o(E)$. First of all, the pre-edge background contribution is removed by substraction from the data by fitting the pre-edge into a line with extrapolation into the post-edge data. The post-edge data is fitted with a smooth spline function in order to subtract $\mu_o(E)$, and the subtracted data is normalized to the edge step μ_o. The results of this treatment is the function $\chi(E)$:

$$\chi(E) = \frac{(\mu(E) - \mu_o(E))}{\mu_o}. \qquad \textbf{(2-33)}$$

Finally, energy is converted into wave number (i.e., from E to k) using the following equation :

$$k = [2m/\hbar^2(E-E_o)]^{\frac{1}{2}}, \qquad \textbf{(2-34)}$$

At this point, the data is $\chi(k)$, which contains only the oscillatory part of the absorption coefficient is normalized to the atomic absorption coefficient. The steps of analysis outlined above are described in Figure. 2.4.

The next part of the analysis is to obtain the structural parameters from the XAFS function. Many approaches are available. The most important methods wil be discussed below. The XAFS contains the contribution of many shells. Shell is understood to be a range of similar bond length. For example, the first shell in CdS would be four S atoms around each Cd and four Cd atoms around each S atom). It is desired, if possible, to separate the contribution of each shell in order to simplify the analysis. This is done

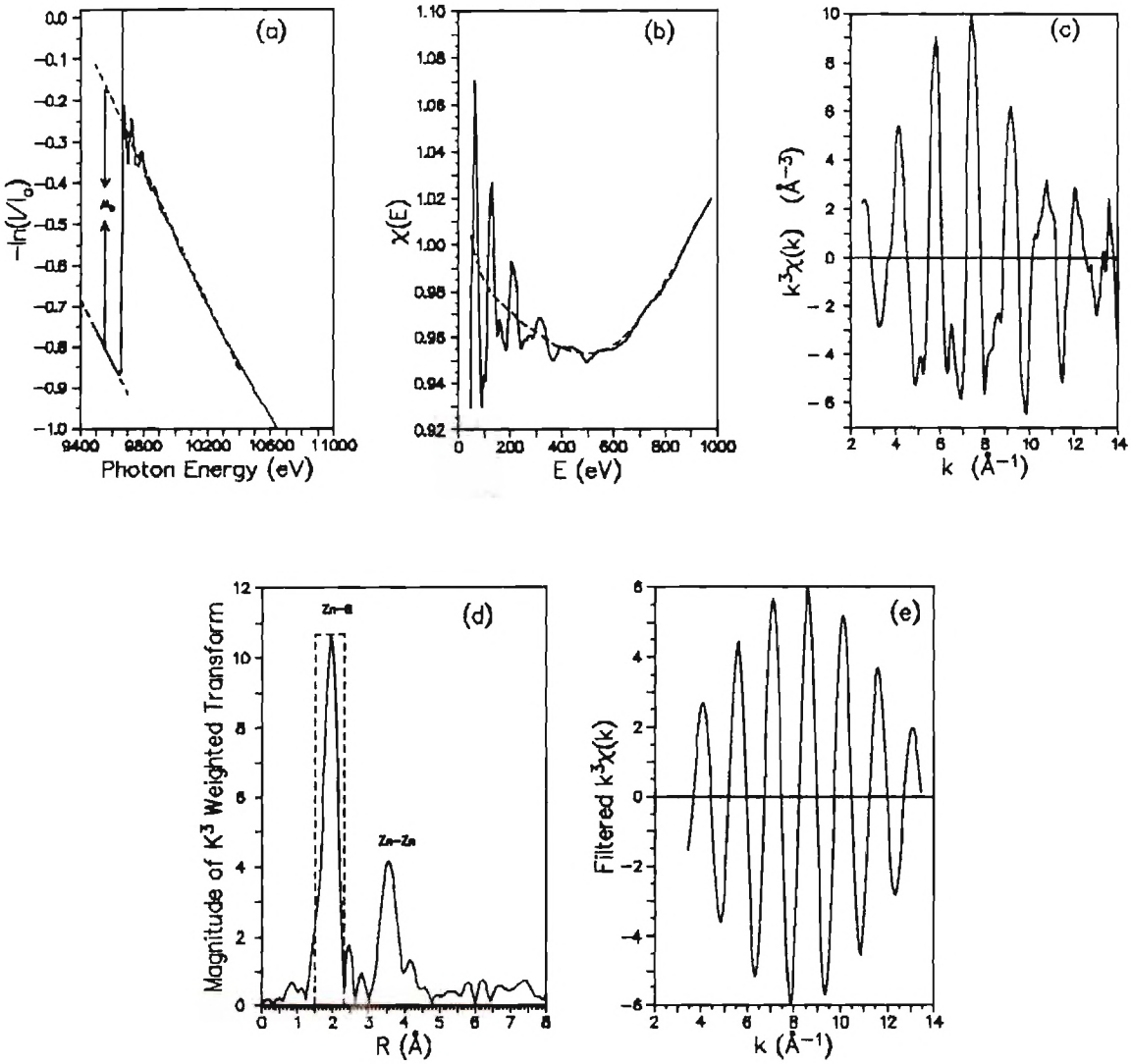

Figure 2.4: Steps in XAFS analysis

a)pre-edge subtraction and data normalization
b)spline background removal
c)k^3 weighted XAFS data
d)Fourier transform and filtering of first shell
e)filtered first shell

by Fourier transforming the data into r' space, where r' is the "phase shifted" distance due to scattering. The Fourier transformed data reveal several peaks, which correspond to a specific shell. The shell of interest is then isolated by filtering with a narrow window and transformed back into filtered data. This new $\chi(k)$ contains only the single shell contribution to the XAFS and can be fitted using known standards (either experimental or theoretical standards) by the XAFS equation to obtain the structural parameters.

A by-product of the Fourier transform method is that the XAFS is separated into two factors: amplitude and phase shift. The amplitude is obtained from the magnitude of the Fourier transformed data, while the phase shift is obtained from the argument of the transform. To illustrate this, the XAFS equation according to (2-27) can be written in the following form:

$$\chi(k) = A(k)\sin(\Phi(k)), \tag{2-35}$$

where A(k) represents the amplitude, and $\Phi(k) = 2kr + \phi(k)$ represents the phase function. Equation 2.35 can be written as

$$\chi(k) = -A(k)Im(e^{i\Phi(k)}) \tag{2-36}$$

Fourier transforming 2.36 into r' space and filtering into k we obtain

$$Z(k) = \frac{1}{2i} A(k)e^{i\Phi}. \tag{2-37}$$

The amplitude is extracted from the magnitude of Z(k) and the phase is extracted from the phase of Z(k). Having the data in this format one can use the phase difference

method and the amplitude ratio methods. The phase difference method is used for a single-distance system to extract the interatomic distance as compared with known standard. In this method, the phase function obtained from Fourier transform of the sample is subtracted from that of a model (designated by the subscript m) sample of known structure according to the following equation:

$$\Phi(k) - \Phi_m(k) = 2k(r - r_m) + \phi(k) - \phi_m(k). \qquad \textbf{(2-38)}$$

By adjusting the choice of the energy origin E_o such that $\phi=\phi_m$, then plotting the phase difference as a function of 2k, a linear curve which passes through the origin should be obtained. The slope corresponds to the bond length difference between the standard and the unknown sample. The ratio method consists of taking the logarithm of the amplitude ratio (A/A_m) according to the following equation (see 2-27):

$$\ln\left[\frac{A(k)}{A_m(k)}\right]=\ln\left[\frac{N}{N_m}\frac{r_m^2}{r^2}\right] + 2k^2\left[\sigma_m^2-\sigma^2\right] + 2\left[\frac{r_m}{\lambda_m(k)}-\frac{r}{\lambda(k)}\right]. \qquad \textbf{(2-39)}$$

Assuming that the mean free paths are equal, and that $(r_m-r) << \lambda$, then the logarithm of the amplitude ratio is linearly related to $2k^2$. The slope is equal to the difference between σ_m^2 (model Debye-Waller factor) and that of the unknown σ^2. The intercept is equal to $\ln(N\ r_m^2)/(N_m\ r^2)$. Thus, by selecting a suitable standard, the structural parameters can be easily obtained. The strength of this method is that it reduces the correlation in the XAFS parameters. In contrast, the greatest source of parameter error in fitting methods is the correlation between N, the number of scatterers,

and σ^2. If the shell of interest consists of more than a single scatterer, then the ratio method will not apply. In this case, least square curve fitting methods are used by employing suitable standards.

XAFS Data Interpretation

The XAFS analysis results are rich in geometrical and chemical information. In this section examples are given in how to interpret XAFS results to obtain valuable structural information.

Assume a general compound composition, $A_aB_bC_c$. From the XAFS A-edge, the fitting results give first shell coordination numbers N(A-B)/A, N(A-C)/A and their distances. If the stiochiometric coefficients *'a'*, *'b'*, or *'c'* are known or their ratios are known, then it is easy to get the coordination number of the other elements by using only the A-edge XAFS results. To explain the procedure of doing this, one notices that the results of the XAFS coordination number are normalized to the total absorbing atoms. Thus the coordination numbers N(A-B)/B and N(A-C)/C can be calculated as follows:

$$\frac{N(A-B)}{B} = \frac{N(A-B)}{A} x \frac{a}{b}$$

$$\frac{N(A-C)}{C} = \frac{N(A-C)}{A} x \frac{a}{c} \qquad \textbf{(2-40)}$$

If, however, the XAFS edges were measured, then by using the above equation the mole fractions can be determined. Thus information about the coordination number of an element B can be obtained by measuring the XAFS of element A and by knowing

the mole ratio of A/B in the sample. The latter value can be obtained from chemical analysis or can be obtained from edge analysis as will be explained below. This method of data interpretation, although simple, was not to the knowledge of this author discussed or used in the literature. The advantage of this interpretation of the XAFS data can be appreciated when one tries to learn about coordination number of low atomic weight element whose XAFS can not be obtained in the transmission mode, and alternatively fluorescence data has to be measured. The fluorescence data is usually poorer in quality than the transmission data and thus requires large number of scans, and also may suffer from self-absorption effects. This method was used in this thesis to interpert results of fitting the Zn-edge of the benzeneselenol capped ZnS clusters and confirmed the analysis results of S-edge fluorescence XAFS of other ZnS clusters.

The X-ray absorption spectra (XAS) enables the estimation of the mole ratio of the elements in the sample by using the edge step heights of the measured edges of the same sample. For example, if a sample contains Zn , Se, and other elements, then the edge step at the Zn-edge (h_{Zn}) and the edge step of Se at the Se-edge (h_{Se}) of the same sample will give the mole fraction n_{Se}/n_{Zn} according to the following equation:

$$\frac{n_{Zn}}{n_{Se}} = \frac{h_{Zn}\mu_{Se}}{h_{Se}\mu_{Zn}}, \qquad \textbf{(2-41)}$$

where μ_i is the absorption cross section at the edge energy of element i. This method was used in this thesis to calculate the mole ratio of Zn/Se in benzeneselenol capped ZnS clusters as will be described in chapter IV.

X-Ray Diffraction

Introduction

X-ray diffraction (XRD) was used in this work to (1) identify the crystal phase of the synthesized nanocrystal, (2) to determine the purity of the sample, and (3) XRD was used to estimate the average size of the clusters.

Size Determination of Small Crystallite

For a crystal to diffract, the scattered vector must terminate at a lattice point. The intensity of diffraction radiation drops dramatically for scattered vector that terminate on the environment of the lattice point. For small crystals, the intensity of diffracted radiation does not diminish as much as in large crystals because the number of unit cells in the small crystal are small. This is shown in the diffraction pattern as broadening in the diffraction line. The crystal size can be estimated from the broadening of the diffraction lines by using the Scherrer equation[11]:

$$\Delta(2\theta) = \frac{0.9\lambda}{L\cos(\theta)} \qquad (2\text{-}42)$$

where 2θ is the full width of the diffraction line at half maximum intensity (FWHM), and L is the width of the crystal. For a spherical shaped crystal, the diffraction lines are broadened according to equation 2-42, and the L=0.75D, where D is the diameter of the crystal. Thus, Eq. (2-42) for spherically shaped crystals is rewritten as

$$\Delta(2\theta) = \frac{1.2\lambda}{D\cos(\theta)} \qquad (2\text{-}43)$$

The above equation was used in this work to measure the cluster size from the width of the diffraction lines. The diffraction pattern was measured using Cu Kα radiation on Phillips APD 1800 diffraction system. The powder sample was pressed in a pellet shape for all the measurements. The diffraction pattern was collected over 3 hours with resolution of 0.025 ° in 2θ. The crystal structure of all samples that were studied were either cubic or hexagonal structures. In the cubic structure, all the crystal axes are perpendicular to each other and are equal in size. In the hexagonal structure, a=b≠c and α=β=90, γ=120. According to Bragg's law, diffraction will occur for these crystal structure according to the following equations:

$$\frac{\lambda}{2\sin(\theta)} = \frac{1}{d_{hkl}},$$

$$\frac{1}{d_{hkl}}(Cubic) = \frac{(h^2+k^2+l^2)}{a^2}, \qquad (2\text{-}44)$$

$$\frac{1}{d_{hkl}}(Hexagonal) = \frac{4}{3a^2}(h^2+hk+k^2)+\frac{l^2}{c^2}.$$

By solving these equations the position of the diffraction peaks can be determined and the lattice parameters a, and b and c can be calculated.

Simulation of Nanocluster Structure

The coordination number of spherical crystals of zinc sulfide and cadmium sulfide in the cubic and hexagonal crystal structure as a function of the crytsal diameter was determined from simulation. In this section, the method of simulation is explained and the results of the calculation are presented.

In the zinc-blende cubic structure, the atoms of type A and of type B are found at the lattice points (0,0,0) and (0.25,0.25,0.25), respectively. From these points a lattice can be generated in three dimensions by using the three symmetry vectors (0.5,0.5,0), (0.5,0.,0.5), and (0,0.5,0.5). For the hexagonal crystal structure, the crystals that were found studied had wurtzite structure. The lattice of this crystal structure is generated by placing atoms of type A at (0,0,0) and at (1/3,2/3,1/2). The atoms of type B are placed at (0,0,3/8), and at (1/3,2/3,7/8). The lattice is generated from symmetry vectors.

A FORTRAN program was written[12] that generated a spherical crystal of a specific radius given the crystal parameters. The program starts by placing atom of type A in the center of the sphere, builds unit cells in all directions for the required size, and inscribes a sphere of chosen radius. Finally, the program counts the total coordination number of the nearest neighbor (first shell) for singly, doubly, triply, and quadruply bonded atoms of each atom type. The average coordination number is then obtained. The program also calculates the average coordination number of the next nearest neighbor (second shell). Figure 2.5 shows a 25 Å diameter spherical cluster of ZnS and two thiophenol capping ligands. The results of ZnS and CdS cubic structures are shown in Appendices A and B, repectively.

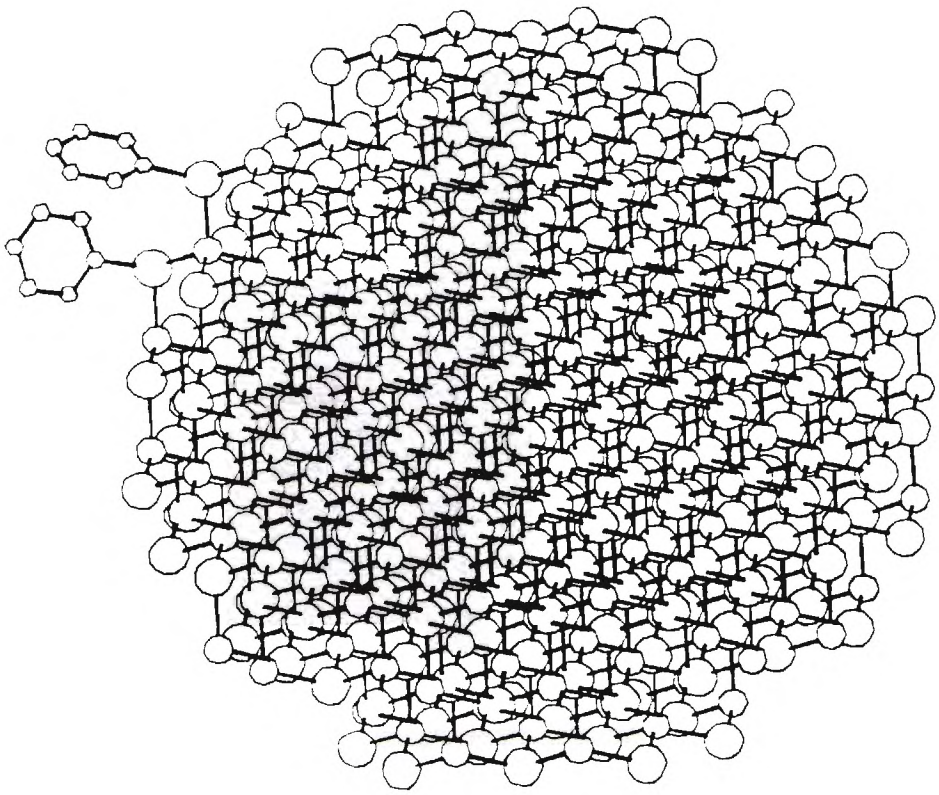

Fig. 2.5. ZnS spherical cluster (25 Å diameter) showing the bulk cubic structure and two thiophenol capping ligands.

Endnotes

1. E. A. Stern, *Phys. Rev. B*, **10** 3027 (1974)

2. J. J. Boland, S. E. Crane, and J. D. Baldeschwieler, *J. Chem. Phys.*, **77**, 142 (1982)

3. G. A. Somorjai, "Chemistry in Two Dimensions: Surfaces," Cornell University. Ithaca, p. 41. (1981)

4. M. P Seah, and W. A. Dench, *Surf. Inter. Anal.*, **1**, 2

5. J. Jaklevic, J.A. Kirby, M.P. Klien, A.S. Ropertson, G.S Brown, and P. Eisenberger, *Solid State communication*,**23**,679(1977)

6. S.M Heald , *X-ray Absorption: Principles, Applications, Techniques of EXAFS, SEXAFS and XANES*, ed D.C Koningsberger and R. Prins (Wiley, New York 1988)

7. J.B Hastings, P. Eisenberger, B.Lengeler, and M.L. Perlman, *Phys. Rev Let.*, **43**,1807(1979)

8. E. A. Stern and M.S. Heald, *Rev. Sci. Inst.*, **50**, 1579(1979); E. A. Stern, B. A Bunker, and S.M. Heald, *Phys. Rev. B*, **21**, 5521(1980).

9. P. A. Lee, P. H. Citrin, P. Eisenberger, and B. M. Kincaid, *Rev. Mod. Phys.*, **53**,769,(1981)

10. Z. Tan, J. Bundick, and S. M. Heald, *Rev. Sci. Instrum.*,**60**,1021(1989)

11. A. Guinier, X-Ray diffraction, p121-142, W. H. Freeman and Company, 1963.

12. Program "znblend" was written by Professor R. H. Felton, and modified by R. S. Shorrosh.

CHAPTER III

CADMIUM SULFIDE NANOCLUSTERS

CdS Cluster Preparation

Cadmium sulfide nanoclusters were prepared by a variety of methods. In general, two classes of clusters were prepared: clusters grown in Nafion films and clusters precipitated from solution in the presence of a capping agent. Capping agents that were used are thiophenol (benzenethiol), and 3-mercaptopropanoic acid. All reagents that were used in the synthesis were as supplied by vendors without further purification. All solvents used were deaerated by bubbling N_2 gas through the liquid for at least 30 minutes. All reactions were carried under nitrogen atmosphere in rubber septa capped Erlenmeyer flasks.

Nafion Grown CdS Clusters

A Nafion membrane is ion exchange polymer that has the following general formula,

$$\begin{array}{l}[(CF_2CF_2)_n\text{-}CF_2CF\text{-}]_m \\ \qquad\qquad\qquad\quad | \\ \qquad\qquad\quad (OCF_2CF\text{-})_l OCF_2SO_3^-M^+ \\ \qquad\qquad\qquad\quad | \\ \qquad\qquad\qquad\quad CF_3\end{array} \qquad (3.1)$$

where n and m can vary to produce different ion exchange capacities, and l is small. The ion-exchange sites in Nafion are thought to aggregate into clusters. These clusters are thought to be joined together with small channels[1]. The fully hydrated 1200 equivalent weight polymer contains approximately 70 ion-exchange site per cluster and about 1000 water molecules, forming a spherical domain that resembles an inverted micelle. The size of the cluster depends on the degree of swelling due to the water content[1].

For the growth of CdS clusters in Nafion, the film is first protonated by boiling in nitric acid, then cadmium ions are introduced into the film by ion exchange. The CdS clusters are formed when film is exposed to H_2S or immersed in aqueous sulfide solution.

Nafion 117 films (1100 g/equiv., 7-mil thickness, Aldrich) were cleaned by boiling the samples in concentrated nitric acid for 30 minutes followed by rinsing twice with boiling deionized water or until sufficiently cleaned of excess acid to produce neutral pH for the rinsing water. The films were then soaked in 1.0 M cadmium nitrate aqueous solution for 12 hours. Excess cadmium was removed form the films by washing and soaking in water. The films were judged clean from excess cadmium by testing the soaking water for cadmium by adding sodium sulfide solutions and looking for the orange color due to formation of CdS. The films were then transferred in a dry box to a glass cell. Several samples of CdS clusters were prepared from the Cd-loaded Nafion films.

The **CdS2W** labelled CdS cluster sample was made by loading the Nafion films with Cd^{2+} as described above. The films then were first dried using paper tissue, followed by drying under vacuum for 2 hours. The film samples were exposed for 1 atm of H_2S and allowed to react for nine days at room temperature. Excess H_2S was removed by

pumping for two days; then the samples were soaked in water for one day. Finally the samples were dried under vacuum for 12 hours. Eight such Nafion film samples were prepared and wrapped in the dry box with 3 mil Mylar film and epoxy sealed for protection from water and oxygen. The **CdS2D** labelled sample was made similarly to CdS2W but was not soaked in water following the reaction with dry H_2S. The **CdS3W** labelled sample was made similar to CdS2W but was dried for 3 days before reaction with H_2S. The reaction time was 15 days. The **CdS3D** labelled sample was made similar to CdS3W but was not soaked in water. The **CdS348W** labelled sample was prepared similar to CdS3W but was reacted for 48 days. The **CdS348D** labelled sample was prepared similarly to CdS348W but was not soaked in water. The **CdNa2S** labelled sample was made by reacting cadmium loaded Nafion with 1M Na_2S solution followed by drying under vacuum for 12 hours.

Thiophenol Capped CdS Clusters

Thiophenol (C_6H_5SH, Eastman) capped CdS clusters were prepared similarly to the literature preparation as reported by Herron *et al.* [2]. The CdS clusters prepared in this manner were synthesized in methanol/water mixture by the addition of 100 ml of cadmium acetate/ methanolic solution to a well stirred solution containing a specific mol ratio of sodium sulfide to thiophenol. The resulting yellow precipitate was filtered in a medium glass frit, washed with methanol, and vacuum dried. The sample prepared with a ratio of 0.5 of S^{2-}/PhS^{1-} gave a slight yellow color. Darker colors were produced when the above ratio was increased, indicating that larger clusters were produced. The concentrations of the sulfide ions and the thiophenol in the reaction mixture were chosen

Page missing from thesis

dissolve the separate components directly in deaerated water and methanol rather than delivering the actual volumes needed from previously prepared stock solutions. With this choice, the solutions were always fresh to minimize any oxidation of the sulfide and the thiophenol. The second modification was to double the number of moles and the volume of each component of the reaction mixture to obtain larger amount of product. Typical yields obtained were about 2 grams of washed and dried samples. The ratios used and volumes used are listed in Table 3.2.

Table 3.2
Reagent Amounts Used in Synthesis of
3-Mercaptopropanoic Acid CdS Capped Clusters

S^{2-}/RSH Ratio	Cd^{2+}	S^{2-}	3-Mercapto
0.5	20.00 mmol	13.33 mmol	13.33 mmol (1.162 ml)
0.75	20.00 mmol	16.00 mmol	8.000 mmol (0.697 ml)
1.0	20.00 mmol	17.78 mmol	4.444 mmol (0.387 ml)
3.0	20.00 mmol	18.18 mmol	3.636 mmol (0.317 ml)
4.0	20.00 mmol	18.57 mmol	2.857 mmol (0.307 ml)
20.0	20.00 mmol	19.51 mmol	0.976 mmol (0.085 ml)

Nafion-Grown CdS Clusters

XRD Results

The XRD pattern of Nafion grown CdS clusters are shown in Figs. 3.1-3.6. All samples display peaks that are consistent with both CdS cubic structure (Hawleyite) and CdS hexagonal structures (Greenockite). Figure 3.3 shows the XRD pattern of CdS2W

Page missing from thesis

Page missing from thesis

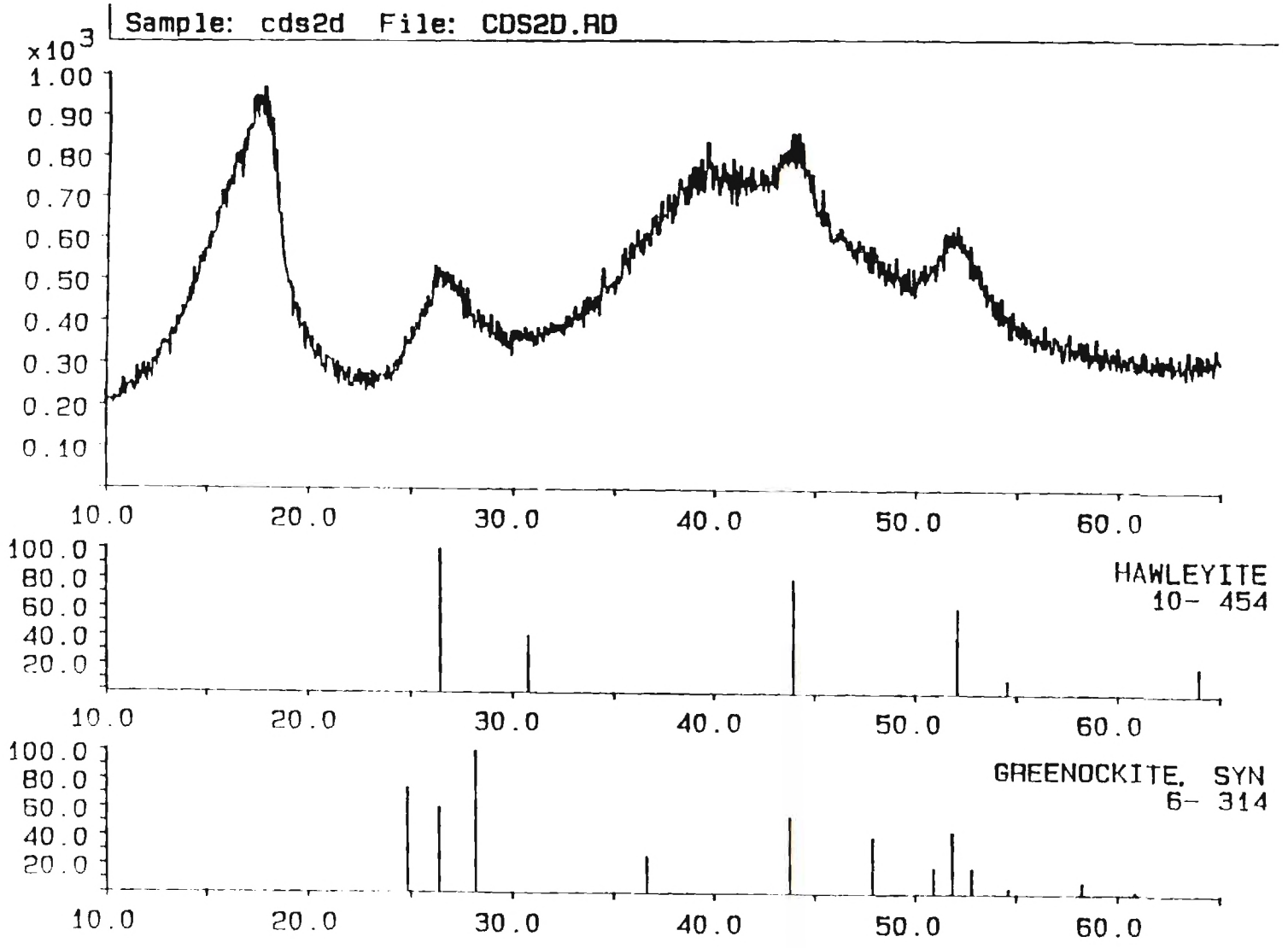

Figure 3.3: XRD of CdS2D cluster grown in Nafion as compared with cubic (Hawleyite) and hexagonal (Geenockite) crystal structures

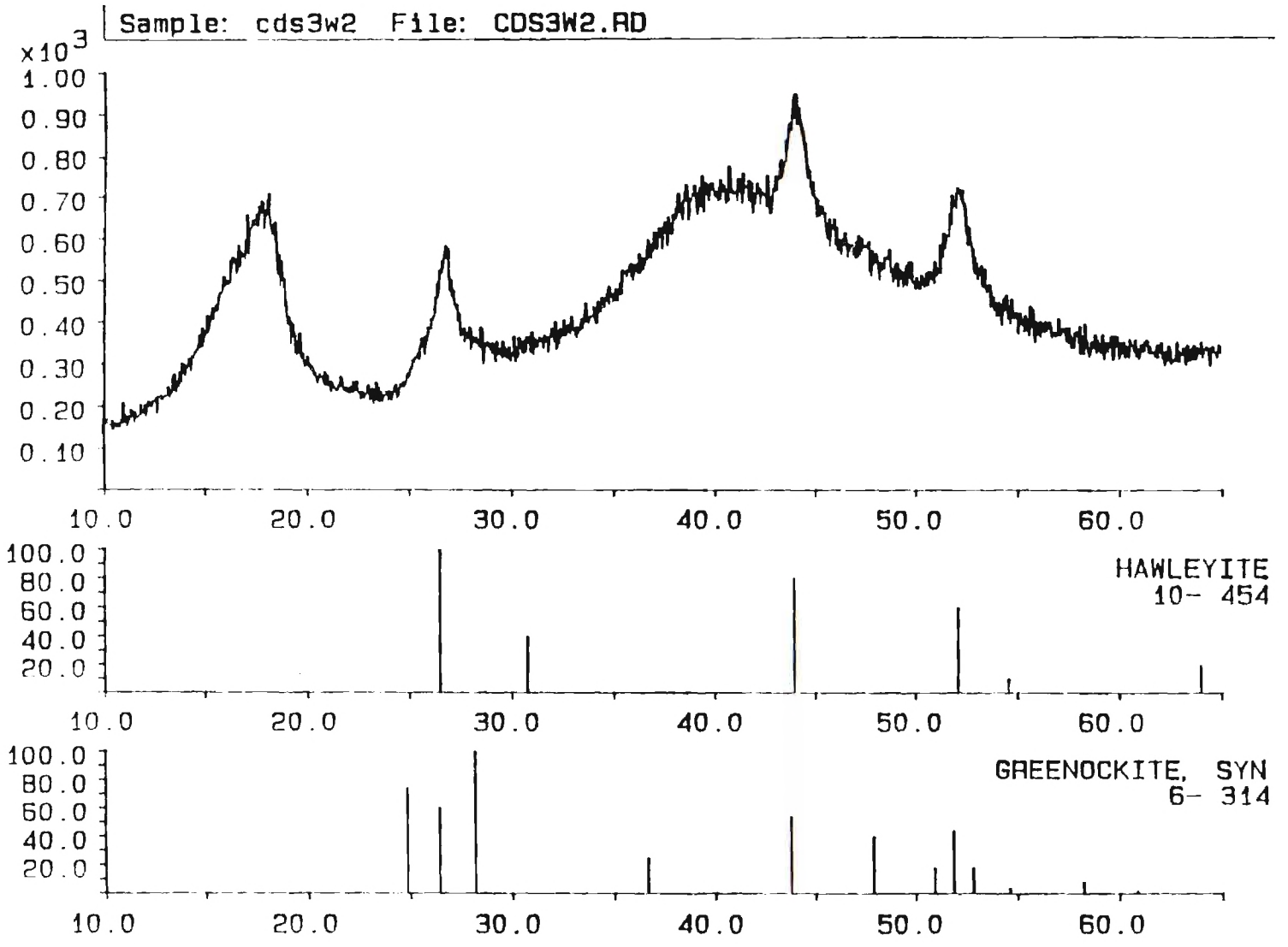

Figure 3.4: XRD of CdS3W cluster grown in Nafion as compared with cubic (Hawleyite) and hexagonal (Geenockite) crystal structures

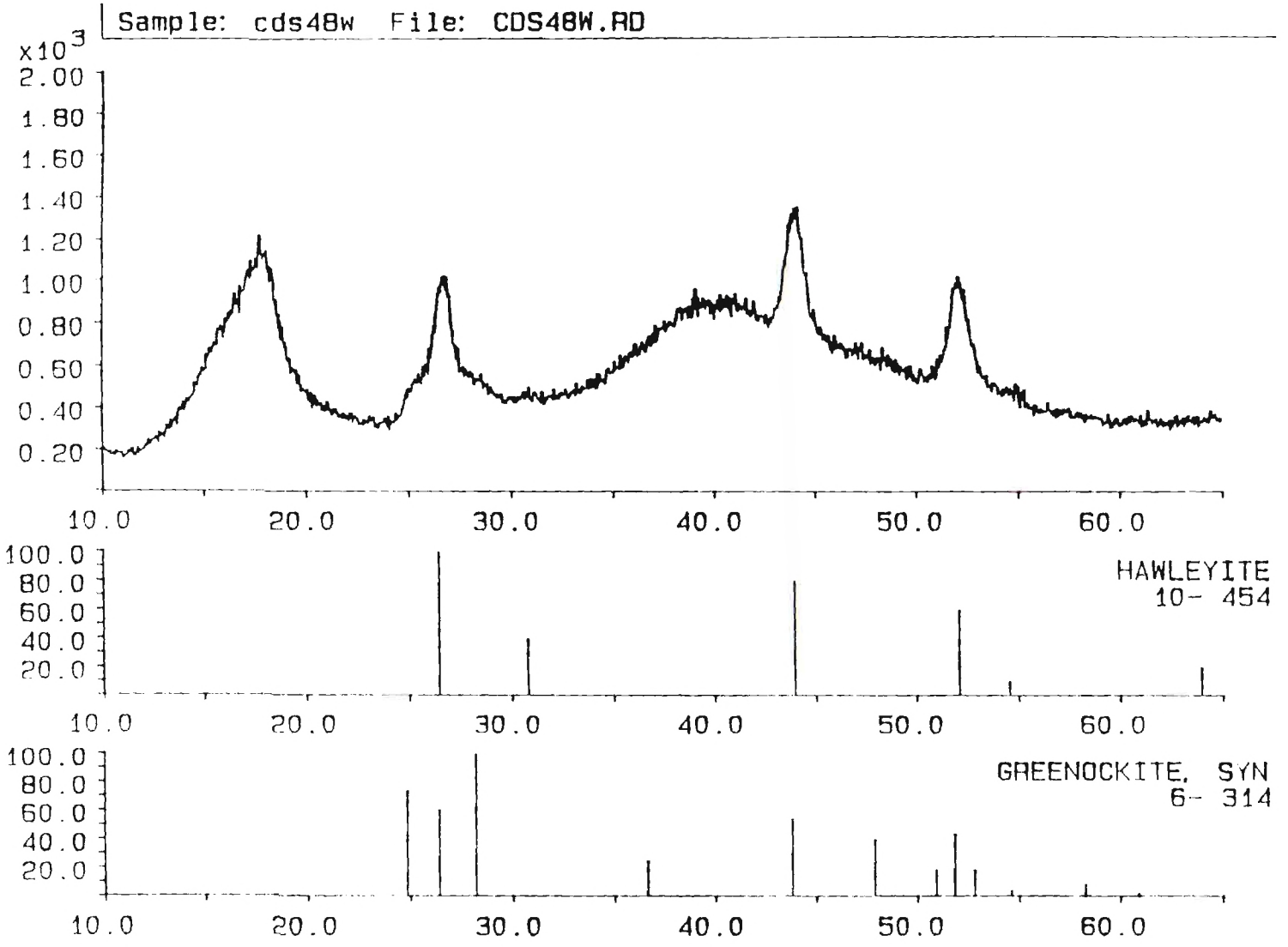

Figure 3.5: XRD of CdS348W cluster grown in Nafion as compared with cubic (Hawleyite) and hexagonal (Greenockite) crystal structures

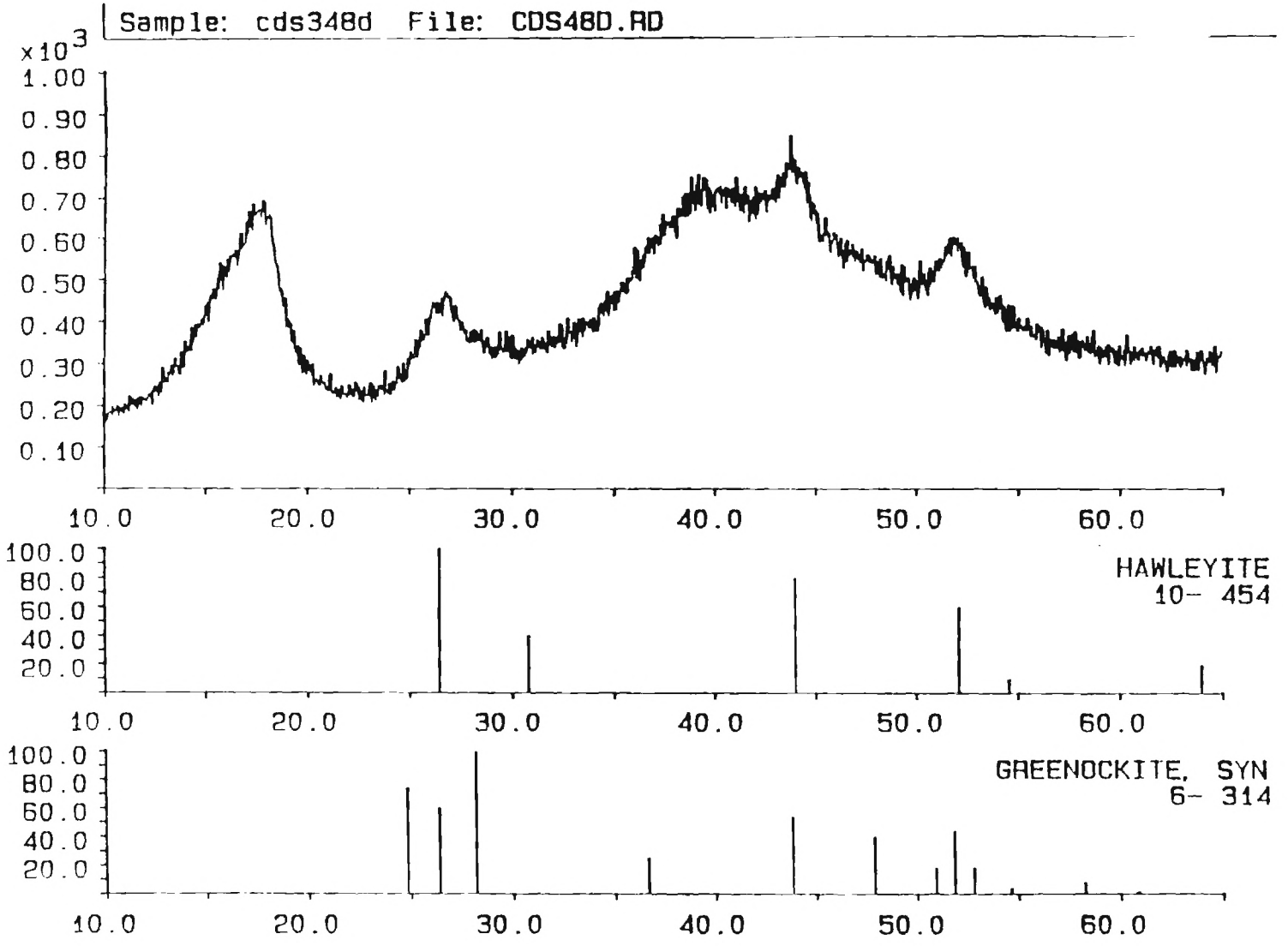

Figure 3.6: XRD of CdS348D cluster grown in Nafion as compared with cubic (Hawleyite) and hexagonal (Greenockite) crystal structures

as compared with cubic CdS and hexagonal CdS peak patterns. As can be seen clearly in this figure, both domains are present in this sample. Also all the diffraction peaks were broadened due to crystal size effect. For estimation of the cluster size the third CdS diffraction peak (the (220) reflection of cubic phase and also (110) reflection of the hexagonal phase) was fitted and the width of the peak at half maximum (FWHM) was used to estimate the size. XRD pattern of CdS3D samples showed very low diffraction peaks that were not useful for size ermination. The results of the fittings are shown in Table 3.3 below. As can be seen from Table 3.3, the CdS2W has the largest cluster size of ~224 Å, and is the largest cluster prepared in this work.

Table 3.3: XRD Results of Nafion Grown CdS Clusters

Sample	Angle (degrees)	FWHM (degrees)	Cluster Diameter (Å)
CdSNa2S	44.086	2.20	51
CdS2W	43.954	0.51	224
CdS2D	43.721	1.63	70
CdS3W	44.080	1.00	114
CdS348W	43.995	0.96	119
CdS348D	43.712	1.65	69

Optical Spectra

The absorption spectrum of the CdS3D sample was measured in a quartz cell under nitrogen. The absorption spectrum is shown in Fig. 3.7. The absorption edge is blue shifted from that of the bulk CdS due to its small cluster size. Also apparent in the same figure is the existence of an exciton peak due to quantum size effects. According

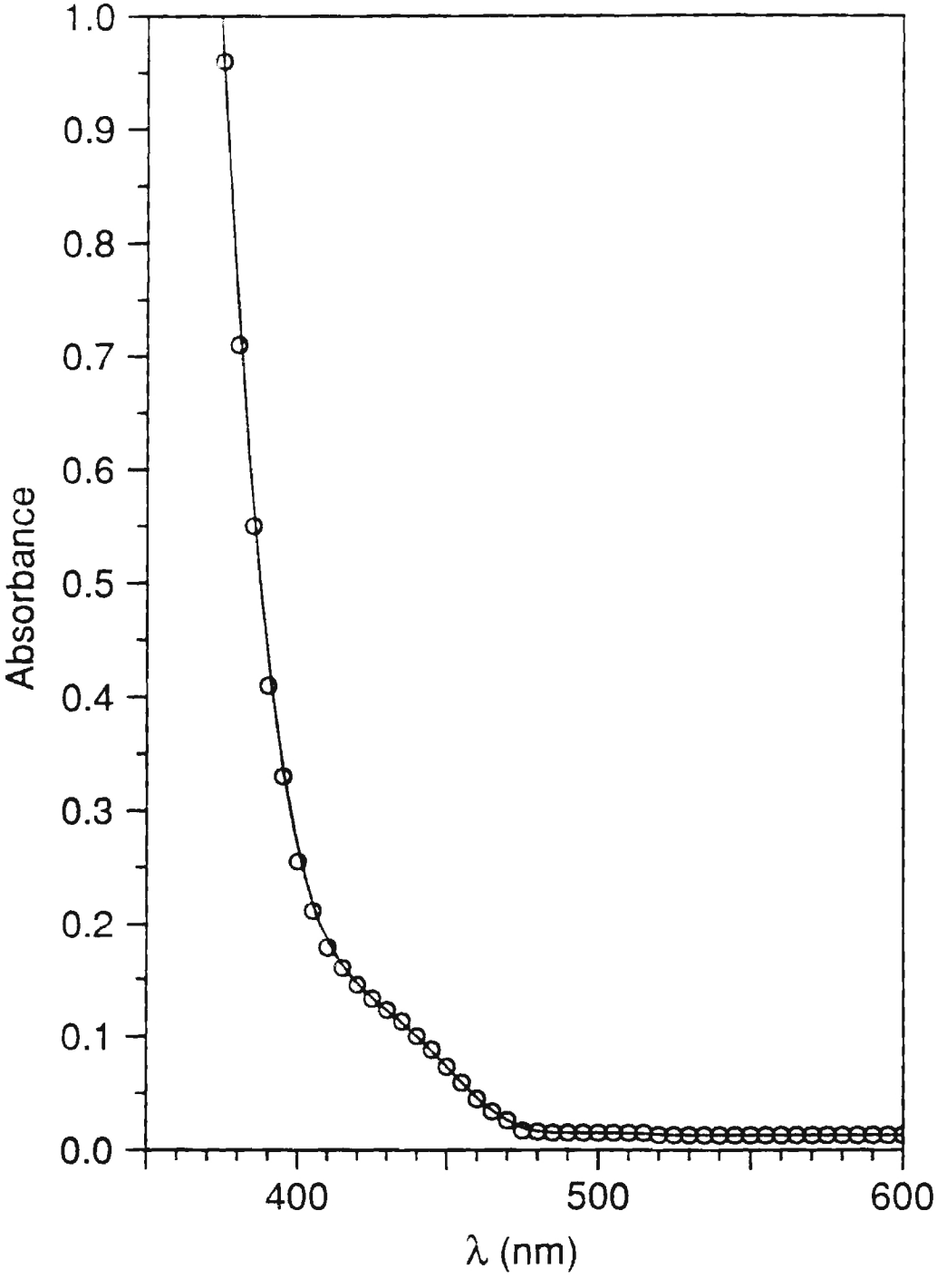

Figure 3.7. Absorption spectra of CdS3D sample in Nafion 117

to literature [2], the cluster size is ~35 Å from correlation with the exciton peak energy. The absorption spectra of the other Nafion grown CdS clusters were not possible to obtain due to high optical density (highly concentrated samples).

XAFS Results

The Cd-edge XAFS was obtain at room temperatures on the X-11A beam line of the National Science Light Source (NSLS) at Brookhaven National Laboratories. The monochromator crystal used for the Cd-edge measurements was Si(311). The Nafion samples consisted of eight layers, epoxy-sealed with 3 mil mylar film. The bulk standards were packed in a 2mm-thick sample holder having a 6x22 mm cutout for the sample. The Cd-O standard used was CdMSO3 (cadmium methanesulphonate dihydrate) and was prepared according to literature [3]. The cadmium in this sample is coordinated with six oxygens: four from four sulphonato groups and two from water. The average Cd-O distance is 2.275 Å. The Cd-S standard used was bulk CdS.

Cd^{2+} in Nafion: The coordination of Cd^{2+} in Nafion in the absence of H_2S was studied with XAFS. Two samples were used: CdDry and CdWet. The CdDry sample was Cd-loaded Nafion which was dried for 12 hours. The CdWet sample was prepared by soaking the CdDry sample in water for 5 minutes. The XAFS transform is shown in Fig. 3.8 and shows that the CdWet and CdDry samples have a Cd-O peak similar to the bulk $CdMSO_3$. The Cd-O transform peak was filtered and analyzed using the ratio method. The XAFS results showed that the average coordination number of Cd in the Nafion is ~5 oxygens. The coordination number of Cd in CdWet was found to be ~6 oxygens. These results are summarized in Table 3.4.

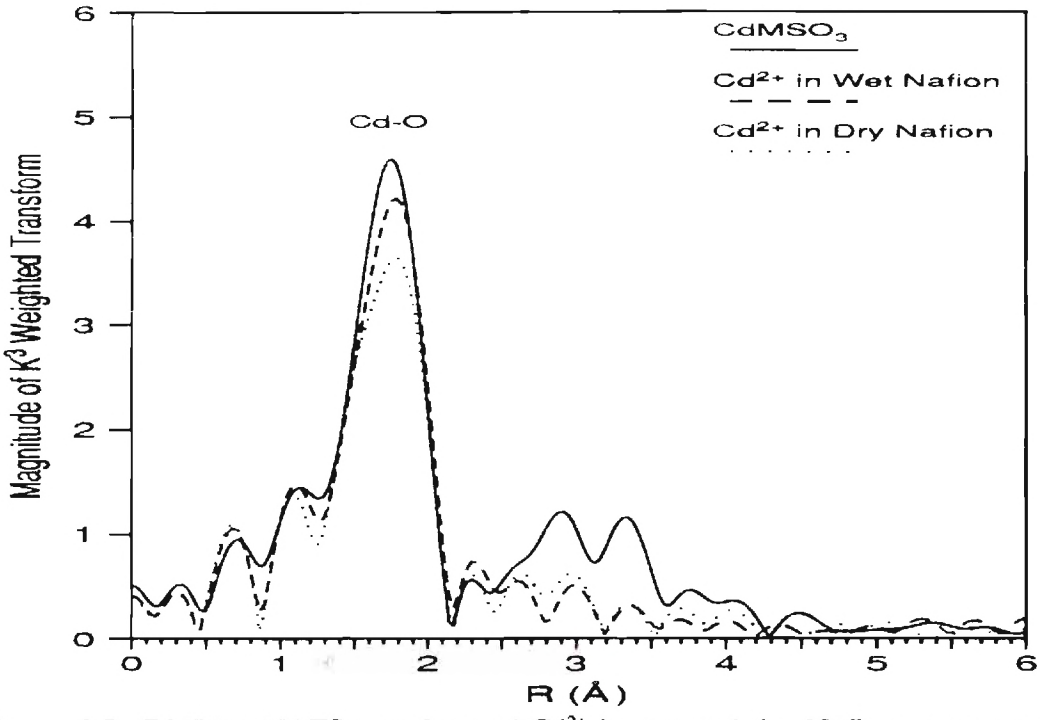

Figure 3.8. Cd-Edge XAFS transform of Cd^{2+} in wet and dry Nafion as compared with $CdMSO_3$

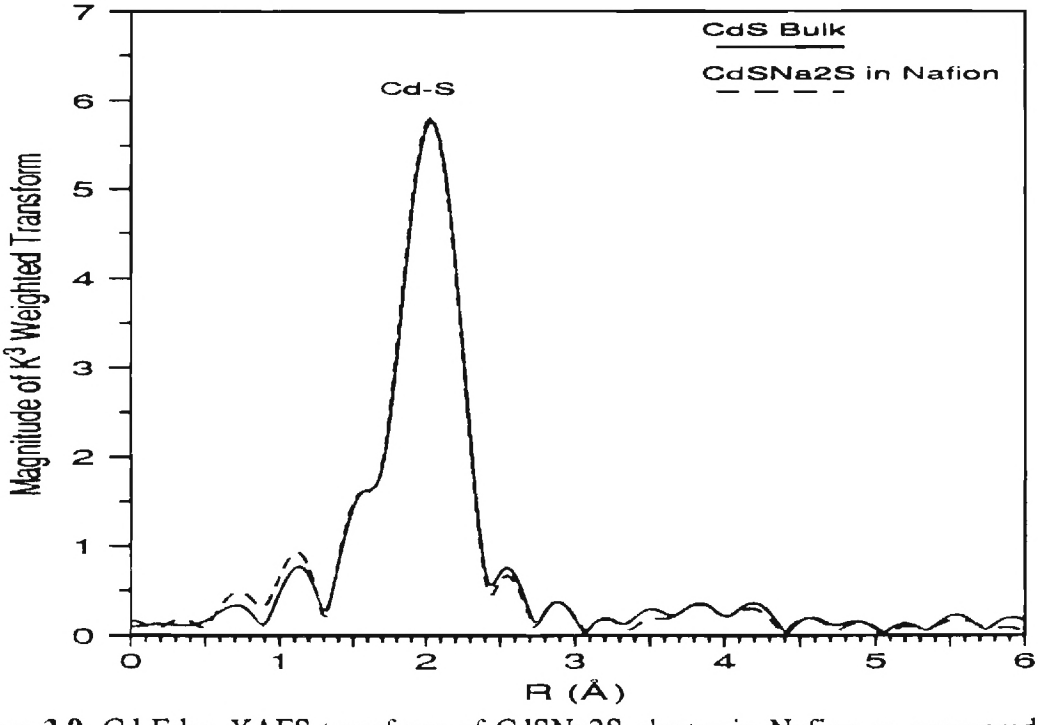

Figure 3.9. Cd-Edge XAFS transform of CdSNa2S cluster in Nafion as compared with CdS Bulk sample.

Table 3.4
Cd-edge Room Temperature XAFS for Cd-Loaded Nafion

Sample	R(Cd-O) (Å)[1]	N(Cd-O)	$\sigma^2_{ref} - \sigma^2_{sample}$ (Å^2)
CdDry	2.27 ± 0.02	5.1 ± 0.5	0.00052 ± 0.00089
CdWet	2.27 ± 0.06	5.6 ± 0.4	0.00029 ± 0.00065

1)The error bars are precision values from analysis

CdS-Grown Nafion Clusters: The XAFS transform of CdSNa2S is shown in Fig. 3.9 as compared to the bulk CdS and shows that the CdSNa2S sample displays the same features as the bulk sample. It is notable that neither the bulk CdS nor the CdSNa2S cluster sample shows a second shell peak at room temperature. The Cd-S first shell was filtered and analyzed. No evidence of Cd-O was detected when trying to fit the first shell with both Cd-S and Cd-O standards, indicating a complete reaction of cadmium in the Nafion. Using the CdS as standard, it was found that the coordination number of the CdSNa2S sample is 4.0, similar to the bulk sample.

The CdS2W XAFS transform is shown Fig. 3.10 as compared to bulk CdS. The analysis of first shell peak showed that the sample was full reacted. The coordination number found ~4 is similar bulk value of 4.

The CdS2D XAFS transform is shown in Fig. 3.11 and shows peaks similar to bulk CdS. As can be seen in the transform, the first shell is somewhat reduced as compared to the bulk sample. Analysis of the first shell showed that this peak actually consisted of Cd-S and Cd-O contributions. The fitting results gave a N(Cd-S)=3.48 and N(Cd-O)= 0.36. These results are shown in Table 3.5.

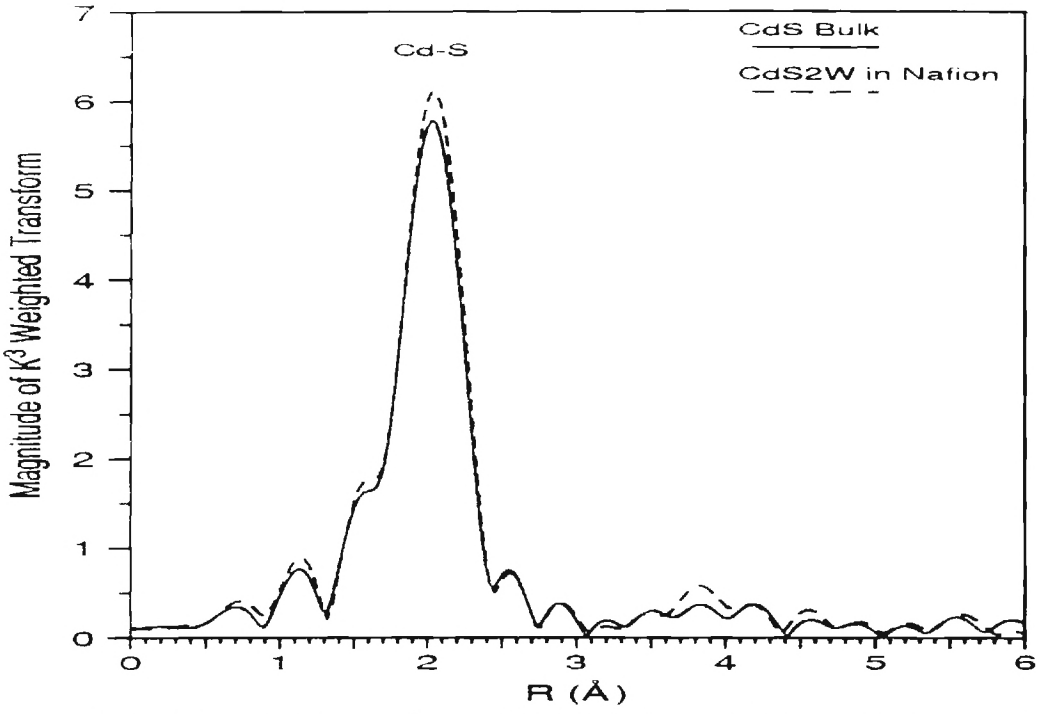

Figure 3.10. Cd-Edge XAFS transform of CdS2W cluster in Nafion as compared with CdS Bulk sample.

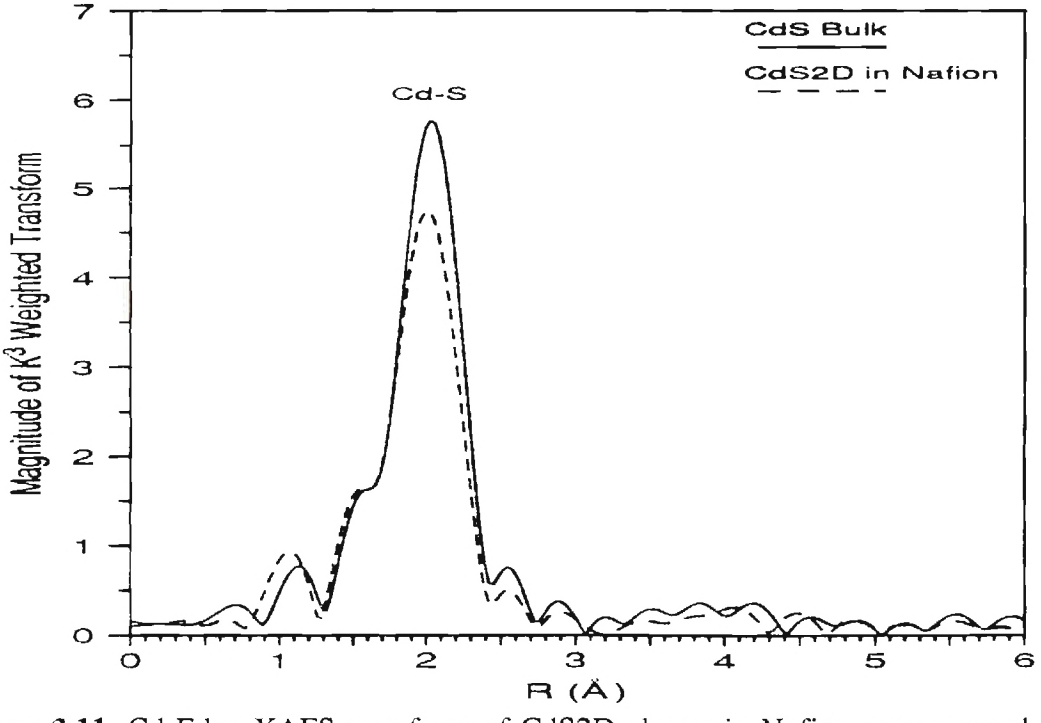

Figure 3.11. Cd-Edge XAFS transform of CdS2D cluster in Nafion as compared with CdS Bulk sample.

The XAFS transform of CdS3W and CdS3D as compared with both CdS bulk and $CdMSO_3$ are shown in Figs. 3.12 and 3.13, respectively. The first shell peak clearly shows the presence of both Cd-O and Cd-S phases. Similarly, the XAFS transforms for CdS48W and CdS48D are shown in Figures 3.14 and 3.15, respectively. The filtered peaks were analyzed by using various standards, and the results of the fittings of these samples are shown in Table 3.6. In all samples, the Cd-S bond length was 2.51 Å, in agreement with XRD results, and the Cd-O is 2.27 Å. The $\Delta\sigma^2$ was small and negligible. The fitting plots are shown in Figures 3.16-3.21.

Table 3.5: Cd-edge XAFS Results for Nafion Grown CdS Clusters. CdSNa2S and CdS2W Samples

Sample	R(Cd-S) (Å)[1]	N(Cd-O)	$\sigma^2_{ref} - \sigma^2_{sample}$ (Å^2)
CdSNaS	2.521 ± 0.001	4.00 ± 0.04	-0.00042 ± 0.00009
CdS2W	2.524 ± 0.002	4.16 ± 0.04	-0.00001 ± 0.00008

1)The error bars are precision values from analysis

Table 3.6
XAFS Fitting Results of CdS2D, CdS3D, and CdS3W Clusters in Nafion

Sample	Cd-S Ref.	Cd-O Ref.	N_{fit}(Cd-S)	N_{fit}(Cd-O)
CdS2D	CdS	$CdMSO_3$	3.48	0.36
CdS3D	CdS	$CdMSO_3$	1.12	3.30
CdS3D	$CdSNa_2S$	CdDry	1.13	3.33
CdS3D	$CdSNa_2S$	CdWet	1.04	3.47
CdS3W	$CdSNa_2S$	$CdMSO_3$	2.12	2.52
CdS3W	$CdSNa_2S$	CdDry	1.96	2.60
CdS3W	$CdSNa_2S$	CdWet	1.80	2.86
CdS348D	CdS	CdDry	2.45	2.12
CdS348W	CdS	$CdSMO_3$	3.98	0.16

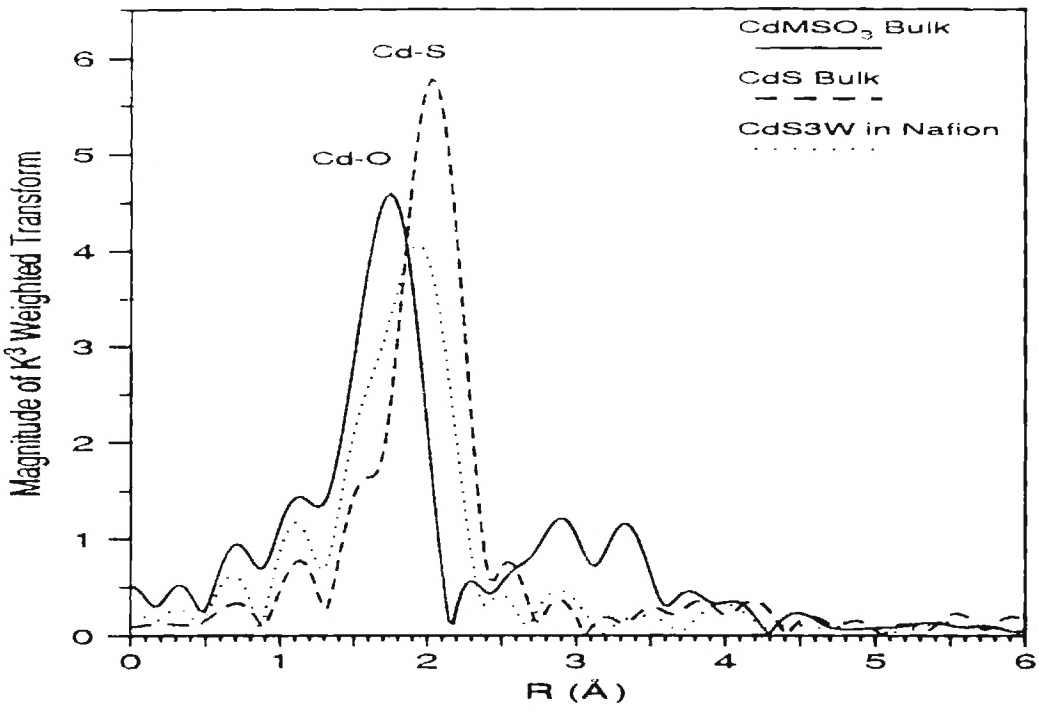

Figure 3.1. Cd-Edge XAFS transform of CdS3W cluster in Nafion as compared with CdS and $CdMSO_3$ bulk samples.

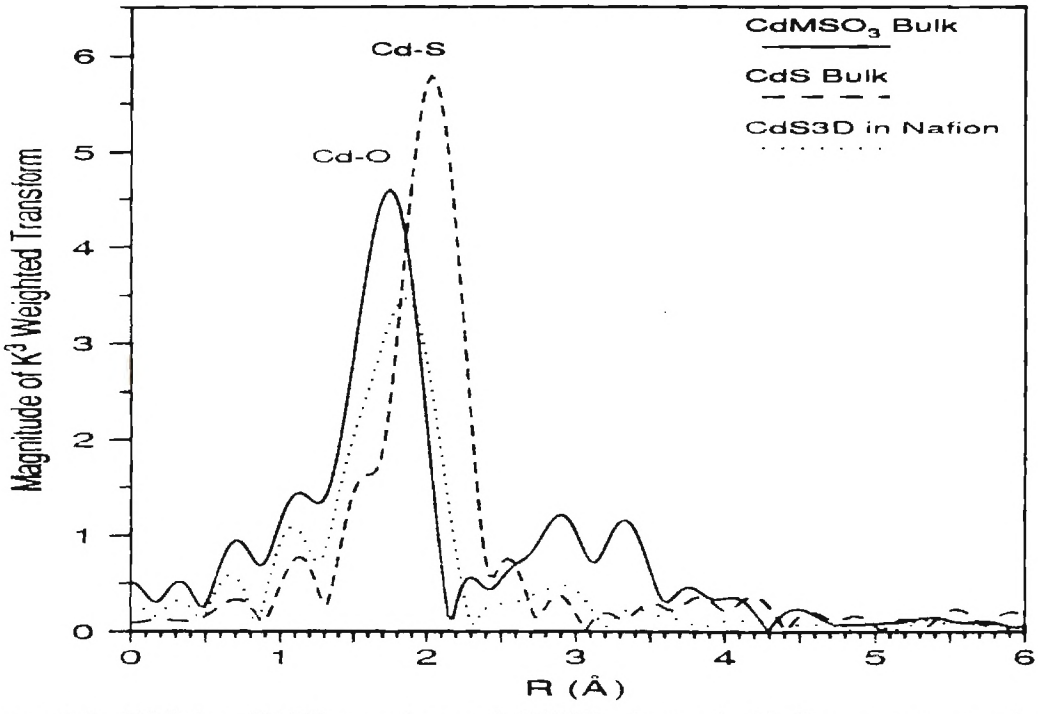

Figure 3.2. Cd-Edge XAFS transform of CdS3D cluster in Nafion as compared with CdS and $CdMSO_3$ bulk samples.

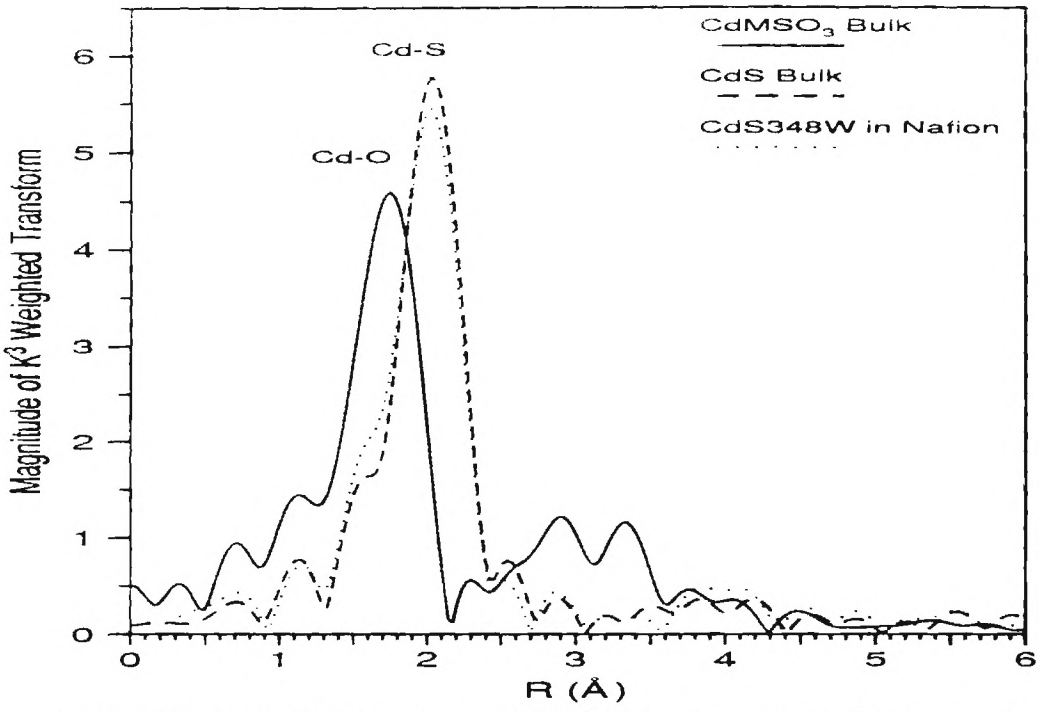

Figure 3.3. Cd-Edge XAFS transform of CdS348W cluster in Nafion as compared with CdS and $CdMSO_3$ bulk samples.

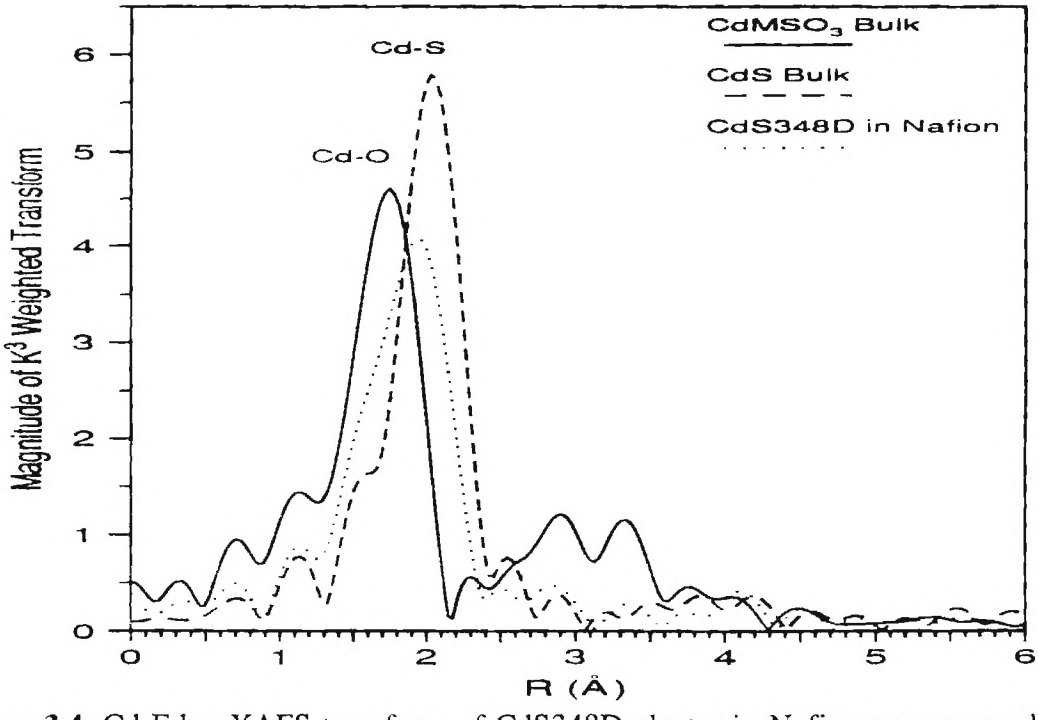

Figure 3.4. Cd-Edge XAFS transform of CdS348D cluster in Nafion as compared with CdS and $CdMSO_3$ bulk samples.

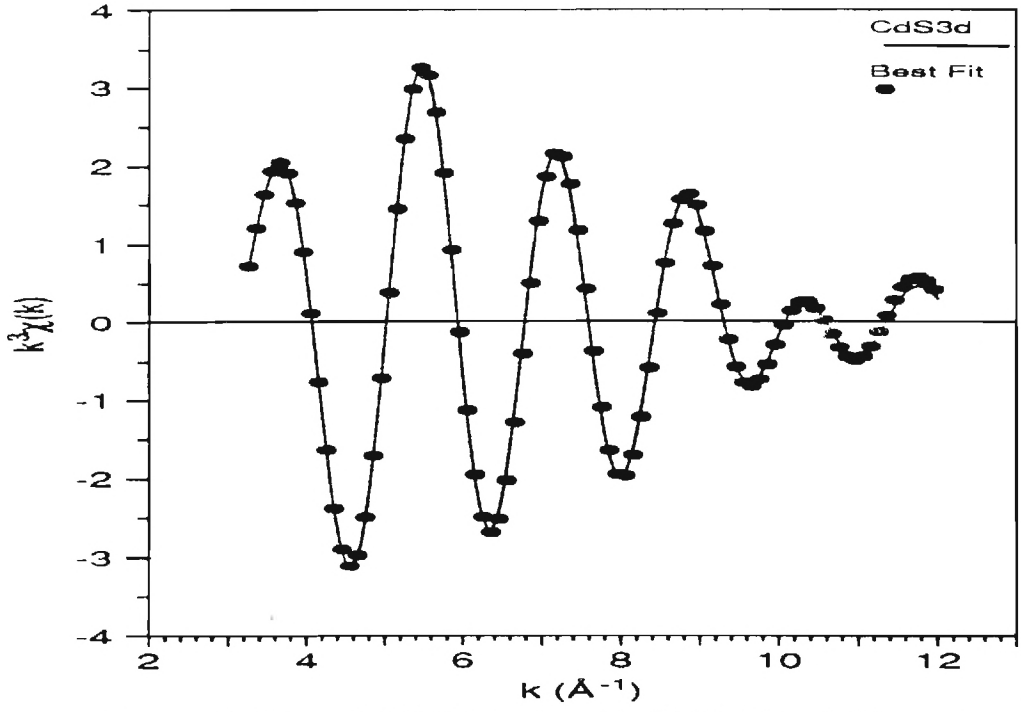

Figure 3.5. First shell fitting of CdS3D cluster with CdSNa2S and CdDry as standards

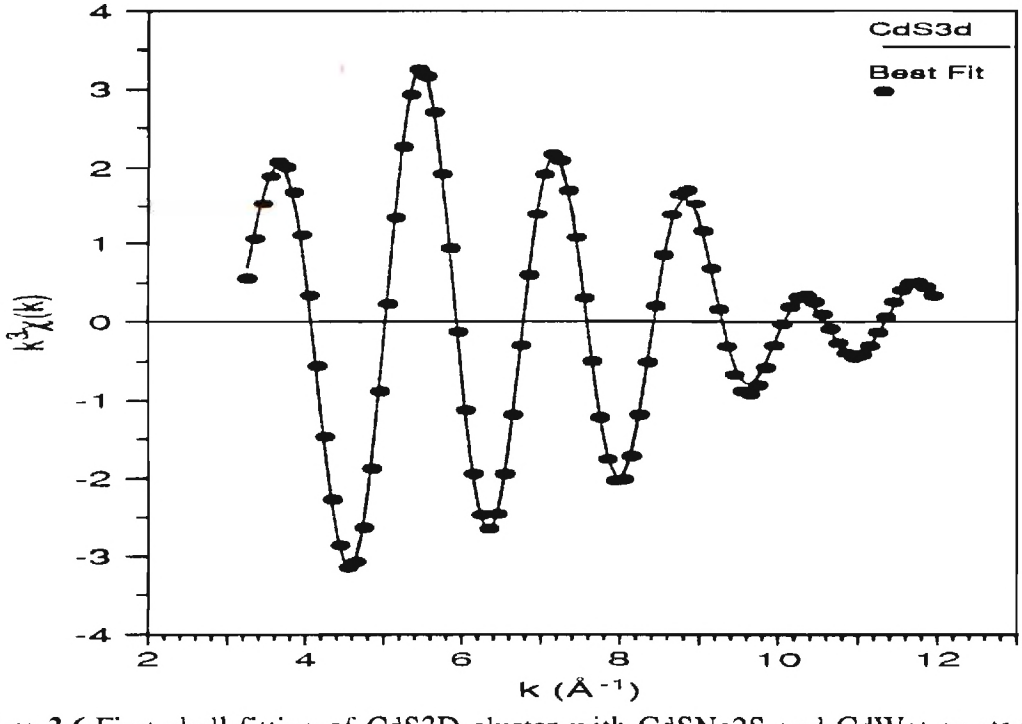

Figure 3.6. First shell fitting of CdS3D cluster with CdSNa2S and CdWet as standards.

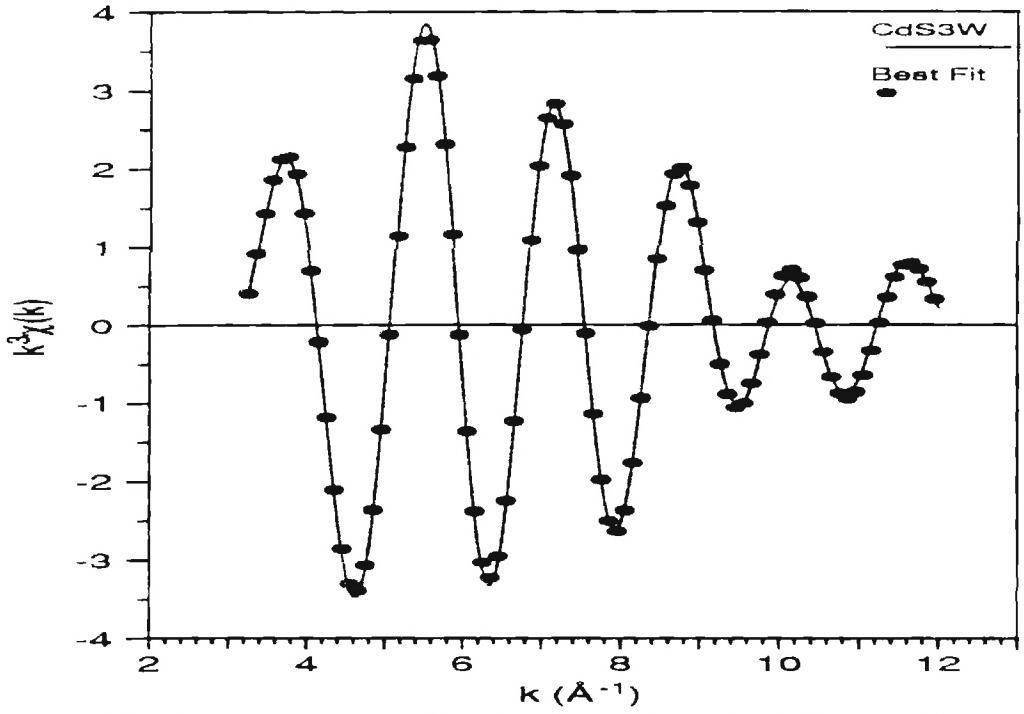

Figure 3.7.First shell fitting of CdS3W cluster with CdSNa2S and $CdMSO_3$ as standards

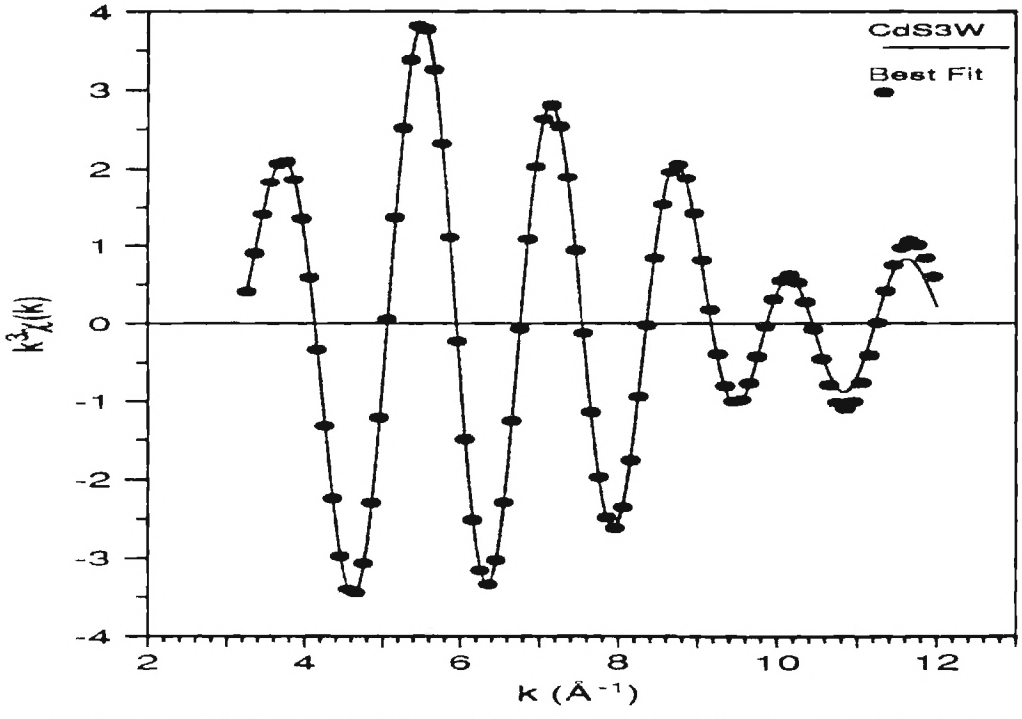

Figure 3.8.First shell fitting of CdS3W cluster with CdSNa2S and CdDry as standards

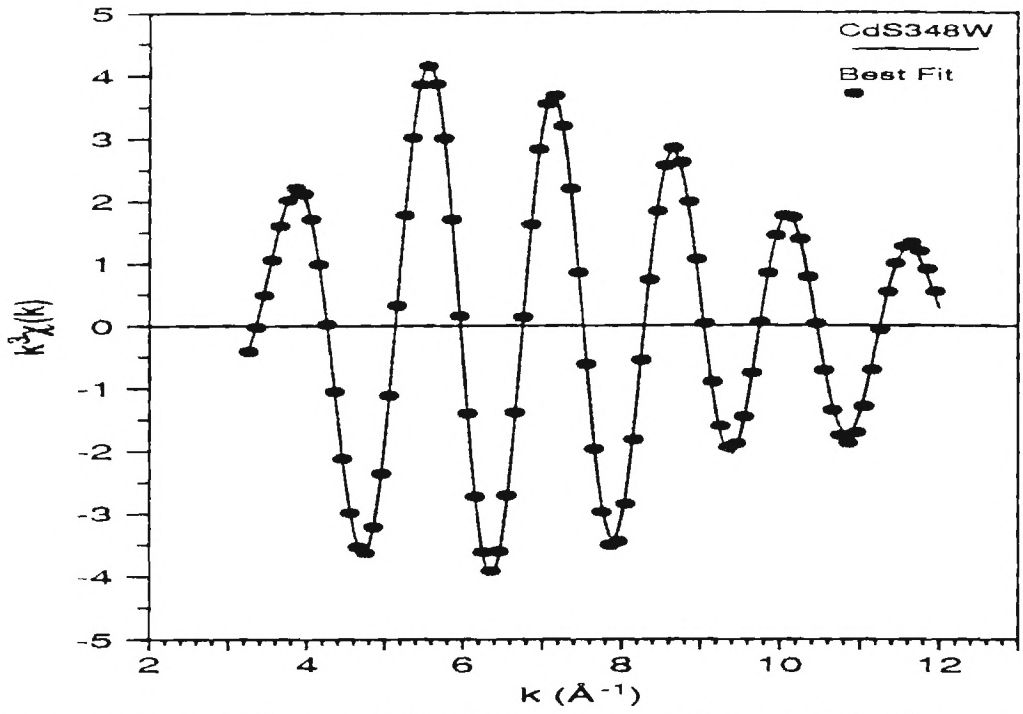

Figure 3.9. First shell fitting of CdS348D cluster with CdS and $CdMSO_3$ as standards

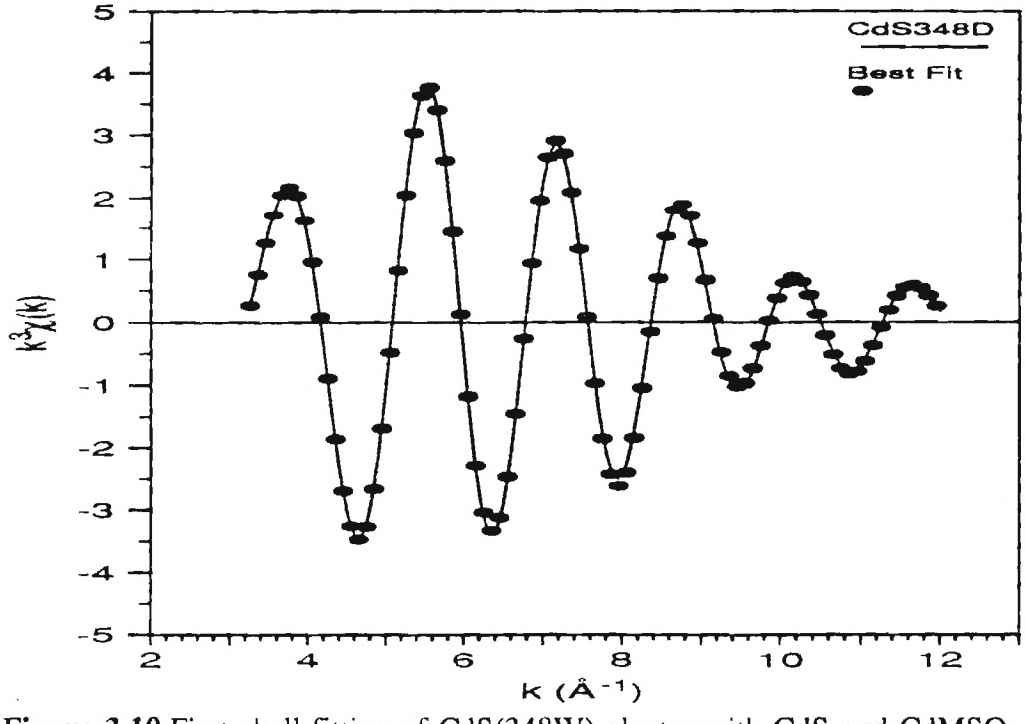

Figure 3.10.First shell fitting of CdS(348W) cluster with CdS and $CdMSO_3$ as standards

Thiophenol Capped CdS Clusters

XRD Results

The diffraction patterns of the thiophenol capped CdS clusters prepared with varying ratio of S^{2-}/SPh^- are shown in Fig. 3.22-26. As displayed in these figures, the high angle diffraction peaks are not resolved even for the largest cluster (R=4.5). The first diffraction peak shows a decrease in the peak width as the sample ratio of S^{2-}/SPh^- increases indicating that the size of the cluster increased. These observations are contrary to the reported results by Herron *et al* [1] where a clearly cubic phase was obtained. In this work, the diffraction pattern of the CdS clusters is of the hexagonal structure and probably mixed with some small ratio of the cubic phase. The fact that the first peak in the diffraction pattern is due to three overlapping peaks makes the size analysis by this method very inaccurate.

Optical Spectra

The optical spectra of these samples were obtained from acetonitrile solutions in 1 cm quartz cell at room temperature. A Cary 14 spectrometer was used. The absorption spectra are shown in Fig. 3.27. All the plots show a peak that is called the exciton peak. The exciton peak energy shifts to lower wavelength (higher energy) as the size of the cluster decreases (increasing S^{2-}/PhS^- ratio). The exciton energies were estimated from the second derivative of the curves. The exciton energies are listed in Table 3.7. Using computational results from literature[4], the sizes of the clusters are estimated.

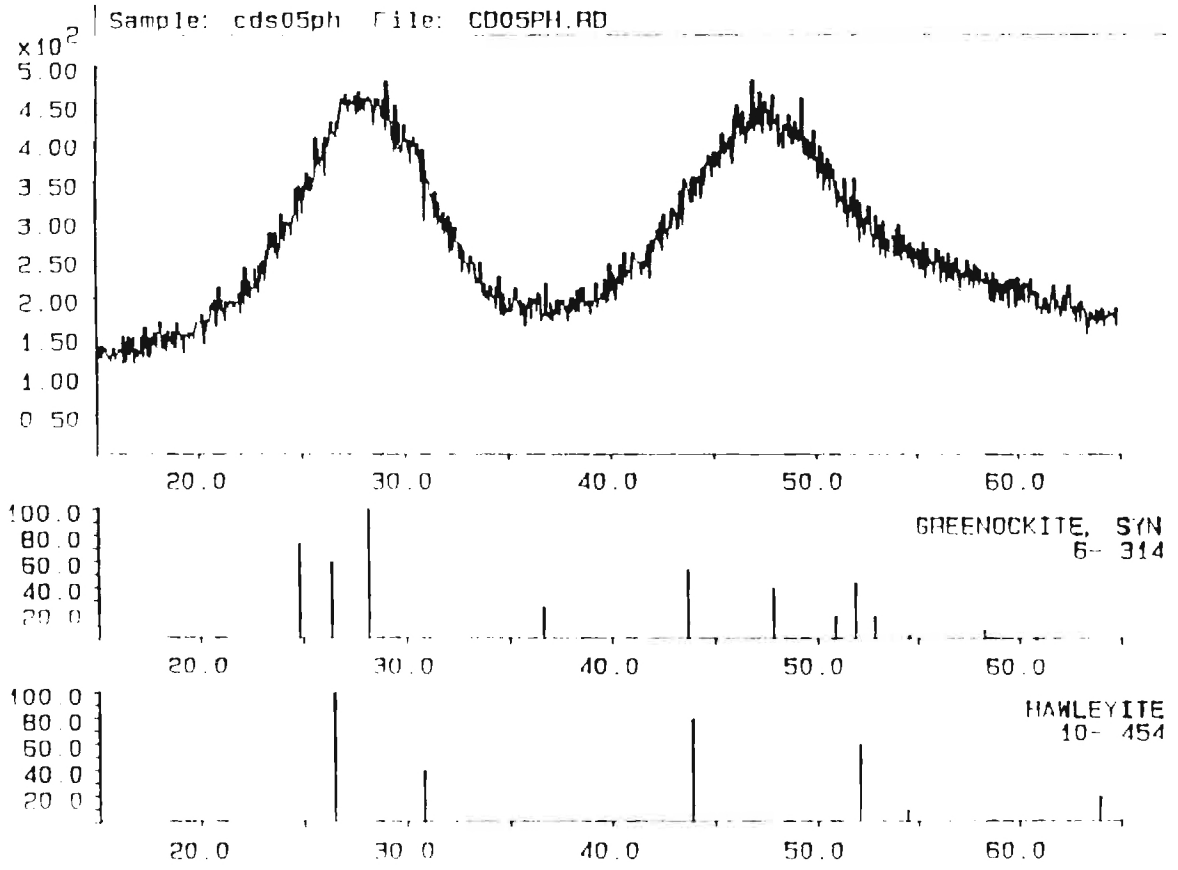

Figure 3.11. XRD of CdS0.5 cluster capped with thiophenol compared with hexagonal (Geenockite) and cubic (Hawleyite) crystal structures.

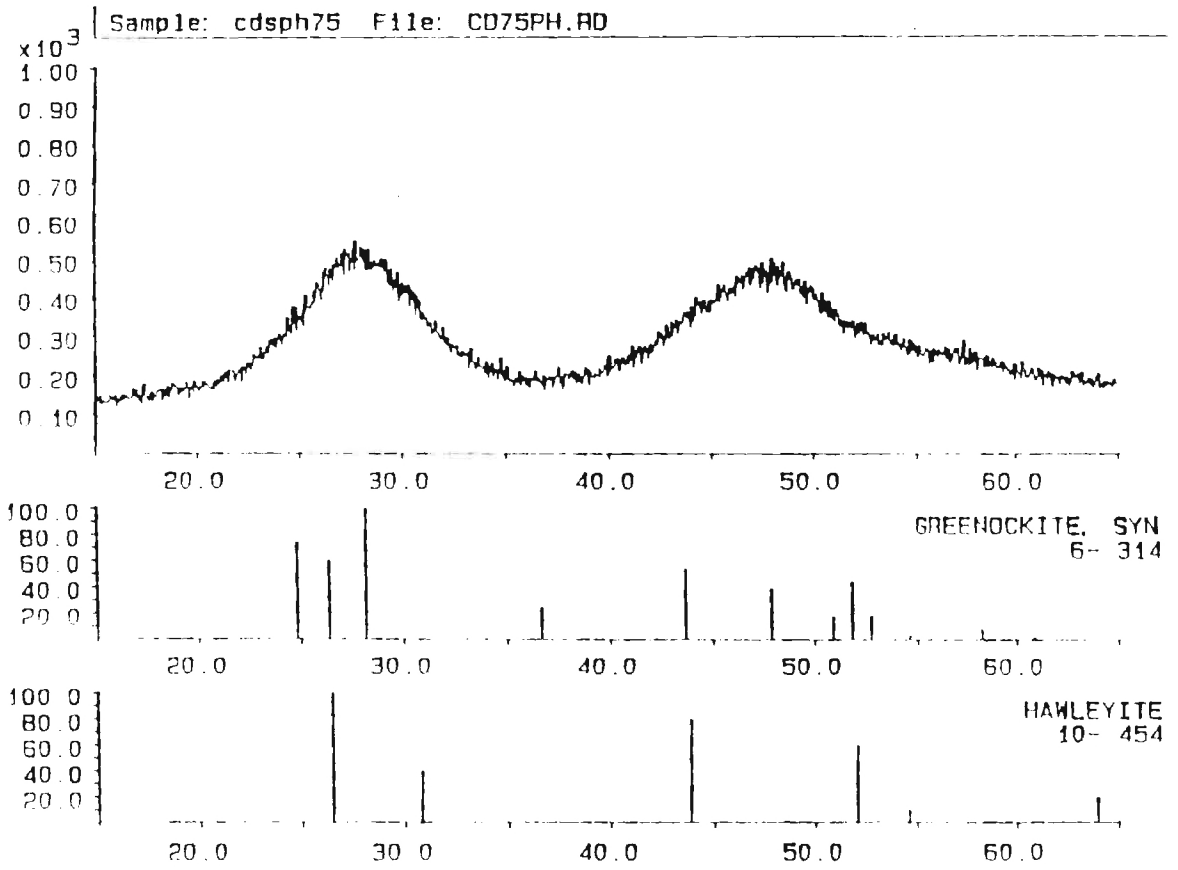

Figure 3.12. XRD of CdS0.75 cluster capped with thiophenol as compared with hexagonal (Geenockite) and cubic (Hawleyite) crystal structures.

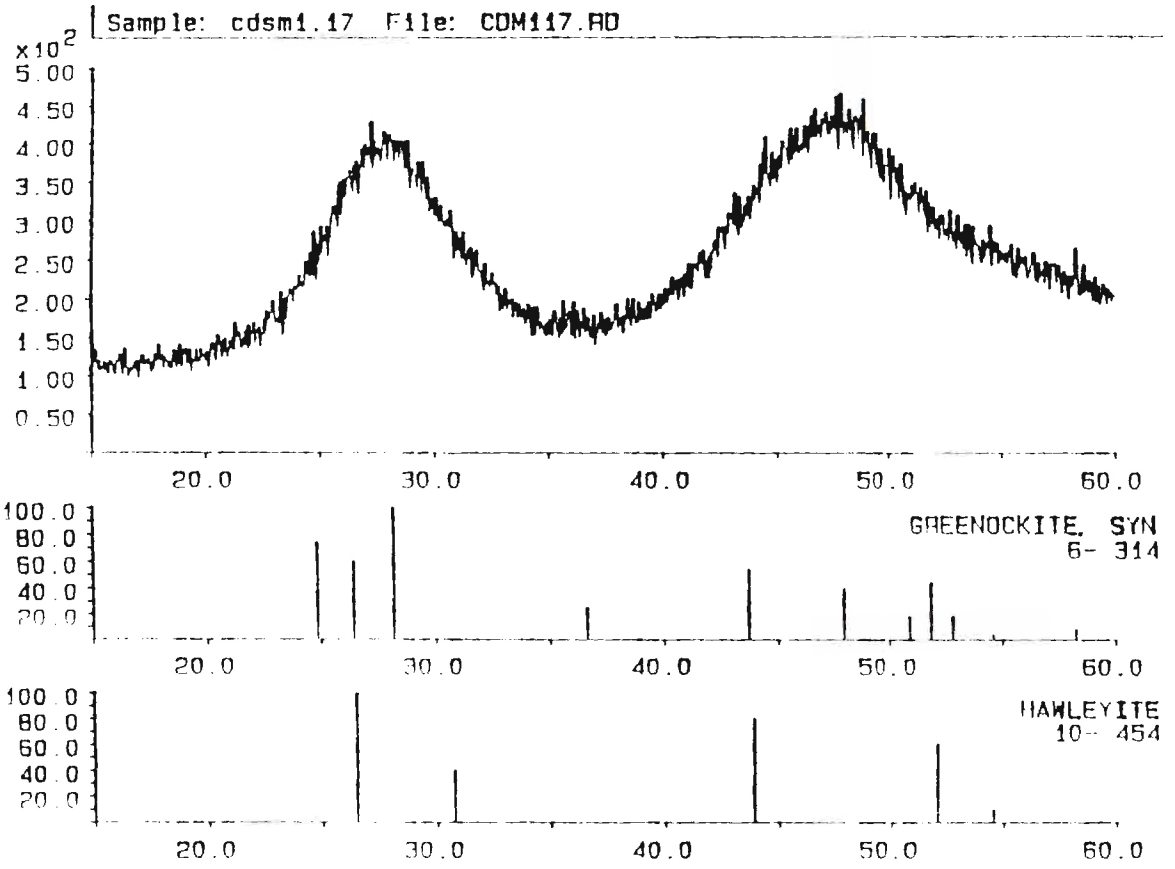

Figure 3.13. XRD of CdS1.17 cluster capped with thiophenol as compared with hexagonal (Geenockite) and cubic (Hawleyite) crystal structures.

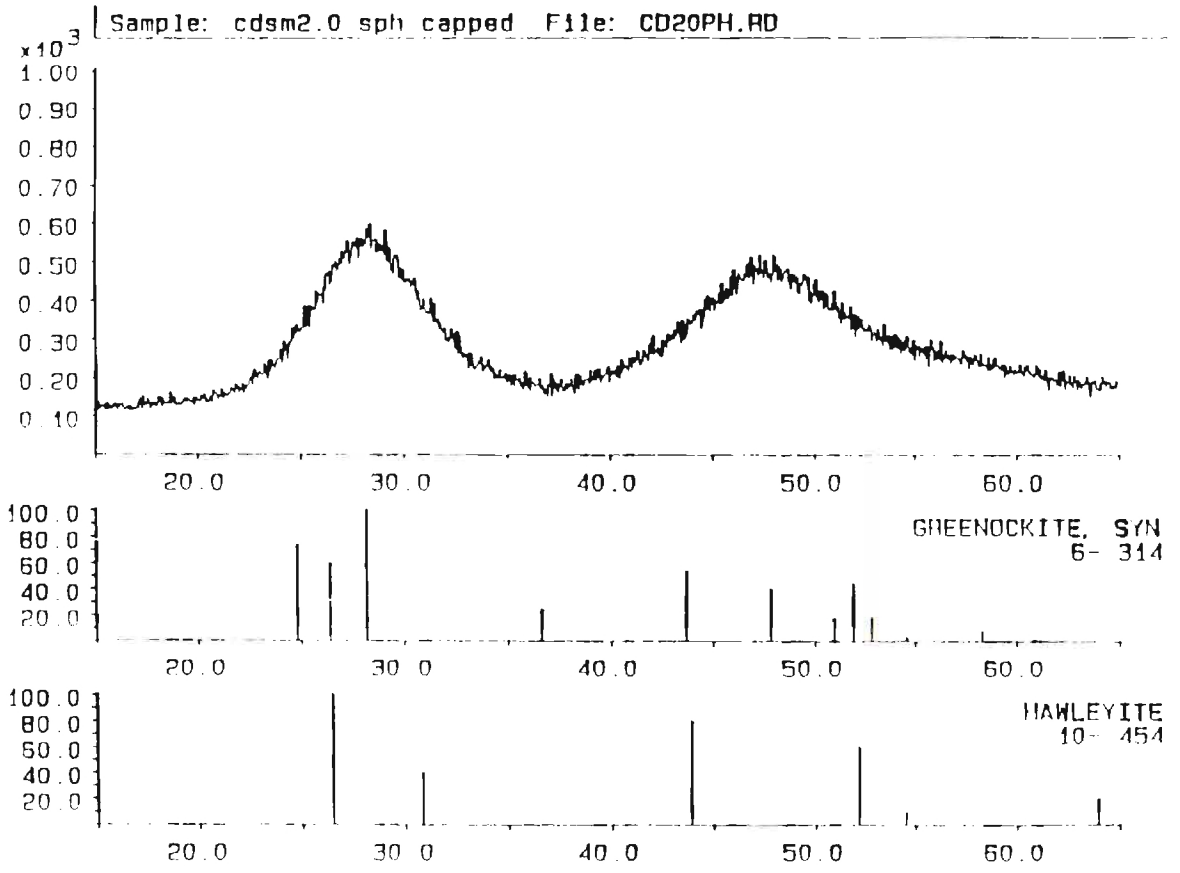

Figure 3.14. XRD of CdS2.0 cluster capped with thiophenol as compared with hexagonal (Geenockite) and cubic (Hawleyite) crystal structures.

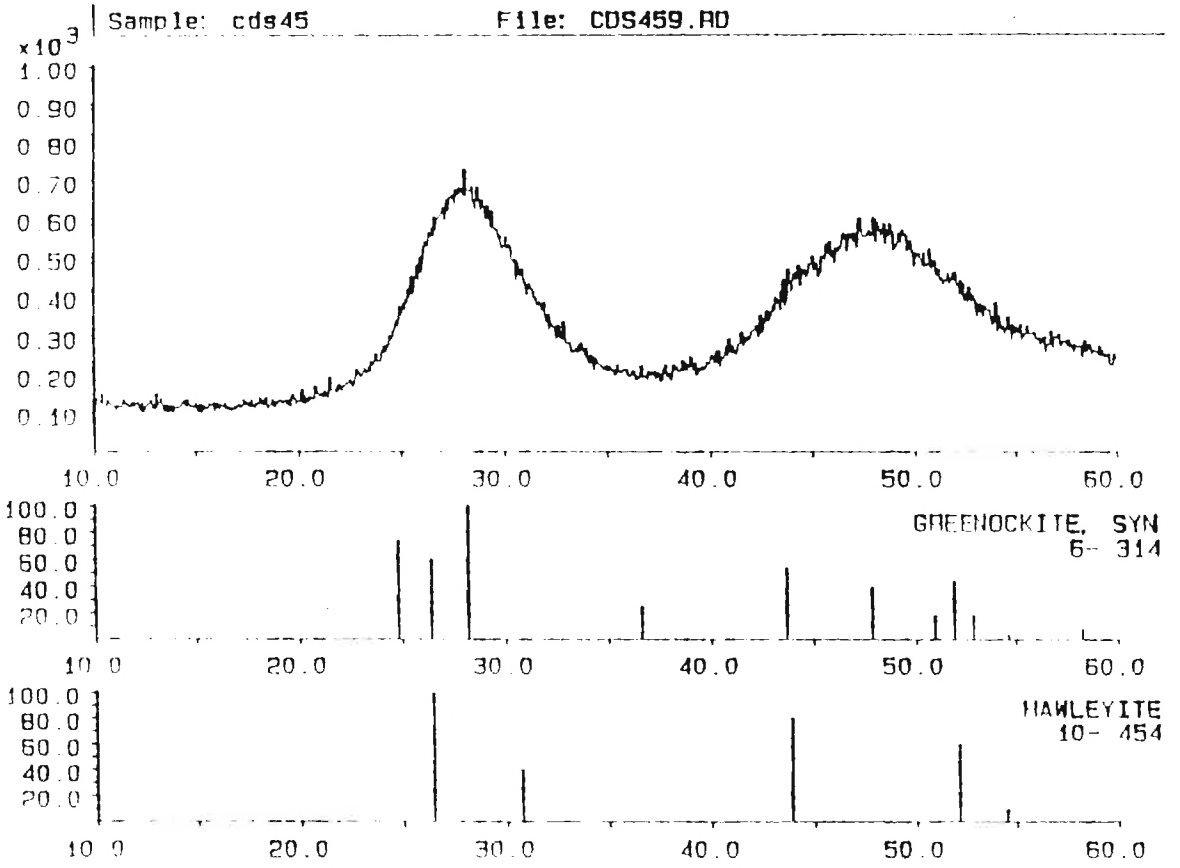

Figure 3.15. XRD of CdS4.5 cluster capped with thiophenol as compared with hexagonal (Geenockite) and cubic (Hawleyite) crystal structures.

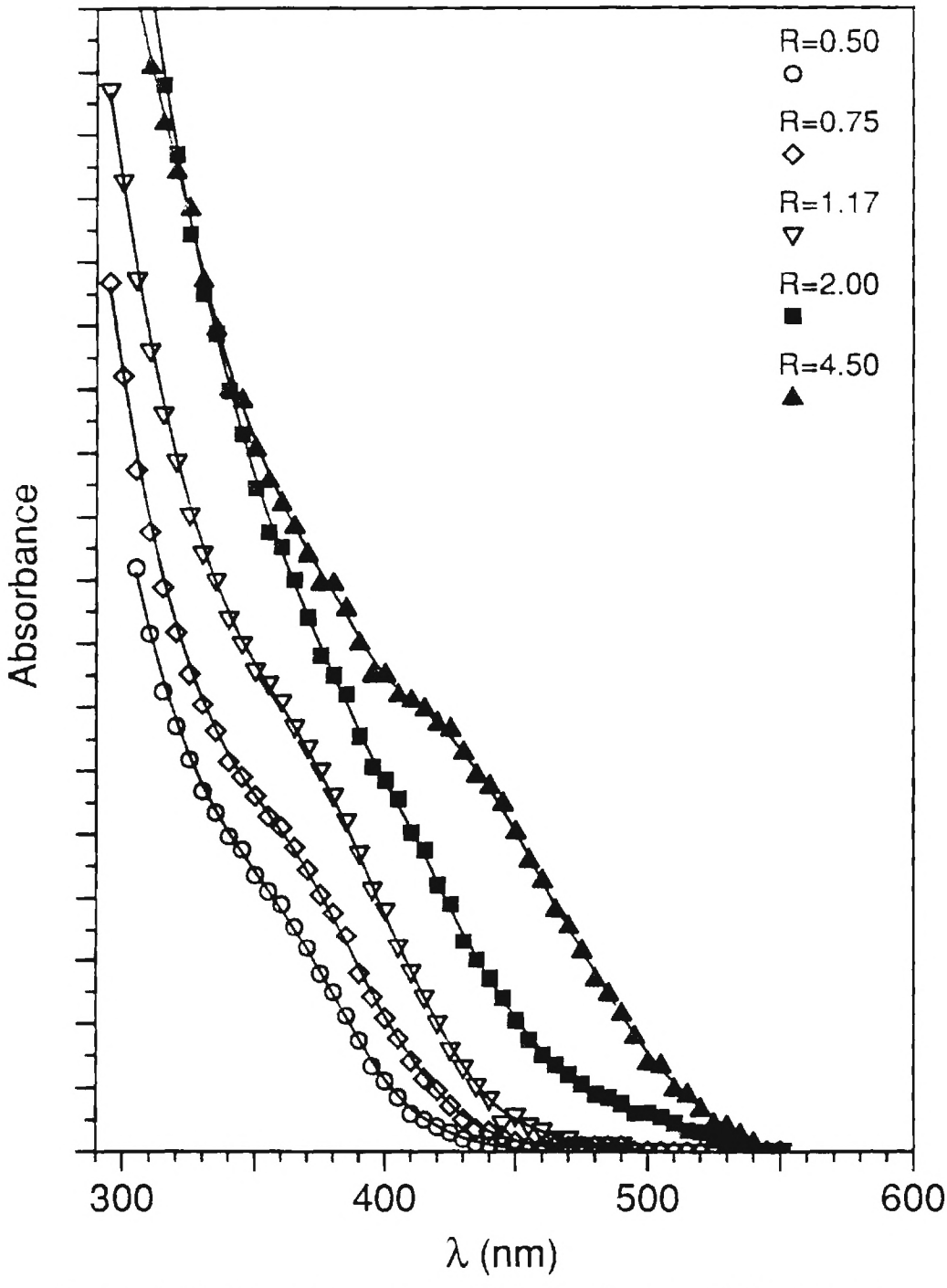

Figure 3.16. Absorption spectra of thiophenol capped CdS cluster in acetonitrile. Note that the samples have different concentrations.

Table 3.7
Exciton Energy and Cluster Size Estimation of CdS Clusters

S^{2-}/SPh^{-1}	Exciton Energy (eV)	Estimated Cluster Diameter (Å)
0.50	3.45	18
0.75	3.35	19
1.17	3.26	20
2.00	3.02	26
4.50	2.82	34

XAFS Results

The Cd-edge XAFS was obtained at liquid nitrogen temperature at X11 beam line on the National Science Light Source (NSLS) at Brookhaven National Laboratories. The monochromator crystal used for the Cd-edge measurements was Si(311). The XAFS samples were prepared by packing the samples in 2mm-thick sample holder and covered with Kapton tape. The sample labelled as CdSSPh is $(Me_4N)_4[Cd_{10}S_4SPh_{16}]$ and is prepared according to literature [5] and is used as a second standard for Cd-S scattering. The XAFS transforms for these samples are shown in Fig. 3.28. None of these CdS clusters has a second shell. The first shell was filtered and analyzed using the ratio method, and the analysis results are shown in Table 3.8. The XAFS results in Table 3.8 show a first shell coordination number that is ~4 for all samples. The coordination number and the average bond length of the CdSSPH agrees well with crystal structure. The $\Delta\sigma^2$ is relatively high and constant for all the samples.

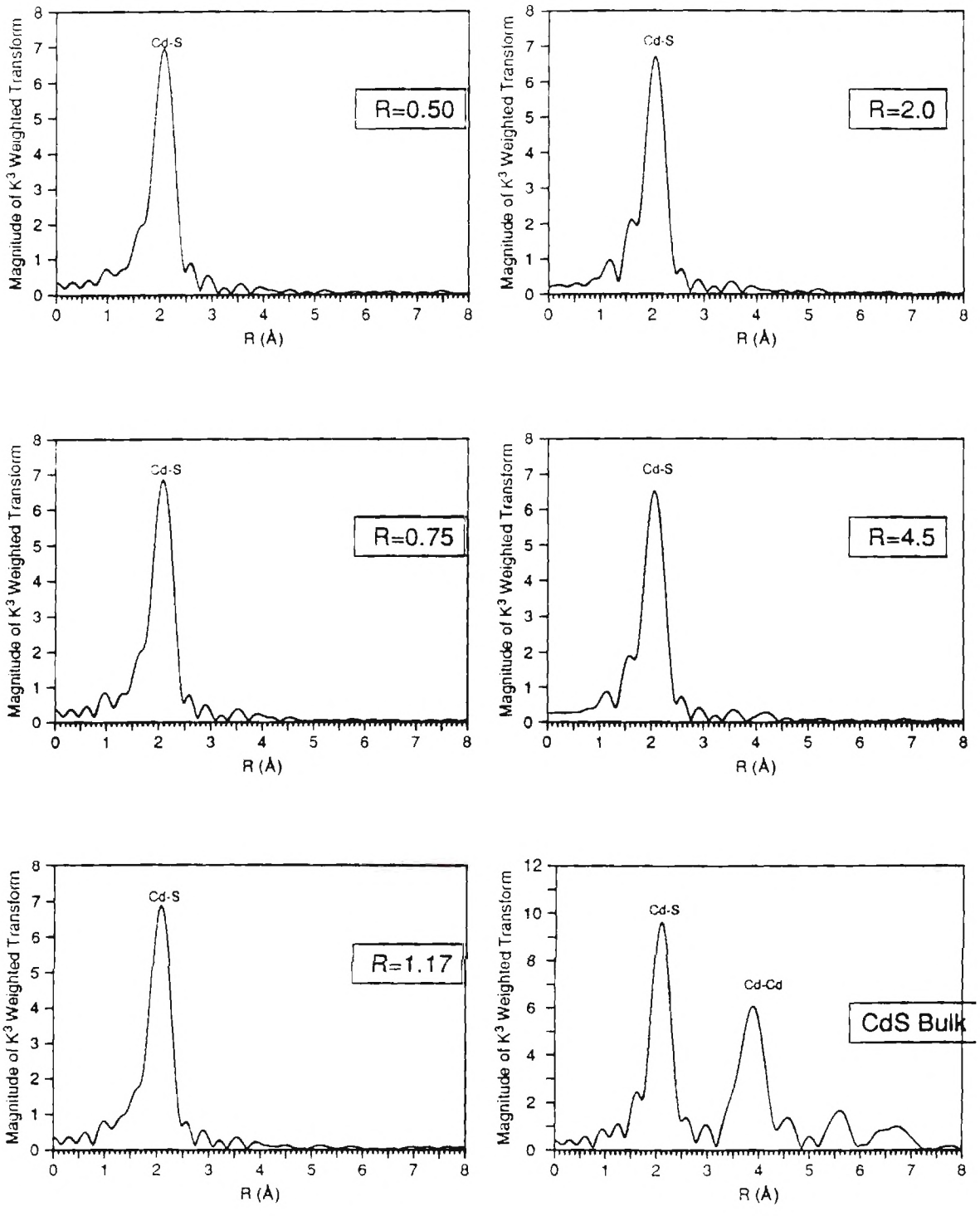

Figure 3.28. Cd-edge XAFS transform of thiophenol capped CdS clusters and CdS bulk sample at 90 K.

The S-edge XAFS was obtained for some of these samples. The XAFS analysis results of the S-Cd shell is shown in Table 3.9. The average CdSSPH coordination number of 1.95(20) is in agreement, within experimental error, with the value of 2.20 from the crystal structure. The average Cd-S bond length from X-ray structure of CdSSPH is 2.542 Å. The XAFS value is 2.530 Å. Based on these numbers, the estimate of the accuracy of Cd-S bond length is ± 0.01 Å.

Table 3.8: Cd-edge First Shell XAFS of Thiophenol Capped CdS Clusters

Sample	R(Cd-S) Å [2]	N	$\sigma^2_{ref} - \sigma^2_{sample}$
CdS0.5	2.528 ± 0.002	4.00 ± 0.03	-0.00213 ± 0.00005
CdS0.75	2.527 ± 0.001	4.04 ± 0.04	-0.00228 ± 0.00005
CdS1.17	2.523 ± 0.002	3.76 ± 0.08	-0.00164 ± 0.00012
CdS2.0	2.526 ± 0.002	3.92 ± 0.08	-0.00222 ± 0.00002
CdS4.5	2.520 ± 0.005	3.82 ± 0.03	-0.00220 ± 0.00004
CdSSPH[1]	2.530 ± 0.004	3.95 ± 0.03	-0.00228 ± 0.00005

1)Room temperature XAFS

2)The error bars are precision values from analysis

Table 3.9: S-edge Room Temperature XAFS Samples
First Shell Data

Sample	R(S-Cd) Å	N	$\sigma^2_{ref} - \sigma^2_{sample}$
CdSM0.75	2.507 ± 0.011	2.92 ± 0.09	-0.00196 ± 0.00034
CdSM2.00	2.506 ± 0.006	3.94 ± 0.27	-0.00522 ± 0.00068
CdSM4.50	2.503 ± 0.007	3.12 ± 0.21	-0.00064 ± 0.00068
CdSSPH	2.524 ± 0.018	1.95 ± 0.20	-0.00013 ± 0.00090

3-Mercaptopropanoic Acid Capped CdS Clusters

XRD Results

The XRD of 3-mercaptopropanoic acid (MPA) capped CdS clusters was obtained for these samples, and the diffraction patterns are shown in Fig. 3.29. All the samples display diffraction patterns consistent with a cubic CdS crystal structure. The diffraction peaks broaden as the ratio of S/MPA decreases indicating a smaller cluster size. The broadening of the first diffraction peak, which is actually a result of the two reflections (111) and (200), is used to estimate the size of the cluster. The results of the least square fitting are shown in Table 3.10. The error bars quoted were calculated assuming an error of 0.1° error (higher error for R=0.5 sample because the peak was very weak and noisier) in 2θ and in the width of the peak.

Table 3.10 : XRD Fitting Results of The (111) Diffraction Peak for 3-Mercaptopropanoic Acid Capped CdS Clusters

Sample	2θ Degrees	FWHM Degrees	Diameter (Å)	Lattice size (Å)	Cd-S (Å)
CdSPW0.5	26.61	7.48	15 ± 3	5.797 ± 0.022	2.510 ± 0.009
CdSPW0.75	26.97	4.28	25 ± 1	5.721 ± 0.021	2.477 ± 0.009
CdSPW1.0	26.87	3.93	28 ± 1	5.752 ± 0.021	2.487 ± 0.009
CdSPW2.0	26.86	3.87	28 ± 1	5.744 ± 0.021	2.487 ± 0.009
CdSPW3.0	26.55	3.13	35 ± 2	5.810 ± 0.021	2.516 ± 0.009
CdSPW4.0	26.55	2.85	38 ± 2	5.810 ± 0.021	2.516 ± 0.009
CdSPW20.0	26.61	2.47	44 ± 2	5.797 ± 0.021	2.510 ± 0.009

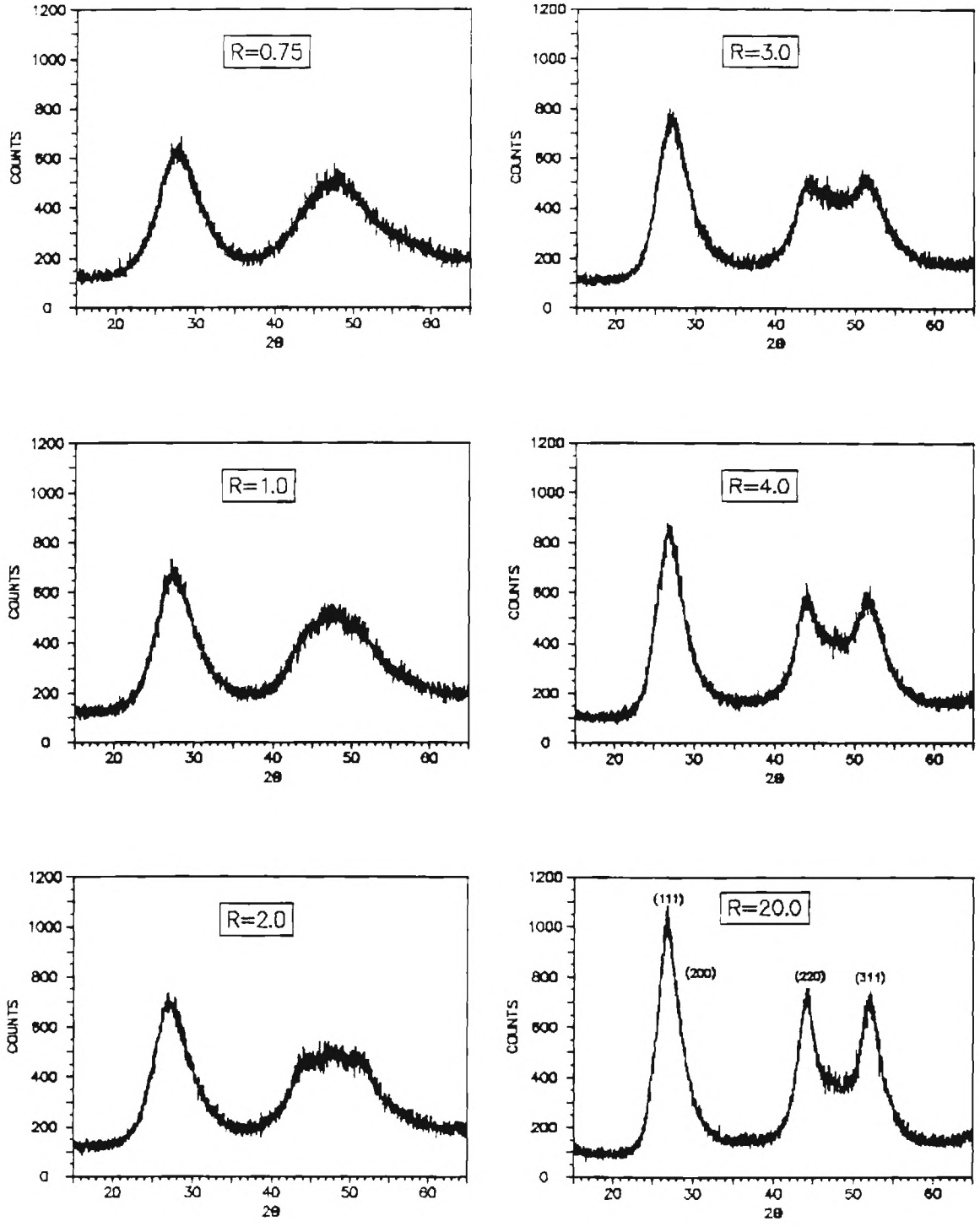

Figure 3.29. X-ray diffraction patterns of 3-mercaptopropanoic acid capped CdS clusters

XAFS Results

The XAFS was measured at liquid nitrogen temperatures in a manner similar to that used with the thiophenol samples at the X-11A beam line at the NSLS. The XAFS transforms are shown in Fig. 3.30. The XAFS of all the samples show a first shell that is similar to the bulk CdS. The first shell for all these samples was filtered and analyzed with CdS bulk as a standard using the ratio method. The results of the analysis are displayed in Table 3.11. Most of the Cd-S bond lengths obtained are consistent with the XRD values and are ~0.005 Å shorter than the bulk standard. The coordination numbers are in good agreement with calculated coordination numbers for spherical CdS clusters having a cubic crystal structure. Only the largest cluster, CdSPW20, shows a significant second shell. The second shell of CdSPW20 sample was filtered and analyzed using the ratio and fitting methods with CdS bulk as standard. The analysis results gave a second shell coordination number of 4.8 ± 0.1 (Table 3.12), which is much reduced from 10.0 for a spherical cluster of size 44 Å diameter. Figure 3.31 compares the experimental and fitted data for the second shell of CdSPW20.

Table 3.11: Cd-edge First Shell XAFS at 100 K

Sample	R (Cd-S) Å [1]	N	$\sigma^2_{ref} - \sigma^2_{sample}$
CdSPW0.5	2.505 ± 0.005	3.11 ± 0.06	-0.00269 ± 0.00010
CdSPW0.75	2.513 ± 0.005	3.44 ± 0.07	-0.00193 ± 0.00010
CdSPW1.0	2.516 ± 0.005	3.59 ± 0.03	-0.00176 ± 0.00004
CdSPW2.0	2.513 ± 0.005	3.58 ± 0.03	-0.00170 ± 0.00005
CdSPW3.0	2.515 ± 0.005	3.54 ± 0.02	-0.00137 ± 0.00002
CdSPW4.0	2.512 ± 0.005	3.62 ± 0.02	-0.00133 ± 0.00003
CdSPW20.0	2.517 ± 0.005	3.61 ± 0.02	-0.00086 ± 0.00003

1)The error bars are precision values from analysis

Table 3.12: Cd-edge LN2 XAFS Second Shell Results of CdSPW20 Sample

Sample	R (Cd-S) Å	N	$\sigma^2_{ref} - \sigma^2_{sample}$
CdSPW20	4.095 ± 0.002	4.8 ± 0.1	-0.00344 ± 0.00017

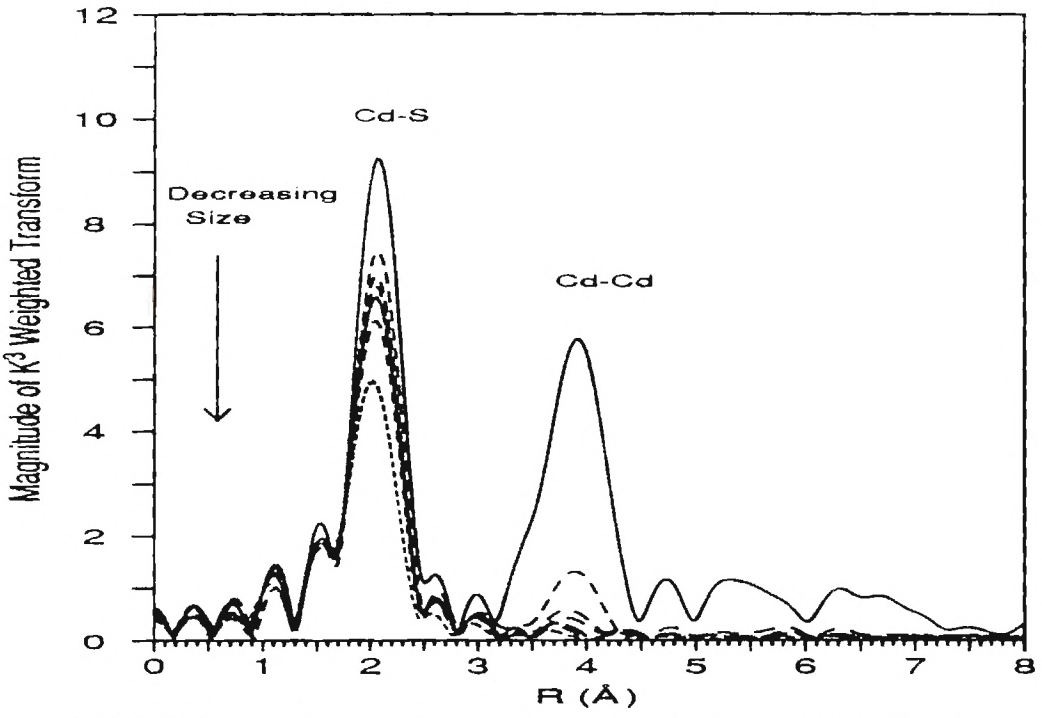

Figure 3.30.XAFS transforms of 3-mercaptopropanoic acid capped CdS clusters as compared with Bulk CdS. Samples are at 90 K

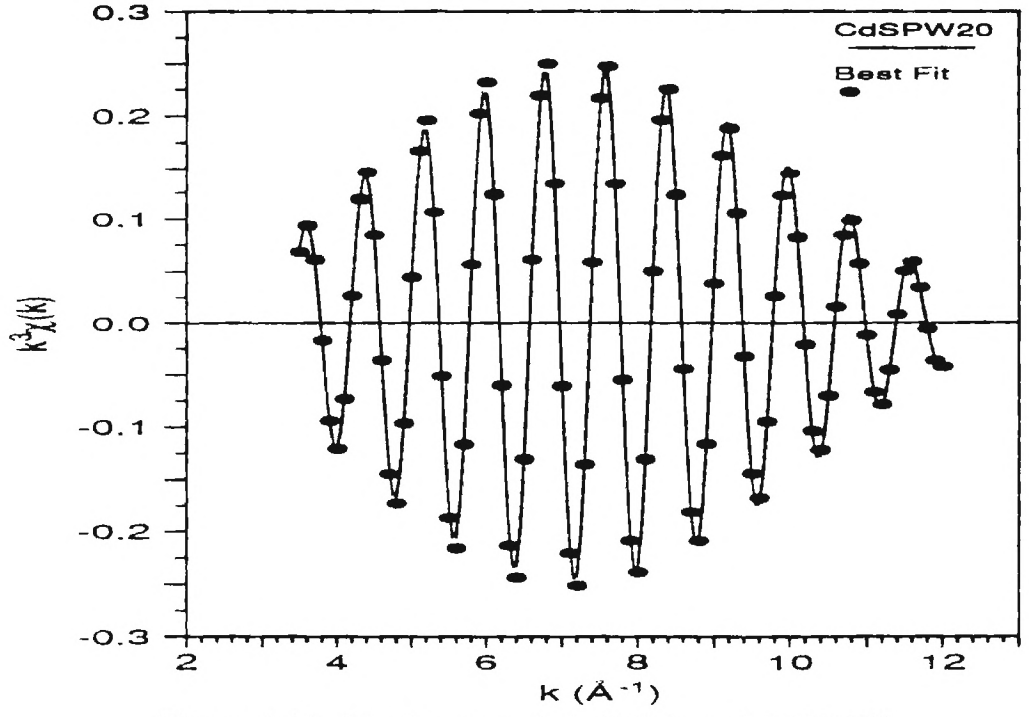

Figure 3.31. Cd-edge second shell fitting of CdSPW20

Discussion

The coordination numbers of Cd-S and Cd-O in Nafion obtained for CdS3W and CdS3D were anomalously small. The reason for this is explained by noting that during the analysis the XAFS is normalized to the total cadmium in the sample; since some cadmium are bonded only to oxygen and others are bonded to sulfur due to incomplete reaction of H_2S with all the cadmium, the coordination numbers obtained from fitting is dependent on the mole fraction of cadmium bonded to sulfur, and the mole fraction of the cadmium atoms bonded to oxygen. The calculation of the actual coordination number of Cd-S is simplified, since the coordination number of Cd-O was already measured by XAFS and found to be 5.1. For example, from Table 3.6, the Cd-S coordination number CdS2D sample was found to be 3.48 and the Cd-O was found to be 0.36. Since the average coordination number of Cd-O in Nafion was found to be 5.1, then 0.36/5.1 = 0.071 is the mole fraction of cadmium that is bonded to oxygen; therefore the fraction of cadmium that is bonded to S is 0.93. The coordination number of Cd-S is then 3.48/0.93 = 3.74 Cd-S per Cd. Thus the 93% of the cadmium in Nafion reacted with H_2S. Similar calculations were performed , and the results are shown in Table 3.13.

In the above calculations, it was assumed the majority of the cadmium atoms in Nafion are either bonded to S or to O atoms, but not to both. This indicates that the H_2S did not diffuse completely in the Nafion film. This assumption is consistent with the results of measuring the X-ray fluorescence for Cd and Se in a similarly prepared CdSe

clusters in Nafion [6]. These experiments showed that the selenium concentration decreased along a cross section of the film.

Table 3.13
XAFS Fitting Results of CdS2D, CdS3D, and CdS3W Clusters in Nafion

Sample	Cd-S Ref.	Cd-O Ref.	N(Cd-S)/Cd	Mole % of Cd-S
CdS2D	CdS	$CdMSO_3$	3.74	93
CdS3D	CdS	$CdMSO_3$	3.20	35
CdS3D	CdSNaS	CdDry	3.23	35
CdS3D	CdSNaS	CdWet	3.25	32
Average CdS3D			3.23	34
CdS3W	CdSNaS	$CdMSO_3$	4.15	51
CdS3W	CdSNaS	CdDry	4.00	49
CdS3W	CdSNaS	CdWET	4.10	44
Average CdS3W			4.08	48
CdS348D	CdS	CdDry	4.10	52
CdS348W	CdS	$CdMSO_3$	4.10	97

The analysis of the CdS clusters prepared in Nafion by reacting the cadmium loaded Nafion film with a solution of sodium sulfide ($CdSNa_2S$ sample) showed no presence of a Cd-O contribution indicating a complete reaction. Also, the analysis of CdS2W showed no presence of Cd-O in the first XAFS peak, which also indicated a complete reaction. In the CdS2D sample a 93% reaction was calculated. The CdS3D and CdS3W showed 34% and 52%, respectively. The CdS348D and CdS348W showed 52%

and 97%, respectively.

Table 3.14 summarizes the results on the Nafion grown samples. The results shows that the samples that were immersed in water after reacting with H_2S exhibit an additional reaction. Furthermore, the drying time of the Cd-loaded Nafion had a dramatic effect on the extent of the reaction. The samples that were dried for 3 days have much smaller %CdS yield than similar samples dried for only 2 hours (35% for CdS3D and 51% CdS3W as compared for 100% for CdS2W and 93% for CdS2d). The samples that were dried similarly but reacted for longer time (CdS348W and CdS348D) have larger yield of CdS than the ones (CdS3W and CdS3D) that reacted for less time. Notice also that the soaked samples CdS3W and CdS348W, have similar sizes. The fact that the percent yield increased while the size remains the same suggests that in some regions in the Nafion the diffusion of H_2S was very small. Thus, when the samples where soaked in water, the H_2S diffused and reacted with the un-cadmium that had not reacted previously in the dry film. This result is consistent with the model used in the above calculation where the cadmium was assumed to be only bonded to either sulfur or to oxygen, and not both.

Table 3.14: Summary Table for CdS Clusters Grown in Nafion

Sample	Drying Time	Reaction Time with Sulfide	Percent Reaction	Size (Å)	N(Cd-S)
CdSNa2S	None	1 day	100	51	4.0
CdS2W	2 hours	9 days	100	224	4.1
CdS3W	3 days	15 days	48	114	4.1
CdS348W	3 days	48 days	97	119	4.1
CdS2D	2 hours	9 days	93	69	3.8
CdS3D	3 days	15 days	35	30	3.2
CdS348D	3 days	48 days	52	69	4.1

The results also suggest that the diffusion of H_2S in Nafion is relatively slow under the conditions of these experiments. It is also clear that the presence of water in Nafion causes the reaction of H_2S with cadmium to proceed faster. The presence of water in Nafion also affects the size of the cluster. The largest CdS cluster in Nafion was CdS2W sample which was dried only for two hours before reacting with H_2S. Both the CdS2D and CdS2W samples have complete reaction. However when CdS2D sample was soaked in water, the size almost tripled. This can be explained by assuming that the water caused the clusters to fuse together so as to increase the size of the clusters. For the other dry samples, the soaking in water will cause the cluster to fuse and will cause the unreacted cadmium to react with the H_2S (not all excess H_2S was removed by pumping). It remains to be answered why the CdS348D sample, when soaked (to make the CdS348W sample) in water, clusters as large as those formed with CdS2W were not found. The reason for this difference between the CdS2D and CdS348D samples is that

the soaking of CdS2D sample causes the clusters to fuse together to form larger clusters; in the case of CdS348D sample, the soaking involves both reacting the unreacted cadmium by diffusing H_2S into the inner regions of Nafion and by fusing the clusters together. It could be that the first process occurs faster than the second process and somehow slows the second process (fusing the clusters together). It is noted in the literature that the addition of sulfide to a solution of CdS clusters causes the formation of larger clusters[2]. To test this possibility, CdS3D sample (all excess H_2S removed) was cut in half; one sample was placed in water while the other sample was placed in 2M sulfide solution. After few minutes the sample in the sulfide solution became reddish while the other sample showed no color change. Thus, the reason for the smaller size in the CdS348W as compared to CdS2W is that the sulfide needed to fuse together the CdS clusters in CdS348D sample was used to react the cadmium that did not react with H_2S gas before soaking.

It is surprising that the CdSNa2S sample was not the largest cluster prepared, considering the fact that the sample was prepared in aqueous solution of sodium sulfide. The reason for this could be due to the presence of sodium ions in the cavities of Nafion. Two sodium ions are needed to replace a cadmium ion which reacted with sulfide ions. In the reaction of H_2S with Cd-loaded Nafion, the protons should replace the cadmium ions to conserve charge. Thus it could be that the presence of sodium ions hinders the growth of the clusters to larger sizes by occupying binding sites in the cavities of Nafion.

Another important result is the existence CdS clusters in Nafion a mixure of cubic and hexagonal crystal structures. In literature studies, the CdS clusters were thought to

be cubic based on the observed diffraction patterns. However, most of the literature work on CdS focused on preparation of smaller clusters less than 55 Å. In the case of CdS in Nafion, the literature work of Herron and Wang[7], where the XRD was reported for a 55 Å diameter cluster, the structure was thought to be cubic even for a 100 °C annealed sample. However, CdS clusters prepared in glasses show a mixed product of hexagonal and cubic phases [8].

The XAFS coordination numbers of CdS3D (3.2) is consistent with coordination numbers calculated for spherical clusters with similar size. The other cluster coordination numbers are consistent with the bulk value of 4.

For thiophenol capped clusters, small clusters were prepared. The size determination was obtained from the correlation of the exciton peak with the size. The difficulty of obtaining the size from XRD is caused by the presence of the three broadened peaks of the hexagonal phase in addition to any cubic phase present. Nevertheless, crude fitting of the XRD peak confirmed the sizes as obtained from the absorption spectra. This is the first synthesis of series of hexagonal CdS clusters. Better XRD line fitting analyses are needed to analyze the sizes of the clusters. The optical spectra of the thiophenol capped clusters shows the shift of the absorption edge with size in a manner consistent with quantum confinement.

The cadmium edge coordination numbers coordination numbers of thiophenol capped clusters is relatively high considering the size of the small sizes of clusters. The reason for this is that the clusters are sulfur rich. This is evident from the sulfur edge analysis where the coordination numbers are less than 4. The ratio of the coordination

number of cadmium edge to the coordination number of the S edge is the mole ratio of S/Cd in the cluster. The test for accuracy of this can be demonstrated for the CdSSPH standard. In this standard the S/Cd=(N(Cd-S)/Cd)/(N(S-Cd)/S) = 3.95/1.95=2.02 which is in excellent agreement with the ratio of 2.0 from the chemical formula. Thus R=0.75 sample has a ratio of S/Cd=1.4 and the larger sample of R=2 has a ratio of S/Cd =1.0. These results suggest that mole ratio of S to Cd decreases as the size increases. Examining Table 3.1, we find the preparation conditions used 14 mmol S and 10 mmol Cd, the ratio of which is in excellent agreement with XAFS ratio of 1.4. The results for the other samples are listed in Table 3.15. The results of the above table are in agreement with results of thiophenol capped ZnS (Chap. IV) and suggest that the reaction product follows the stoichiometry of the preparation. This result is in disagreement with the results of CdS preparation of the literature[2].

Table 3.15: Comparison of S/Cd Mole Ratios with Synthesis Conditions.

Sample	S/Cd from XAFS	S/Cd of Synthesis
CdS0.75	1.38 ± 0.04	1.4
CdS2.00	0.99 ± 0.08	1.2
CdS4.5	1.22 ± 0.08	1.1
CdSSPH	2.03 ± 0.02	2.0 (from formula)

The 3-mercaptopropanoic acid (MPA) capped CdS clusters show a smooth increase in the cluster size as the ratio of S^{2-}/RS^{-1} increases. The diffraction pattern showed the presence of cubic (zinc-blende) CdS clusters. No evidence was found for the hexagonal structure. The XAFS first shell data showed a coordination number which is in good

agreement with a simulation, assuming a spherical clusters. The second shell for most the clusters was very small except for the CdSPW20 sample. However, the second shell coordination number did not agree with simulation. The disagreement of the second shell coordination number, while the first shell was in good agreement with simulation suggested that the XAFS of the second shell was only due to an ordered portion of the cluster, and the disordered portion was not contributing to the second shell due to large Debye-Waller factor. Thus a model is suggested for the MPA clusters where the cluster is made of two portions: the outer part being disordered in the XAFS second shell domain, and the inner part of the cluster is ordered and similar to the bulk crystal. This model, used to calculated the thickness of the disordered shell, is described in more detail in the next chapter for ZnS clusters. The calculation of the disordered thickness, as will be shown in chapter IV, revealed that the disordered layer thickness is ~4 Å, similar to the second shell distance.

The absence of second shell in CdS clusters was also reported in a recent XAFS study on CdS cluster[9]. The authors reported a second shell coordination number of 2.5 for an annealed sample, and attributed the decrease in the XAFS second shell to possible disorder in the surface of the clusters. Also, the authors reported XAFS Cd-S bond lengths similar to the bulk. The XRD lattice size showed contraction with decrease in the cluster size. In the current work, we have used similar assumption about surface disorder and estimated the thickness of the disordered shell to be about the second shell distance. No contraction in the XRD lattice size was found for the MPA clusters. XRD bond length and XAFS bond length were in good agreement.

It was shown that MPA capped large clusters have a significant XAFS second shell suggesting that the MPA clusters are more crystalline than the CdS nanoclusters reported in the literature[9]. No second shell was found for thiophenol capped CdS clusters. The drawback of the MPA clusters is their low solubility in common solvents. Further modification of the synthesis procedure or employment of different capping groups may aid in preparing clusters that are more soluble .

Endnotes

1. W. Y. Hsu, and T. D. Gierke, *J. Membrane Sci.*, **13**, 307, 2528(1983)

2. N. Herron, Y. Wang, and K. H. Eckert, *J. Am. Chem. Soc.* **112**, 1322 (1990).

3. *Acta Cryst.* (1978). **B34**, 1504(1978)

4. M. V. Rama, and R.A. Friesner, *J. Chem. Phys.*, **95**, 8309(1991).

5. I. G. Dance, A. Choy, and M. Scudder, *J. Am. Chem. Soc.*, **106**, 6285(1984)

6. E. Smotkin, R. M. Brown, L. K. Rabenberg, K. Salomon, A. J. Bard, A. Campion, M. A. Fox, T. E. Mallouk, S. E. Webber, and J. M. White, *J. phys. Chem.*, **94**, 7543(1990).

7. Y. Wang, A. Suna, G. McHugh, *J. Chem. Phys.* **92**, 6927(1990).

8. H. Minti, M. Eyal, R. Reisfeld, and G. Berkovic, *Chem. Phys. Lett.*, **183**, 277(1991).

9. M. A. Marcus, L. E. Brus, C. Murray, M. G. Bawendi, A. Parasad, A. P. Alivisatos, *Nanostructured Materials*, **1**, 323(1992).

CHAPTER IV

ZINC SULFIDE NANOCLUSTERS

ZnS Cluster Preparation

Zinc sulfide nanoclusters were prepared with a variety of methods. In general, two classes of clusters were prepared: clusters grown in Nafion films, and clusters precipitated from solution in the presence of a capping agent. Capping agents that were used included thiophenol (benzenethiol), 3-mercaptopropanoic acid, 2-aminoethanethiol, and benzeneselenol. All reagents that were used in the synthesis were as supplied by vendors without further purification. All solvents used were degassed by bubbling N_2 gas through the liquid for at least 30 minutes. All reactions were carried under nitrogen atmosphere in rubber septa-capped Erlenmeyer flasks.

Nafion Grown ZnS Clusters

Nafion films (Aldrich) were cleaned by boiling the samples in concentrated nitric acid for 30 minutes followed by rinsing twice with boiling deionized water or until sufficiently cleaned of excess acid to produce neutral pH for the rinsing water. The films were then soaked in 1.0 M zinc nitrate aqueous solution for 12 hours. Excess zinc was removed from the films by washing and soaking in water. The films were judged clean from excess zinc by testing the soaking water for zinc by adding sulfide solutions and

looking for cloudiness in the water due to formation of ZnS. The films were then transferred in a dry box to a glass cell. The samples were vacuum dried for 3 days and then were exposed to 1 atm of H_2S gas for 15 days. No noticeable growth of ZnS clusters occurred in this method. Other zinc loaded samples were immersed in 1M sodium sulfide solution under nitrogen resulting in the immediate growth of white ZnS clusters. The samples were then rinsed to remove excess sulfide by washing the samples in deionized water and by further soaking. The films were judged clean of excess sulfide, if after 3 hours of soaking, the films did not release sulfide to the water. The soaking water was tested for sulfide by adding cadmium nitrate solutions and looking for production of orange CdS. Five layers of clean ZnS-Nafion grown clusters were vacuum dried, transferred to the dry box, and epoxy-sealed with 3 mil Mylar film for XAFS measurement.

Thiophenol Capped ZnS Clusters

Thiophenol (C_6H_5SH, Eastman) capped ZnS clusters were prepared similarly to the synthesis of CdS sulfide clusters as reported by Herron et al. [1]. The ZnS clusters prepared in this method were synthesized in methanol/water mixture by the addition of 200 ml of zinc acetate methanol solution to a well stirred solution made to a specific mole ratio of sodium sulfide to thiophenol. The resulting white precipitate was filtered in a medium glass frit, washed with methanol, and vacuum dried. Different cluster sizes were prepared by this method by varying the mole ratio of sulfide to thiophenol. By increasing this ratio, larger clusters were produced. The concentrations of the sulfide ions and the thiophenol were chosen to satisfy a total charge balance according to the

following formula:

$$2[Zn^{2+}] = 2[S^{2-}] + [PhS^{-}], \quad (4.1)$$

where PhSH stands for thiophenol.

Table 4.1
Thiophenol ZnS Capped Clusters

S^{2-}/PhSH Ratio	Zn^{2+}	S^{2-}	PhSH
1.0	20.00 mmol 200 ml MeOH	13.33 mmol 67 ml H_2O 67 ml MeOH	13.33 mmol 01.37 ml 66 ml MeOH
2.0	20.00 mmol 200 ml MeOH	16.00 mmol 80 ml H_2O 80 ml MeOH	8.000 mmol 0.821 ml 40 ml MeOH
6.5	20.00 mmol 200 ml MeOH	18.57 mmol 93 ml H_2O 93 ml MeOH	2.857 mmol 0.293 ml 14 ml MeOH
12.0	20.00 mmol 200 ml MeOH	19.20 mmol 96 ml H_2O 96 ml MeOH	1.600 mmol 0.164 ml 8 ml MeOH
20.0	20.00 mmol 200 ml MeOH	19.51 mmol 98 ml H_2O 97 ml MeOH	0.976 mmol 0.100 ml 5 ml MeOH

The literature synthesis called for mixing 100 ml of the metal solution to 100 ml solution made by mixing a certain volume of 0.1M (50% methanol/water) sulfide solution with certain volume of 0.2M thiophenol methanol solution. In the current synthesis, the receipe was essentially followed by using the same concentrations, but dissolving the

separate components directly in water and methanol rather than delivering the actual volumes needed from previously prepared stock solutions. With this choice, the solutions were always fresh to minimize any oxidation of the sulfide and the thiophenol. Another modification of literature method was made to get larger amount of product . This was done by doubling the number of moles and the volume of each component of the reaction mixture. Typical yields are in the order of 2 grams of washed and dried samples. The ratios used and volumes used are all listed in Table 4.1

3-Mercaptopropanoic Acid Capped ZnS Clusters

3-mercaptopropanoic acid ($HSCH_2CH_2COOH$, Aldrich) capped ZnS clusters were prepared in aqueous (no methanol) solution using the same procedure as described for thiophenol capped ZnS clusters. Ratios used in this synthesis are shown in Table 4.2

An alternative synthesis of 3-mercaptopropanoic acid (MPA) capped ZnS cluster in aqueous medium was performed by injecting 0.042 ml (0.48 mmol) of 3-mercaptopropanoic acid into 200 ml of 0.10 M zinc acetate solution. The resulting solution was adjusted in pH by titrating with 1.0 M KOH solution until a pH of 8 was reached and a precipitate of zinc hydroxide presumably formed. To this mixture, 200 mL (39.2 mmol) of sodium sulfide was added upon stirring. The reaction mixture was further stirred for half hour, then was filtered, washed with methanol and water, and vacuum dried. This synthesis gave the largest cluster size as found by x-ray diffraction. This apparent size sensitivity to the pH is explored further in the section on an amine capping agent.

Table 4.2
Reagent Amounts Used in Synthesis of
3-Mercaptopropanoic Acid ZnS Capped Clusters

S^{2-}/RSH Ratio	Zn^{2+}	S^{2-}	3-Mercapto
1.0	20.00 mmol	13.33 mmol	13.33 mmol (1.162 ml)
2.0	20.00 mmol	16.00 mmol	8.000 mmol (0.697 ml)
4.0	20.00 mmol	17.78 mmol	4.444 mmol (0.387 ml)
5.0	20.00 mmol	18.18 mmol	3.636 mmol (0.317 ml)
6.5	20.00 mmol	18.57 mmol	2.857 mmol (0.307 ml)
20.0	20.00 mmol	19.51 mmol	0.976 mmol (0.085 ml)
50.0	20.00 mmol	39.20 mmol	0.784 mmol (0.068 ml)

Benzeneselenol Capped ZnS Clusters

Benzeneselenol (C_6H_5SeH, Aldrich) clusters were prepared in the same method as of the thiophenol ZnS clusters described above. In this preparation a 3-necked 500-mL round bottom flask was used to which 200 ml of methanol/water solution of specific ratio of sulfide/selenol was added. Due to the high toxicity of selenol and its air sensitivity, the exposure of the selenol/sulfide mixture was minimized by adding the zinc solution with stirring via four canulas, minimizing the addition time. The resultant precipitate of the reaction was allowed to settle, and the solvent was removed via cannula. More deaerated methanol was added and the reaction mixture was stirred for 5 minutes to rinse the product from excess selenol (orange color). This cycle of rinsing was repeated until no further change in the solution color was observed. The fine product was transferred with methanol via cannula to a Buchner funnel sealed from the top with an inverted funnel. The filtration in this way was carried under nitrogen to minimize any oxidation

of the product, which was then vacuum dried. The product color was slightly yellowish and becomes whiter upon further washing with methanol. Ratios used for this preparation are shown in Table 4.3. Note that the ratio of 1.5 was prepared in Zn^{2+} rich solution.

Table 4.3
Reagent Amounts Used in The Synthesis of
Benzene Selenol ZnS Capped Clusters

S^{2-}/PhSeH Ratio	Zn^{2+}	S^{2-}	PhSeH
1.5	14.13 mmol 141 ml MeOH	9.42 mmol 47 ml H2O 47 ml MeOH	6.379 mmol 1.00 ml 47 ml MeOH
2.0	20.00 mmol 200 ml MeOH	16.00 mmol 80 ml H2O 80 ml MeOH	8.000 mmol 1.254 ml 40 ml MeOH
6.5	20.00 mmol 200 ml MeOH	18.57 mmol 93 ml H2O 93 ml MeOH	2.857 mmol 0.448 ml 14 ml MeOH
12.0	20.00 mmol 200 ml MeOH	19.20 mmol 96 ml H2O 96 ml MeOH	1.600 mmol 0.250 ml 8 ml MeOH
20.0	20.00 mmol 200 ml MeOH	19.51 mmol 98 ml H2O 97 ml MeOH	0.976 mmol 0.153 ml 5 ml MeOH

2-Aminoethanethiol Capped ZnS Clusters

The 2-aminoethanethiol ($H_2NC_2H_4SH$, Aldrich) capped ZnS clusters were prepared in water by using a mole ratio 20 of sulfide/aminothiol. The reaction was conducted by dissolving 10 mmol of zinc acetate and 0.487 mmol of the aminothiol in 100 ml water at a pH of 6.5. To this solution aqueous sulfide solution made of 9.75 mmol sodium

sulfide in 100 ml water was added. The reaction mixture was stirred for 30 minutes, and the product was filtered and washed with methanol and water. Different cluster sizes were prepared by this method, and using the same ratio, by adjustment of the pH of the zinc/aminothiol mixture with 2M KOH or 1M HCl as titrants. Three such samples were prepared using pH's of 4.5, 6.5 (no KOH or HCl was added), 8.0, and 12.0. Note that the order of mixing of reactants differs from those previously described.

Nafion Grown ZnS Clusters

XRD Results

The XRD pattern of ZnS prepared by immersing the Zn-loaded Nafion in sulfide aqueous solution was obtained as explained in Chapter I. The diffraction patterns appear in Fig. 4.1. The peaks that are labeled with "*" are due to the Nafion film while the other labelled peaks are due to ZnS crystals. As can be shown from Fig. 4.1, the diffraction peaks correspond to the cubic zinc blende structure and verifies the presence of a crystalline ZnS phase. The broadening of the peaks is due to the crystal size as discussed earlier.

Table 4.4
ZnS Grown Nafion: XRD Fitting Results

Angle (deg)	FWHM (deg)	Diameter (Å)	Lattice Size (Å)	Bond Length (Å)
28.821	1.999	55 ± 3	5.316 ± 0.018	2.321 ± 0.008

The results of the fitting of the (111) peak are summarized in Table 4.4. The error bars quoted were calculated upon assuming a 0.1° error in measuring the 2Θ and the peak width. The (111) peak position is slightly shifted from the bulk material, indicative of a smaller lattice size and bond length (2.321 Å versus 2.342 Å of the bulk). The relatively large cluster size of 55 Å cluster is the largest ZnS cluster that was prepared in this work.

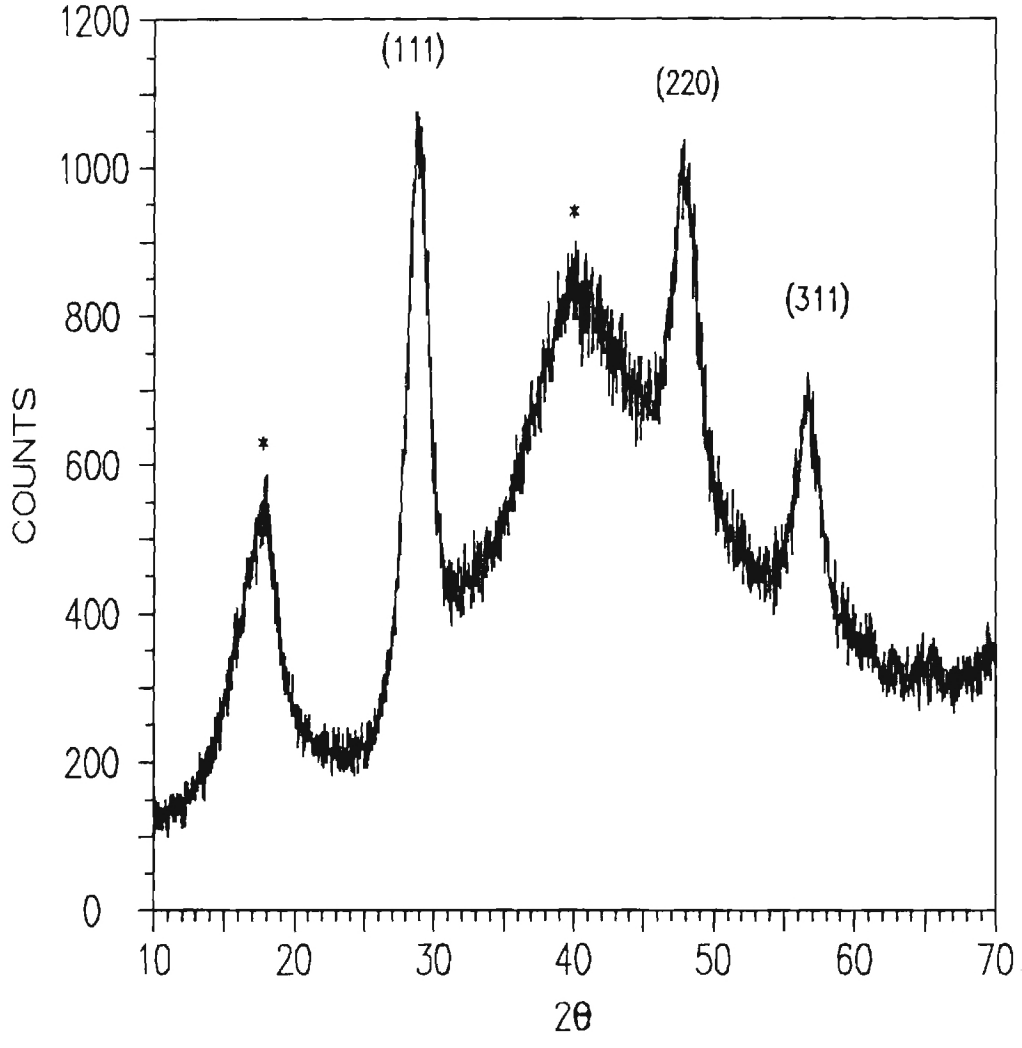

Figure 4.1. XRD of ZnS loaded Nafion film. The "*" labeled peaks are due to the Nafion film.

XAFS Results

The Zn-edge XAFS measurements were obtained at room temperatures on X11 beam line on the National Synchrotron Light Source (NSLS) at Brookhaven National Laboratories. The monochromator used for the Zn-edge measurements was Si(111).

The environment of zinc in Nafion was studied by using a thick dry Nafion film loaded mostly with Zn^{2+} and with very small amount of H_2Se diffused to the surface[2]. The XAFS of this sample was obtained in the transmission mode, thus the bulk of the film is unreacted Zn^{2+} in Nafion cavities. The model compound ZnO (wurtzite) was used for the XAFS analysis. The literature distance of the tetrahedral Zn-O bond is 1.978 Å[3].

The Fourier transform (FT) of the XAFS of both the standard ZnO and the Zn loaded Nafion is shown in Fig. 4.2 and clearly shows the Zn-O shell. A small second shell is also apparent, but it is too small for analysis. The Zn-O shell was filtered and analyzed using the ratio method. The analysis results revealed that the zinc is coordinated with four oxygens with an average distance of 1.963 ±0.002 Å. These results are summarized in Table 4.5. The results are in agreement with the work of Ding et. al. [4] who found R=1.96 Å, N=4, and σ^2_{sample}=0.00436 Å^2

Table 4.5
XAFS Analysis Results of Zn loaded Nafion
Using ZnO as Reference

R(Zn-O) (Å)[1]	N(Zn-O)	$\sigma^2_{ref} - \sigma^2_{sample}$
1.963 ± 0.002	4.1 ± 0.1	-0.00230 ± 0.00151

1)The error is the precision from analysis in this and the other XAFS tables.

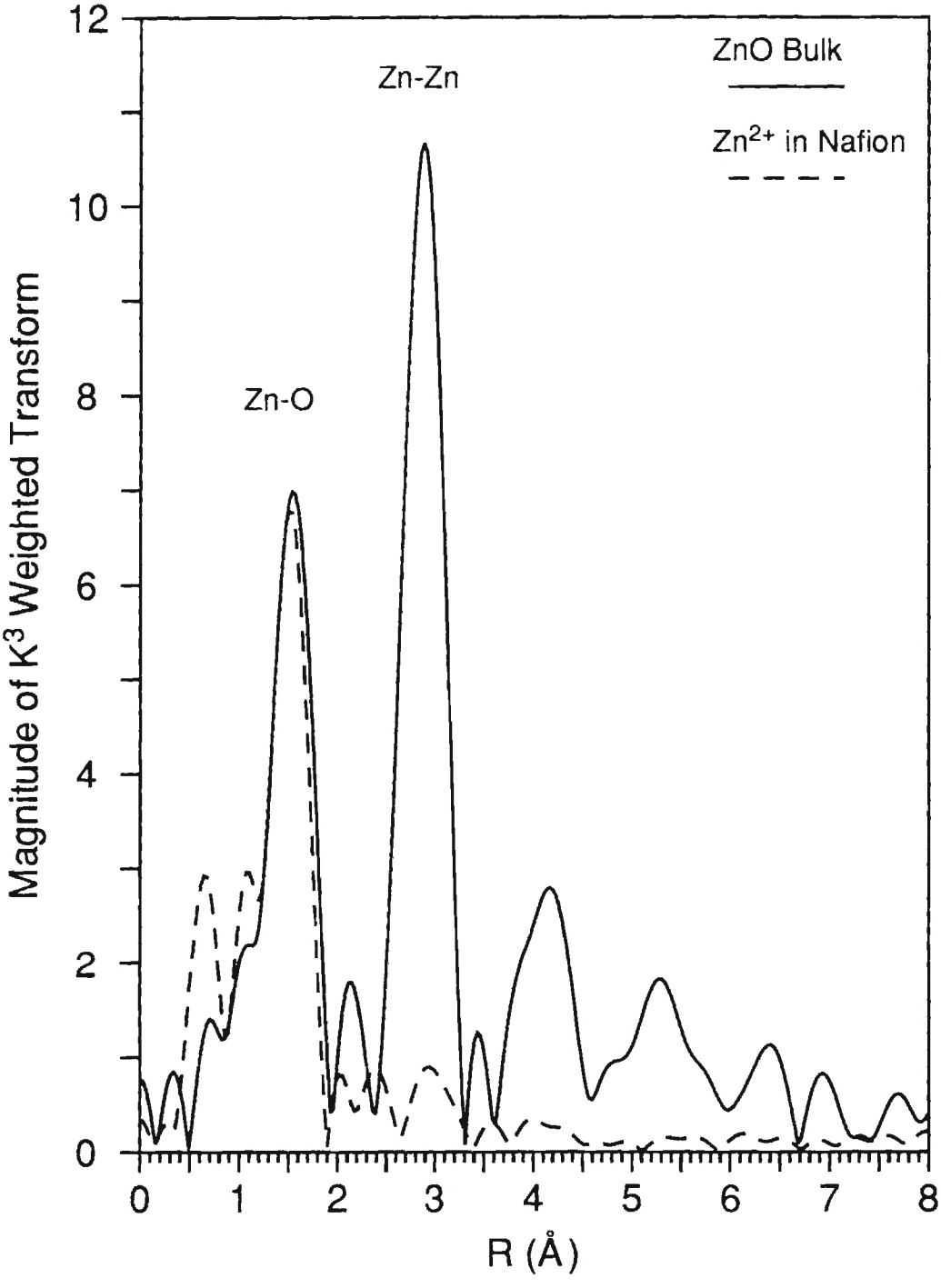

Figure 4.2:Zn-edge XAFS transform of ZnO bulk and Zn^{2+}-loaded Nafion.

The Nafion grown ZnS cluster sample was also studied with XAFS. The ZnS (wurtzite) bulk was used as standard for XAFS analysis. The transformed XAFS of both the ZnS standard and the clusters sample are shown in Fig. 4.3. The first two shells were filtered separately and were analyzed using the ratio method and least square fitting method using the ZnS bulk standard. The XAFS analysis of the Zn-S shell revealed a coordination number of 3.38 ± 0.02 and bond distance 0.011 Å shorter than the bulk(2.333 ±0.002 Å) and slight disorder as compared with the bulk. Figure 4.4 is a plot of the fitting of the filtered first shell. The second shell analysis revealed a coordination number of 7.13 ± 0.14 and a second shell distance similar to the bulk, but higher disorder with the respect to the bulk. These results are summarized in Table 4.6. The errors quoted were obtained from the fitting results and are consistent with the standard deviation of the results obtained from analysis of separately grouped scans of the same sample. In the analysis, the first and the second coordination numbers of the standard, bulk ZnS, are 4 and 12, respectively.

Table 4.6 : First and Second Shell Zn-edge XAFS Results of Nafion Grown ZnS Cluster

Shell Number	R (Å)[1]	N	$\sigma^2_{ref}-\sigma^2_{sample}$ (Å^2)
Shell #1 Zn-S	2.333 ± 0.002	3.38 ± 0.02	-0.00076 ± 0.00004
Shell #2 Zn-Zn	3.827 ± 0.012	7.13 ± 0.14	-0.00243 ± 0.00021

1)The error bars are precision values from analysis. Also in the other XAFS tables.

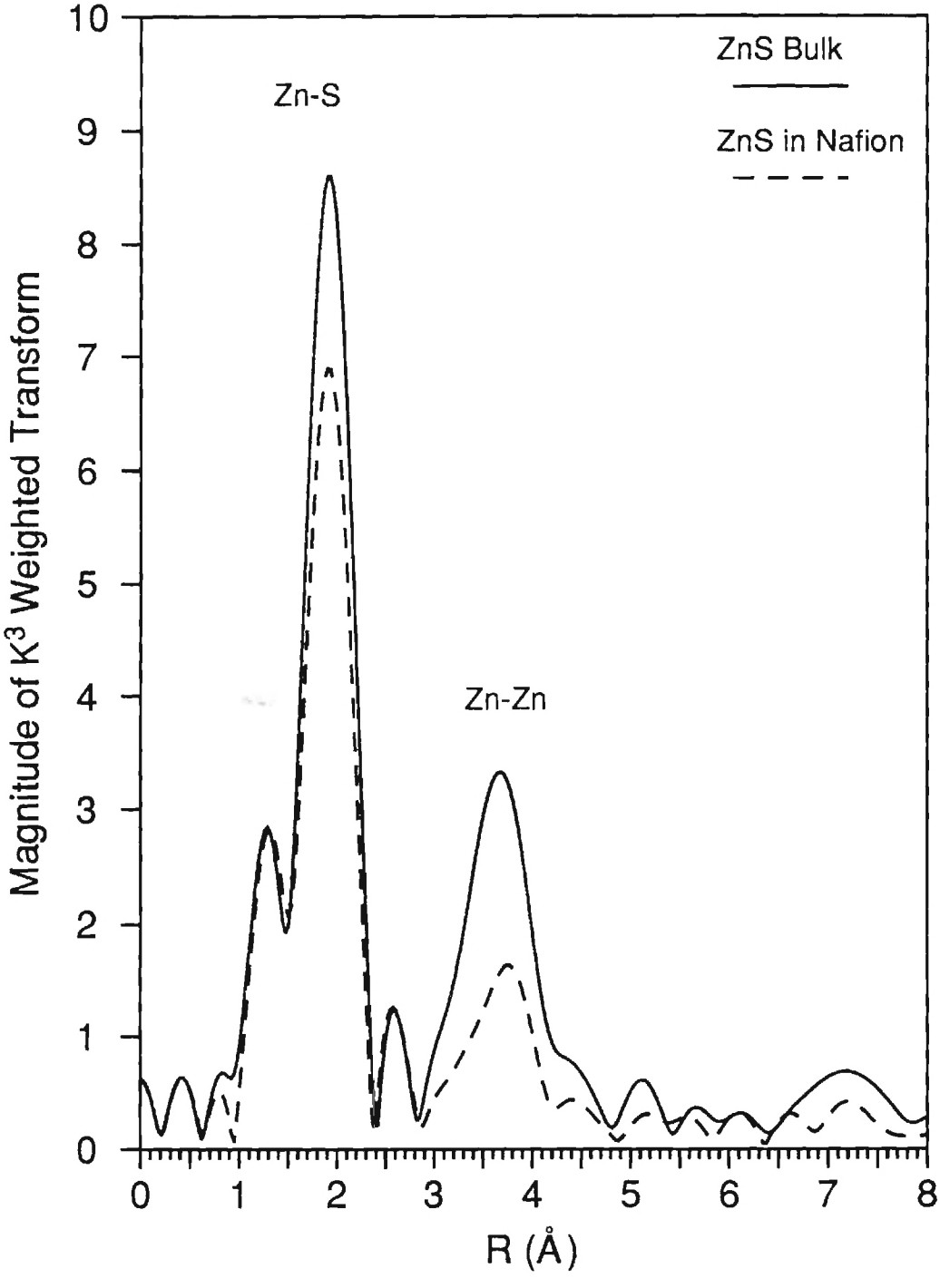

Figure 4.3. Zn-edge XAFS transform of ZnS bulk and Nafion grown ZnS.

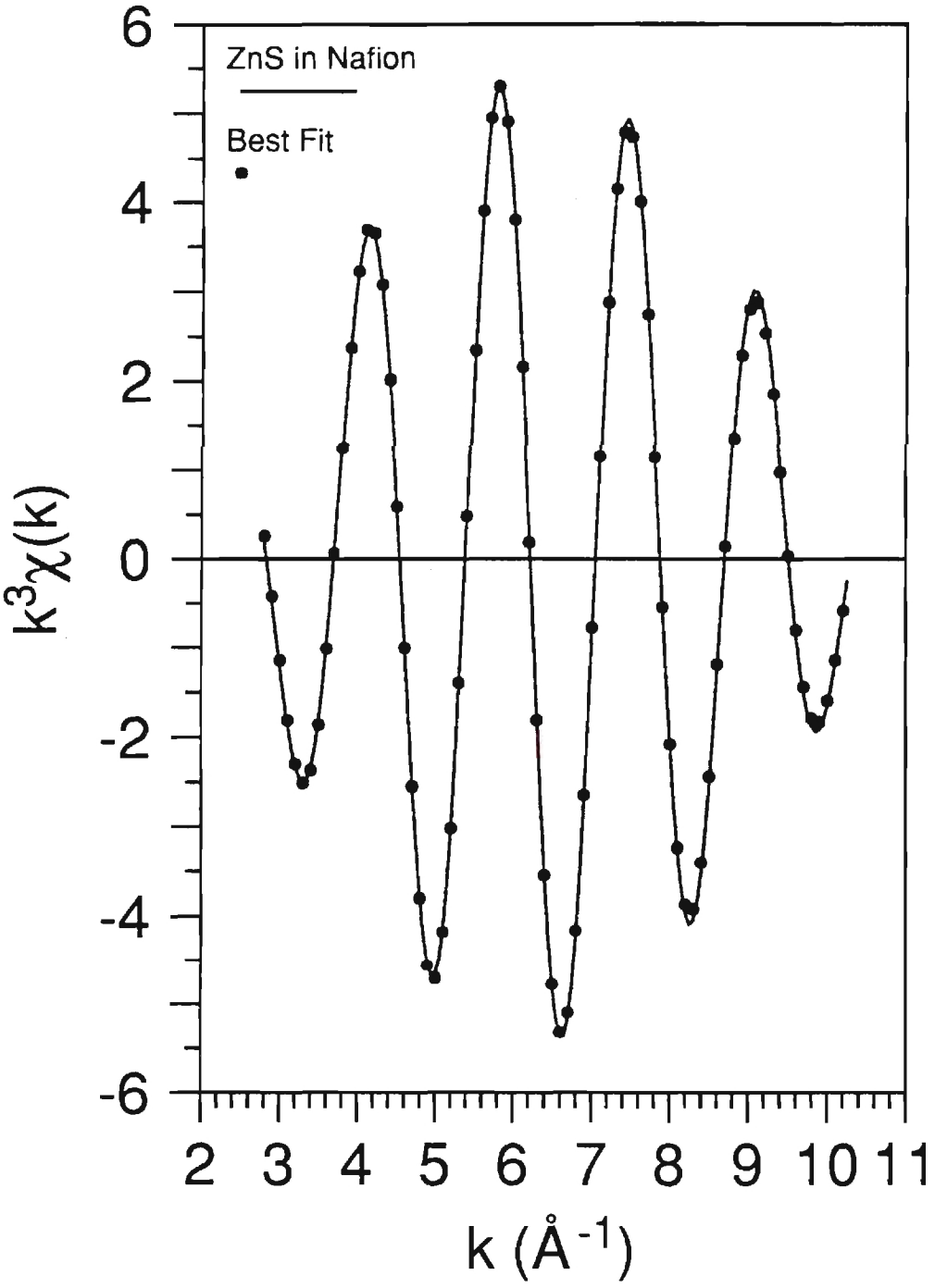

Figure 4.4. Filtered Zn-edge XAFS transform of ZnS bulk and Zn^{2+}-loaded Nafion.

Thiophenol Capped ZnS Clusters

XRD Results

The ZnS clusters were synthesized in methanol/water solutions as described. The synthesis of different cluster sizes was achieved by increasing the ratio of sulfide/thiophenol in the reaction mixture. The cluster size was estimated from x-ray powder diffraction (XRD) techniques as described earlier. The broadening of the (111) diffraction peak of the clusters was used to measure the crystal size according to the Scherrer equation. Figure 4.5 shows the diffraction pattern of the cluster. It is apparent from Fig. 4.5 that as the size increases the higher diffraction peaks become more resolved. The first peak in the diffraction pattern is actually consists of two peaks: (111) and (200). In bulk ZnS (lattice constant is 5.4093 Å), the intensity of (200) (2θ=33.09°) diffraction peak is about 10% of that of the (111) (2θ=28.56°) diffraction peak. In ZnS clusters, the broadening of the diffraction peaks causes the (200) and (111) peaks to overlap. The (111) and (200) reflections were fitted and the results for all the samples are listed in Table 4.7, as is the Zn-S bond length.

Table 4.7 : XRD Results for Thiophenol Capped ZnS Clusters

Sample	2θ	FWHM	Diameter Å	Lattice size	Zn-S Å
ZnS1.0	29.11	6.40	17 ± 1	5.309 ± 0.0017	2.299 ± 0.008
ZnS2.0	28.67	4.83	23 ± 1	5.369 ± 0.0018	2.334 ± 0.008
ZnS6.5	28.69	3.93	28 ± 1	5.385 ± 0.0018	2.332 ± 0.008
ZnS12.0	28.65	3.64	30 ± 1	5.392 ± 0.0018	2.335 ± 0.008
ZnS20.0	28.41	3.22	35 ± 2	5.436 ± 0.0019	2.353 ± 0.008

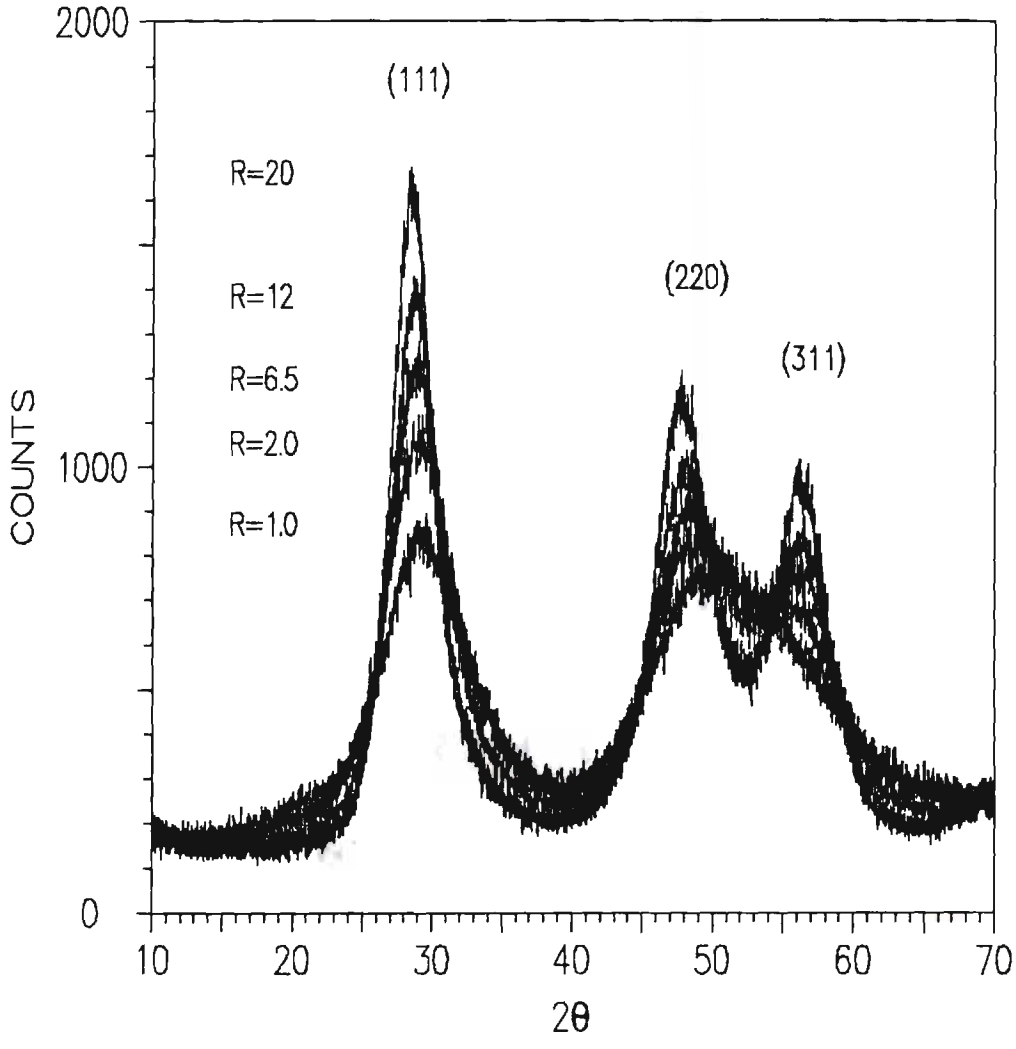

Figure 4.5 XRD of thiophenol capped ZnS clusters

XAFS Results

The Zn-edge and S-edge XAFS were obtained for these samples. The model sample, $(Me_4N)_2[Zn(SPh)_4]$, labeled as ZnPh4 in Table 4.8 was prepared according to Dance et. al. [5] and characterized by chemical analysis (Calculated: C, 54.24; %H, 5.22; %S,21.30. Found: %C, 54.18 ; %H, 5.20 ; %S, 21.36). The Zn-edge measurement were performed at liquid nitrogen temperature in the transmission mode at the X19A beam line using the Si(111) monochromator. The S-edge measurements were carried out at room temperature in the fluorescence mode, using Si(111) monochromator. For the Zn-edge measurements, samples were prepared by spreading the sample over Scotch brand Magic tape, then folding the tape to form 8 layers. The sample then was mounted on a copper sample holder having a 6 x 22 mm cutout for the sample and was covered with 2 mil Kapton tape. For the S-edge experiment, the samples were prepared by spreading a thin layer of the sample over a Kapton tape. Self-absorption effects on the data analysis were minimized by using similarly prepared standards, which contained a similar mole fraction of sulfur. Corrections due to self-absorption are discussed later in this section. The Zn-edge liquid nitrogen temperature XAFS transforms of the clusters and the ZnS bulk standard are shown in Fig. 4.6. It is clear from this figure that all the clusters have peaks similar to those of the bulk standard. However, the second shell is much reduced, especially, for the smaller clusters. The first and the second shells were filtered separately and analyzed using the ratio method with ZnS bulk as a standard. The analysis results are summarized in Tables 4.8 and 4.9. The S-edge transform of the ZnS clusters and that of the standard are shown in Fig. 4.7. This figure shows similar behavior as the

Zn-edge transform. Analysis results for the first shell are summarized in Table 4.10; correction for self-absorption requires knowlege of the chemical composition and is discussed in the following section. Table 4.15 shows the corrected results of table 4.10.

Table 4.8: Zn-Edge Liquid N_2 XAFS of Thiophenol Capped ZnS Clusters First Shell Results

Sample	R (Å)	N	$\sigma^2_{ref} - \sigma^2_{sample}$ (Å^2)
ZnS1.0	2.339 ± 0.003	3.57 ± 0.07	-0.00173 ± 0.00014
ZnS2.0	2.332 ± 0.001	3.45 ± 0.07	-0.00172 ± 0.00014
ZnS6.5	2.333 ± 0.001	3.45 ± 0.04	-0.00098 ± 0.00014
ZnS12.0	2.333 ± 0.001	3.38 ± 0.07	-0.00014 ± 0.00007
ZnS20.0	2.335 ± 0.001	3.60 ± 0.04	-0.00084 ± 0.00004
ZnSPH4	2.358 ± 0.002	4.23 ± 0.12	-0.00091 ± 0.00009

Table 4.9: Zn-edge Liquid N_2 XAFS of Thiophenol Capped ZnS Clusters Second Shell Results

Sample	R (Å)	N	$\sigma^2_{ref} - \sigma^2_{sample}$ (Å^2)
ZnS2.0	3.828 ± 0.002	2.88 ± 0.14	-0.00581 ± 0.00035
ZnS6.5	3.837 ± 0.003	3.98 ± 0.12	-0.00272 ± 0.00015
ZnS12.0	3.830 ± 0.003	4.56 ± 0.05	-0.00116 ± 0.00006
ZnS20.0	3.833 ± 0.008	5.42 ± 0.11	-0.00215 ± 0.0008

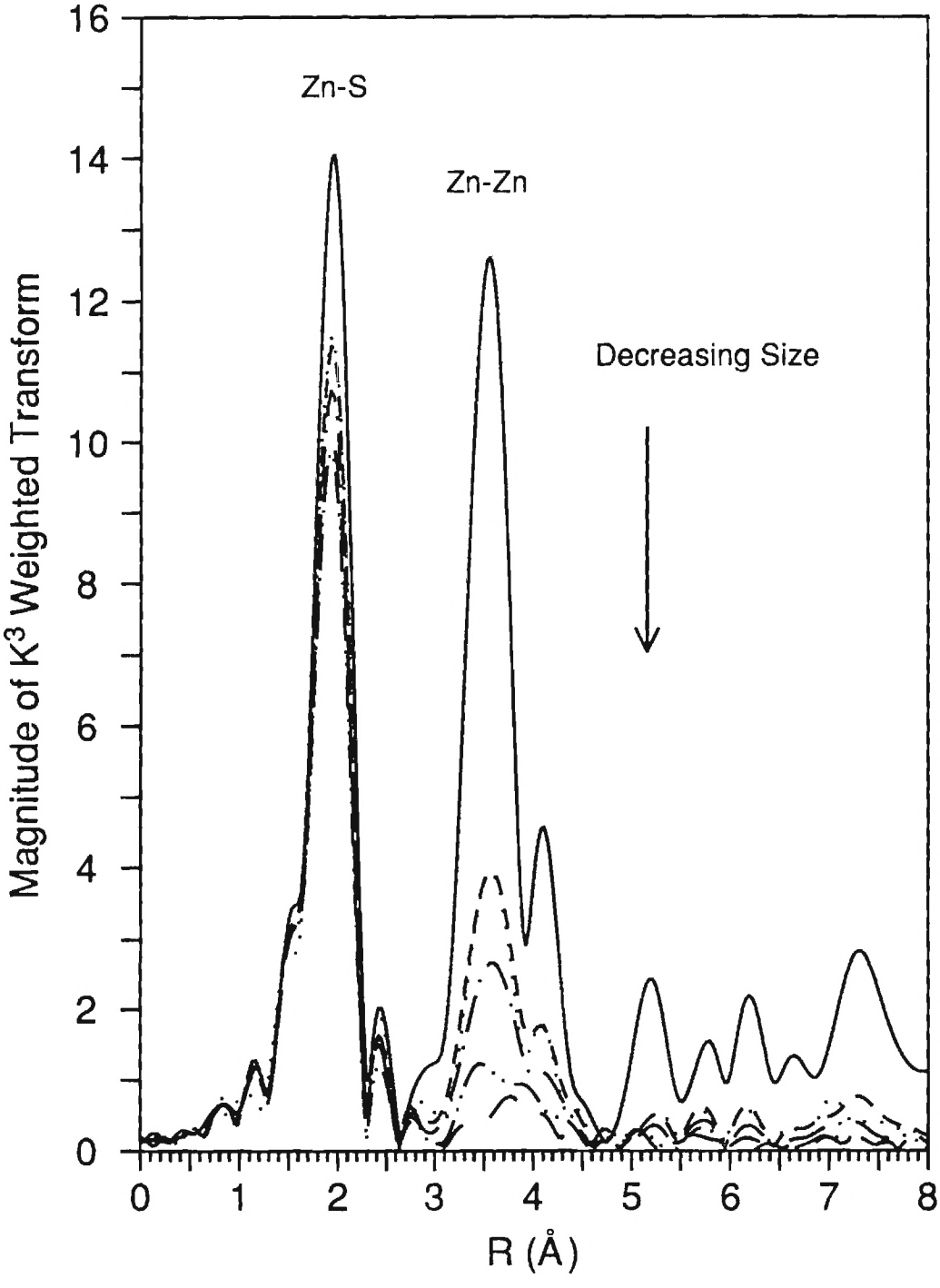

Figure 4.6. Zn-edge XAFS transform of ZnS bulk and thiophenol capped ZnS clusters.

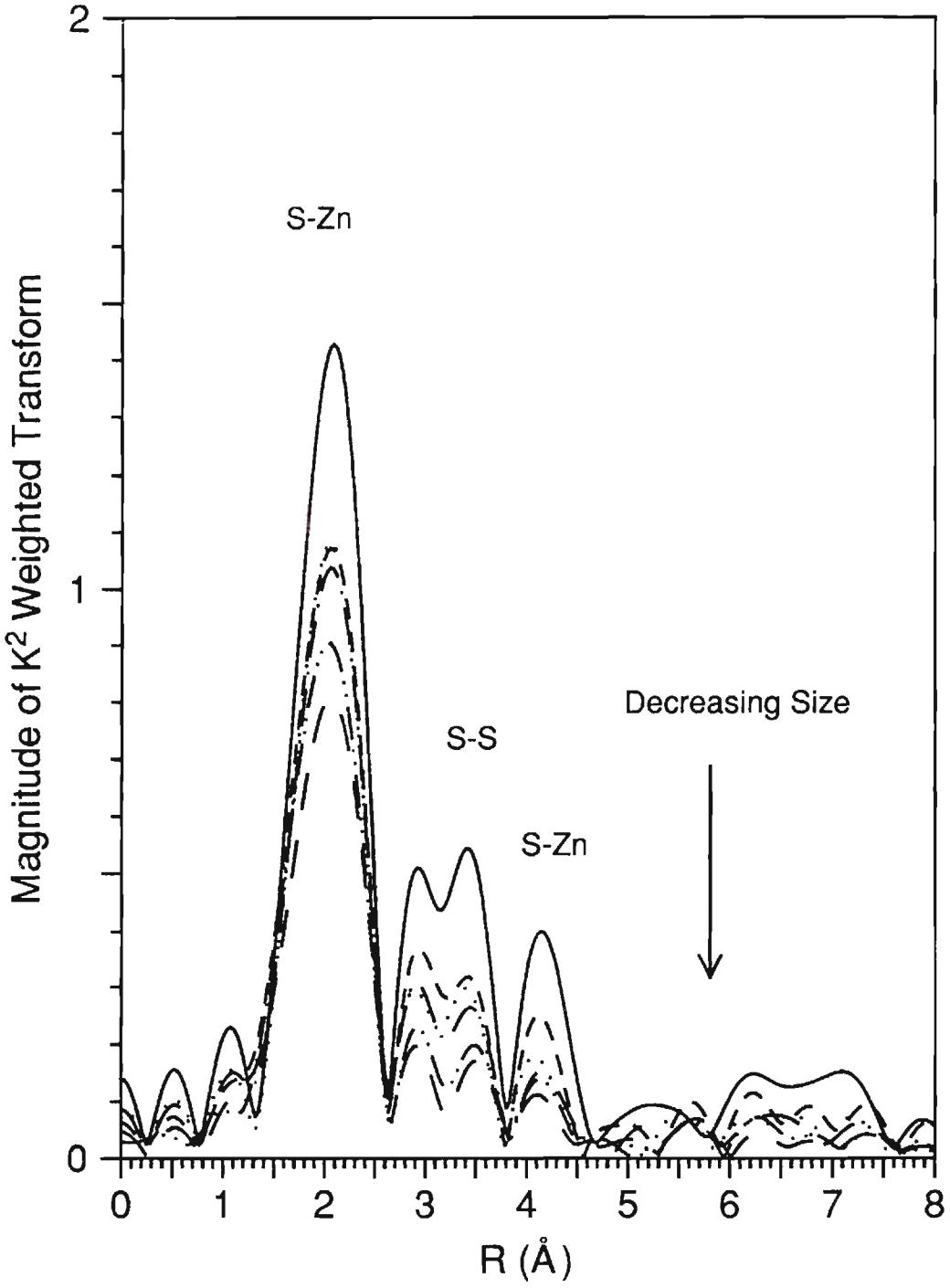

Figure 4.7.S-edge XAFS transform of ZnS bulk and thiophenol capped ZnS Clusters.

Table 4.10: S-edge Room Temperature XAFS of Thiophenol Capped ZnS Clusters First Shell Results (uncorrected for Self-Absorption)

Sample	R (Å)	N	σ^2_{ref} - σ^2sample (Å^2)
SZn1.0	2.340 ± 0.006	2.76 ± 0.20	-0.00139 ± 0.00055
SZn2.0	2.320 ± 0.009	3.06 ± 0.12	-0.00128 ± 0.00034
SZn6.5	2.330 ± 0.002	3.44 ± 0.10	-0.00151 ± 0.00027
SZn12.0	2.332 ± 0.001	3.38 ± 0.07	-0.00108 ± 0.00021
SZn20.0	2.324 ± 0.004	3.56 ± 0.07	-0.00105 ± 0.00022

As can be seen in Fig. 4.7, the S-edge XAFS does not show a S-C peak in the transformed spectra.

Chemical Analysis

The following are the results of the chemical analysis on the ZnS samples prepared in methanol/water solution and capped with thiophenol. The samples were analyzed for C,H, and S by Atlanta Microlab, Inc. The zinc analysis was performed by digesting a dry sample with aqua regia solution then titrating the neutralized sample with EDTA using Erichrome Black T indicator. The results of the chemical analysis are presented in Table 4.11. The total percentage does not add to 100. It is suspected that the impurity is mostly water (broad peak in the ir at ~3300 cm^{-1}) and trace quantities of acetate salt (weak peaks in the ir at 1608, 1554, 1407 cm^{-1}). Vacuum drying the R=6.5 sample at ~100 °C for 12 hrs revealed that the sample contained 3% H_2O, and the water ir peak was greatly reduced. Table 4.12 is corrected for the percentage due to the presence of water. The procedure of correcting for the presence of H_2O is to assume that the total percent does not add to 100 due to the %O that was not accounted for. Thus for the ZnS1.0

sample, the %O is 3.49. Since the mass ratio of H/O in H_2O is 2/16, then the %H that is due to water is 3.49(2/16)=0.44. Therefore, the %H from the sample (excluding the %H from water) is 2.2-0.44=1.76%, and the percent water in the sample is 3.49+0.44=3.93%. To correct for the remaining elements, the percent of each element should be divided by 1-0.0393=0.9607. Thus %H will be 1.76/0.9607=1.83, %C=25.64/0.9607=26.69, %S=24.96/0.9607=25.98, and %Zn=43.71/0.9607=45.50. Similar calculations were performed for the rest of the samples.

Since the carbon must come from the thiophenol, and since the ratio of S/C in thiophenol is 1/6, it is possible to calculate the mole fraction of thiophenol. The mol fraction of sulfide is obtained from subtracting the mole fraction of thiophenol from the total mole fraction of sulfur. The empirical formula was calculated, and the final results are summarized in Table 4.13.

Table 4.11: Chemical Analysis Results for Thiophenol Capped ZnS Clusters

Sample	%C	%H	%S	%Zn	100-Tot
ZnS1.0	25.64	2.20	24.96	43.71	3.49
ZNS2.0	17.65	1.72	26.94	49.70	3.99
ZnS6.5	8.52	1.125	28.78	58.35	3.23
ZnS12	5.54	0.85	30.41	60.99	2.21
ZnS20	3.96	0.74	28.46	61.92	4.92

Table 4.12 : Corrected Chemical Analysis Results for Thiophenol Capped Clusters

Sample	%C	%H	%S	%Zn
ZnS1.0	25.59	1.83	25.98	45.50
ZNS2.0	18.47	1.28	28.21	52.04
ZnS6.5	8.84	0.75	29.86	60.54
ZnS12	5.68	0.59	31.19	62.54
ZnS20	4.19	0.13	30.13	65.54

Table 4.13 : Chemical Analysis Calculation Results for Thiophenol Capped Clusters

Sample Ratio	mmol per 1 g sample						Empirical Formula	
	C	H	S	Zn	S^{2-}	SPh^-		S^{2-}/SPh^-
Zns1.0	22.22	18.21	8.10	6.96	4.40	3.70	$ZnS_{0.63}SPh_{0.53}$	1.2
ZnS2.0	15.39	12.68	8.80	7.96	6.23	2.56	$ZnS_{0.78}SPh_{0.32}$	2.4
ZnS6.5	7.36	7.43	9.31	9.26	8.09	1.23	$ZnS_{0.87}SPh_{0.13}$	6.7
ZnS12	4.73	5.84	9.73	9.57	8.94	0.79	$ZnS_{0.93}SPh_{0.082}$	11.3
ZnS20	3.49	1.31	9.40	10.03	8.81	0.58	$ZnS_{0.88}SPh_{0.058}$	15.2

Using the chemical analysis results, it was possible to correct for the self-absorption effect on the amplitude of the S-edge XAFS results. By using Eqs. (2-29) and (2-30), the reduction in the coordination number and the $\Delta\sigma^2$ were computed, and the results are listed in Table 4.14. $C_0(S)$ is the absorption fraction of sulfur in the sample, and A_0 is the ratio of the fluorescence amplitude to the absorption amplitude. As can be

can be seen from Table 4.14, the correction for $\Delta\sigma^2$ is negligible. However, a correction is necessary for the coordination number, especially for the smallest clusters where the absorption fraction of S is relatively larger than the standard. Thus, for ZnS1.0 sample, the coordination number should be corrected by the multiplication factor (0.786/0.773)=1.02. If the self-absorption effect is ignored, then at the most, 2% error is introduce in the XAFS coordination number for the ZnS clusters, which is within the experimental error. Table 4.15 summarizes the corrected S-edge results.

The results of the chemical analysis allows also the calculation of the coordination number for S from the Zn-edge results. As was discussed in chapter II, the ratio of the Zn-S coordination number (from the Zn-edge) to the mole ratio of S/Zn (from chemical analysis) is the coordination number of Zn with S. Thus, by using the results of Zn-edge in Table 4.8, it was possible to calculate the coordination number of S in the clusters. The results of the calculation is found in Table 4-16. As can be seen from Table 4-16, the coordination numbers obtained directly from S-edge, and the coordination numbers obtained from Zn-edge and chemical analysis agree favorably. However, the SZn20.0 sample seems to be in error. The reason of the discrepancy in the result of this sample is most clearly shown from chemical analysis. The chemical analysis for the large clusters shows that the mole ratio of S/Zn is 1.01 while the SZn20.0 sample has a ratio of 0.94. This ratio seems to be in error. If this ratio is taken to be similar to the R=12 and R=6.5 samples (i.e 1.01) then the calculated coordination number will be 3.56 which is in excellent agreement of the S-edge result.

Table 4.14: Calculation results of Self-Absorption Amplitude Reduction for S-edge ZnS samples

Sample	$C_o(S)$	A_0	$\Delta\sigma^2$
ZnS(Bulk)	0.391	0.786	-0.00110
ZnS1.0	0.410	0.773	-0.00116
ZnS2.0	0.404	0.777	-0.00145
ZnS6.5	0.387	0.789	-0.00109
ZnS12.0	0.391	0.786	-0.00110
ZnS20.0	0.375	0.796	-0.00104

Table 4.15: S-edge Room Temp. XAFS for Thiophenol Capped ZnS Clusters First Shell Corrected for Self-Absorption

Sample	R (Å)	N	$\sigma^2_{ref} - \sigma^2_{sample}$ (Å^2)
SZn1.0	2.340 ± 0.006	2.81 ± 0.20	-0.00139 ± 0.00055
SZn2.0	2.320 ± 0.009	3.10 ± 0.12	-0.00128 ± 0.00034
SZn6.5	2.330 ± 0.002	3.43 ± 0.10	-0.00151 ± 0.00027
SZn12.0	2.332 ± 0.001	3.38 ± 0.07	-0.00108 ± 0.00021
SZn20.0	2.324 ± 0.004	3.51 ± 0.07	-0.00105 ± 0.00022

Table 4.16: Calculation of Sulfur 1st Shell from Zn-Edge Data and Chemical Analysis

Sample	N(Zn-S)/S
SZn1.0	3.08
SZn2.0	3.14
SZn6.5	3.45
SZn12.0	3.34
SZn20.0	3.84
SZn20.0[a] (corrected)	3.56

a)Assuming S/Zn=1.01

3-Mercaptopropanoic Acid Capped ZnS Clusters

The 3-mercaptopropanoic acid (abbreviated as MPA throughout) capped ZnS cluster samples were prepared in water as describe earlier. The size was controlled by changing the mole ratio of the sulfide to the thiol and keeping the number of moles of zinc constant. These samples are labeled with PW to indicate the use of 3-mercaptopropanoic acid as the capping species and water as solvent solvent. Other type of ZnS clusters were also prepared. One sample labeled with ZnSPH45 is the sample synthesized by adding the sulfide solution to a mixture made of zinc, thiol, and potassium hydroxide. The addition of KOH precipitated the zinc as zinc hydroxide (pH~8). Addition of sulfide solution formed ZnS clusters as inferred by XRD and XAFS.

XRD Results

The XRD patterns were obtained for these samples and are shown in Fig. 4.8. The Fig. 4.17 shows also the XRD of ZnSPH45 sample which was prepared by pH adjustment

of the reaction mixture. The XRD analysis results are summarized in table 4.17. These results were obtained by fitting the (111) and (200) peaks of the XRD pattern. The XRD results for all MPA-capped ZnS cluster samples show the presence of single phase of cubic structure. The Zn-S bond length as obtained from the fit is about 0.01 Å shorter than the bulk bond length and can be attributed to experimental error. It is noticeable, however, that in the ZnSPH45 sample the bond length is about 0.02 Å shorter than that of the bulk ZnS.

XAFS Results

The Zn-edge XAFS data were collected in the transmission mode at 90 K on beam line X11-A at NSLS using a Si(311) monochromator. The Zn-edge XAFS transform is shown in Fig. 4.10 for ZnS bulk and the capped clusters. The transform clearly shows the similar shells of the ZnS clusters and the ZnS bulk. The second shell is shown to decrease uniformly with the decrease in the size. The first and the second shells were filtered and analyzed separately using the ratio method with ZnS bulk as a reference standard. The results of the analysis are summarized in Tables 4.18 and 4.19. The Zn-S first shell bond length is within 0.01 Å of that of the bulk in agreement with the XRD results. The second shell XAFS results show a gradual increase in the coordination number with size. The $\Delta\sigma^2$ seems also to be correlated with the size of the cluster, and the coordination number of the second shell is somewhat lower than that of a thiophenol cluster of comparable size.

The S-edge transform for the bulk and the capped clusters is shown in figure 4.11 and 4.12. All the clusters display first and second shells similar to the bulk standard.

The position of the peak is shifted for the second shell and also is narrower than that of the bulk sample. The smaller clusters, as shown in Fig. 4.12, show a third peak between those S-Zn and S-S peak. These peaks (if real) could be of the S-C second shell.

The first and the second shell were filtered separately and analyzed using the ratio method with ZnS bulk as standard, and the results are displayed in Tables 4.20 and 4.21. The bond length of the first shell is similar to Zn-S values for the large clusters. However, the smaller clusters have about S-Zn 0.01 Å shorter than the Zn-S which could be due to analysis error or due to the effect of the S-C on the first shell for the small clusters. The $\Delta\sigma^2$ is relatively constant (~ -0.003 $Å^2$) in most of the clusters in contrast to the Zn-edge results. The second shell coordination numbers are larger than the Zn-edge values, and the second shell distance is shorter than the bulk value (3.825 Å) and increase with size. The second shell $\Delta\sigma^2$ are positive in contrast to the Zn-edge results.

Table 4.17 : XRD Results for 3-Mercaptopropanoic Acid Capped ZnS

Sample	2θ	B(2θ)	Diameter Å	Lattice size	Zn-S Å
ZnSPW1.0	28.86	4.8458	22	5.354	2.318
ZnSPW2.0	28.57	4.6644	23	5.407	2.341
ZnSPW4.0	28.65	4.1957	25	5.392	2.335
ZnSPW5.0	28.69	3.9070	28	5.385	2.332
ZnSPW6.5	28.76	3.5333	31	5.372	2.326
ZnSPW20.0	28.67	3.1656	35	5.389	2.333
ZnSPW50.0	28.67	3.0041	37	5.389	2.333
ZnSPH45.0	28.81	2.7478	40	5.363	2.322

Table 4.18: Zn-edge LN_2 XAFS for 3-Mercaptopropanoic Acid Capped ZnS Clusters. First Shell Results

Sample	R (Å)	N	$\sigma^2_{ref} - \sigma^2_{sample}$ (Å^2)
ZnSPW1.0	2.334 ± 0.003	3.37 ± 0.04	-0.00256 ± 0.00013
ZnSPW2.0	2.333 ± 0.001	3.51 ± 0.03	-0.00240 ± 0.00009
ZnSPW4.0	2.332 ± 0.001	3.24 ± 0.03	-0.00174 ± 0.00009
ZnSPW5.0	2.330 ± 0.001	3.48 ± 0.03	-0.00172 ± 0.00004
ZnSPW6.5	2.332 ± 0.001	3.37 ± 0.04	-0.00124 ± 0.00010
ZnSPW20.0	2.334 ± 0.001	3.62 ± 0.04	-0.00115 ± 0.00004
ZnSPW50.0	2.333 ± 0.001	3.73 ± 0.04	-0.00119 ± 0.00004
ZnSPH50.0	2.330 ± 0.002	3.51 ± 0.03	-0.00141 ± 0.00004

Table 4.19: Zn-edge LN_2 XAFS for 3-Mercaptopropanoic acid Capped ZnS Clusters. Second Shell Results

Sample	R (Å)	N	$\sigma^2_{ref} - \sigma^2_{sample}$ (Å^2)
ZnSPW1.0	3.824 ± 0.004	1.95 ± 0.04	-0.00330 ± 0.00010
ZnSPW2.0	3.832 ± 0.007	2.19 ± 0.04	-0.00358 ± 0.00009
ZnSPW4.0	3.827 ± 0.003	2.62 ± 0.04	-0.00274 ± 0.00016
ZnSPW5.0	3.824 ± 0.002	3.36 ± 0.07	-0.00275 ± 0.00014
ZnSPW6.5	3.826 ± 0.003	3.88 ± 0.11	-0.00269 ± 0.00012
ZnSPW20.0	3.824 ± 0.001	4.64 ± 0.09	-0.00200 ± 0.00003
ZnSPW50.0	2.825 ± 0.001	5.34 ± 0.05	-0.00124 ± 0.00008
ZnSPH45.0	2.816 ± 0.002	4.46 ± 0.05	-0.00179 ± 0.00007

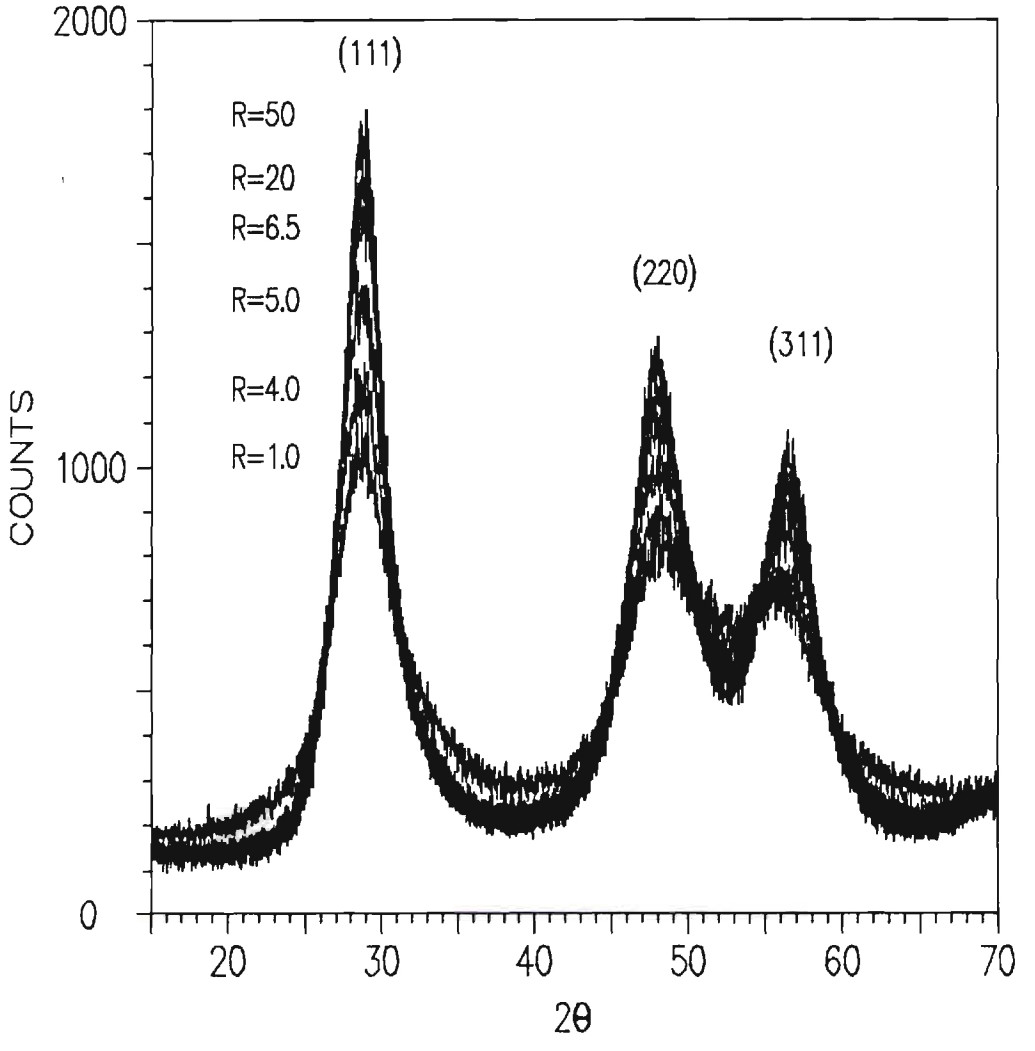

Figure 4.8. XRD 3-Mercaptopropanoic acid capped ZnS clusters.

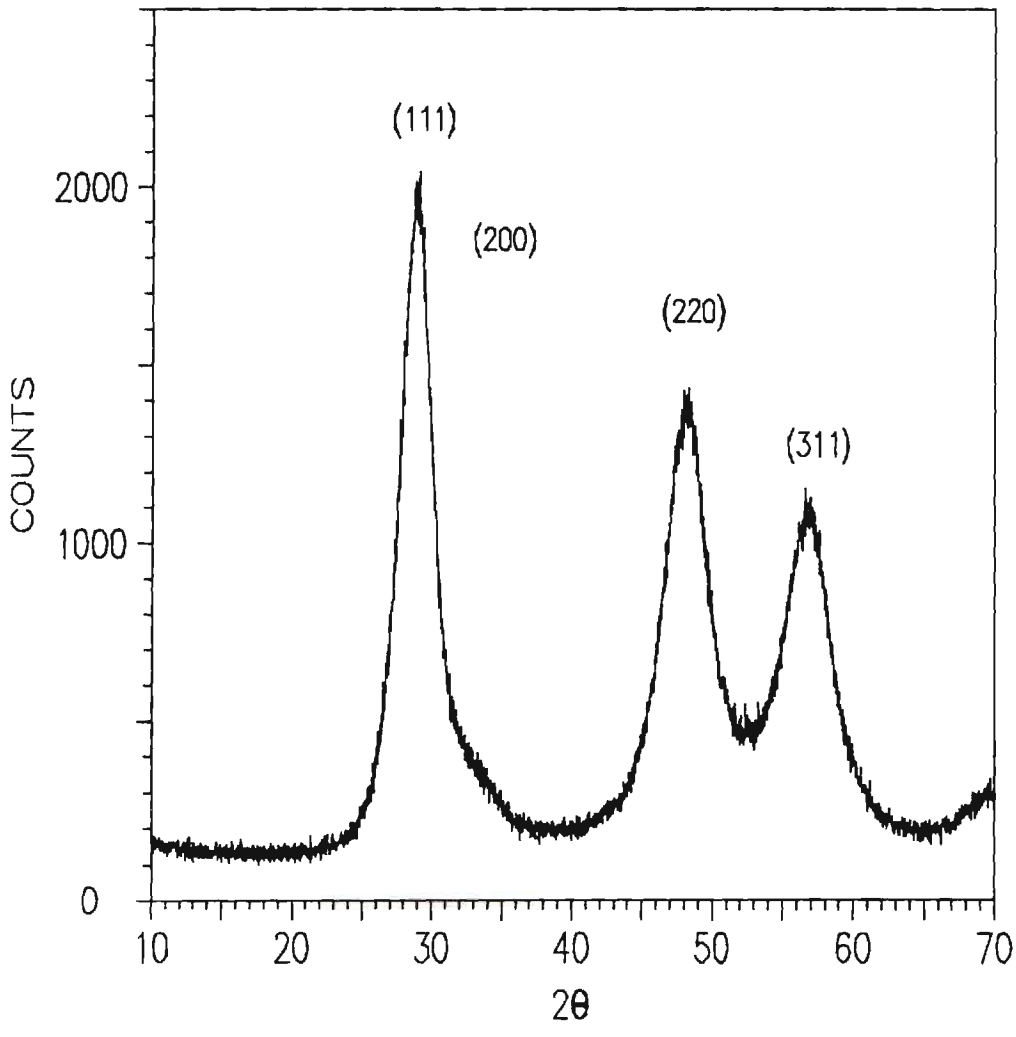

Figure 4.9. XRD of ZnSPH45 cluster.

Table 4.20: S-edge Room Temperature XAFS for 3-Mercaptopropanoic Acid Capped ZnS Clusters. First Shell Results

Sample	R (Å)	N	$\sigma^2_{ref} - \sigma^2_{sample}$ (Å^2)
ZnSPW1.0	2.317 ± 0.002	3.35 ± 0.13	-0.00252 ± 0.00028
ZnSPW2.0	2.322 ± 0.001	3.54 ± 0.04	-0.00221 ± 0.00007
ZnSPW4.0	2.322 ± 0.002	3.83 ± 0.04	-0.00279 ± 0.00015
ZnSPW5.0	2.333 ± 0.002	3.54 ± 0.07	-0.00179 ± 0.00024
ZnSPW6.5	2.333 ± 0.001	3.47 ± 0.14	-0.00282 ± 0.00045
ZnSPW20.0	2.341 ± 0.001	3.66 ± 0.04	-0.00342 ± 0.00010
ZnSPW50.0	2.333 ± 0.001	3.59 ± 0.04	-0.00281 ± 0.0004

Table 4.21: S-edge Room Temperature XAFS for 3-Mercaptopropanoic Acid Capped ZnS Clusters. Second Shell Results

Sample	R (Å)	N	$\sigma^2_{ref} - \sigma^2_{sample}$ (Å^2)
ZnSPW1.0	3.798 ± 0.008	3.74 ± 0.03	+0.00116 ± 0.00012
ZnSPW2.0	3.786 ± 0.008	4.33 ± 0.12	+0.00204 ± 0.00031
ZnSPW4.0	3.789 ± 0.007	4.92 ± 0.04	+0.00258 ± 0.00023
ZnSPW5.0	3.805 ± 0.006	6.02 ± 0.06	-0.00046 ± 0.00008
ZnSPW6.5	3.803 ± 0.005	5.08 ± 0.05	+0.00248 ± 0.00005
ZnSPW20.0	3.810 ± 0.001	6.51 ± 0.06	+0.00095 ± 0.00002
ZnSPW50.0	3.813 ± 0.003	7.70± 0.08	+0.00057 ± 0.00003

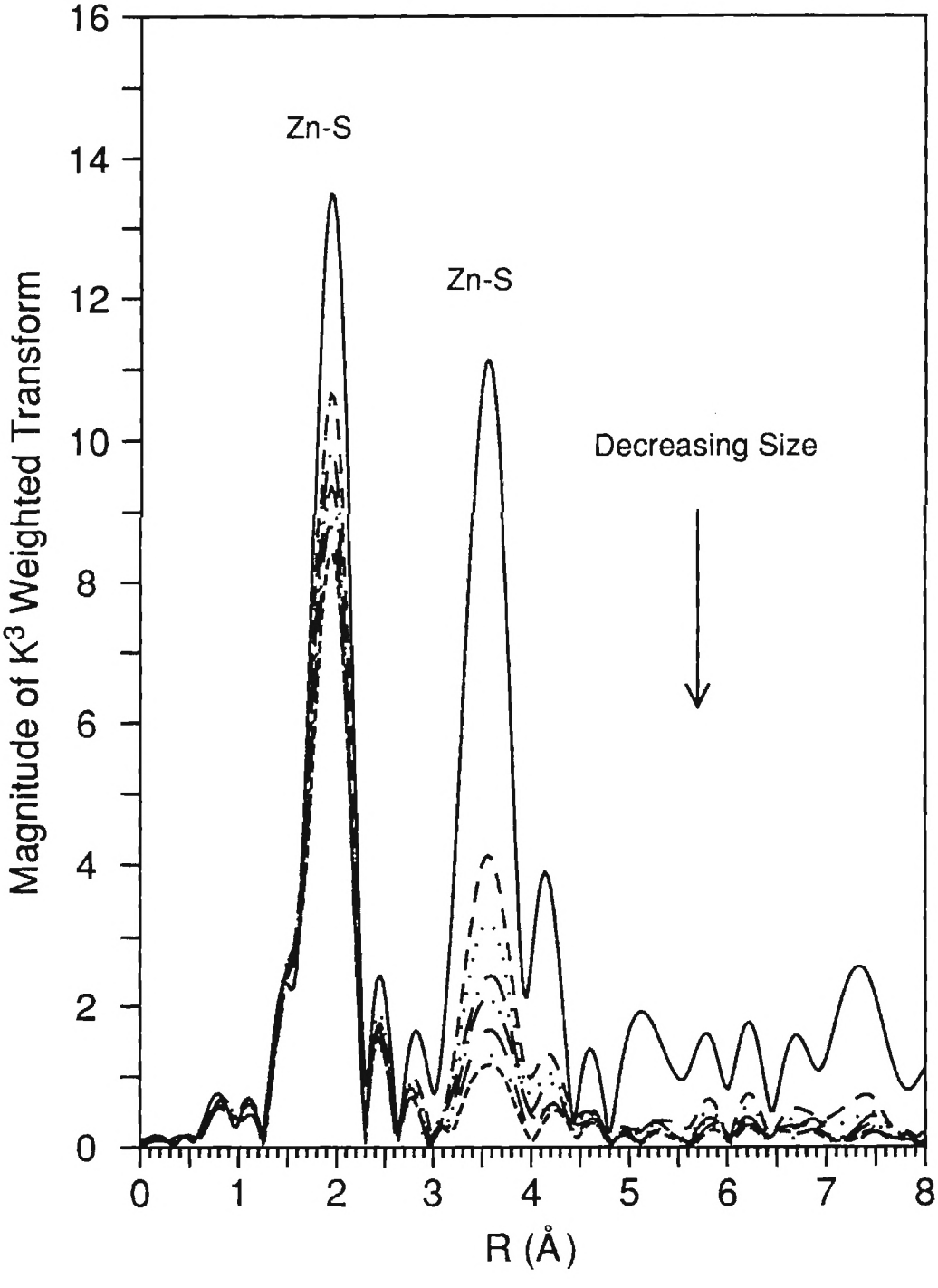

Figure 4.10. Zn-edge XAFS transform of ZnS bulk and 3-mercaptopropanoic acid capped ZnS clusters.

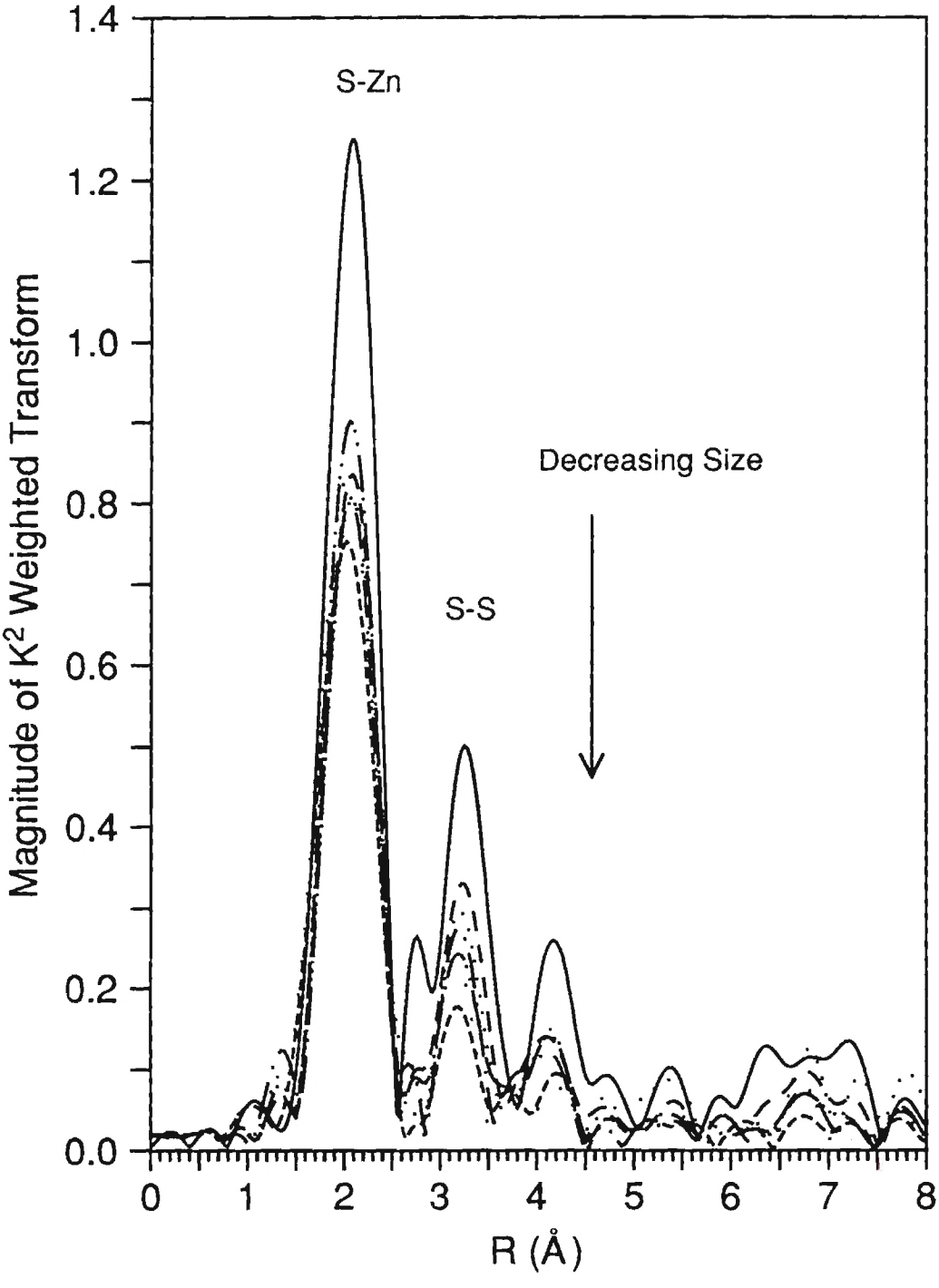

Figure 4.11. S-edge XAFS transform of ZnS bulk and 3-mercaptopropanoic acid capped ZnS clusters.

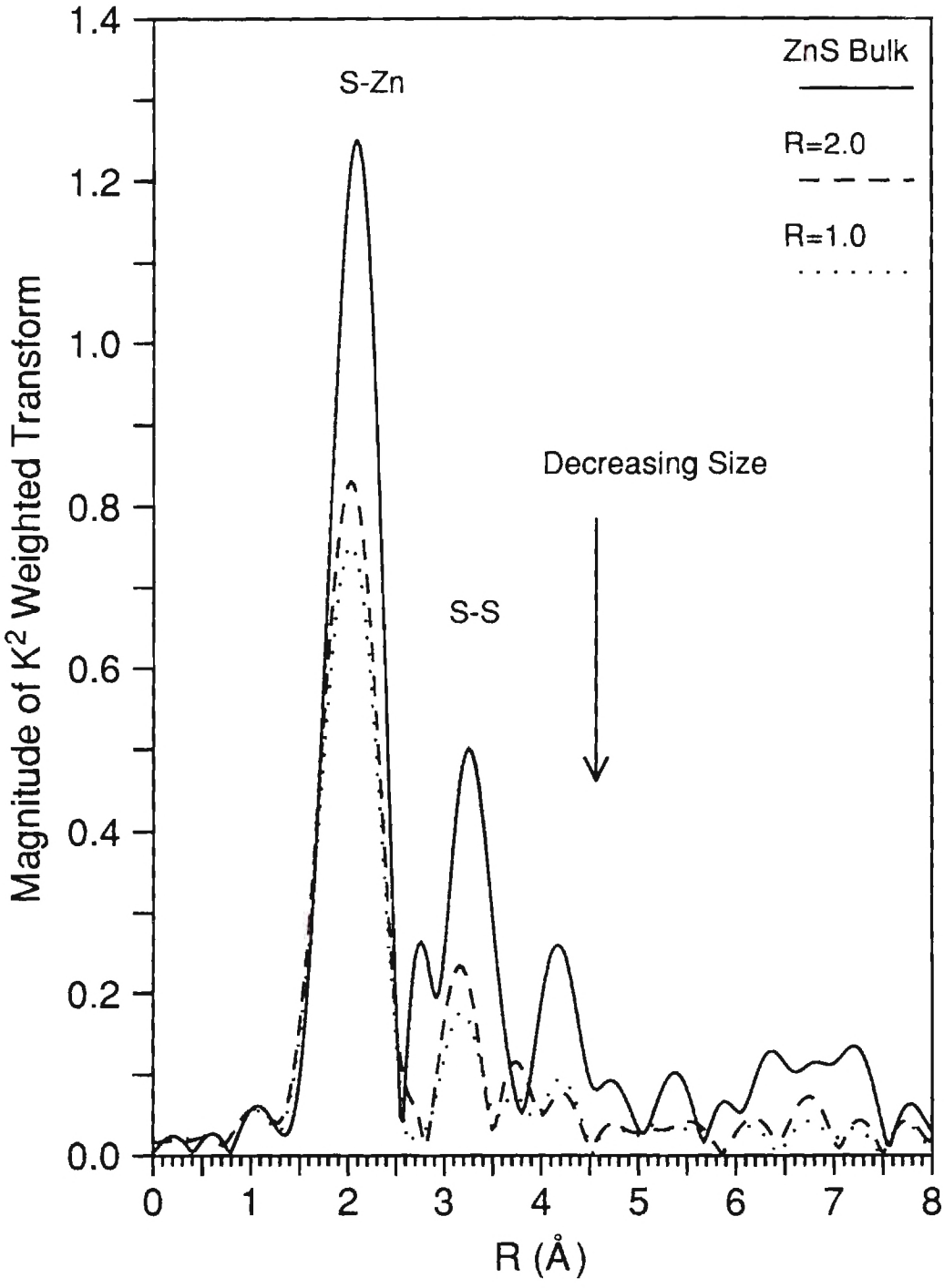

Figure 4.12. S-edge XAFS transforms of ZnS bulk and 3-mercaptopropanoic acid capped ZnS clusters with ratios 1 and 2.

Benzeneselenol Capped ZnS Clusters

XRD Results

The XRD results are summarized in Table 4.22. The estimated errors in the calculation of the diameter, lattice size, and bond length are based upon the error of measuring the peak width and location ($\Delta 2\theta$=0.1°,B(2θ)=0.1°). The bond lengths are 0.01 Å shorter than the bulk ZnS. As can be seen from Table 4.22, only two sizes were obtained from the five prepared samples. This is a remarkable difference compared to samples with thiophenol as cap. The XRD patterns are shown in Fig. 4.13 and show a zinc blende (cubic) structure. The ZnSSe1.5 XRD of Fig 4.14 was obtained starting from lower angles and shows sharp peaks. These sharp peaks did not match with PhSe-SePh. A peak search did not reveal any probable structure, which may indicate that the impurity is due to some unknown compound that may be similar to compounds reported by Dance et. al [4]. Analysis of the peak area of the strongest peak with respect to the (111) peak of the zinc blende indicated a rough estimate of a maximum fraction of 7% of the unknown impurity. The other clusters did not have these sharp reflections.

XAFS Results

Se-edge and Zn-edge XAFS were collected at liquid nitrogen temperatures on beam line X19-A using a Si(220) monochromator. Both edges were measured on the same XAFS sample. However the ZnSSe6.5 Zn-edge was obtained on X11-A using a different XAFS sample than the one used for Se-edge XAFS. Thus, no XAFS chemical quantitation was possible for this sample. XAFS quantative chemical analysis depended

on knowledge of the absorption cross section of Zn and that of Se.

Table 4.22 : ZnSSe XRD Results

Sample	2θ	B(2θ)	Diameter (Å)	Lattice size	Zn-S (Å)
ZnSSe01	28.916	4.7578	23 ± 1	5.344 ± 0.018	2.314 ± 0.008
ZnSSe02	28.750	4.8161	23 ± 1	5.374 ± 0.018	2.327 ± 0.008
ZnSSe65	28.763	4.0119	27 ± 1	5.372 ± 0.018	2.326 ± 0.008
ZnSSe12	28.845	4.1478	27 ± 1	5.357 ± 0.018	2.319 ± 0.008
ZnSSe20	28.812	4.1012	27 ± 1	5.363 ± 0.018	2.322 ± 0.008

Since the same sample is used for both XAFS edges and thus the density is the same, then the fraction of Se/Zn can be computed by measuring the X-ray edge step height according to equation (4.2)

$$\frac{X_{Zn}}{X_{Se}} = \frac{h_{Zn}\ \mu_{Se}}{h_{Se}\ \mu_{Zn}} \qquad (4.2)$$

where X is the mole fraction, μ is the absorption cross section, and h is the edge step. Table 4.23 shows the edge results of ZnSSe samples. The cross section ratio of Se/Zn=0.705 was calculated from the ratio of the edge-step of ZnSe and SeZn and agrees well with 0.677 as estimated from McMaster's tables [6] . This ratio (0.677) and the fact that the same samples were used for both edges enabled the calculation of the mole fraction of Se/Zn.

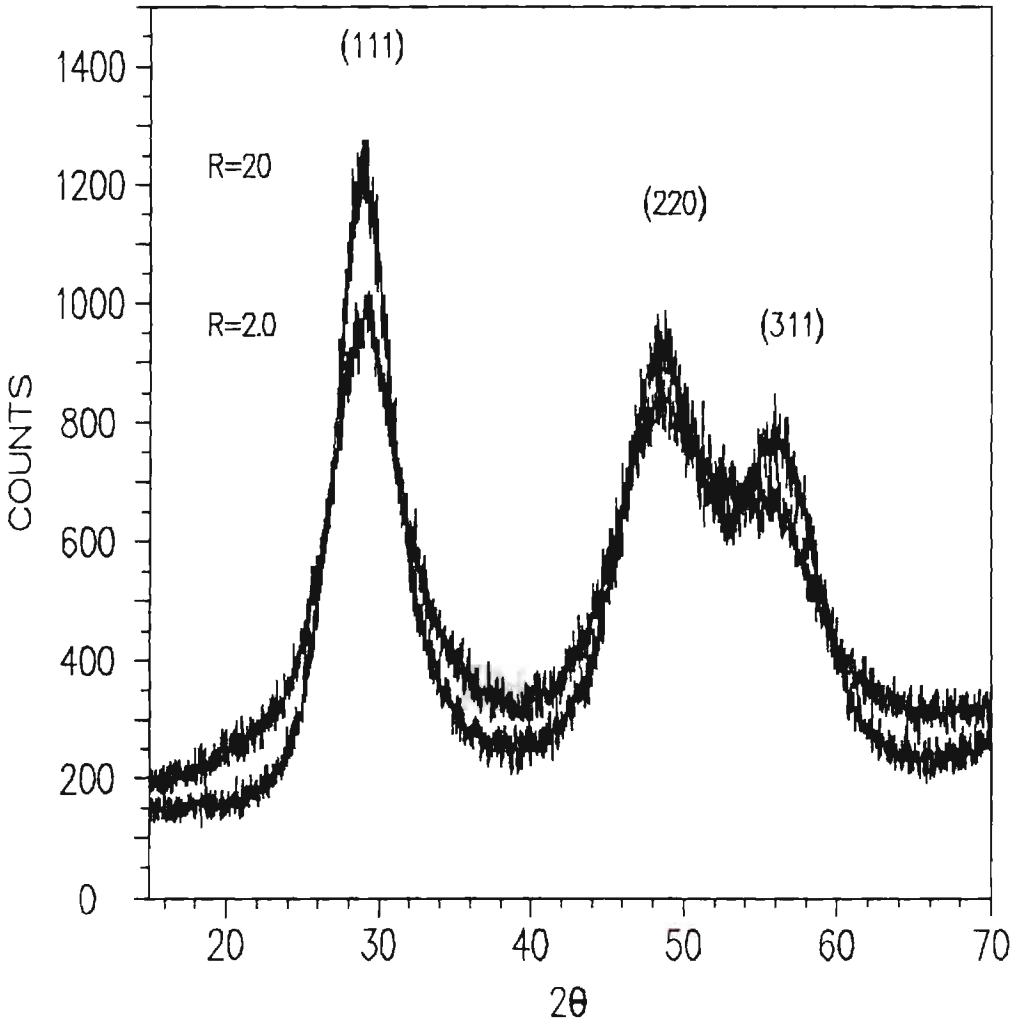

Figure 4.13. XRD of benzeneselenol capped ZnS clusters for R=2.0 and R=20

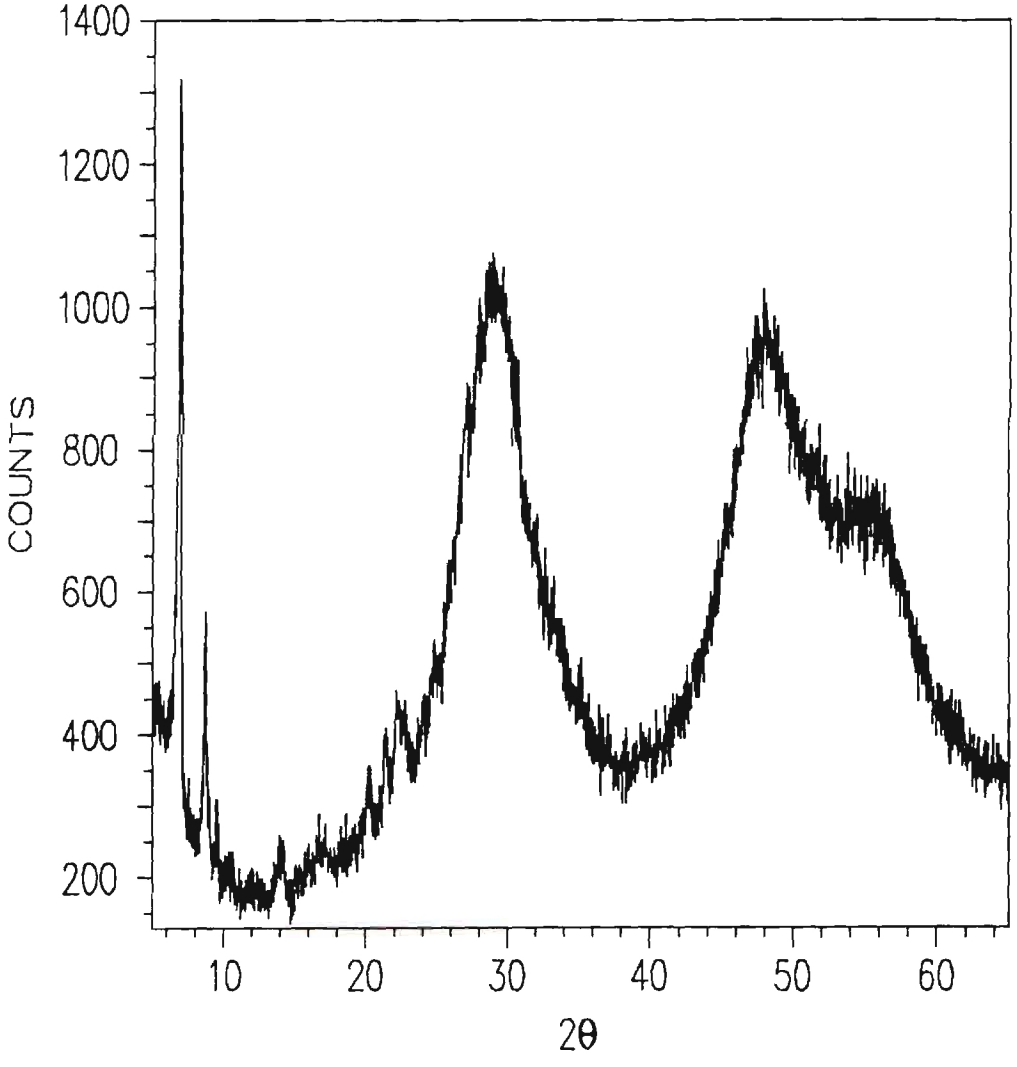

Figure 4.14. XRD of benzeneselenol capped ZnS clusters R=1.5

As can be seen in Table 4.23, the SeZnS1.5 sample has the highest mole fraction Se/Zn of 0.48. If charge balance is assumed, then for SeZnS01, $S^{-2}/PhSe^{-1}=1.6$ as compared to 1.5 from synthesis. The rest of the ratios are also displayed in Table 4.23 along with empirical formula. The mole fraction of Se in SeZnS02 is particularly low relative to the XRD size. Table 4.23 also displays the edge energy for each sample. The edge energies for most of the Se samples are shifted from SeZn standard.

Table 4.23: Data of Zn and Se Edges for Benzeneselenol Capped Clusters

Sample	E0 (eV)	Step Height	Layers	Se/Zn	S/Se	Empirical Formula
ZnS (BulK)	9662.78	1.503	8			
ZnSSe01	"	0.288	8			
ZnSSe02	"	1.463	16			
ZnSSe12	"	1.653	16			
ZnSSe20	"	2.442	16			
SeZn (Bulk)	12660.66	1.059	8	1.04		
SeZnS01	12656.15	0.186	16	0.477	1.6	$ZnS_{0.762}PhSe_{0.477}$
SeZnS02	12658.97	0.075	16	0.076	12.7	$ZnS_{0.962}PhSe_{0.076}$
SeZnS12	12659.66	0.059	16	0.054	18.0	$ZnS_{0.973}PhSe_{0.054}$
SeZnS20	12658.97	0.064	16	0.039	26.5	$ZnS_{0.981}PhSe_{0.037}$

The Se-edge transforms are shown in Figs. 4.15-4.18. The transforms in Figs. 4.15 and 4.16 show the Se-Zn shell of the clusters that matches that of the bulk ZnSe shell but with smaller amplitude. Figures 4.17 and 4.18 shows the Se-C shell which is obvious for all the clusters. The two shells Se-Zn and Se-C were filtered separately and analyzed using the ratio method. The Se-Zn shell was analyzed with ZnSe bulk standard. The result of the analysis are summarized in Table 4-24 and shows that each cluster has an average coordination of 2 Zn to each Se. The quoted errors for this analysis were obtained from the fitting results. However, the chemical environment of the standard and the reference is different (Se-Zn in standard, and Se-Zn and Se-C in the ZnSSe samples). Thus the quoted error bars are underestimated due to limited chemical transferability. The Se-C shell was analyzed using FEFF (theoretical standard) and the results are shown in Table 4-25. It is clear that the Se is coordinated with an average of one carbon arising from phenyl ring of benzeneselenol. Fitting of the Se edge with Se metal as one of the standards did not confirm the presence of Se-Se bonds.

Table 4-24: Se-edge LN_2 (~100 K) XAFS
Se-Zn First Shell

Sample	R	N	$\sigma^2_{ref} - \sigma^2_{sample}$
SeZnS01	2.482 ± 0.002	2.3 ± 0.1	-0.00231 ± 0.00012
SeZnS02	2.502 ± 0.002	2.2 ± 0.1	-0.00212 ± 0.00031
SeZnS65	2.489 ± 0.003	2.3 ± 0.1	-0.00291 ± 0.00012
SeZnS12	2.504 ± 0.002	2.0 ± 0.1	-0.00121 ± 0.00014
SeZnS20	2.495 ± 0.005	1.8 ± 0.1	+0.00047 ± 0.00004

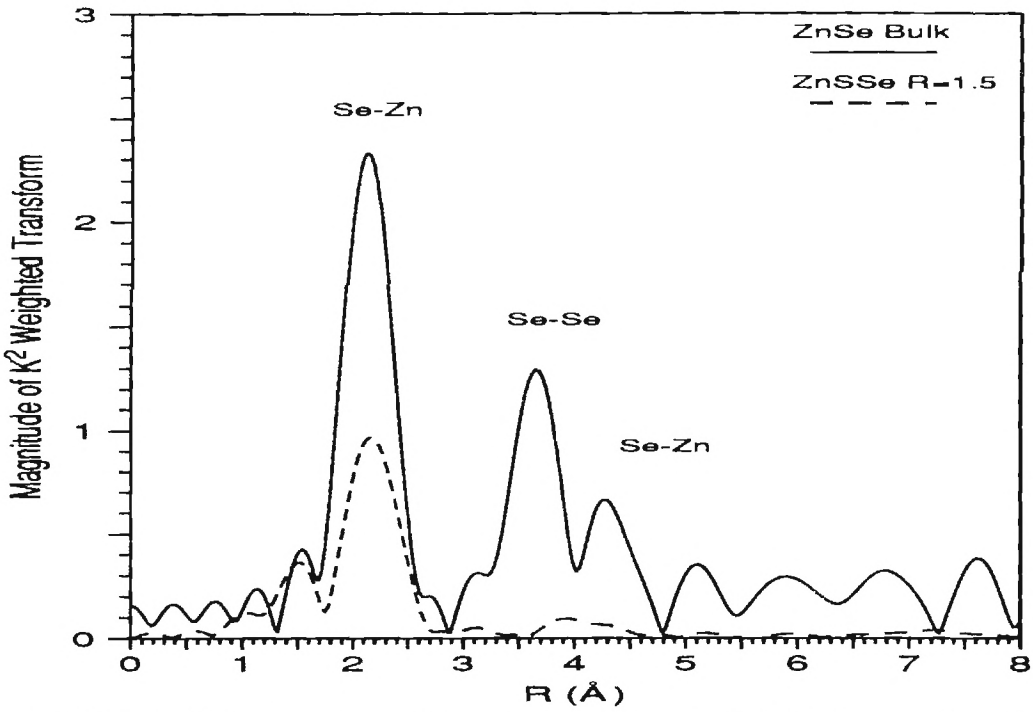

Figure 4.15. Se-Edge transform of benzeneselenol capped ZnS clusters (R=1.5) as compared with ZnSe bulk.

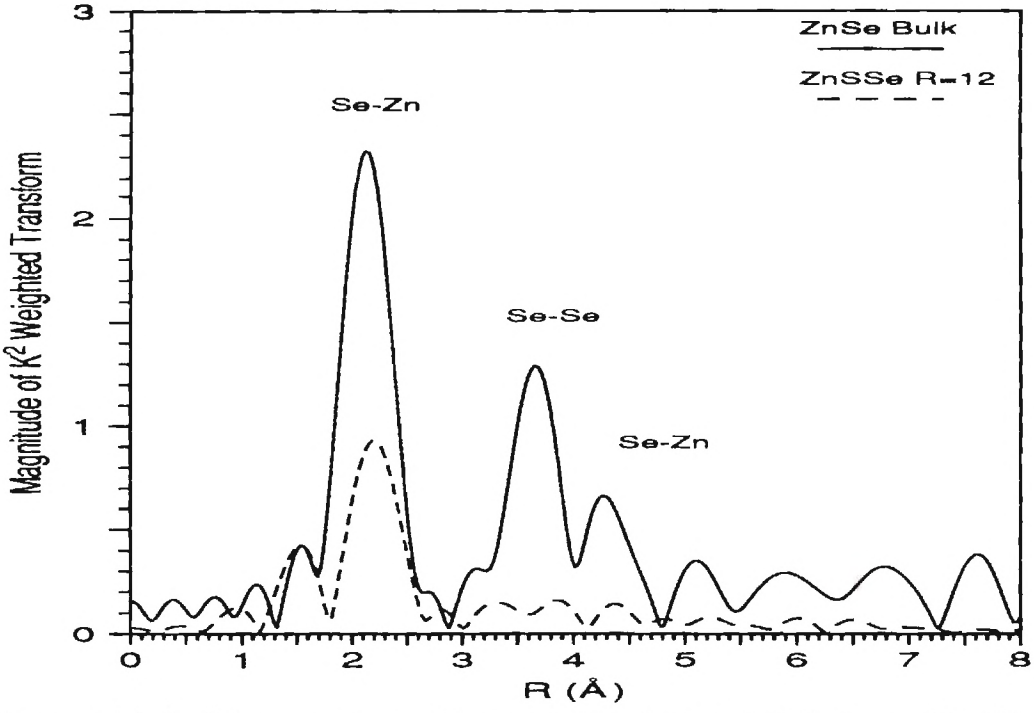

Figure 4.16. Se-Edge transform of benzeneselenol capped ZnS cluster (R=12) as compared with ZnSe bulk.

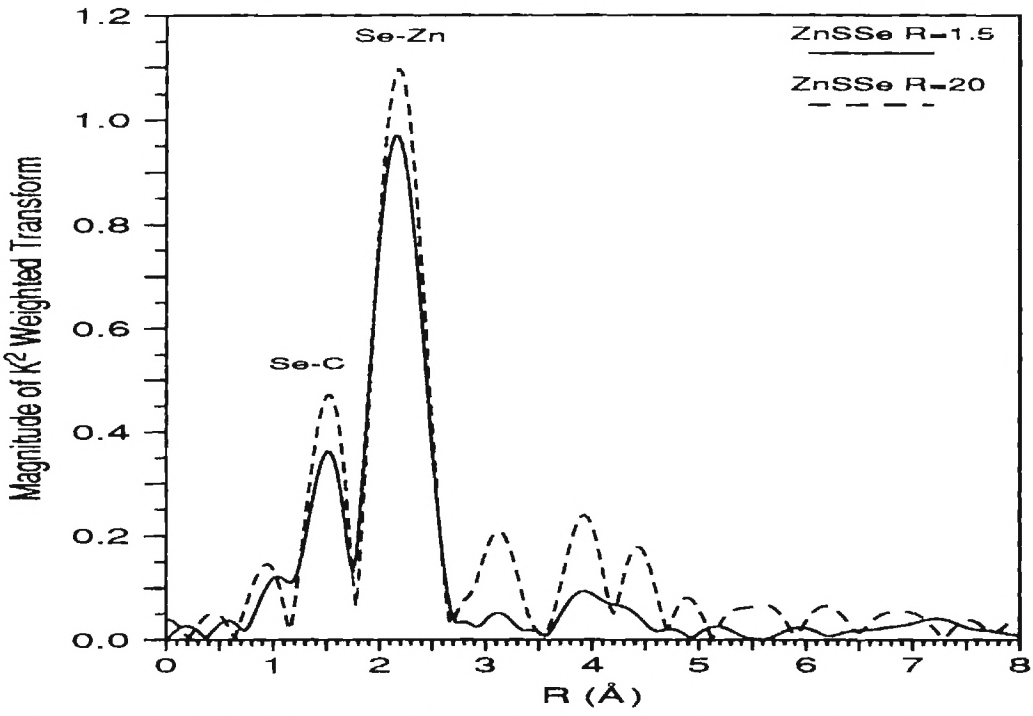

Figure 4.17. Se-Edge transform of benzeneselenol capped ZnS clusters. R=1.5 and R=12

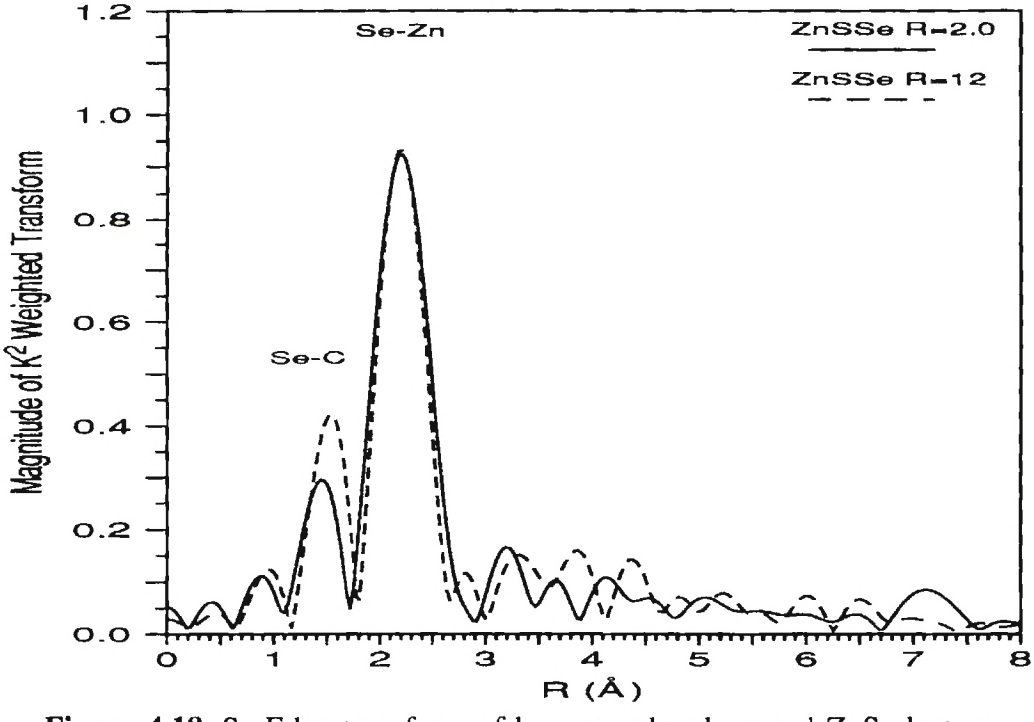

Figure 4.18. Se-Edge transform of benzeneselenol capped ZnS clusters. R=2.0 and R=12

Table 4.25: Se-edge LN_2 (~100 K) XAFS
Se-C First Shell
σ^2ref =0.002

Sample	R	N	$\sigma^2_{ref} - \sigma^2_{sample}$
SeZnS01	1.924 ± 0.002	1.09 ± 0.2	0.00129 ± 0.00015
SeZnS02	1.914 ± 0.003	0.87 ± 0.3	0.00302 ± 0.00041
SeZnS65	1.913 ± 0.006	0.97 ± 0.1	0.00271 ± 0.00015
SeZnS12	1.960 ± 0.004	1.00 ± 0.1	0.00339 ± 0.00005
SeZnS20	1.941 ± 0.002	1.02 ± 0.1	0.00398 ± 0.00010

The Zn-edge transforms of the benzeneselenol capped ZnS cluster are shown in Figs. 4.19-4.21. In Fig. 4.19 the R=1.5 sample's transform is compared with ZnS and ZnSe bulk samples. It is shown that the first shell of the cluster transform for R=1.5 sample is between the Zn-S and Zn-Se which is consistent with the chemical analysis results of Table 4.23 where the fraction of Se is relatively high compared with S. In contrast, the R=20 sample (Fig. 4.20) shows a first peak that almost matches the Zn-S bulk. Again this is consistent with low fraction of Se in the larger clusters relative to the S (Table 4-23). Figure 4.21 shows the transforms for all the samples and indicates that all exhibit essentially the same peak except the R=1.5 sample which has the highest Se fraction. The first shell of each cluster was filtered and fitted with both Zn-S and Zn-Se shells. Comparison of the fit and filtered data are shown in Figs. 4.22-4.25. The results of the fittings are shown in Table 4.26. However, the XAFS is normalized to Zn, and to get the actual average coordination number of S and Se to Zn, the coordination number

found from XAFS should be divided by the mole fraction of S and Se. (from Table 4-23), respectively. The results of this analysis is summarized in Table 4.27.

Table 4.26 : Zn-Edge XAFS First Shell Fitting Results for Benzeneselenol Capped ZnS Clusters

Sample	N1(S)	N(Se)	$\Delta\sigma^2$(S) $Å^2$	$\Delta\sigma^2$ (Se) $Å^2$	R(Zn-S) Å	R(Zn-Se) Å
ZnSSe1.5	2.52	0.81	-0.001	-0.0011	2.350	2.469
ZnSSe2.0	3.38	0.11	-0.0014	-0.0023	2.332	2.446
ZnSSe12	3.61	0.090	-0.00110	-0.0035	2.332	2.446
ZnSSe20	3.57	0.089	-0.00131	-0.0035	2.333	2.446

Table 4.27 : Zn-Edge XAFS First Shell Coordination Numbers for Benzeneselenol Capped ZnS Clusters

Sample	N(Zn-S)	N(Zn-Se)
ZnSSe1.5	3.3	1.7
ZnSSe2.0	3.5	1.5
ZnSSe12	3.7	1.7
ZnSSe20	3.6	2.3

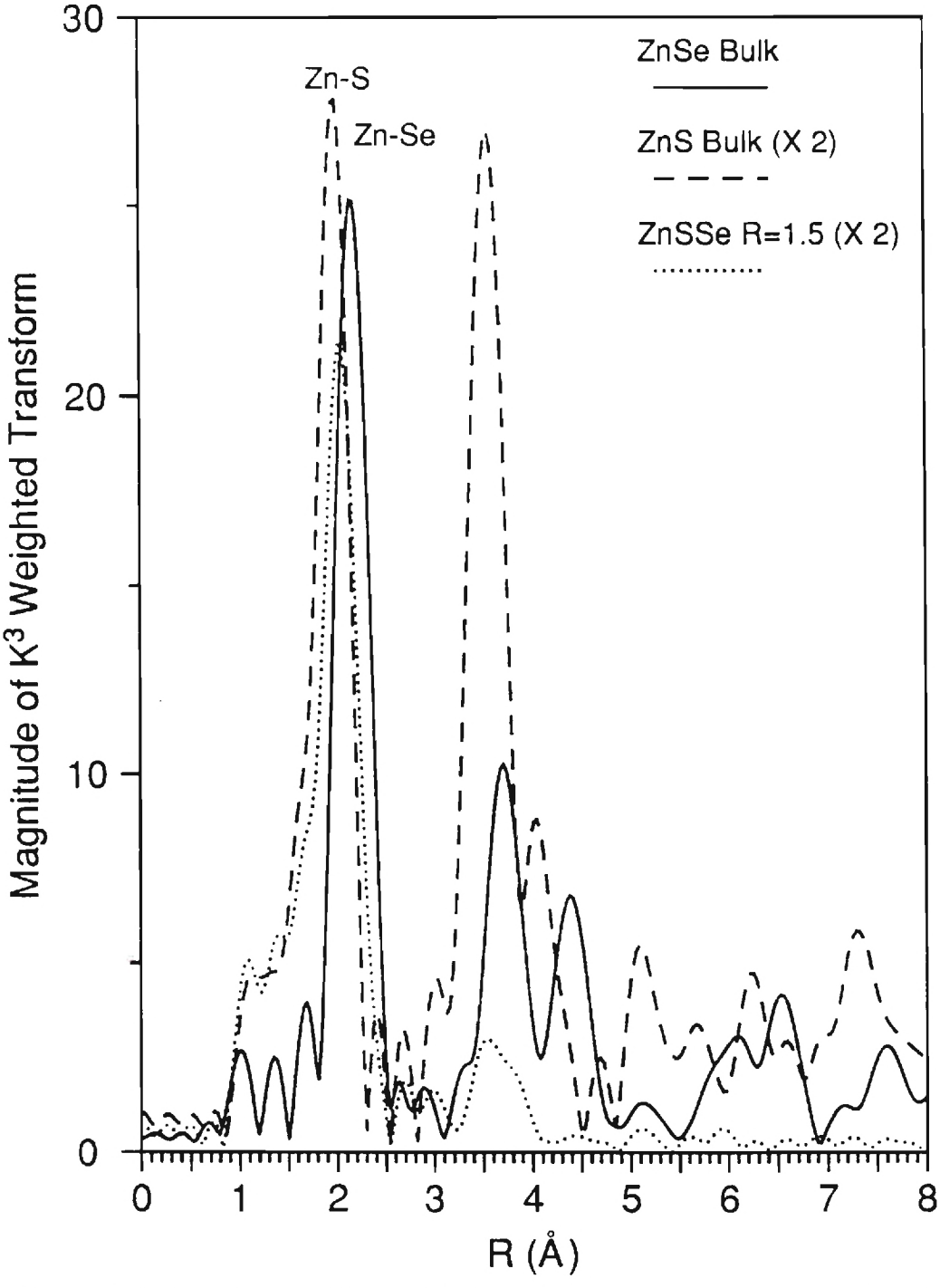

Figure 4.19. Zn-edge transform of ZnSSe R=1.5 as compared with ZnS bulk and ZnSe bulk

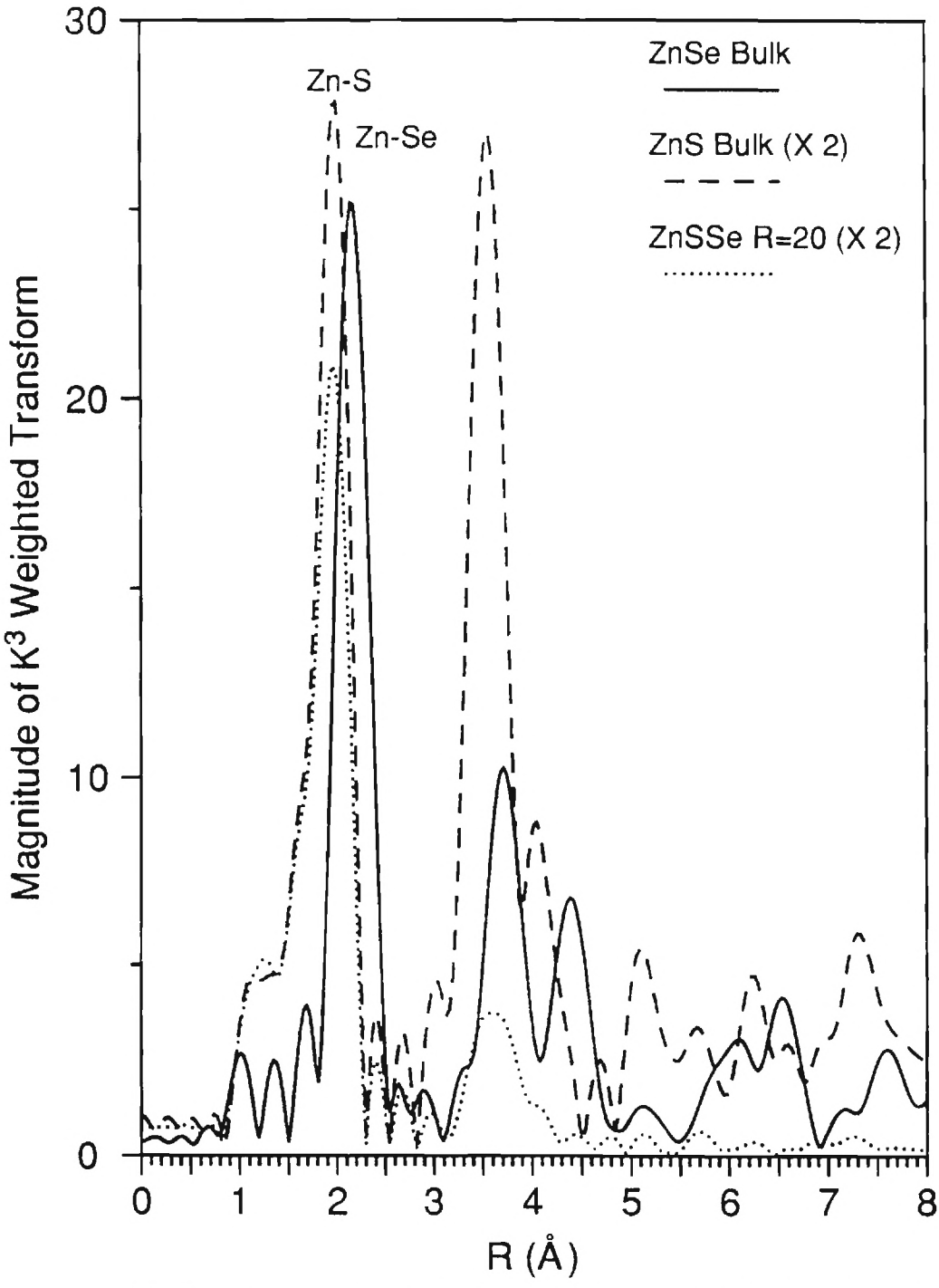

Figure 4.20. Zn-edge transform of ZnSSe R=20 as compared with ZnS bulk and ZnSe bulk

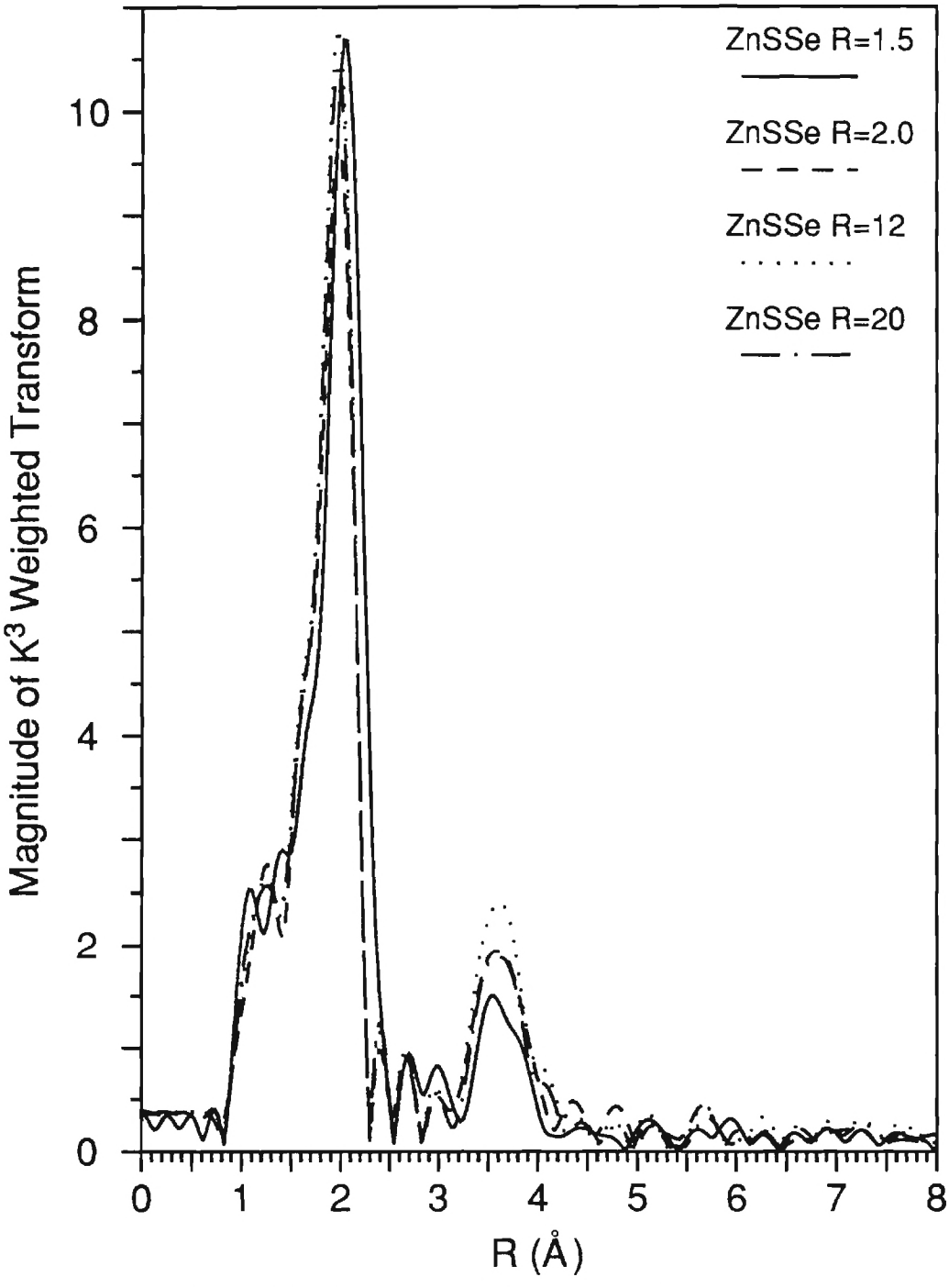

Figure 4.21. Zn-edge transform of ZnSSe samples

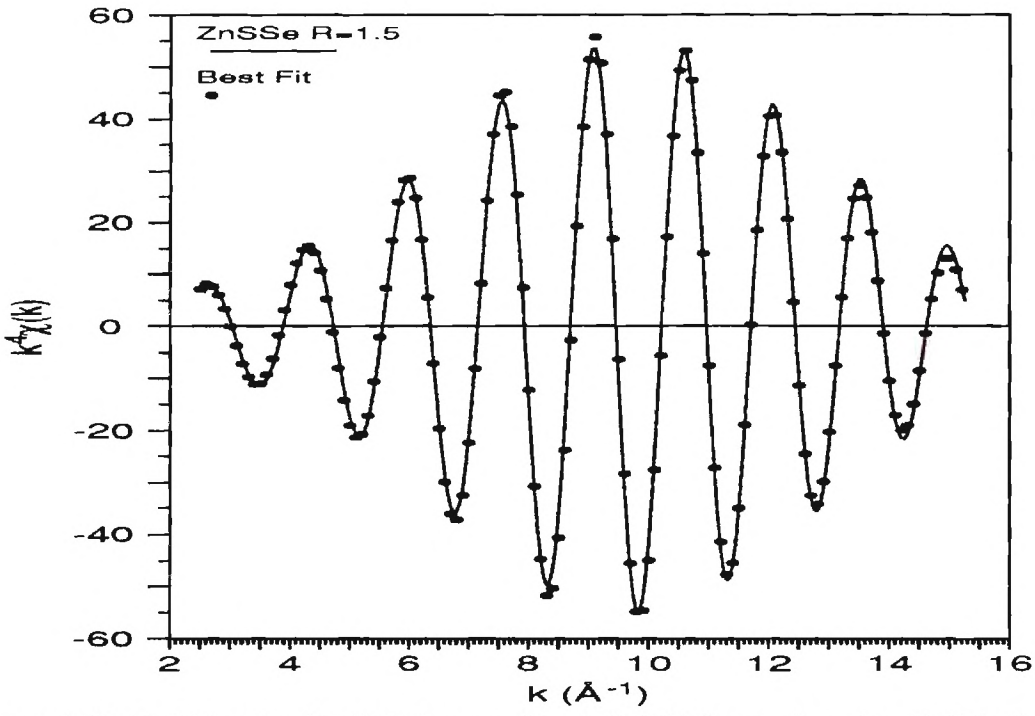

Figure 4.22. Zn-Edge 1st Shell fitting results of ZnSS1.5 sample using ZnS bulk and ZnSe bulk as standards

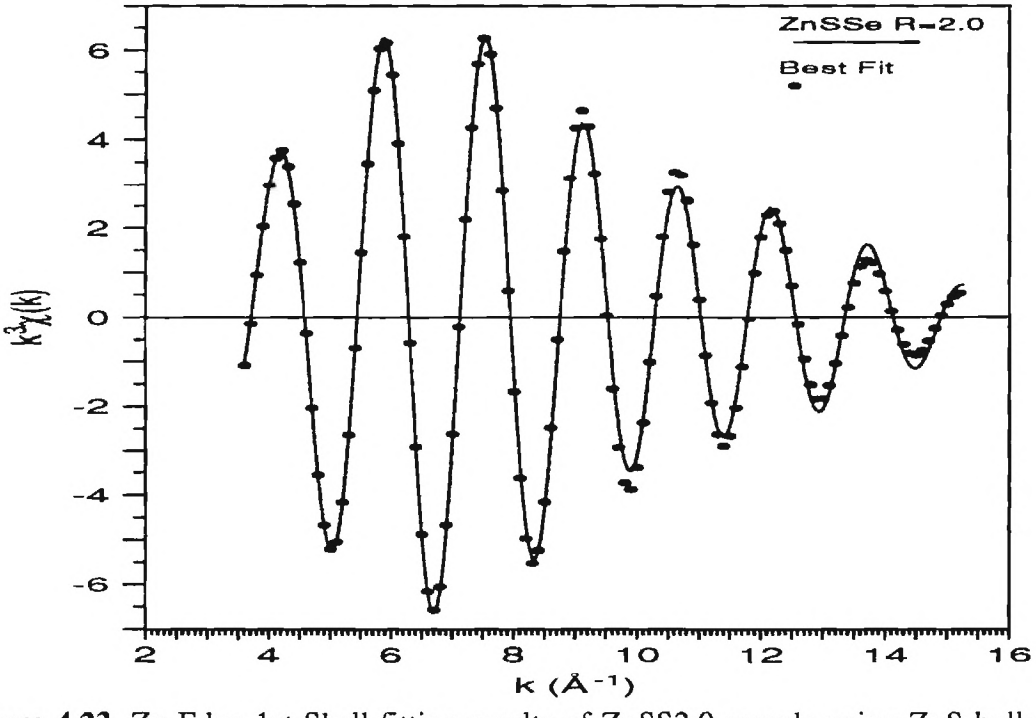

Figure 4.23. Zn-Edge 1st Shell fitting results of ZnSS2.0 sample using ZnS bulk and ZnSe bulk as standards

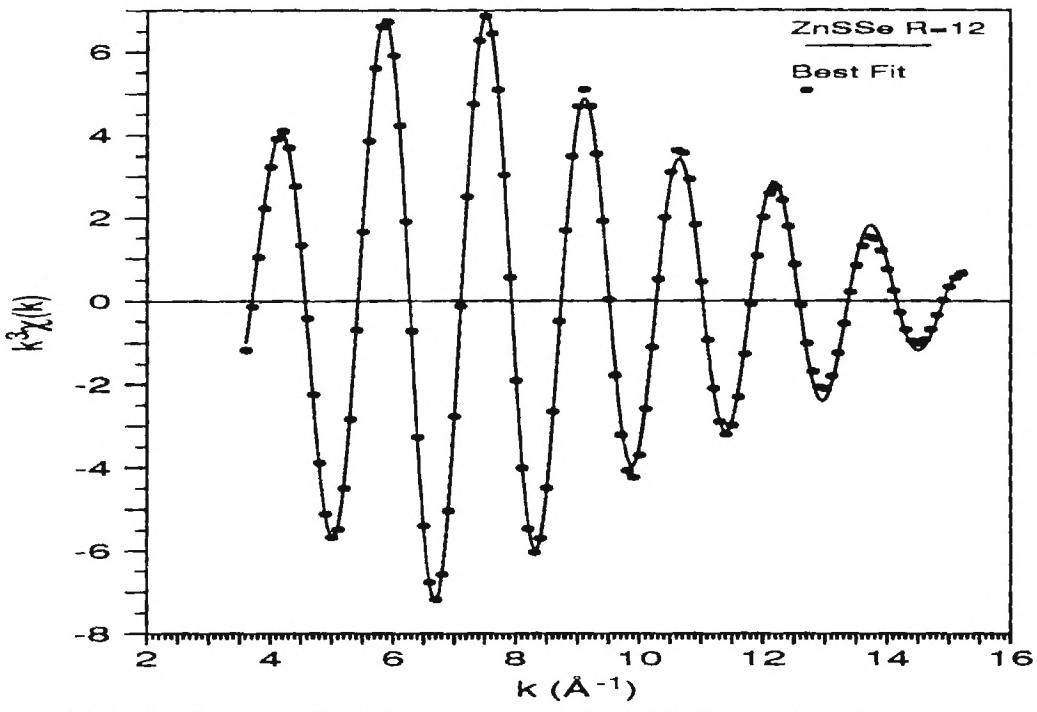

Figure 4.24. Zn-Edge 1st Shell fitting results of ZnSS12 sample using ZnS bulk and ZnSe bulk as standards

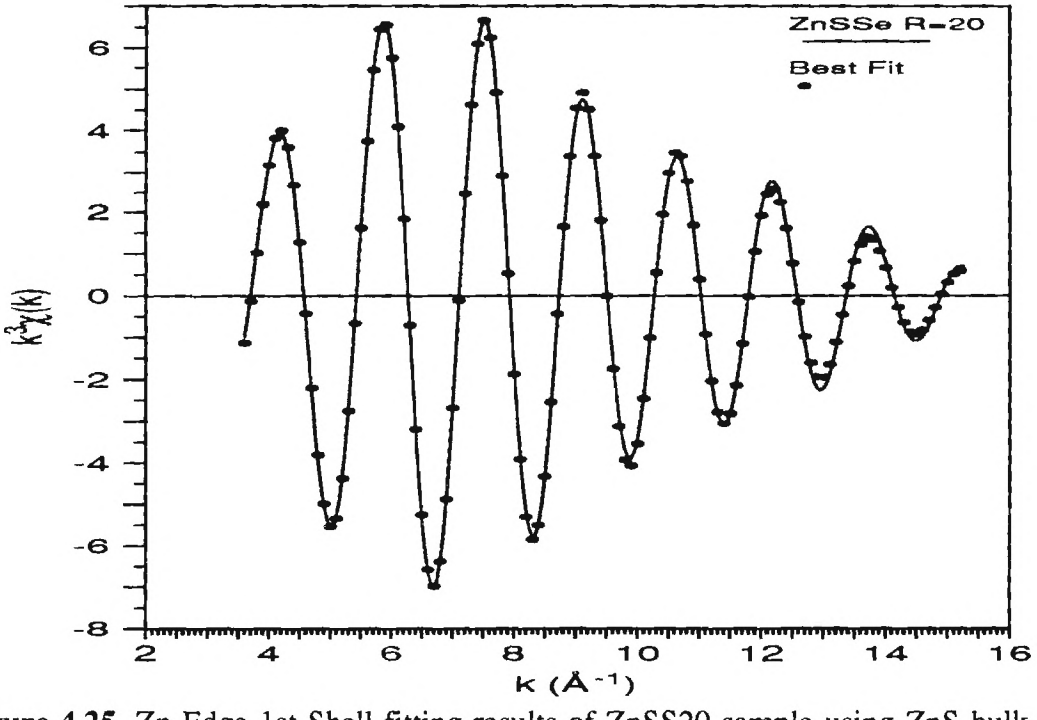

Figure 4.25. Zn-Edge 1st Shell fitting results of ZnSS20 sample using ZnS bulk and ZnSe bulk as standards

2-Ethaneaminothiol Capped ZnS Clusters

These clusters were all prepared using the same ratio (20) of aminothiol to sulfide, however, the pH of the Zn/amine solution was adjusted. The XAFS Zn-edge was obtained only for the sample ZnSAm20 which was prepared at pH=8. The XRD pattern was obtain for all samples. The purpose of the synthesis of these compounds was to investigate the effect of the pH on the cluster size and to use these samples for STM imaging experiments.

XRD Results

The XRD results are summarized in Table 4.28 below and show that the clusters prepared in different acidic solutions (pH of 4.5, and 6.5) did not vary in size. The pH=8.0 sample was the smallest prepared cluster of this group. The pH=12 sample was the largest cluster prepared. Table 4.28 shows that the samples prepared in basic solutions shows bond lengths of about 0.02 Å shorter than the bulk value. The samples prepared in acid solution shows bond length consistent with the bulk samples. Figure 4.23 shows the XRD pattern for the different clusters.

XAFS Results

The XAFS measurement was obtained at beam line X19-A at 90 K in the transmission mode using a Si(220) monochromator. The XAFS transform is shown in figure 4.24, and the usual shells due ZnS are shown. The first and second shells were analyzed using the ratio method and the results of the analysis are displayed in Table 4.29. The XAFS bond length is consistent with XRD. The first and second shell

4.29. The XAFS bond length is consistent with XRD. The first and second shell coordination numbers are reduced from the bulk material as seen in other clusters. Fig. 4.25 shows the fitting of the first shell.

Table 4.28 : ZnSAm20 XRD Results

Sample	2θ	B(2θ)	Diameter (Å)	Lattice size	Zn-S (Å)
ZnSAm20 pH=4.5	28.554	3.4023	32 ± 1	5.410 ± 0.019	2.343 ± 0.008
ZnSAm20 pH=6.5	28.606	3.4141	32 ± 1	5.400 ± 0.018	2.338 ± 0.008
ZnSAm20 pH=8.0	28.788	4.0907	27 ± 1	5.367 ± 0.018	2.324 ± 0.007
ZnSAm20 pH=12	28.866	3.1730	39 ± 2	5.371 ± 0.018	2.326 ± 0.008

Table 4.29 : First and Second Shell Zn-edge XAFS Results of Aminothiol Capped ZnSAm20 (pH=8) Cluster

Shell Number	R (Å)	N	σ^2ref -σ^2sample
Shell #1 Zn-S	2.330 ± 0.002	3.54 ± 0.04	-0.00103 ± 0.00007
Shell #2 Zn-Zn	3.829 ± 0.004	3.82 ± 0.18	-0.00336 ± 0.00018

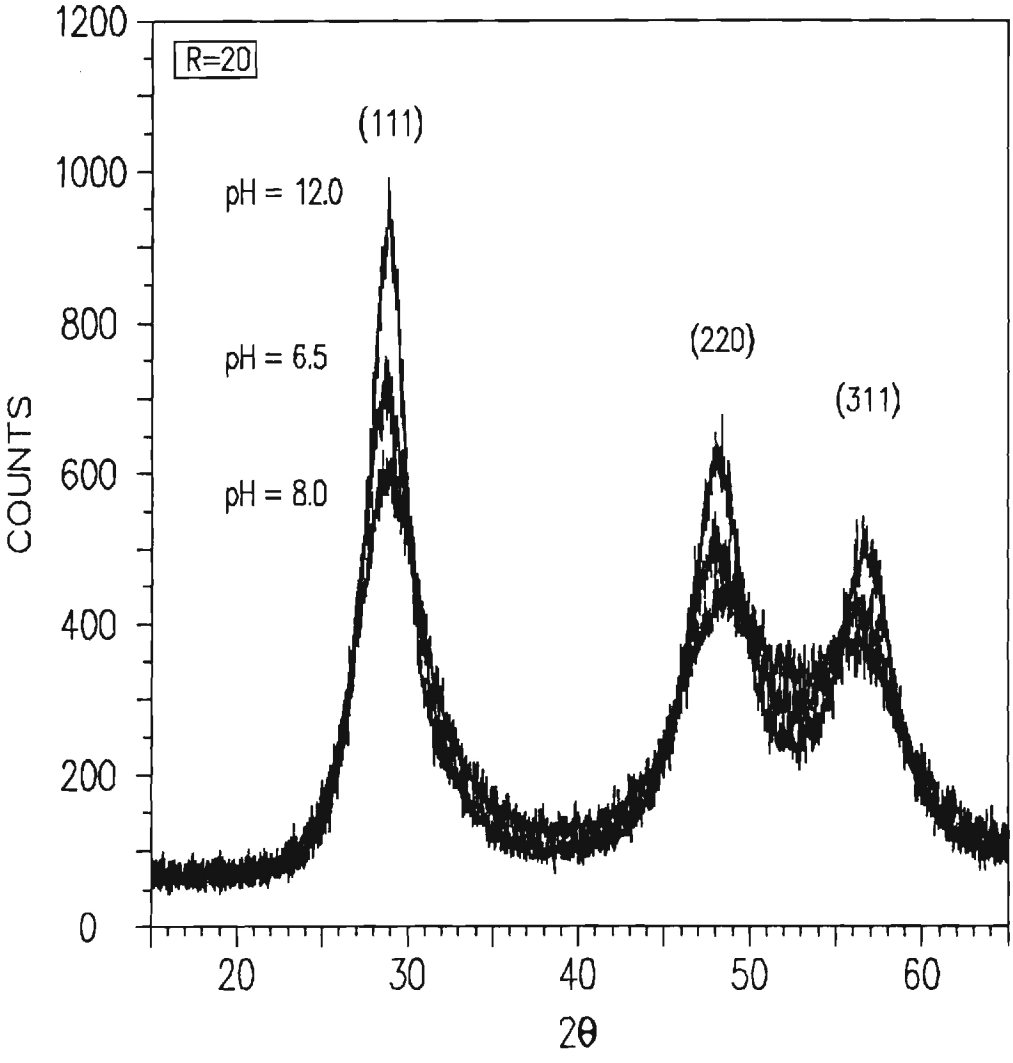

Figure 4.26. XRD of 2-ethaneaminothiol capped ZnS clusters

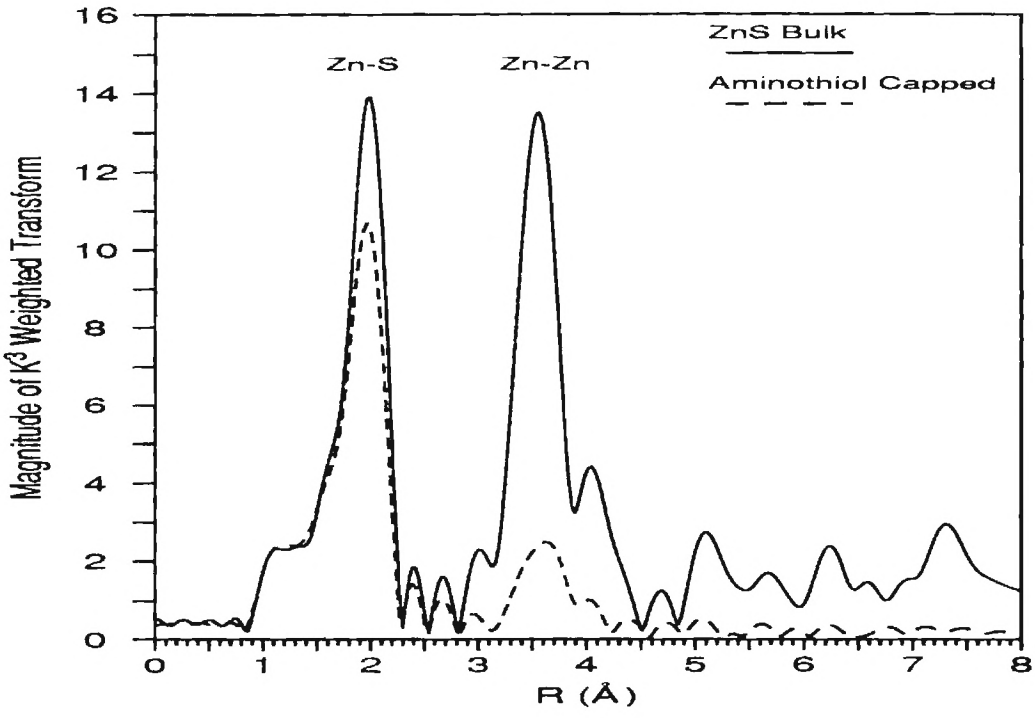

Figure 4.27. Zn-edge XAFS transform of ZnS bulk and ZnSAm20 (pH=8.0) clusters

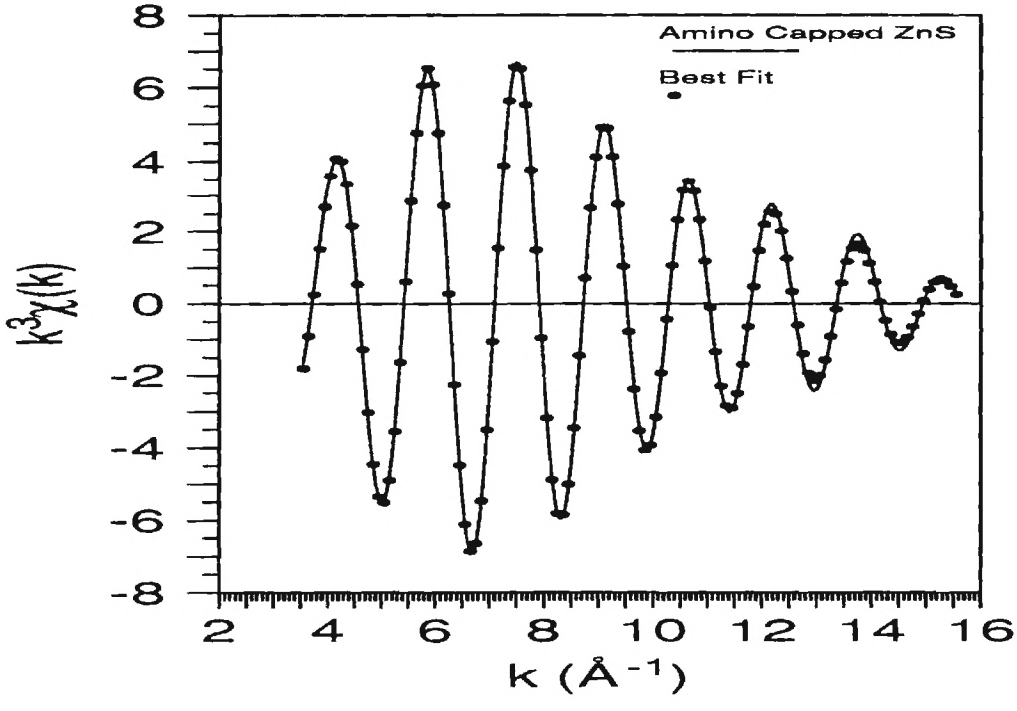

Figure 4.28. Zn-edge first shell fitting of ZnSAm20 (pH=8.0)

ZnS Uncapped Cluster

XRD Results

One sample of ZnS cluster was prepared in water without the addition of any capping group. The XRD was obtained for this sample and the results of the analysis are displayed in Table 4.30.

Table 4.30: XRD Fitting Results of ZnS Uncapped Cluster

Angle (deg)	FWHN (deg)	Diameter (Å)	Lattice Size (Å)	Bond Length (Å)
28.701	3.151	38.5 ± 1.6	5.383 ± 0.018	2.331 ± 0.008

XAFS Results

The XAFS measurements were performed in the same setup as the aminothiol clusters. The transform is shown in Fig. 4.26 and shows a relatively strong second shell. The first and the second shells were analyzed and the results of the analysis are displayed in Table 4.31. The fitting of the first shell is shown in Fig. 4.27. From the XAFS results, it is shown that the second shell is almost half that of the bulk material.

Table 4.31 : First and Second Shell Zn-edge XAFS Results of Uncapped ZnS Clusters

Shell Number	R (Å)	N	$\sigma^2_{ref} - \sigma^2_{sample}$
Shell #1 Zn-S	2.330 ± 0.001	3.66 ± 0.04	-0.00063 ± 0.00007
Shell #2 Zn-Zn	3.817 ± 0.003	5.87 ± 0.12	-0.00296 ± 0.00013

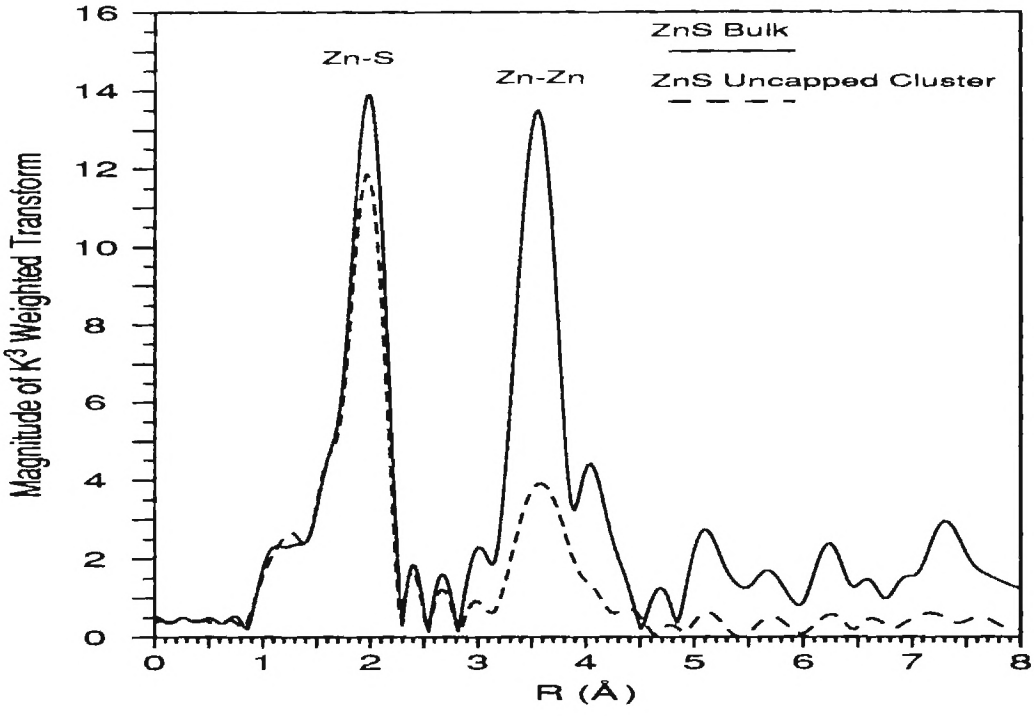

Figure 4.29. Zn-edge XAFS transform of uncapped ZnS cluster

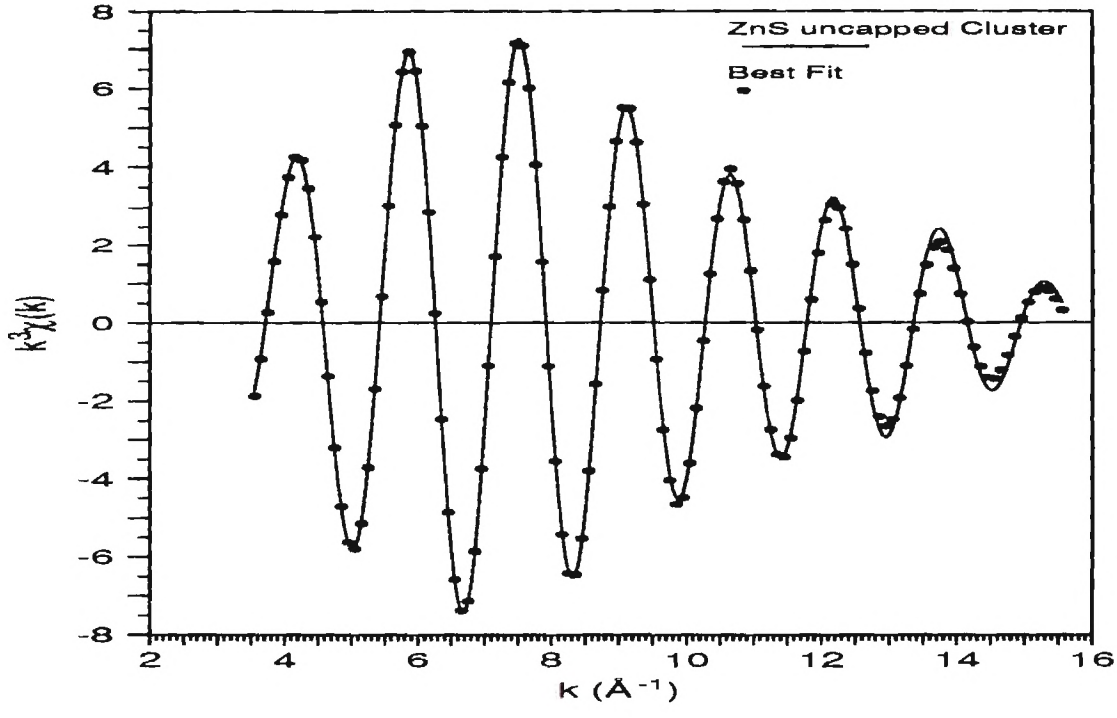

Figure 4.30. Zn-edge first shell fitting of uncapped ZnS cluster

Discussion

The XAFS and the XRD of Nafion grown clusters showed that the synthesized clusters were crystalline ZnS sulfide. This synthesis is, to our knowledge, was the first synthesis of ZnS in Nafion film. Previous methods of synthesizing ZnS by reacting Zn-loaded dry Nafion films with H_2S did not succeed. Water is required to hydrolyze H_2S to $HS^- + H^+$, which may catalyze the reaction. The production of a small amount of ZnS clusters in slightly wet films, and the synthesis of ZnS clusters in aqueous solution supports this hypothesis. Another factor may be the difficulty of breaking the relatively strong Zn-O bond, where the oxygen(s) are provided by the sulfonate of the polymer.

The XAFS analysis did not show any Zn-O shell indicating that the Zn has fully reacted with the sulfide. The coordination number found for this cluster was very small relative to the cluster size, hinting that the shape of the cluster is probably not spherical. This is most probable since the clusters are confined to grow in the cavities of the polymer films, which probably is not spherical and thus leaving a larger number of Zn atoms in the surface causing the coordination number to be smaller. The second shell coordination number is also much smaller than what simulation suggests (~12). These observations made it difficult to learn much about the cluster structure other than to conclude that the clusters in Nafion are probably not spherical or regularly shaped. Another factor for the disagreement of the simulation and the XAFS is that the ZnS clusters in nafion are mostly amorphous. However, the sharp diffraction peaks in the XRD pattern of the Nafion samples are due to the crystalline domain of the clusters.

These complications in studying the Nafion ZnS clusters caused us to focus on different methods of preparing ZnS clusters.

The XAFS of thiophenol, MPA, and benzeneselenol capped clusters showed a first shell coordination number for both the Zn and S edges which agrees remarkably with simulations. The agreement between XAFS and simulation indicates that the clusters that were precipitated from the reaction are spherically shaped. Furthermore, since XAFS coordination numbers agree well with simulated (perfect crystal) clusters that have the same size as found from XRD, then it is possible to conclude that these clusters are mostly crystalline. Note that the XAFS first shell measures the short range order while the XRD samples only the crystalline domain which is long range order. The XAFS second shell however is more sensitive to disorder than the first shell. The thiophenol ZnS clusters second shell XAFS results did not agree with the simulation results. In fact all ZnS prepared samples (for all different capping groups) samples showed a second shell that is very sensitive to the size of the particle. Also from simulation, it was found that the second shell coordination number for a spherical zincblende cluster is linear with size. The second shell coordination numbers of the clusters were compared with simulated values and were also linear. Figure 4.31 shows a plot of Zn second shell coordination number versus the size of the cluster for both thiophenol capped clusters and for MPA capped clusters and simulated clusters. It is noted that all the plots in Fig. 4.31 have

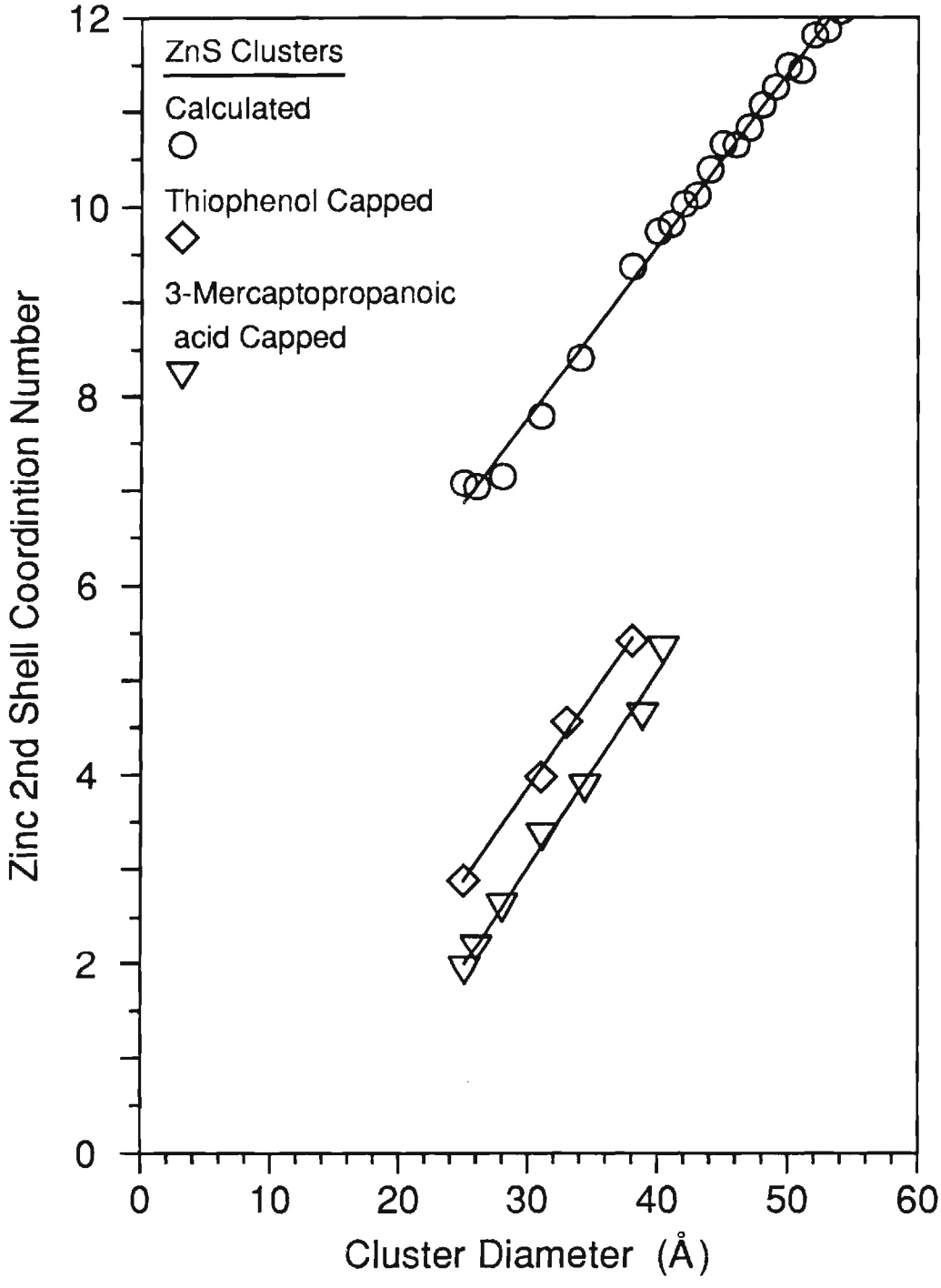

Figure 4.31. Plot of the Zn second shell coordination number in ZnS clusters as compared with calculated values.

the similar slope (~0.2). The intercepts of the experimental clusters are lower. The fact that the experimental and simulated clusters have similar slopes suggests that the clusters are spherical. But why do the intercepts different? Before attempting to answer this question, note that the larger the experimental intercept, the closer the experimental clusters are to the simulated clusters. Thus the intercept of this graph is an indicative of the degree of crystallinity as "seen" by the XAFS and in turn implies the existence of a disordered domain in the clusters. This may appear to be contradictory to the conclusion of the first shell results that the clusters are mostly crystalline. To resolve this apparent contradiction, note that the effect of disorder in XAFS and on XRD is not the same. The XAFS disorder is related to the motion of the scattering atoms relative to the central (absorbing) atom. The XRD disorder is related to structural defects and stacking faults in the unit cell of the crystal. The XAFS Debye-Waller factor of the disordered domain can be large enough that the XAFS signal vanishes or is greatly reduced while such disorder will not affect the XRD. Furthermore, since the disorder is only exhibited by the second shell, and not by the first shell, this suggests a structural model for the clusters in which the clusters are made of two layers or phases one of which appears disordered in the XAFS second shell. The suggested model assumes that one phase that constitutes the core of the cluster is crystalline and resembles very much the bulk material; the second layer is the outer layer, and it is disordered (Fig. 4.32).

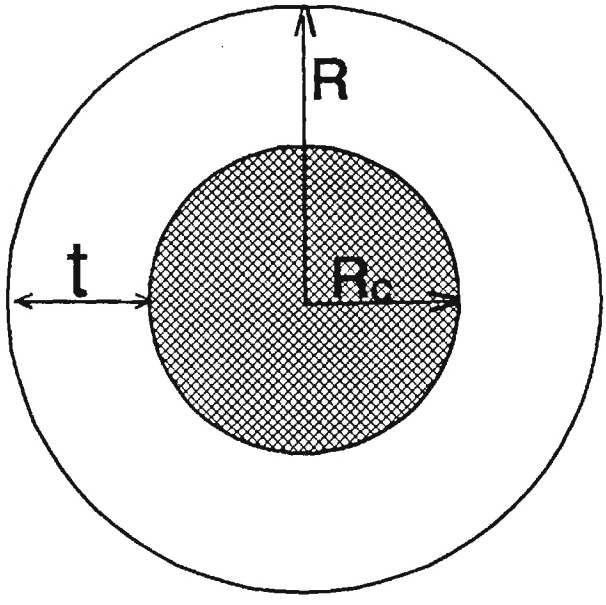

Figure 4.32. Spherical ZnS clusters with ordered shell of radius R_c and disordered shell of width t

The above model will be used to calculate the thickness of the disordered spherical shell which gives rise to the reduction in the second shell XAFS coordination number. In a naive way, one would look up in the simulation Table the diameter of the cluster that gives similar second shell coordination number and thus calculate the thickness of the disordered shell. The problem with this approach is that the XAFS coordination number of Zn is normalized to the total Zn in the cluster. Since the Zn in the outer, disordered shell is assumed not to contribute to the second shell, then the coordination number will be zero. To account for this difficulty, the fraction of zinc atom in the crystalline portion to the total Zn atoms in the sphere can be calculated by using the fraction of the volume of the crystalline sphere to that of the total sphere. This ratio is then multiplied with the coordination number of the inner sphere to give the second shell coordination as measured by XAFS. Therefore, the method of calculation consists of first guessing the radius of the crystalline sphere then using that radius to calculate the volume fraction of the crystalline sphere. The coordination number of this sphere then is obtained from simulation. This procedure is then iterated until the product of the volume fraction with the second shell gives the experimental second shell. The following equations describe the above procedure,

$$N(Zn) = \frac{4}{3}\pi R^3 n' \tag{4.3}$$

$$N_C(Zn) = \frac{4}{3}\pi R_C^3 n' \tag{4.4}$$

$$f(R,R_C) = \frac{N_C(Zn)}{N(Zn)} = \frac{R_C^3}{R^3} \quad (4.5)$$

$$N_2 = f(R,R_C)\ x\ N_2(R_C) \quad (4.6)$$

where n' is the number density of Zn atoms, $f(R,R_c)$ is the fraction of Zn atoms in the crystalline sphere of radius R_c, R is the radius of the cluster, N(Zn) and $N_C(Zn)$ are the numbers of Zn atoms in the total sphere and the crystalline spherical portion, respectively. $N_2(R_C)$ is the second shell coordination number of a sphere with radius of R_C and is obtained from simulation, and N_2 is the calculated XAFS second shell coordination number due to the crystalline portion of the cluster. From Eq. (4.6) it is possible to calculate the thickness of the disordered shell of the cluster, t, from the difference in R and R_c. Tables 4.32, and 4.33 list of the calculations for all samples of thiophenol and MPA capped ZnS clusters, respectively. As can be seen from Table 4.32, the calculated crystalline sizes for thiophenol increase with increase in the total size of the cluster, but the thickness of the disordered shell, t, remains relatively constant (Avg 2.6 Å). The MPA capped ZnS clusters shows similar results, but the thickness of the disordered shell is shown to decrease with increase in the cluster size. These results suggest that the thiophenol clusters are more crystalline than the MPA capped clusters, and that in the MPA capped clusters the crystalline fraction increases with size. Thus the disorder may depend on the nature of the capping group.

Table 4.32
Calculation of The Disordered Layer Thickness in Thiophenol Capped ZnS Clusters

$N_{XAFS}(R)$	$N_{Calc}(R)$	2R (Å)	$2R_C$ (Å)	$f(R,R_C)$	t (Å)
2.88	2.83	22.5	17.6	0.48	2.5
3.98	3.95	27.9	23.4	0.59	2.3
4.56	4.58	29.7	25.8	0.66	1.95
5.42	5.43	34.2	30.2	0.69	2.0

Table 4.33
Calculation of The Disordered Layer Thickness in 3-Mercaptopropanoic Acid Capped ZnS Clusters

$N_{XAFS}(R)$	$N_{Calc}(R)$	2R (Å)	$2R_C$ (Å)	$f(R,R_C)$	t (Å)
1.95	1.92	22.6	16.4	0.38	3.1
2.19	2.15	23.4	17.0	0.38	3.2
2.62	2.56	25.2	19.0	0.43	3.1
3.36	3.40	28.0	22.6	0.52	2.7
3.88	3.86	31.0	25.3	0.54	2.9
4.64	4.61	34.6	29.3	0.61	2.7
5.34	5.32	36.4	31.8	0.67	2.3

In the above discussion, the second shell XAFS coordination number was assumed to originate only from the crystalline fraction of the cluster. It may be the case that the noncrystalline fraction does contribute slightly to the second shell. In this case, the reported value for the noncrystalline thickness would be a lower bound to the actual noncrystalline thickness. To further refine this model and to better estimate the thickness,

the disordered shell thickness t was modelled as a linear or quadratic function of R, and quadratic with a contribution from the disordered layer. A best fit of the experimental values was found for each model for the MPA capped ZnS clusters, and the results are summarized in Table 4.34. These results suggest that the thickness of the disordered shell is best described as a quadratic function. The second shell contribution (1.15) from the disordered layer improved the results of the fit and increased the thickness of the disordered layer.

Table 4.34
Calculation of The Disordered Layer Thickness in 3-Mercaptopropanoic Acid Capped ZnS Clusters Employing Different Models (σ=0.1)

Diameter (Å)	t(linear) (Å)	t(quadratic) (Å)	t(quadratic)+ $N_{disordered}$ (Å)
22.6	3.29	3.15	4.11
23.4	3.23	3.00	4.00
25.2	3.10	2.99	3.79
28.0	2.89	2.82	3.48
31.0	2.67	2.66	3.19
34.6	2.40	2.48	2.91
36.4	2.26	2.40	2.81
	χ^2=30 t(R)=4.98-0.1487R	χ^2=16.3 t(R)=4.96-0.193R+2.8610^{-3} R^2	χ^2=10.25, $N_{disordered}$=1.15 t(R)=8.47-0.508R+0.01083R^2

The reduction of the second shell coordination number for ZnS cluster that was prepared in water without the addition of any capping group was modeled using Eq. (4.6). The thickness of the disordered shell was calculated to be ~2 Å. A similar number was found for the aminothiol capped ZnS. These numbers are similar for what was found for

thiophenol clusters (2.2 Å) and are on the order of a Zn-S bond length. In the MPA ZnS clusters, the thickness is also in the order of a Zn-S distance.

So far, the origin of the reduction of the XAFS second shell is explained in the basis of the existence of a noncrystalline layer. The first shell coordination numbers as found for Zn-edge and S-edge were not affected by existence of the disordered shell. For the first shell coordination number to be reduced due to a relatively large disorder, the root mean squared variation in the Zn-S bond has to be large. The second shell disorder depends on the second moment of the Zn-Zn distance distribution. The Zn-Zn distance variation can be affected by a bond angle variation in the Zn-S-Zn bond angle. The bond angle variation due to bending will affect only the second shell bond length but not the first shell distance; thus the first shell contribution to the XAFS signal will not be affected by a bond angle variation, but the second shell will. The model accounts for the observed XAFS results for the first and second shell as a function of the size of the cluster.

To answer the question, how does the capping group affect the disorder in the surface, the bonding of the capping group to the surface of the cluster needs to be addressed. Also, the question of coverage of the clusters with the capping group as a function of the size needs to be understood. These two points hopefully will clarify the affect of the capping group on disorder of the outer shell of the cluster.

The capping thiol can be bonded to zinc in two different ways (Fig. 4.34). The first bonding scheme is to be terminally bonded to a single Zn. The second possibility is to bridge between two Zn atoms on the cluster's surface. The XAFS results for the thiophenol capped clusters and the benzeneselenol capped clusters combined with the

chemical analysis clearly distinguished between the two bonding schemes. To begin, the Se-edge results of Table 4.24 showed that the capping group is bonded to two Zn atoms and one C atom of the phenyl group. Furthermore, the Zn-edge results of the benzeneselenol capped clusters (Table 4.27) further complemented the results of Se-edge data by showing that the Se which is bonded to Zn has two Zn-Se bonds per Se. Thus strong evidence, from both the Se-edge and Zn-edge results, confirms Se is primarily a bridging ligand between two Zn atoms at the surface of the cluster.

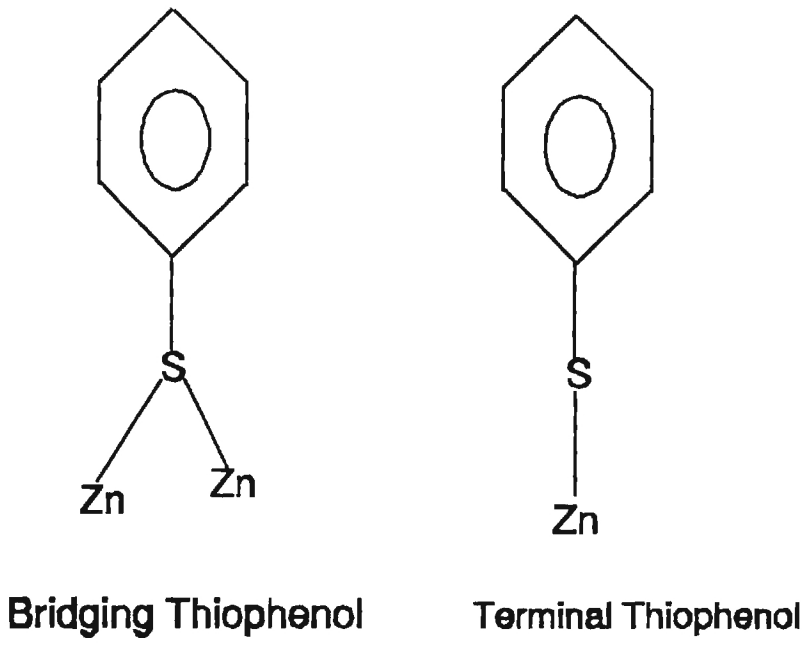

Figure 4.33. The two possibilities of thiophenol bonding to the surface of the cluster

In the case of thiophenol capped ZnS clusters, it is not possible to measure directly the XAFS of the thiol S-edge and the XAFS yields the total S-edge XAFS coordination number. However, the combination of the chemical analysis and S-edge or Zn-edge results allowed the distinction between terminal and bridging thiophenol. The total S first-shell coordination number N will depend on the coordination of thiophenol and the coordination of the sulfide S in the cluster. This coordination will depend on the mole fraction of each in the cluster as shown in the following equations,

$$N = aX + b(1-X) , \tag{4.7}$$

which is rearranged to

$$N = (a-b)X + b , \tag{4.8}$$

where a is the coordination number of S^{2-} to Zn and b is the coordination number of PhS^- to Zn. A plot of sulfur coordination number versus the mole fraction of S^{-2} will give as an intercept the average coordination of the thiophenol to zinc in the cluster. The slope of such plot will be the difference in the average coordination numbers of the sulfide and the thiophenol, respectively. From the slope and the intercept, an estimate of the coordination number of sulfide in the cluster would be obtained.

Plotting the experimental sulfur first shell coordination number versus the sulfide mole ratio of sulfide to total sulfur gave a linear plot as shown in Fig. 4.34. From the model, the intercept 1.93 ± 0.53 gives the average coordination number of thiophenol in the cluster. Thus, the thiophenol bonding in the cluster is mostly bridging between two zincs rather than being terminally bonded. The estimated coordination of sulfide in the

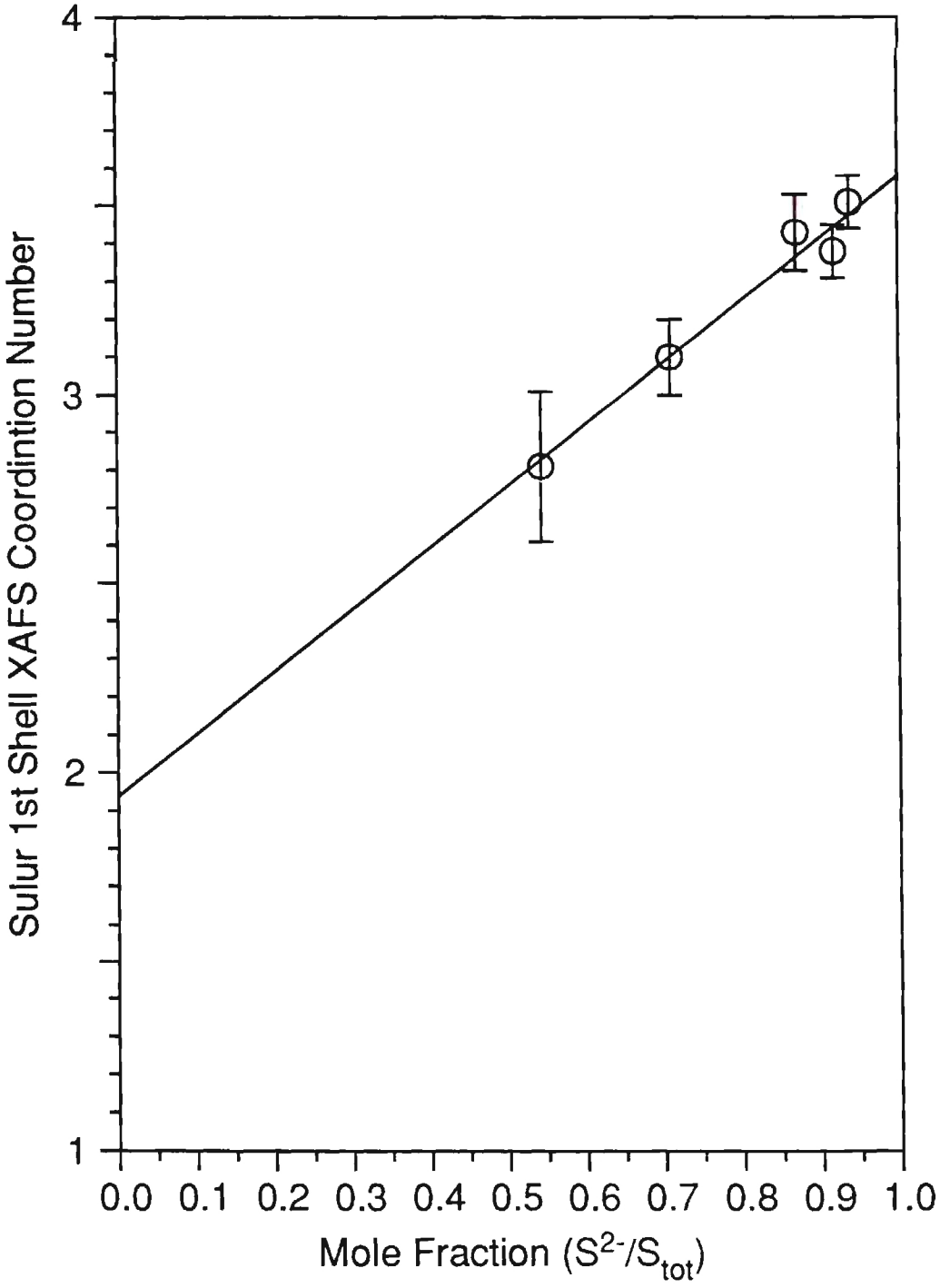

Figure 4.34. Plot of S-edge coordination number versus mol fraction of (sulfide)/(total sulfur)

cluster is 3.57 ± 0.74 as obtained from the slope, 1.64 ± 0.51, and indicates that the coordination number of sulfide in the cluster is less than its four-fold coordination in the bulk, which means that some of the sulfide in the clusters are not completely coordinated with Zn which is expected for surface atoms. The error bars quoted were calculated from the joint error in the slope and intercept for confidence level of 1 σ. A similar plot can be obtained by using the sulfur coordination number from the Zn-edge analysis as was shown in Table 4.16. Using the same model as above, the slope was found to be 1.25 ± 0.31) and the intercept was found to be (2.34 ± 0.27). Again, an intercept of ~2 gives the coordination number of thiophenol. The combination of slope and intercept gave an estimate of sulfide coordination number of 3.59 ± 0.41. Thus, by examining the S-edge and the Zn-edge results, it is shown that the thiophenol is primarily a bridging ligand between two Zn atom in the surface of the cluster. Combining the Zn-edge and S-edge results gives 2.14 ± 0.30 for the coordination of thiophenol with Zn and 3.58 ± 0.42 for the coordination number of sulfide with Zn. The later value was assumed to be constant; this assumption is examined below.

It is clear from the above discussion that the ZnS clusters capped with thiophenol and benzeneselenol have the capping groups mostly in bridging positions. Having established this result, we turn to investigate the question of coverage of the surface of the clusters. In the case of thiophenol capped ZnS clusters, the chemical analysis showed that the amount of thiophenol decreases with size in a manner consistent with the synthesis conditions. Furthermore, with the aid of simulation, it is possible to estimate the number of thiophenol on the surface. For example, the ZnS1 sample which has a

diameter of ~18 Å will have from simulation 92 S atoms and 80 Zn (minimum of 36 of which are on the surface) atoms. Thus, since this sample has a mole ratio of 0.457 mole thiophenol to one mole sulfur, then the estimated number of thiophenol will be 42 atoms of thiophenol per cluster (alternatively, a similar number can be calculated from PhS/Zn mol ratio and number of Zn atoms, 42 for this sample). Furthermore, since a minimum of 36 atoms of Zn are on the surface, then each Zn will also be bonded to 2 thiophenols. Thus, the smallest cluster has all the surface Zn capped with thiophenol. The results of similar calculations for the rest of the thiophenol clusters are shown in Table 4.35 below.

Table 4.35: Calculation of Number of Thiophenol Capping Molecules on The Surface of ZnS Clusters

Sample	D(Å)[a]	#S	#Zn	#PhS[b]	$\#Zn_{surface}$ (min)	$PhS/Zn_{surface}$ (max)
$ZnS_{0.63}SPh_{0.53}$	18	92	80	42,42	36	1.17
$ZnS_{0.78}SPh_{0.32}$	23	164	152	48,49	60	0.81
$ZnS_{0.87}SPh_{0.13}$	29	298	312	39,41	120	0.33
$ZnS_{0.93}SPh_{0.082}$	31	370	420	30,34	168	0.20
$ZnS_{0.88}SPh_{0.058}$	33	490	480	30,28	136	0.21

a) Adjusted by ±1 Å to best agreement with XAFS numbers.
b) The first number was calculated from PhS^-/S_{tot} mol ratio. The second number was calculated from PhS^-/Zn mol ratio.

The striking results displayed in the above table suggest that the number of thiophenol capping atoms does not vary significantly with different cluster sizes but the the number of Zn surface atoms increases with size. Thus the coverage of the surface ranges from greater than 100% to 20% percent and decreases with increase in size.

Using the results of Table 4.35 and the simulated coordination number, the coordination number of sulfide was calculated assuming the thiophenol coordination number is 2.0 as found earlier. The calculations showed that the coordination number of sulfide to Zn for the cluster sizes of Table 4.35 are as follows: 4.0, 3.80, 3.82, 3.93, and 3.7. The average is 3.85 ± 0.17 which compares favorably with the experimental value of 3.59 ± 0.41. Therefore, the coordination number of sulfide to zinc as was obtained from Eq. (4.8) is an average value for the five clusters.

How do these results relate to the conclusion that the disordered shell thickness is relatively constant in the ZnS thiophenol clusters? As was found earlier, the disordered shell is about 2.2 Å which means that all Zn that are in the disordered shell are surface Zn atoms. So it seems that the fraction of surface Zn atoms that is bonded to the capping group is not only factor that affects the width of the disordered shell, but also the number of thiophenol atoms that are on the surface. The smallest ZnS thiophenols cluster (R=1) is shown to be completely covered with thiophenol and the second shell to be unmeasurable in XAFS. Thus the number of thiophenol in the cluster affect seems to be the primary factor in the determining the width of the disordered crystal shell.

For the aminothiol cluster (pH=8 sample), the disordered layer thickness was found to be similar to that of the thiophenol clusters. Also the same number for the disordered shell was found for the cluster that was prepared without adding any capping group. Indeed this cluster must be capped with either solvent molecules and/or the acetate ions from the zinc acetate. Although the XAFS did not show Zn-O shell, it does not follow that the surface does not contain Zn-O, but it may suggest that the Zn-O

bonds fraction is too small to be measured in XAFS. In light of these results, the fact that the MPA capped ZnS clusters have a larger disordered shell could be due to relatively high coverage of the clusters with capping group. However other factors may have caused the MPA capped ZnS clusters to have relatively larger noncrystalline shell. For the thiophenol and MPA clusters, the two type of clusters were prepared in different solvents: Water for MPA capped clusters, and methanol/water for the thiophenol clusters. It also could be that the growth kinetics of the clusters is dependant upon the capping group and the solvent system, and thus the nucleation growth for the two clusters is different. This may be supported by the fact that it required lower ratios of RSH/S^{2-} for the MPA capped ZnS clusters to obtain the same size as that of thiophenol capped clusters. This suggests that the reaction rate of the MPA capping groups is slower than the reaction rate of thiophenols. Thus MPA capping group will stop the growth of the cluster after the size has grown larger than the thiophenol. The reason for this could be due to the possibility of the capping group being tied in an acid-base equilibrium with the HS^- and S^{2-} and the solvent, making it less available for reaction with the cluster surface. This rate of reaction may affect the growth of the cluster causing it to be more disordered. Additionaly, the synthesis of MPA clusters in methanol/water solution did not produce sizes larger than 26 Å. However, when the samples were synthesized in water, larger clusters were produced. The solubility of the cluster in water may have been the factor since the cluster could have grown in solutions until it grew large enough to precipitate, resulting in a larger average cluster product. All these factors will affect the order or the disorder of the cluster.

For the benzeneselenol clusters, it was mentioned that varying the $PhSe/S^{2-}$ in a manner similar to that used in the thiophenol *synthesis produced only* two different sizes, in contrast to the thiophenol capped clusters. Thus the growth of the clusters seems to depend not only on the solution system but also on the capping group itself. In this case the surface bonds, Zn-SePh-Zn, are much different from the core Zn-S bonds. However in thiophenol clusters, the surface bonds, Zn-SPh-Zn, are similar to the bulk atom bonds.

For the benzeneselenol capped clusters, it has been shown already that the capping group is a bridging ligand between two clusters. It remains therefore to address the issue of surface coverage of the clusters. The combination of chemical analysis and Zn-edge analysis can be shown to give direct information about the surface coverage on the surface. Using information given in Table 4.24, it is possible to calculate the fraction of Zn that is bonded to benzeneselenol. For example, the ZnSSe12 sample has an average cluster size of 27 Å and $PhSe/(PhSe+S^{2-})$ ratio of 0.053. From simulation, the cluster will have 276 Zn atoms of which 124 are at the surface, and a total of 336 atoms of PhSe and S, and the number of PhSe atoms on the surface is 18 atoms. Since the surface Zn numbers 124 (minimum) atoms , then the surface Zn is ~15% (maximum) capped, similar to the ZnS clusters. Similar calculations can be done to the rest of the benzeneselenol capped clusters. The results of these calculation are shown in the Table 4.36 bellow.

Table 4.36: Calculation of Number of Benzeneselenol Capping Molecules on The Surface of ZnS Clusters

Sample	D (Å)	#(S+PhSe)	#Zn	#PhSe	$\#Zn_{surface}$ (Min)	$PhSe/Zn_{surface}$ (max)
$ZnS_{0.762}SePh_{0.477}$	23	164	152	63,72	60	1.1
$ZnS_{0.962}SePh_{0.076}$	23	164	152	12,12	60	0.20
$ZnS_{0.973}SePh_{0.054}$	27	336	276	18,15	124	0.14
$ZnS_{0.981}SePh_{0.037}$	27	336	276	12,10	124	0.09

The results for benzeneselenol are similar to results found for thiophenol capped clusters (Table. 4.35), namely, the number of capping group is relatively constant for all the clusters. The striking difference between these clusters and the thiophenol clusters is that a thiophenol cluster has about twice the number of capping groups as those of a benzeneselenol cluster of the same size. This may explain why the size of the benzeneselenol clusters did not change significantly with change with the mol ratio of PhSe/S as reagents as found for thiophenol clusters. Thus capping the ZnS clusters with benzeneselenol is less favorable than capping with thiophenol. This is not very surprising since the Zn-Se bond length (2.45 Å) is larger (weaker) than the Zn-S bond (2.34 Å). On the other hand, the thiophenol S-Zn bridging bond (2.39 Å) is similar to sulfide S-Zn (2.34 Å). Since the increase in the cluster size is kinetically controlled, the stronger the capping groups bond, the slower are they being replaced by sulfide ions, and thus the cluster growth terminates faster. In the other hand, the weaker are the capping bonds, the more easily the sulfide ions replace them, and the cluster grows for longer time until all sulfides are used, leaving larger clusters.

From the above discussion, it has been shown that XAFS results of the ZnS clusters combined with *chemical analysis* and X-ray diffraction measurements enabled the characterization of the cluster structure. The reduction of the second shell coordination number was explained using a model that described the cluster as consisting of a crystalline domain and a disordered domain; the later is related to the bond angle variation in Zn-S-Zn angles. The capping groups were shown to be bridging to the Zn surface atoms. Also, the number of capping atoms was found to be relatively insensitive to the cluster size, and thus the coverage is highest for the smallest clusters. Also it was shown that the identity of the capping cluster affects the coverage of the surface and the size of the synthesized cluster. The syntheses of thiophenol clusters and MPA capped clusters showed that size of the cluster can be controlled by simply varying the ratio of sulfide to the capping group in the clusters or by changing the pH of the reaction solution.

The interpretation of XAFS Zn-edge results in conjunction with the chemical analysis has enabled the calculation of the coordination numbers of the other elements in the sample. In the case of thiophenol, the Zn-edge first shell results combined with chemical analysis, verified the S-edge results and showed that if one only measures the Zn-edge XAFS and performs chemical analysis, then no need of S-edge data is required to obtain the first-shell coordination number. In the case of the benzeneselenol, the first shell Zn-edge XAFS verified the Se-edge results and also gave coordination numbers for sulfur. These important observations can be appreciated by noting the difficulty of measuring S-edge XAFS (and other low atomic number elements) which must be performed in the fluorescence mode and corrected for self-absorption effects.

Endnotes

1. N. Herron, Y. Wang, and K. H. Eckert, *J. Am. Chem. Soc.* **112**, 1322 (1990).

2.Samples were supplied by A. J. Bard, and the XAFS was collected by R. H. Felton, and L. Furenlid.

3. S. C. Abraham and J. L. Bernstein, *Acta Cryst.* **25,** 1233 (1969)

4. Y. S. Ding and S. L. Cooper, *Polymer Research at Synchrotron Radiation Sources* BNL-51847, 1985

5. I. G. Dance, A. Choy, and M. L. Scudder. *J. Am. Chem. Soc.* **103**, 1423(1984)

6. W.H McMasters, N. Kerr Del Grande, J. H. Mallett, J. H. Hubbell, **Compilation of X-Ray Cross Sections**, National Bureau of Standards.

CHAPTER V

SCANNED PROBE MICROSCOPIC IMAGING OF ZINC SULFIDE NANOCLUSTERS

Introduction

Zinc sulfide clusters were imaged with Scanning Tunneling Microscopy (STM) and with Atomic Force Microscopy (AFM). In the following sections the basic principles of STM and AFM are presented. Then the imaging experiments are described, the results are presented and discussed.

Basic Principles of Scanning Tunneling Microscope (STM)

The scanning tunneling microscope (STM) consists of a W or Pt-Ir alloy probe tip, which is attached to a piezoelectric transducer. When the tip is brought into close proximity of a conducting sample's surface, the wave function of the tip and that of the surface overlaps. When a bias voltage is applied between the tip and the sample, a current flow originates due to electron tunneling between the tip and the sample. The direction of the electron tunneling depends on the polarity of the bias voltage. When the probe tip is biased with negative voltage, electrons tunnel from the tip into unoccupied states of the sample. When the sample is biased with negative voltage, the electrons tunnel from occupied states of the sample in the tip probe.

By scanning the probe tip across small regions of the sample, the tunneling current is measured and amplified into voltage and compared with a reference voltage. The difference voltage is also amplified and used in a feedback loop circuit to drive the z piezo. The tip height is adjusted to keep a constant tunneling current. This mode of operation is the constant current mode and is the most used mode. Thus in this mode the tip height is recorded as a function of the x,y location, and a topographical map of the surface is obtained directly for any conducting surface, even for a non-atomically flat surface. The main disadvantage of this mode of operation is the finite response time of the feedback loop which limits the scan speed. Another mode of operation of STM is the constant height mode. In this mode the tip height is held constant, and the feedback loop is slowed down or completely turned off. The tip scans a region of the surface and measure the change in tunneling current as a function of x,y location. The rapid change in the tunneling current as a function of the location contains in it the topographic information. The main advantage of this method is the fast scanning rate which enables dynamic studies. On the other hand, extracting height information from the recorded variations in the tunneling current in the constant current mode is difficult because the dependance of the tunneling current on the distance is usually not known. Also this mode requires a flat surface, otherwise the tip would crash.

The tunneling current for metallic surface is exponentially related to the height according to the following equation:

$$I \propto I_o e^{-A\sqrt{\Phi}z} \tag{5.1}$$

where A = 1.025 $ev^{-1/2}$ $Å^{-1}$, Φ is the barrier height between the tip and the sample surface, and z is the gap distance. For a typical value of 4 eV for Φ, then a distance modulation of 0.1Å will cause the current to drop by 20%, and for a clean surface the STM gives an accurate height topography. The dependance of the current on the height becomes very complicated when an adsorbate is on the surface of the metal, and the height information becomes very difficult to interpret without understanding the electronic interaction of the adsorbate and the metal surface and their interactions with the tip.

Atomic Force Microscopy Basic Principles

The force microscope utilizes the force interaction between the tip and the sample to obtain image information. The tip is attached to a cantilever spring and is deflected in response to the force between the sample an the tip. The image is collected as the sample is scanned horizontally relative to the tip, and the z deflection of the tip as function of x,y location on the tip is recorded by a deflection sensor. The spring constants used are between 0.001 and 100 N/m and motions from 1 micron to 0.1 Å can be measured by deflection sensors.

There are two major modes used in obtaining the AFM image: The contact mode and the noncontact mode. In the noncontact mode, the tip is 10-100 nm from the sample. At such distances, Van der Waals, electrostatic, magnetic, or capillary forces can be sensed and give topographic and other information about the sample surface. At small

separations of ~1 Å, the tip is in contact with the sample. In this mode, ionic repulsive forces allow the surface topography to be traced with high resolution.

Under the above modes there are two sub-modes of operations: dynamic and static modes. In the static mode the tip bends in response to the force F which acts on the tip. The deflection distance is proportional to the force according to Hooke's law $F=c_B z$ where c_B is the spring constant, and z is the deflection distance. For a typical rectangular 1x10x100 μm^2 Si cantilever, the spring constant is 0.42N/m which allows a force of the order 10^{-10} to 10^{-6} N to be measured. The tip deflection can be kept constant by regulating the height of the sample relative to the tip. This mode is called the equiforce mode. The height profile is interpreted as surface topography. In another measurement mode ,the variable deflection mode, the sample height is kept constant, and the variation of the cantilever position is measured.

In the dynamic mode of operation the lever is oscillating close to its resonance frequency, and a distance dependant force F(z) shifts the resonance force. For a rectangular lever described above, the n^{th} frequency is approximated as:

$$f_n \sim 0.32\sqrt{\frac{c_B - F'}{m}} \qquad (5.2)$$

where c_B is the spring force constant and F' is the gradient of the force in the z direction. In this mode the feedback loop keeps the frequency constant (FM-detection) or keeps the amplitude constant (slope detection).

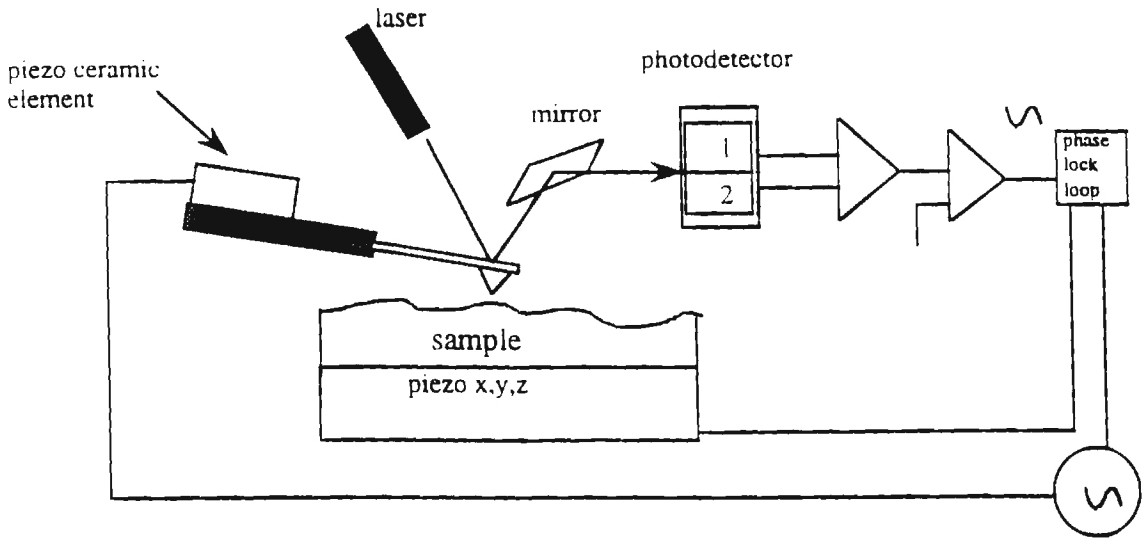

Figure 5.1: Atomic Force Microscope

Experimental

Solution Preparation of ZnSPH45 and ZnSNH20(pH12)

The ZnS clusters imaged with STM and AFM were ZnSPH45 (pH 8.5 samples) and ZnSNH20(pH 12) samples. The synthesis and characterization of these sample were explained in chapter IV. Aqueous solutions of these samples were prepared by heating the sample in deionized water for 12 hours at 90 °C under nitrogen. Optical spectra of these samples in water were obtained in a 1 cm quartz cell and are shown in Fig. 5.2. The optical spectra of these samples show a sharp peak at 295 nm for ZnSPH50 sample and 313 nm for ZnSAM20 sample. The concentrations of these samples were estimated as 0.3 mM (as ZnS) from the absorption spectra[1].

Preparation of Mg^{2+}- Modified Mica for AFM

Several 0.25 inch diameter disks of Muscovite Green mica (New York Mica Co.) were cleaved repeatedly by the tape press method and placed individually into 1.5 ml microcentrifuge tubes filled with 10 mM $MgCl_2$. The disks were allowed to submerge in the solution and stand overnight (~24 hr). Each disk was then removed, rinsed gently with nanopure water (18 MΩ-cm), and individually placed into another 1.5 ml microcentrifuge tube filled with nanopure water. The microcentrifuge tubes were capped, collected, and placed into a beaker filled with nanopure water. The beaker was then placed into an

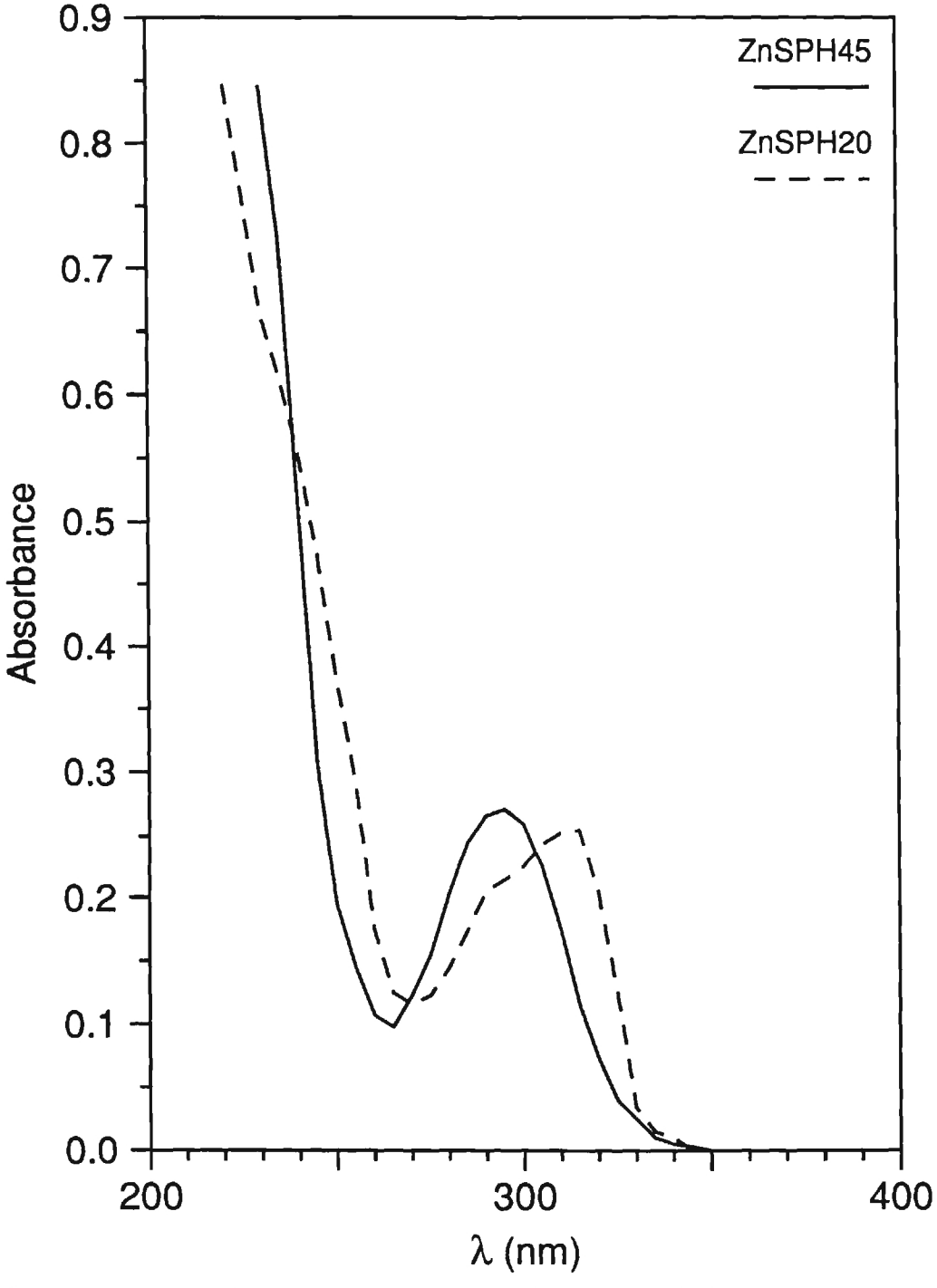

Figure 5.2: Absorption spectra in water for ZnSPH45 and ZnSNH20 samples.

ultrasonic bath and sonicated at room temperature for 30 min. Upon completion of sonication, the disks were removed from their respective microcentrifuge tubes, rinsed gently with nanopure water, blown dry with compressed gas (chlorofluorocarbons), and dried in vacuo (<10 mm Hg) at 110° C overnight (~18 hr). Upon cooling and removing from the disks from the vacuum oven, they were stored in a desiccator until used.

Preparation of Nanocluster Samples for AFM Imaging

The ZnSPH45 solution was diluted by mixing 10 μL of the ZnSPH45 solution with 90 μL of nanopure water (MΩ-cm). The solution was vortex-stirred for 5 sec in a microcentrifuge tube. A 15 μL aliquot of this solution was placed directly on a disk of Mg^{2+}-modified mica already glued to a 1.5 cm (diameter) steel shim. The sample was placed into a petri dish, covered, and allowed to stand for 5 min. The sample was then "wicked" dry with a Kimwipe and covered by inverting a 1 L tall-form beaker fitted with a gas inlet and outlet over the sample. A flow of dry N_2 (4 L/min) was inititiated through the beaker for 30 min before the sample was removed and placed on the AFM piezo for imaging.

Preparation of Gold Substrates for STM Imaging

Several 3/8 inch diameter disks of Au/mica (muscovite green mica with one side layered with ~2500 Å gold by vapor deposition at elevated temperatures) were allowed to soak in the surface modifier (5mM $HSCH_2CH_2COOH$ or $HSCH_2CH_2N(CH_3)_2$) for 1 hr. The disks were then gently rinsed with nanopure water (18.3 MΩ-cm) and placed individually into microcentrifuge tubes filled with the nanocluster stock solutions (i.e.

ZnSPH45 or ZnSNH20). The tubes were capped and allowed to stand overnight (~18 hr). The disks were then removed from their solutions, rinsed gently with nanopure water, "wicked dry" with a Kimwipe, and stored in covered petri dishes in a desiccator until imaged.

Imaging of ZnSPH45 Samples

A Nanoscope II (Digital Instruments) was utilized for imaging purposes. In the AFM imaging experiments, each of the samples were imaged under a minimum constant force (1-3 nN) as dictated by force curves obtained frequently during the imaging procedure. Humidity was kept well below 15% by applying a 1 L/min flow of dry N_2 to the imaging chamber at all times. Z-heights were obtained by examining 40nm X 40nm areas encompassing an individual nanocluster image and determining the Z-range between the lowest and highest pixels within the area. Figure 5.3 shows AFM images of ZnSPH45 sample that was prepared on Mg-treated mica surface. Figure 5.3 reveals that the imaged clusters are spherically shaped. The height distributions are shown in Fig. 5.4. The average height was 25 Å (σ = 5 Å). The AFM diameters were determined by measuring the maximum and the minimum widths of each cluster. The average diameter of the clusters was 36 nm which is much larger than expected. This large width is due to the effect of the large tip, as will be explained in the discussion section. No clusters were found on untreated mica surfaces.

The clusters were also imaged by STM on gold coated mica that was pre-treated with 2-dimethylaminoethanethiol hydrochloride ($(CH_3)_2NCH_2CH_2SH.HCL$). The gold sample was soaked for 24 hours in the aqueous cluster solution (pH=7.5) and rinsed by

dipping in water. After drying, the sample was imaged by STM in the constant current mode. The STM images revealed very stable, mostly spherical clusters with an average size of 47 Å (σ = 12 Å). When untreated gold samples were used, no STM cluster images were found. Also no clusters were found when 3-mercaptopropanoic acid treated gold was used. Figure 5.5 shows the STM images of ZnSPH45, and Fig. 5.6 shows the diameter distribution.

Imaging of ZnSNH20 Sample

Imaging by AFM of a freshly cleaved mica surface that was soaked in ZnSNH20 solution showed large clusters that were thought be due aggregation of the clusters. Immediately following, another freshly cleaved mica surface that was not treated with the ZnSNH20 solution was imaged. After several scans the clean surface was covered with clusters. These clusters were thought to be ZnSNH20 clusters transferred from the previous experiment by the tip. The clusters were spherically shaped and were easily moved by the AFM tip. Figure 5.7 shows an AFM image of these clusters, and Fig. 5.8 shows height distribution of the clusters. The average height was found to be 15 Å (σ = 2 Å). The average diameter was found to be 35 nm, which is clearly exagerated over the expected diameter. Imaging the ZnSNH20 sample on Mg-treated mica surface did not show the clusters.

STM imaging of the ZnSNH20 sample was successful only on 3-mercaptopropanoic acid treated gold surface. No clusters were found on untreated gold surfaces or an amine treated gold surface. Figure 5.9 show STM images of ZnSPH20

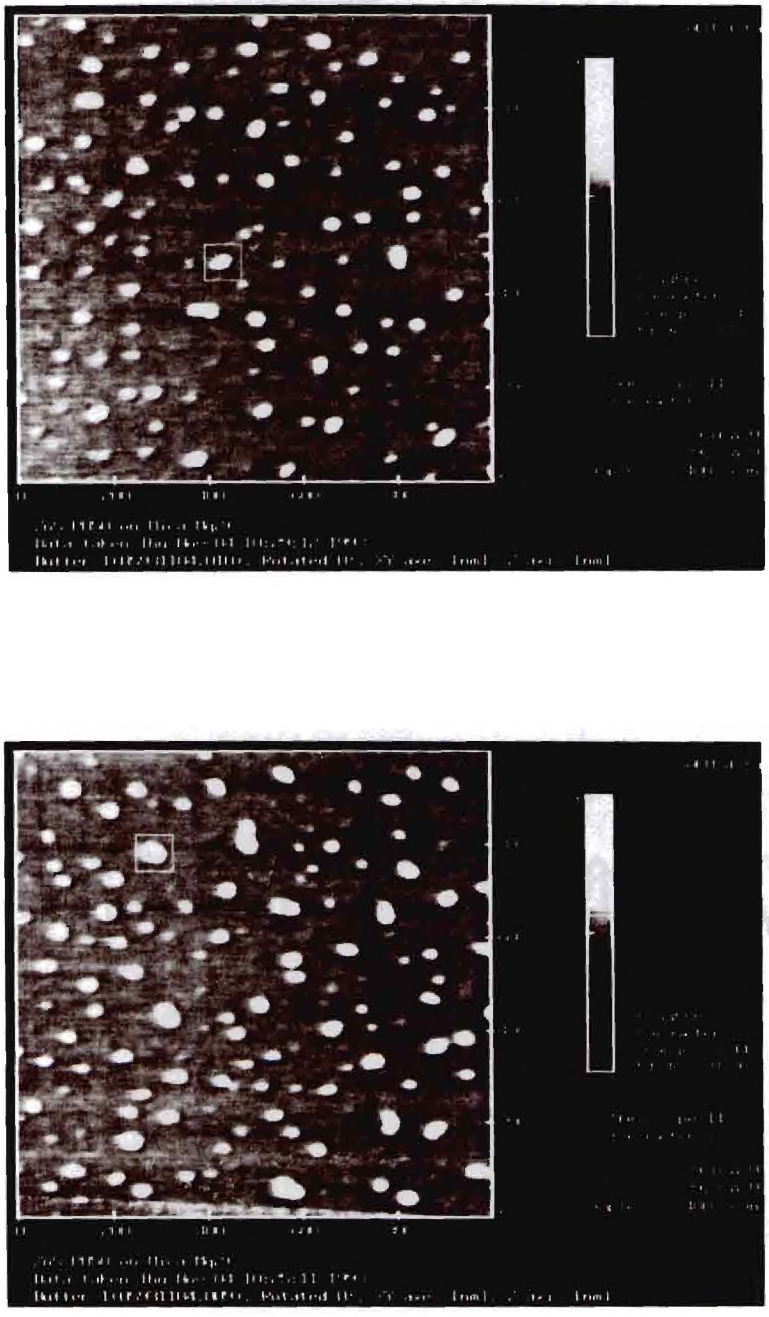

Figure 5.3. AFM images of ZnSPH45 clusters on Mg-treated Mica surface. Image dimensions are 900 nm x 900 nm.

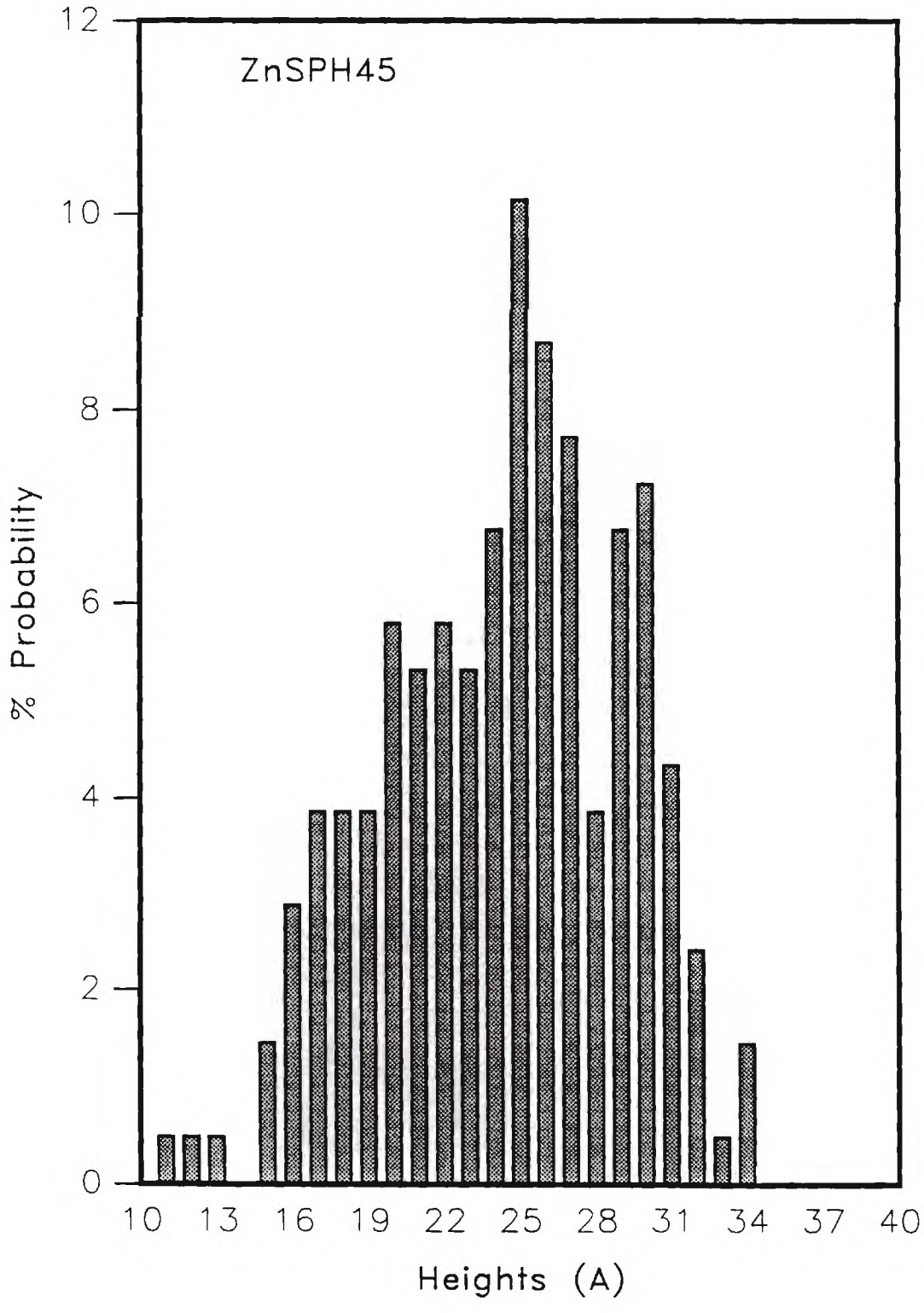

Figure 5.4. AFM height distribution of ZnSPH45 clusters on Mg-treated Mica surface. The average of 207 clusters is 25 Å, and σ is 5 Å.

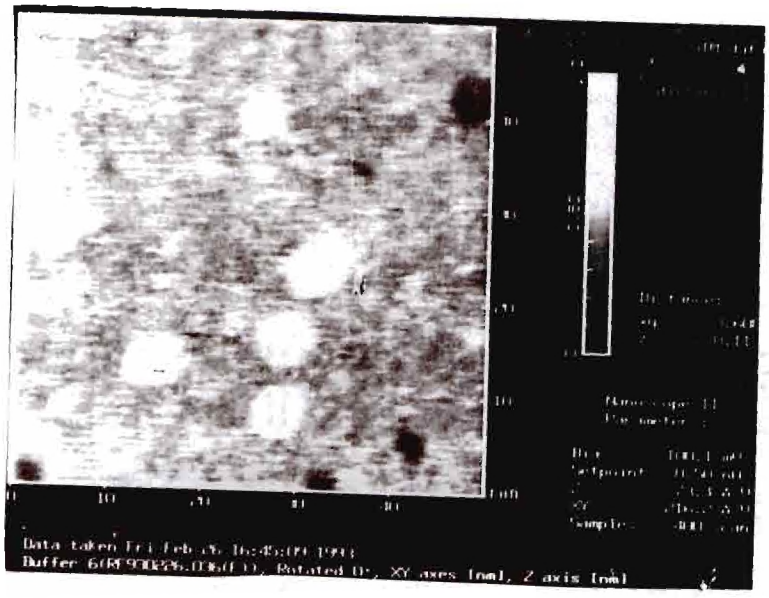

Figure 5.5. STM images of ZnSPH45 clusters on treated gold surface. The image dimensions are 50 nm x 50 nm.

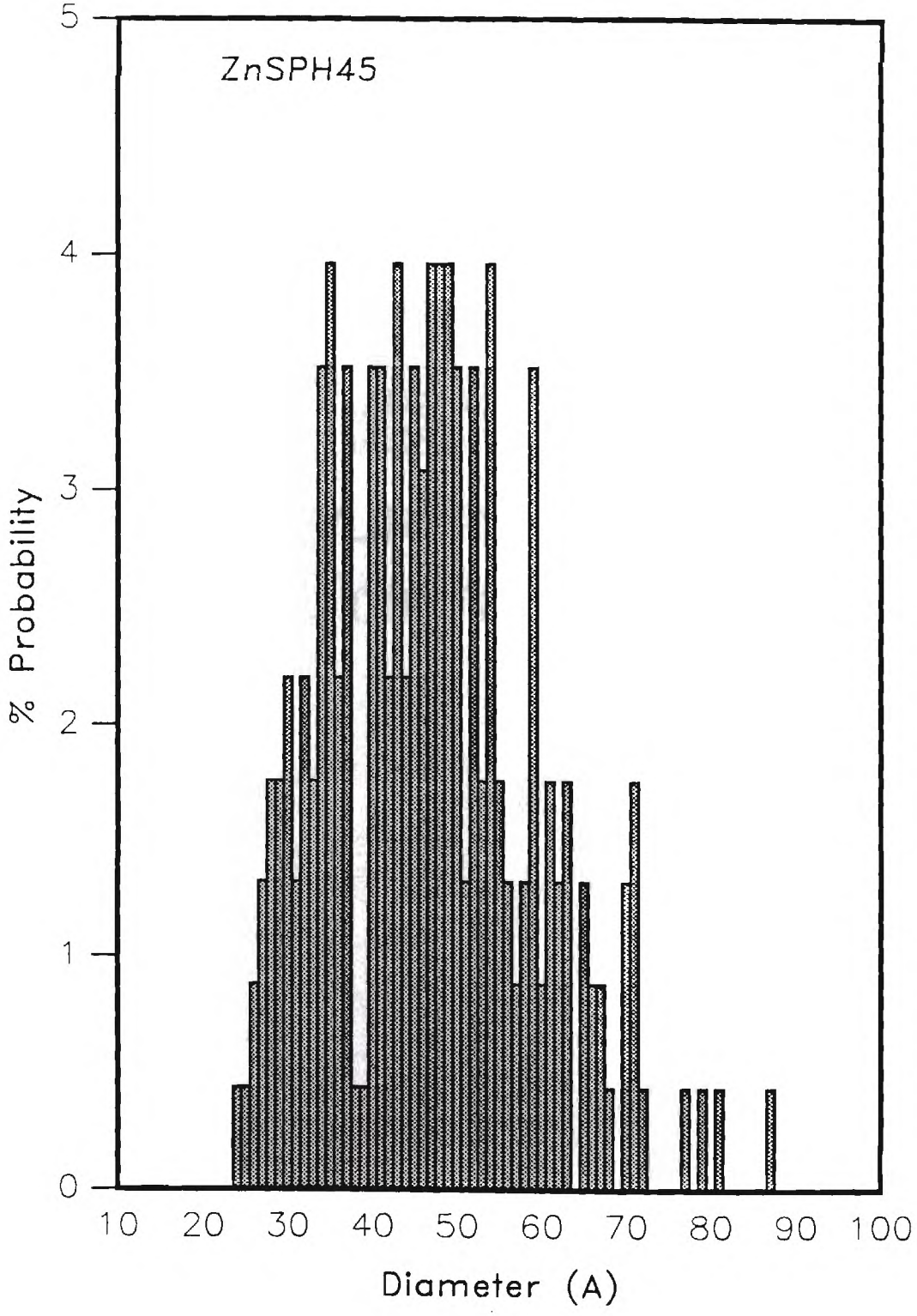

Figure 5.6. STM diameter distribution of ZnSPH45 clusters on treated gold surface. The average of 227 clusters is 47 Å, and σ is 13 Å.

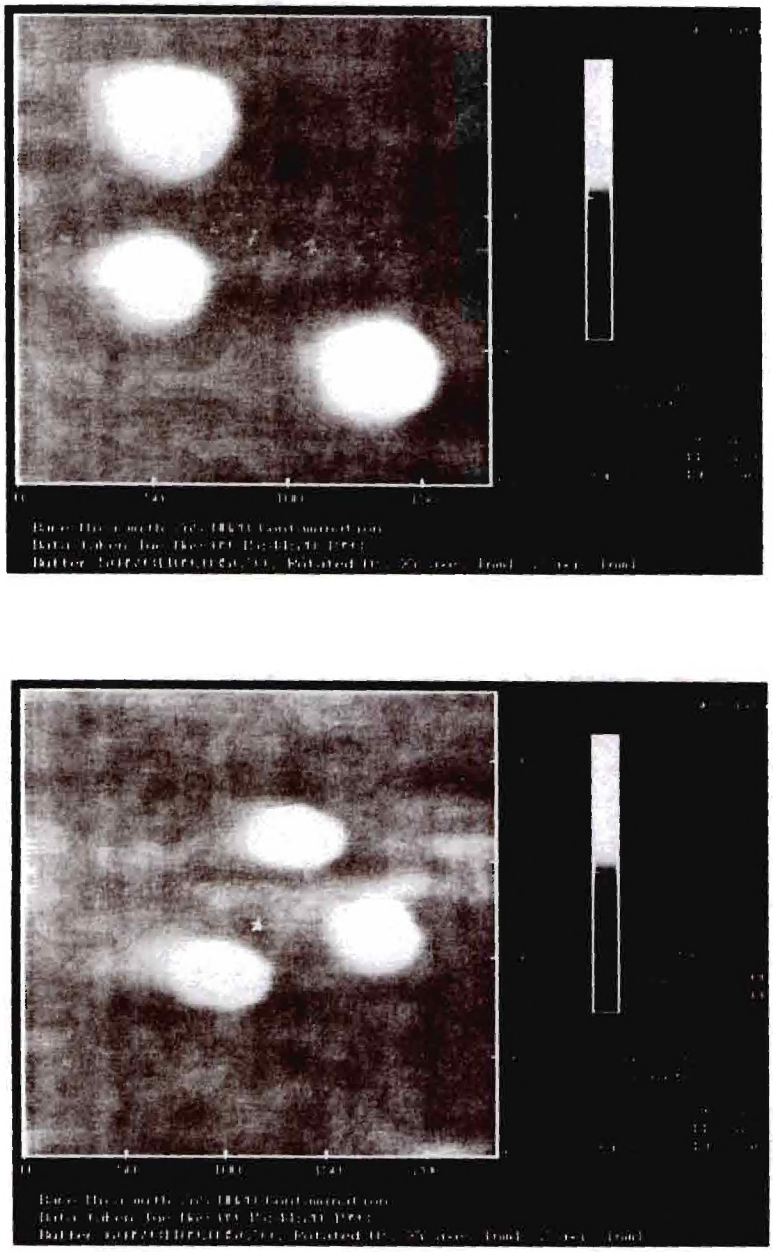

Figure 5.7. AFM images of ZnSNH20 clusters on Mica surface. Image dimensions are 160 nm X 160 nm (top), and 225 nm x 225 nm (bottom).

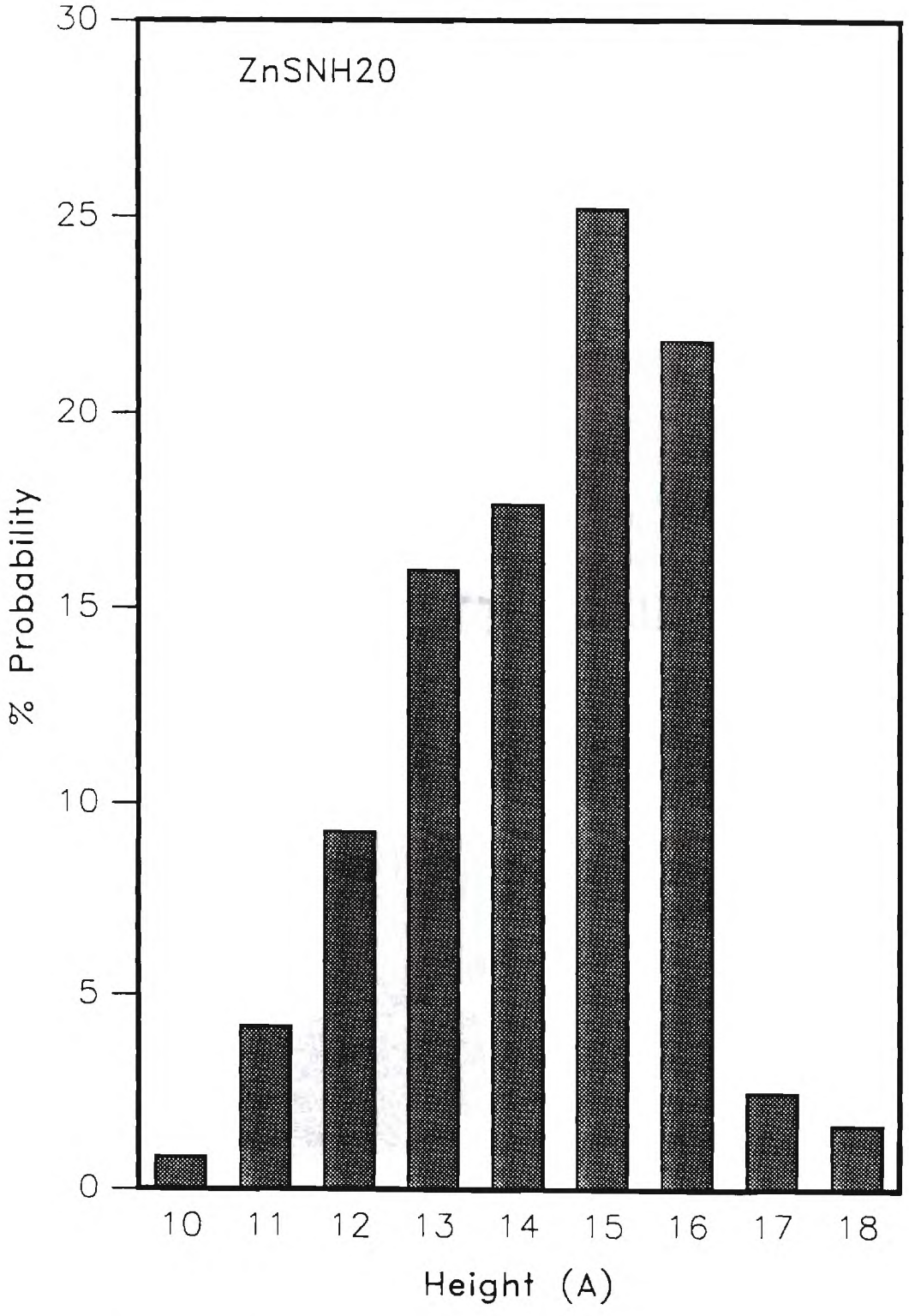

Figure 5.8. AFM Height distribution of ZnSNH20 clusters on Mica surface. The average height of 119 clusters is 15 Å and σ is 2 Å.

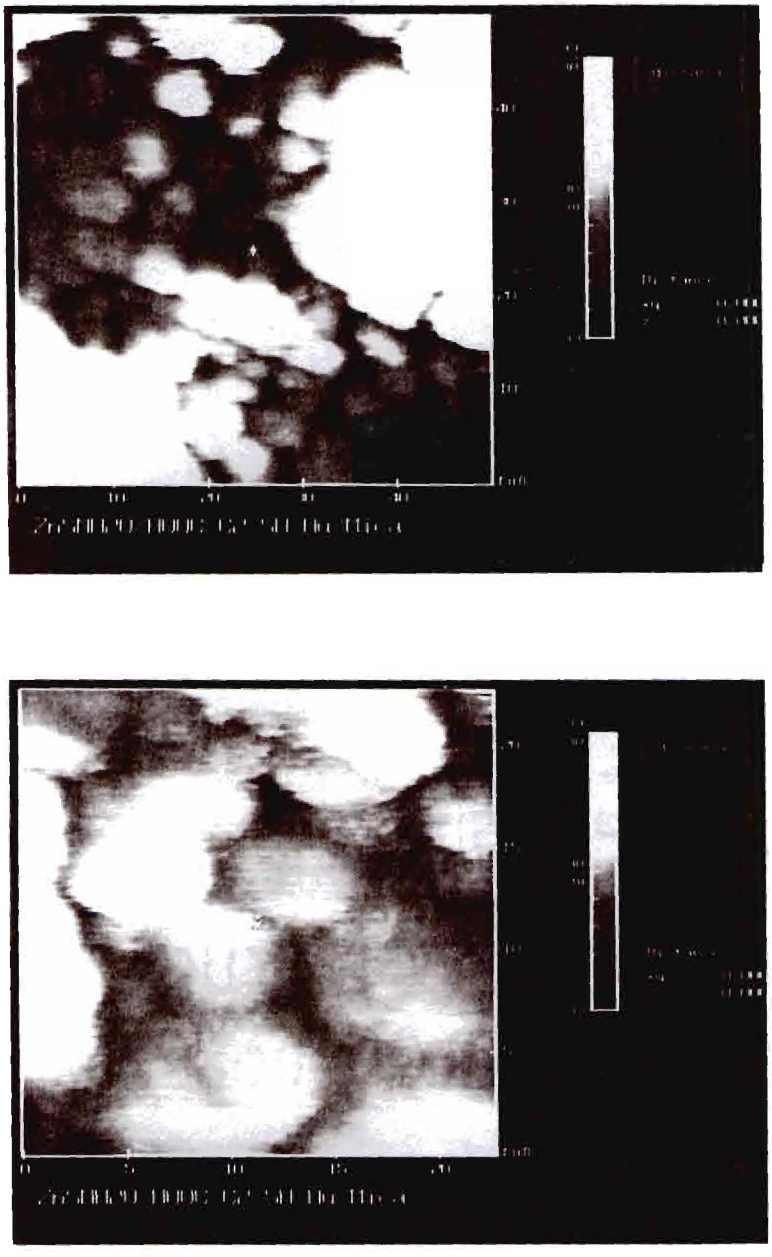

Figure 5.9. STM images of ZnSNH20 clusters on treated gold surface. the Image dimensions are 50 nm x 50 nm (top), and 22nm x 22 nm (bottom).

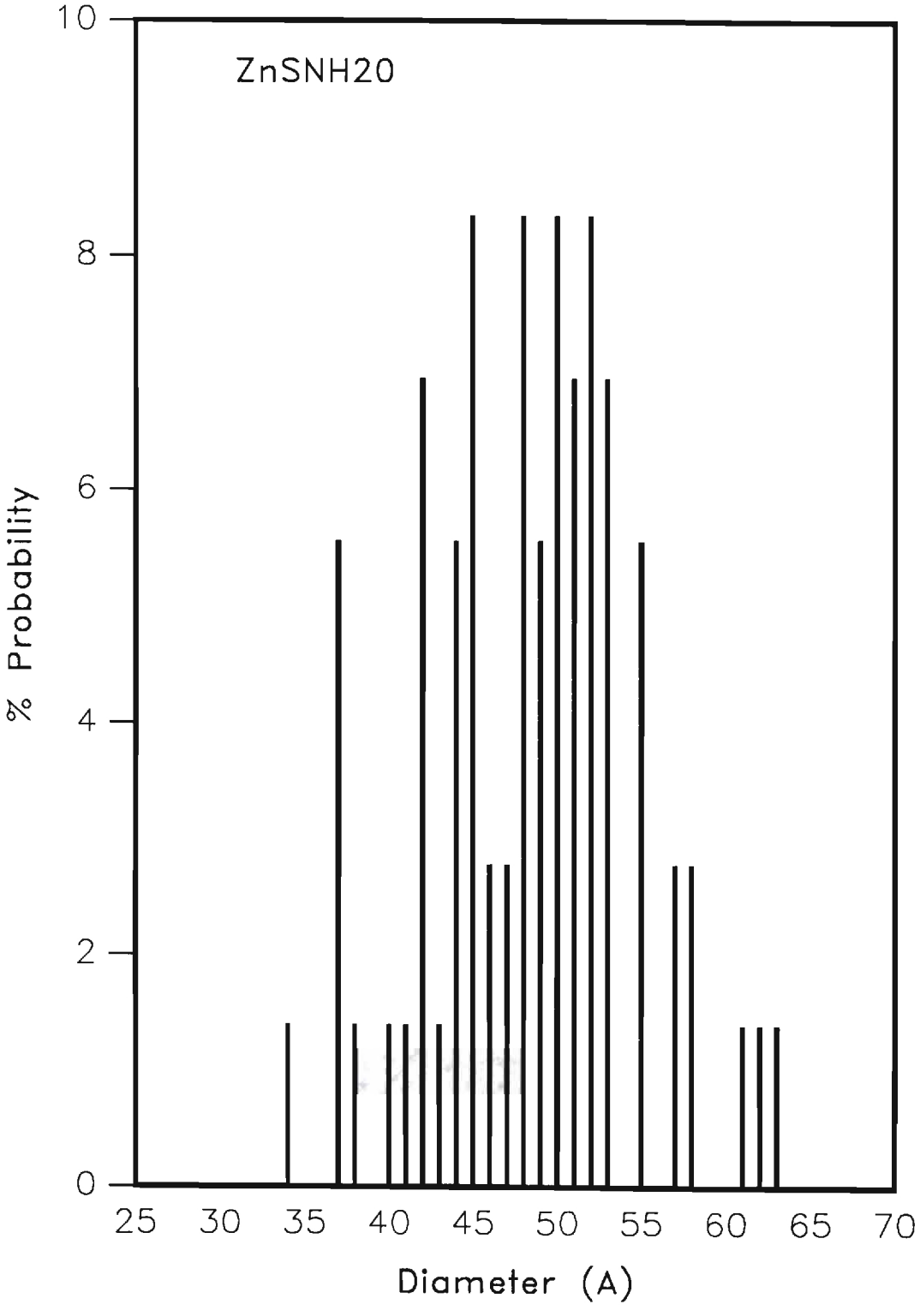

Figure 5.10. STM diameter distribution of ZnSNH20 clusters on treated gold surface. Average diameter of 72 clusters is 49 Å, and σ is 7 Å.

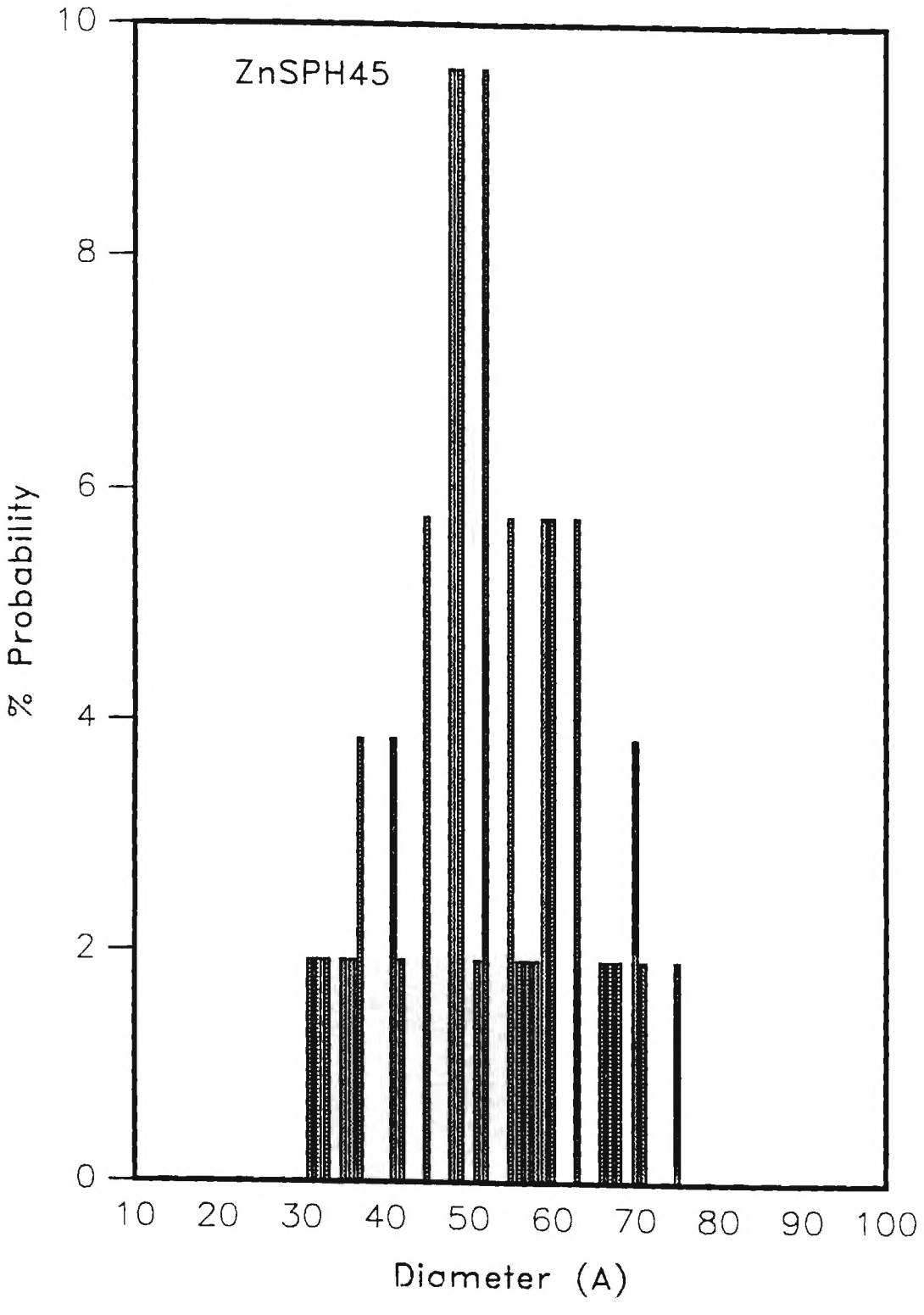

Figure 5.11. Corrected AFM diameter distribution of ZnSPH45 clusters on Mg-treated Mica surface. The average diameter of 52 clusters is 53 Å, and σ is 11 Å.

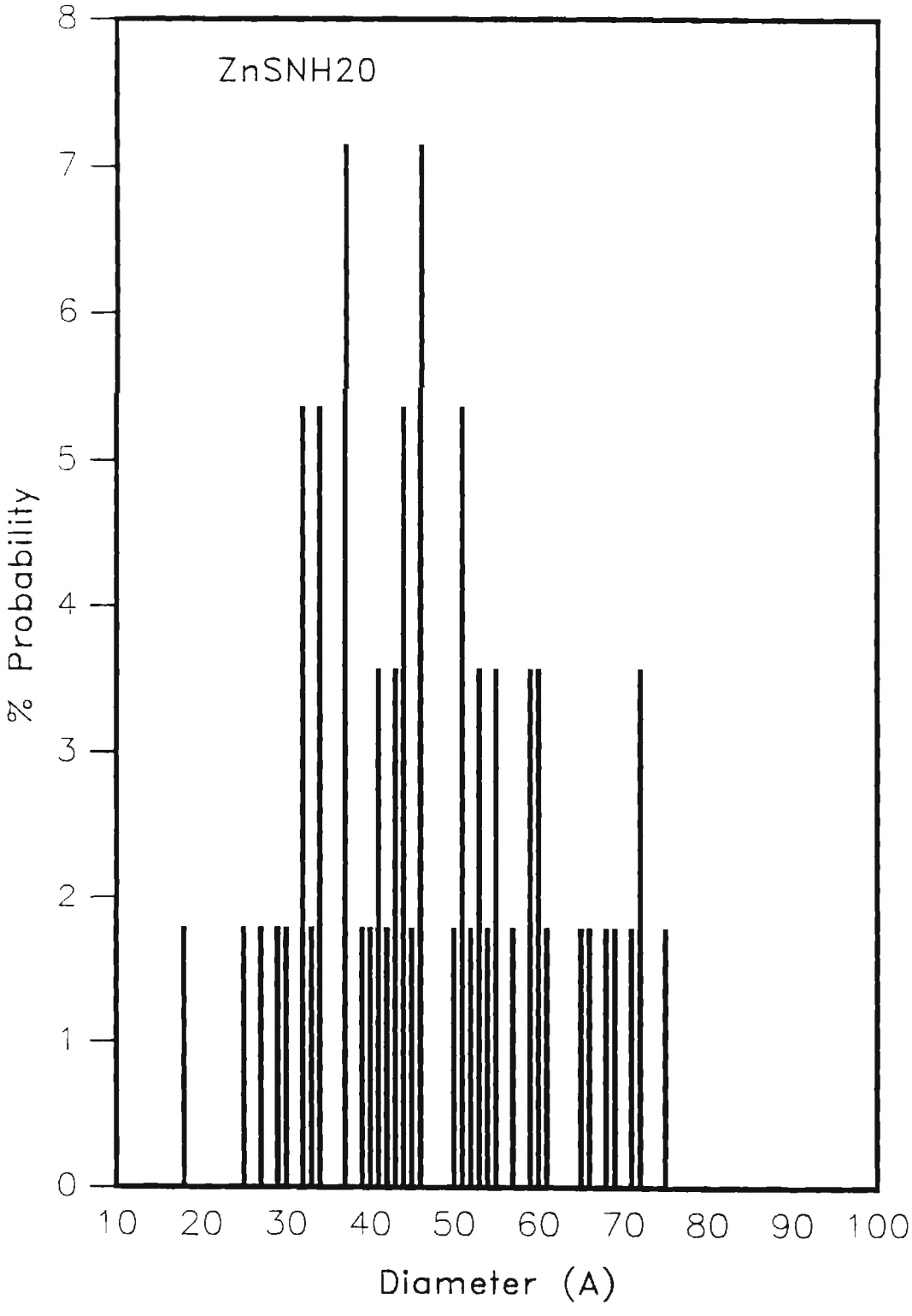

Figure 5.12. Corrected AFM Diameter distribution of ZnSNH20 clusters on Mica surface. The average diameter of 56 clusters is 48 Å and σ is 14 Å.

sample on acid treated gold surface and shows spherical clusters. The diameters of the clusters were measured as above for the ZnSPH45 clusters. The average diameter was found to be 49 Å (σ= 7 Å). Figure 5.10 shows the diameter distribution of ZnSNH20 clusters.

Discussion

The fact that the ZnSPH45 samples were only possible to image on Mg-treated mica and on an amine-treated gold surface suggests that the nature of the interaction between the cluster and the surface is mainly electrostatic. In the case of the amine-treated surface, the basic solution of the cluster(pH ~8.5) insures that the carboxylate groups of the cluster capping groups are deprotonated, causing the electrostatic interaction between positively charged amine of the surface and the negatively charged carboxylate of the capping groups of the clusters. In the case of the Mg-treated mica surfaces, the electrostatic interactions are between the negatively charged clusters and the positively charged mica surface. The positive charge of the mica surface is due to the replacement of potassium ions with magnesium ions on the surface. Also the fact the ZnSNH20 clusters were imaged only on an acid (3-mercaptopropanoic acid) treated gold surface and on freshly cleaved mica suggests that the interaction between the surface and the clusters are mainly electrostatic. The acidic solution (pH ~6)of the ZnSNH20 sample insured that the amine capping groups are protonated and thus are able to interact with the carboxylate groups of the modified surface. In the case of the mica surface, the interaction between the surface and the ZnSNH20 cluster is less well understood. However the lack of

adsorption on Mg-treated surface supports the fact that ZnSNH20 adsorption on acid treated surface is due to electrostatic interactions.

The STM diameter distributions (ZnSPH45: Avg. = 47 Å, σ = 13 Å; ZnSNH20: Avg. = 49 Å, σ = 7 Å) are in reasonable agreement with average sizes obtained from XRD (~40 Å). The AFM sizes are affected by the large imaging tip which gives larger apparent sizes. For small sizes, this effect can be satisfactorily modeled[2] with a spherical tip of radius R and a spherical particle of radius r. The apparent width can be shown[2] to be $4(rR)^{1/2}$. Thus to get an estimate of the cluster dimension, the tip radius should be measured. To do this, 5nm colloidal gold (Aurobeads G5) were imaged on Mg-treated mica. The width measurements were obtained as above. The AFM sizes were used to calculate the tip radius. The average tip radius was found to be 32nm with σ of 6 nm. This number is in agreement with the 30-50 nm reported in the literature[2]. This value was then used to calculate the AFM widths for ZnSPH45 and ZnSNH20 samples; the distributions are shown in Fig. 5.11 and 5.12, respectively. The corrected AFM average diameter for ZnSPH45 sample was found to be 53 Å (σ = 11 Å). For ZnSNH20 sample, the corrected AFM average diameter was found to be 48 Å (σ = 14 Å). These numbers are in good agreement with the STM numbers. The error estimation for corrected average diameters obtained from AFM is ~2 Å by assuming ±0.5 nm error in the uncorrected AFM diameters.

The AFM gave heights that are anomalously low even for the TEM calibrated 5 nm gold beads (Avg. = 25 Å, σ = 3 Å). Such results of low AFM heights are known in the literature, but no definitive explanations are available[3]. Some possible explanations

are that the heights are reduced due to interactions between the tip and the sample such as to modify the vertical movement of the tip by tilting the cantilever[4]. This modification of the movement of the tip causes the optical detector to register lower heights. Also the presence of water, due to humidity or from sample preparations, can cause capillary forces to tilt the cantilever, causing lower height values[4].

Endnotes

1.Rossetti, J. L. Ellison, J. M. Gibson, and L. E. Brus, *J. Chem. Phys.*, **80**, 4464(1984).

2. T. Thundat, X.-Y. Zheng, S. L. Sharp, D. P. Allison, R. J. Warmack, D. C. Joy, and T. L. Ferrell, *Scanning Microscopy*, **6**, 903(1992).

3. S. J. Eppell, F. R. Zypman, and R. E. Marchant, *Langmuir*, **6**, 2281(1993).

4. T. Thundat, R. J. Warmack, D. P. Allison, L. A. Bottomley, A. J. Lourenco, and T. L. Ferrell, *J. Vac. Sci. Tech. A*, **10**, 630(1992).

CHAPTER VI

CONCLUSIONS

The work presented in the previous chapters has clearly demonstrated the effectiveness of XAFS in the study of nanoclusters of ZnS and CdS; the results of the ZnS were very much different than that of the CdS. The ZnS clusters were always found in the cubic crystalline phase. The XAFS of ZnS clusters showed a relatively strong second shell that was much reduced from what was expected due to surface bond truncations. The reduction of the second shell was explained with a model that assumed the presence of a disordered layer of the cluster where bond angles vary and thus affects the apparent second shell coordination, but not the first shell. The XAFS second shell coordination number was used to calculate the thickness of the disordered layer. This thickness was found to be the largest for small clusters and in the order of a first shell distance . The effect of the capping group and number of capping groups were shown to affect the thickness of the disordered shell. Combination of the chemical analysis with XAFS coordination number allowed the calculation of the coordination number of the thiophenol capping group. This capping group was found to be mostly in a bridging bonding position rather than in a terminating position. To probe the geometry of the surface directly, ZnS clusters were synthesized with benzeneselenol as a capping group.

The coordination number of selenium with zinc was measured directly in XAFS and was found to be ~2 indicating a bridging position. XAFS analysis of the Zn-edge for the same compound gave an indirect method to calculate the coordination number of selenium. The results from both the selenium edge and the zinc edge gave consistent result for all the samples. The XAFS also provided valuable chemical information concerning the chemical stoichiometry of the clusters, when combined with analysis results, gave coordination numbers for edges that were not measured. The results of the ZnS showed that the capping of the surface in most clusters is incomplete. The smallest cluster however was almost completely passivated by the capping group; in larger clusters ~20% of the surface sites were capped. We have shown that a smooth range of cluster size can be prepared for ZnS ranging from 18 Å to 40 Å by using different ratios of capping group to sulfide in the reaction mixture. Alternatively, the adjustment of the pH of the mixture was shown to dramatically affect the size of the clusters. Clusters capped with terminal thiamine and thiocarboxylates were prepared and used for imaging using AFM and STM methods. The ZnSPH45 sample, which was capped with 3-mercaptopropanoic acid, was shown to stick with high coverage on Mg-treated mica surface. The ZnSNH20 sample, which was capped with 2-aminoethanethiol, was shown to stick on a 3-mercaptopropanoic acid treated gold surface. For both samples, the nature of the interactions between the clusters and the surface were electrostatic interactions. The widths obtained from AFM and STM were consistent and agreed with the XRD diameters, within the uncertainty of the measurements. Both samples were mostly spherical. The height information from AFM was anomalous.

The CdS results were less satisfactory. The clusters prepared in methanol/water solutions and capped with thiophenol showed mostly a wurtzite structure which was in contrast to the literature results. The size of these clusters were obtained from the absorption spectra. The XAFS did not show any second shell structure for these clusters, even for the largest cluster (~30 Å). The CdS clusters prepared in water and capped with 3-mercaptopropanoic acid was found to be of cubic phase only. The XAFS of these clusters show second shell structure for the largest cluster(~45 Å). Smallest clusters showed a very weak second shell. The reduction in the second shell was also modeled with the above model. The results showed a thicker disordered layer in the cluster of CdS than those of ZnS. The reaction conditions of the CdS clusters prepared in Nafion films were studied. Results have shown that the crystal structures of the cluster are a mixture of both the hexagonal and the cubic phases. The length of the reaction and the presence of water in the Nafion film during reactions were shown to affect the reaction very dramatically. We have learned that a reasonably small cluster can be prepared in solution. However, larger clusters were produced for reactions prepared by reaction with H_2S, if the film was relatively wet before the reactions. Fully reacted films, keeping the size of the cluster in the quantum confined range (<60 Å), are difficult to prepare because the length of the reaction time affects the size of the cluster. The XAFS of the Nafion grown cluster showed that the films had not reacted uniformly. XAFS results confirmed the idea that the diffusion of H_2S in the films is a very slow process in dry Nafion. The XAFS showed that the results can be only explained if the cadmium coordination was modeled such as to be either bonded to S or to O but not to both, indicating that the interior part of the films did not react with H_2S.

APPENDIX A

Table A.1. Spherical Nanocrystal Calculational Results for a Cubic ZnS Cluster (a = 5.2540 Å)

Diameter of the Cluster (Å)	Atom Type A/B	Number of Atoms of Each Coordination Type				Average 1st Shell Coordination Number	Average 2nd Shell Coordination Number
		Single	Double	Triple	Quadruple		
14	A	0	24	4	10	2.63	6.95
	B	0	0	12	16	3.57	4.86
15	A	0	0	24	14	3.37	7.58
	B	4	12	12	16	2.91	4.68
16	A	0	0	24	14	3.37	7.58
	B	4	12	12	16	2.91	4.68
17	A	12	6	12	38	3.12	7.41
	B	0	24	12	32	3.12	5.62
18	A	0	30	24	38	3.09	8.09
	B	0	0	36	44	3.55	5.97
19	A	0	30	24	38	3.09	8.09
	B	0	0	36	44	3.55	5.97

Diameter of the Cluster (Å)	Atom Type A/B	Number of Atoms of Each Coordination Type				Average 1st Shell Coordination Number	Average 2nd Shell Coordination Number
		Single	Double	Triple	Quadruple		
20	A	0	36	24	56	3.17	8.48
	B	0	12	24	68	3.54	6.23
21	A	0	0	36	80	3.69	8.90
	B	12	36	24	68	3.06	6.03
22	A	0	0	36	80	3.69	8.90
	B	12	36	24	68	3.06	6.03
23	A	12	24	36	92	3.27	8.63
	B	0	12	48	92	3.53	6.64
24	A	12	36	24	116	3.30	8.68
	B	0	36	28	116	3.44	6.79
25	A	0	48	60	128	3.34	9.15
	B	0	12	52	152	3.65	7.05
26	A	0	24	60	152	3.54	9.36
	B	0	36	52	152	3.48	7.04
27	A	0	0	60	276	3.75	9.46
	B	24	48	52	152	3.20	6.90
28	A	0	6	48	212	3.77	9.56
	B	24	60	52	176	3.22	7.15
29	A	4	30	52	212	3.58	9.42
	B	12	36	72	192	3.42	7.44

Diameter of the Cluster (Å)	Atom Type A/B	Number of Atoms of Each Coordination Type				Average 1st Shell Coordination Number	Average 2nd Shell Coordination Number
		Single	Double	Triple	Quadruple		
30	A	0	60	64	246	3.50	9.54
	B	0	36	72	252	3.60	7.87
31	A	0	0	88	282	3.76	9.73
	B	24	72	72	252	3.31	7.79
32	A	0	12	88	318	3.73	9.76
	B	0	96	72	288	3.42	8.07
33	A	0	60	84	346	3.58	9.84
	B	4	36	96	348	3.63	8.52
34	A	0	24	84	382	3.73	9.94
	B	28	60	96	348	3.44	8.41
35	A	12	96	84	384	3.47	9.75
	B	0	24	96	424	3.74	8.92
36	A	24	48	96	442	3.57	9.80
	B	12	48	108	436	3.60	8.97
37	A	0	60	120	502	3.65	10.03
	B	0	84	96	508	3.62	9.21
38	A	0	54	144	538	3.66	10.11
	B	0	60	132	544	3.66	9.37
39	A	12	54	132	586	3.65	10.07
	B	0	72	132	580	3.65	9.52

Diameter of the Cluster (Å)	Atom Type A/B	Number of Atoms of Each Coordination Type				Average 1st Shell Coordination Number	Average 2nd Shell Coordination Number
		Single	Double	Triple	Quadruple		
40	A	0	126	108	622	3.58	10.12
	B	12	24	132	652	3.74	9.74
41	A	12	60	120	712	3.69	10.17
	B	24	72	156	676	3.60	9.82
42	A	24	72	156	724	3.62	10.16
	B	0	72	132	748	3.71	10.03
43	A	0	60	144	844	3.75	10.33
	B	12	120	148	808	3.61	10.12
44	A	24	72	168	880	3.66	10.26
	B	0	108	136	892	3.69	10.39
45	A	0	132	180	952	3.65	10.37
	B	0	36	196	988	3.78	10.66
46	A	0	108	168	988	3.70	10.40
	B	12	60	196	988	3.72	10.65
47	A	4	96	160	1108	3.73	10.44
	B	36	108	168	1088	3.65	10.83
48	A	28	96	208	1132	3.67	10.83
	B	0	96	180	1160	3.74	11.07
49	A	24	102	196	1244	3.70	10.42
	B	0	120	192	1244	3.72	11.26

Diameter of the Cluster (Å)	Atom Type A/B	Number of Atoms of Each Coordination Type				Average 1st Shell Coordination Number	Average 2nd Shell Coordination Number
		Single	Double	Triple	Quadruple		
50	A	0	138	220	1328	3.71	10.51
	B	0	96	216	1352	3.75	11.48

APPENDIX B

Table B.1. Spherical Nanocrystal Calculational Results for Cubic CdS Cluster (a = 5.8180 Å)

Clusters Diameter (Å)	Atom Type A/B	Number of Atoms of Each Coordination Type				Average 1st Shell Coordination Numnber	Average 2nd shell Coordination Number
		Single	Double	Triple	Quadruple		
10	A	0	0	0	6	4.00	4.00
	B	12	0	4	0	1.50	2.75
11	A	4	0	4	6	2.86	5.14
	B	0	12	0	4	2.50	3.50
12	A	4	0	4	6	2.86	5.14
	B	0	12	0	4	2.50	3.50
13	A	0	0	4	10	3.71	5.14
	B	12	12	0	4	1.86	3.57
14	A	0	24	4	10	2.63	6.95
	B	0	0	12	16	3.57	4.86
15	A	0	24	4	10	2.63	6.95

Clusters Diameter (Å)	Atom Type A/B	Number of Atoms of Each Coordination Type				Average 1st Shell Coordination Numnber	Average 2nd shell Coordination Number
		Single	Double	Triple	Quadruple		
	B	0	0	12	16	3.57	4.86
16	A	0	0	24	14	3.37	7.58
	B	4	12	12	16	2.91	4.68
17	A	0	0	24	14	3.37	7.58
	B	4	12	12	16	2.91	4.68
18	A	12	6	12	38	3.12	7.41
	B	0	24	12	32	3.12	5.62
19	A	12	6	12	38	3.12	7.41
	B	0	24	12	32	3.12	5.62
20	A	0	30	24	38	3.09	8.09
	B	0	0	36	44	3.55	5.92
21	A	0	36	24	56	3.17	8.48
	B	0	12	24	68	3.54	6.27
22	A	0	36	24	56	3.17	8.48
	B	0	12	24	68	3.54	6.27
23	A	0	0	36	80	3.69	8.90
	B	12	36	24	68	3.06	6.09
24	A	12	24	36	92	3.27	8.63
	B	0	12	48	92	3.53	6.83
25	A	12	24	36	92	3.27	8.63
	B	0	12	48	92	3.53	6.83

Clusters Diameter (Å)	Atom Type A/B	Number of Atoms of Each Coordination Type				Average 1st Shell Coordination Numnber	Average 2nd shell Coordination Number
		Single	Double	Triple	Quadruple		
26	A	12	36	24	116	3.30	8.68
	B	0	36	28	116	3.44	7.06
27	A	0	48	60	128	3.34	9.15
	B	0	12	52	152	3.65	7.40
28	A	0	24	60	152	3.54	9.36
	B	0	36	52	152	3.48	7.31
29	A	0	0	60	176	3.75	9.46
	B	24	48	52	152	3.20	7.13
30	A	0	30	60	176	3.55	9.38
	B	12	36	52	176	3.42	7.46
31	A	4	30	52	212	3.58	9.42
	B	12	36	72	192	3.42	7.71
32	A	28	54	52	236	3.34	9.28
	B	0	24	60	252	3.68	8.32
33	A	0	60	64	246	3.50	9.54
	B	0	36	72	252	3.60	8.18
34	A	12	24	100	282	3.56	9.59
	B	0	60	72	288	3.54	8.39
35	A	0	60	88	318	3.55	9.79
	B	0	48	72	336	3.63	8.63
36	A	0	60	84	346	3.58	9.84

Clusters Diameter (Å)	Atom Type A/B	Number of Atoms of Each Coordination Type				Average 1st Shell Coordination Numnber	Average 2nd shell Coordination Number
		Single	Double	Triple	Quadruple		
	B	4	36	96	348	3.63	8.75
37	A	0	24	84	382	3.73	9.94
	B	28	60	96	348	3.44	8.62
38	A	12	96	84	394	3.47	9.75
	B	0	24	96	424	3.74	9.24
39	A	0	36	84	490	3.74	9.99
	B	36	72	120	436	3.44	9.05
40	A	0	60	120	502	3.65	10.03
	B	0	84	96	508	3.62	9.42
41	A	0	54	144	538	3.66	10.11
	B	0	60	132	544	3.66	9.59
42	A	12	54	132	586	3.65	10.07
	B	0	72	132	580	3.65	9.74
43	A	0	126	108	622	3.58	10.12
	B	12	24	132	652	3.74	10.01
44	A	12	60	120	712	3.69	10.17
	B	24	72	156	676	3.60	10.00
45	A	24	72	156	724	3.62	10.16
	B	0	72	132	748	3.71	10.25
46	A	36	96	144	772	3.58	10.10
	B	0	72	124	808	3.73	10.45

Clusters Diameter (Å)	Atom Type A/B	Number of Atoms of Each Coordination Type				Average 1st Shell Coordination Numnber	Average 2nd shell Coordination Number
		Single	Double	Triple	Quadruple		
47	A	24	72	168	880	3.66	10.26
	B	0	108	136	892	3.69	10.58
48	A	0	96	180	892	3.68	10.31
	B	0	84	172	904	3.71	10.61
49	A	0	108	168	988	3.70	10.40
	B	12	60	196	988	3.72	10.80
50	A	12	108	168	1024	3.68	10.37
	B	24	72	172	1024	3.70	10.87

VITA

Raed Saed Shorrosh was born to Saed and Samera Shorrosh on September 23, 1965 in Nazareth, Israel. After graduating from high school in Nazareth, he entered Cumberland College in KY. In 1998 he graduated with bachelors degree in chemistry and mathematics from Cumberland college. The same year he entered the graduate program at Georgia Institute of Technology, specializing in physical chemistry.